



HAL
open science

Dynamics of freely transported fibers in confined viscous flows: Role of shape and flexibility

Jean Cappello

► To cite this version:

Jean Cappello. Dynamics of freely transported fibers in confined viscous flows: Role of shape and flexibility. Physics [physics]. Université Paris Cité, 2020. English. NNT: 2020UNIP7136 . tel-03260710

HAL Id: tel-03260710

<https://theses.hal.science/tel-03260710>

Submitted on 15 Jun 2021

HAL is a multi-disciplinary open access archive for the deposit and dissemination of scientific research documents, whether they are published or not. The documents may come from teaching and research institutions in France or abroad, or from public or private research centers.

L'archive ouverte pluridisciplinaire **HAL**, est destinée au dépôt et à la diffusion de documents scientifiques de niveau recherche, publiés ou non, émanant des établissements d'enseignement et de recherche français ou étrangers, des laboratoires publics ou privés.

THÈSE DE DOCTORAT
de l'Université de Paris

Spécialité : Physique

École doctorale n°564: Physique en Ile-de-France

réalisée

au Laboratoire de Physique et Mécanique des Milieux Hétérogènes

sous la direction de Anke LINDNER et Olivia du ROURE

présentée par

Jean CAPPELLO

Sujet de la thèse :

**Dynamics of freely transported fibers in
confined viscous flows:
Role of shape and flexibility**

soutenue le 24 janvier 2020

devant le jury composé de :

M ^{me} .	CÉCILE COTTIN-BIZONNE,	UCBL	Rapportrice
M.	LUCA BRANDT,	KTH	Rapporteur
M.	HOWARD STONE,	Princeton University	Examinateur
M.	SIMON HAWARD,	OIST	Examinateur
M ^{me} .	CAMILLE DUPRAT,	Ecole Polytechnique	Invitée
M.	FRANÇOIS GALLAIRE,	EPFL	Invité
M ^{me} .	ANKE LINDNER,	ESPCI	Directrice de thèse
M ^{me} .	OLIVIA DUROURE,	ESPCI	Directrice de thèse

Résumé

L'étude des problèmes d'interaction fluide-structure à bas nombre de Reynolds en situations confinées est une étape fondamentale pour comprendre la locomotion de micro-organismes dans les sols ou dans des conduits biologiques ou biomédicaux mais aussi les mouvements des longues fibres optiques introduites dans des fractures rocheuses et utilisées comme sondes dans l'industrie pétrolière.

Dans ce travail de thèse, nous nous intéressons à la dynamique d'un système modèle, constitué d'une fibre libre transportée par un écoulement laminaire dans une cellule de Hele-Shaw. La hauteur de la fibre est voisine de la hauteur du canal et ce confinement a des conséquences importantes sur le transport des fibres, qui présente des propriétés très spécifiques, comme par exemple la dérive d'une fibre inclinée par rapport à l'écoulement. En raison des frottements visqueux avec les murs supérieur et inférieur du canal, la fibre agit comme un obstacle mobile et perturbe l'écoulement. Ces perturbations sont à l'origine d'une anisotropie des forces hydrodynamiques qui amènent à la dérive et aux oscillations de l'objet entre les murs latéraux du canal. La question à laquelle ce travail répond est la suivante : comment la dynamique de transport d'une fibre initialement droite et rigide est-elle modifiée lorsque celle-ci est remplacée par un objet plus complexe ? Nous avons choisi d'étudier le cas de fibres *flexibles* transportées par un écoulement visqueux en géométries confinées en nous concentrant sur les cas de fibres orientées perpendiculairement et parallèlement à l'écoulement. Les fibres perpendiculaires se courbent, et nous montrons que la flèche de la déformation est proportionnelle à un nombre élasto-visqueux. Nous caractérisons quantitativement l'influence du confinement sur la déformation. Les fibres parallèles se déforment et acquièrent une forme sinusoïdale dont l'amplitude décroît au niveau des extrémités. Nous mettons en évidence expérimentalement l'existence d'un seuil d'instabilité. Afin de compléter ce travail, nous avons choisi de nous intéresser au rôle de la géométrie dans le cas de fibres rigides. En ajoutant un bras supplémentaire à une fibre initialement droite nous obtenons une fibre en forme de L. Ce nouvel objet subit sous écoulement une rotation jusqu'à une orientation d'équilibre suivie d'une dérive lors de laquelle la fibre s'approche des murs latéraux du canal. Lorsque la fibre est suffisamment proche du mur, la dérive s'arrête et l'interaction entre l'objet et le mur est à l'origine d'une dynamique très riche. De plus, en jouant sur leurs propriétés de symétrie, nous montrons que nous pouvons contrôler de façon très robuste la trajectoire des particules.

Ces effets sont étudiés à l'aide d'expériences de microfluidiques combinées à des simulations numériques basées sur la résolution de l'équation de Brinkman modifiée. Nous contrôlons la géométrie, l'orientation et les propriétés mécaniques des particules d'hydrogels à l'aide d'une technique de micro-fabrication. Afin de caractériser le module d'Young et le coefficient de Poisson des hydrogels, nous avons développé deux nouvelles techniques

de mesure in-situ permettant d'accéder à ces propriétés sans avoir besoin de les extraire du liquide environnant.

Mots clés

FIBRES, CONFINEMENT, ECOULEMENT VISQUEUX, MICROFLUIDIQUE, MICROFABRICATION, CELLULE DE HELE-SHAW, INTERACTION FLUIDE-STRUCTURE, FLEXIBILITÉ, GÉOMETRIE, SYMÉTRIE, TRAJECTOIRE, CARACTÉRISATION MÉCANIQUE IN-SITU , MODULE D'YOUNG, COEFFICIENT DE POISSON

Abstract

Studying confined situations of fluid structure interactions in viscous flows is important to understand locomotion of micro-organisms in soils or medical conducts as well as the movement of long fibers in fractures, where they are used as in-situ probes in oil recovery.

Here we look at the dynamics of a model system, constituted by a fiber freely transported in a Hele-Shaw cell by pressure-driven flows. The fiber height is comparable to the channel height and the confinement plays a fundamental role in fiber transport, which shows specific characteristics, as for example lateral drift for fibers not aligned with the flow. Due to viscous friction with top and bottom walls particles act like moving obstacles and induce strong flow perturbations. These perturbations are at the origin of anisotropy in the friction forces leading to lateral drift and oscillatory movement between lateral walls. In this PhD we study how the transport dynamics are perturbed when the particle becomes more complex than a straight and rigid fiber. Two degrees of complexity have been studied in parallel: we either add flexibility to the fiber or we change its shape and focus our investigations on their transport. Flexible fibers perpendicular to the flow bend while parallel fibers deform in a sine shape that flatten out at the edges. We show that the bending of the perpendicular fiber is proportional to an elasto-viscous number and we fully characterize the influence of the confinement on the deformation of the fiber. Experiments on parallel flexible fibers reveal the existence of an instability threshold. Complementary, we change the shape of the fiber by adding an additional arm, forming an L-shaped fiber. This induces fiber rotation until a stable equilibrium orientation. Lateral drift is subsequently observed until the interaction with side walls becomes important. Tuning the fiber asymmetry allows for a precise control of particle trajectories, including the approach of side walls, robust even against small perturbations.

We investigate these effects with a combination of well-controlled microfluidics experiments and simulations using modified Brinkman equations. We control the shape, orientation and mechanical properties of our particles using micro-fabrication techniques. To characterize the Young's modulus and the Poisson's ratio of the hydrogels we develop two independent novel in-situ measurement methods.

Keywords

FIBERS, CONFINEMENT, VISCOUS FLOW, MICROFLUIDICS, MICROFABRICATION, HELE-SHAW CELL, FLUID-STRUCTURE INTERACTION, FLEXIBILITY, COMPLEX SHAPE, SYMMETRY, TRAJECTORY, IN-SITU MECHANICAL CHARACTERIZATION, YOUNG'S MODULUS, POISSON'S RATIO

Remerciements

Quel exercice difficile de remercier en seulement quelques lignes toutes les personnes qui se sont investies, m'ont accompagné, aidé et fait grandir durant ces trois années de thèse. Vous êtes nombreux, je risque sûrement d'oublier du monde, ne m'en veuillez pas.

Tout d'abord, je tiens à remercier mes deux fantastiques directrices de thèse Anke Lindner et Olivia du Roure. J'ai énormément appris auprès d'elles au cours de ces années de doctorat : scientifiquement, sur la façon d'aborder un problème, contourner les difficultés, en découvrir de nouvelles, se poser les bonnes questions... Bref, à faire de la science! J'ai eu la chance de profiter des qualités incroyables qu'elles ont démontrées envers moi: enthousiasme, confiance, disponibilité, bienveillance et gentillesse... Merci ! J'aimerais également remercier Camille Duprat, ma "troisième directrice de thèse". Camille a été présente du début à la fin, de la prise en main du système expérimental jusqu'aux analyses de résultats et interprétations. Pour tout cela, je la remercie énormément. Anke, Olivia et Camille n'ont pas "seulement" dirigé ma thèse. Elles étaient déjà présentes lors de ma 3^{ème} année de licence, lorsque j'ai réalisé mon stage de fin d'années auprès d'elles, stage qui m'a donné par la suite envie de revenir au PMMH pour la thèse.

Pour les simulations numériques et les modélisations, j'ai eu la chance de profiter de l'expertise de François Gallaire. Travailler avec François a été une expérience formidable: c'est une personne très enthousiaste, curieuse et précise, qui a toujours su trouver le temps de discuter, m'aider et proposer de nouvelles idées, malgré son emploi du temps chargé ! Et bien sûr, j'aimerais remercier Mathias Becher, post-doctorant chez François, avec qui j'ai eu le plaisir de collaborer durant toute ma thèse. Sans Mathias, ce manuscrit serait sûrement plus court de moitié tant il m'a apporté scientifiquement.

Un grand merci à Simon Haward, président du jury, avec qui discuter est toujours un plaisir. Et merci aussi pour cet excellent Whisky Japonais ! Je témoigne toute ma reconnaissance à Howard Stone pour avoir accepté d'examiner mon travail et pour les discussions stimulantes et constructives qui ont suivi la soutenance. Howard a joué un rôle important pour moi dans ma décision de faire une thèse. C'est en effet à la suite d'un stage à Princeton sous sa direction (et celle d'Alban Sauret et de François Boulogne) que je me suis passionné de la physique des fluides. J'aimerais aussi remercier Cécile Cottin-Bizonne et Luca Brandt pour avoir accepté de juger mon travail et de rédiger les rapports, et pour toutes leurs questions et remarques très enrichissantes.

Je remercie ensuite le laboratoire PMMH qui m'a accueilli pour la première fois en 2014 pour un stage court de L3. Fort de cette belle expérience, j'y suis retourné en stage

de 6 mois en M2 et comme lorsque l'on aime, on ne compte pas, j'y suis resté pour la thèse. Cela fait donc presque quatre ans que je fais partie du laboratoire, et c'est vraiment un endroit fabuleux. L'ambiance est incroyable, et les générations de doctorants qui s'y succèdent ont su garder celle-ci très joviale et bienveillante. Je remercie Philippe et Damien, directeurs du laboratoire, pour leur super travail, aussi bien dans la gestion quotidienne du laboratoire que lors du déménagement. évidemment, le quotidien du laboratoire doit aussi énormément à Fred et Claudette (et David qui a remplacé temporairement Claudette) : elles sont incroyablement efficaces et rendent les tâches administratives toujours plus simples (ce qui n'est pas une mince affaire !).

Essayons maintenant de citer les doctorants et post-doctorant qui m'ont accompagné au cours de mes trois ans de thèse. Il y a, bien sûr, tous les membres du groupe : Marine, qui m'a accueilli lorsque j'étais en stage, m'a appris à prendre en main le système expérimental, et avec qui j'ai collaboré par la suite pour l'étude sur les fibres en "L". Bien plus qu'une mentor, Marine est devenue une amie avec qui j'ai partagé beaucoup de délires et de potins ! Il y a aussi Yanan, qui associe une extrême gentillesse et des qualités scientifiques impressionnantes, et qui est toujours là pour expliquer de nouvelles choses ou donner des conseils (toujours avisés !). J'aimerais évidemment citer Charles, qui m'a pris sous son aile et m'a intégré au sein du groupe et du labo. Nous avons partagé énormément de super moments : des soirées foot au voyage à Denver pour l'APS, suivi des vacances à NYC... tu vas beaucoup me manquer ! J'aimerais aussi remercier Francesca et Lucie, les deux "mamans" du groupe : arrivées presque en même temps que moi, elles m'ont toujours apporté leurs conseils sur beaucoup de points et de questions ! Je remercie aussi Lucas (le maître des hélices) qui va soutenir sa thèse dans un an et demi, Martyna et Noa avec qui je suis allé en conférence en Slovénie, rendant le séjour très agréable, ainsi qu'Andreas et Zhibo. Bien sûr, je n'oublie pas Lars, qui commence sa thèse et qui prend en main le système expérimental à une vitesse impressionnante. Merci pour les relectures minutieuses de mon manuscrit. Je suis sûr que tu vas faire une super thèse ! Francesco, également, qui me donne envie de rester un peu plus pour avoir l'occasion de partager encore quelques bières ensemble ! Et enfin Vincent, qui a fait un super travail lors de son stage chez nous, je te souhaite le meilleur pour la suite et j'espère avoir de tes nouvelles très vite:).

Je remercie tous les doctorants et post-doctorants, et en particulier les membres du bureau. Le bureau a commencé avec Gaspard et Benoit, deux personnes avec qui j'ai lié une incroyables amitié et avec qui j'ai tout partagé ; le boulot, les problèmes plus personnels, les (très/trop nombreuses) bières ! Vous me manquez déjà, mais je suis sûr que l'on restera en contact malgré la distance, on a partagé trop de moments pour que l'on s'éloigne ! Le bureau s'est ensuite agrandi et a accueilli PH, toujours là pour lancer un nouveau débat passionné ! Merci pour tout le travail de psychologie de fond que tu as mené pendant 3 ans sans t'essouffler. Vinrent ensuite Hector, le roi du vélo qui a fait germé chez moi une nouvelle passion, Mathias, et les parties de pétanque et discussions foot, et César, le papa fou toujours prêt à faire la fête. Arrivés après le déménagement à Jussieu, ils ont contribué à rendre le bureau encore plus agréable et festif ! Tous les 6, vous êtes de super copains !

Mes pensées vont aussi aux autres doctorants, déjà là lorsque je suis arrivé : Eliot, Vincent (Vincenzo), Thibault (Lord Chastel : le doyen), Floflo, Thomas et Alex pour

les anciens. Mais aussi Adeline alias Sara Conor, Jessica, Salomé et Yacine pour "moins anciens". J'aimerais aussi citer les doctorants de ma promo : les deux JoJos et les soirées aux arènes, Gaby et sa voix de baryton qui fait léviter ses particules, Valentin, Reda, Emmanuel, Ambre et Roberta. Puis les nouvelles générations de doctorants : Manon, notre super déléguée des doctorants, toujours très dynamique, Saurabh le poète, Armand le blagueur, Bill le conteur, et les nouvelles pousses: Mousse, Chloé et Magda, Maika, Dirach, Tian, Tao, Sébastien, et tous les autres.

J'aimerais aussi remercier les copains de l'ENS : Hugo, Gab, Alex, Mich-Mich, Comby, Loulou et Arthur, qui m'ont accompagné dans l'expérience de la thèse dans des domaines tous très différents ; ainsi que mes amis de longue date Maxime, Yann et Seb, qui ont toujours été là pour moi !

Mes pensées vont aussi Annick, J.P. et Clara. J'ai beaucoup de chance d'avoir trouvé une belle famille aussi gentille et sympa !

Je voudrais dire un grand MERCI à ma famille, mes parents mes sœurs, et mes cousins et cousines. Vous êtes d'un soutien sans faille et toujours là ! Et merci beaucoup pour tout ce que vous avez fait lors de la soutenance, grâce à vous la journée s'est passée à merveille et le pot était incroyable (et je crois très apprécié par tout le monde, notamment la dégustation de limoncello et les plats de lasagnes !).

Bien sûr je tiens à remercier Anouk. Merci d'avoir partagé toutes les émotions par lesquelles on passe en trois années de thèse. Merci d'avoir essayé de comprendre ce que je faisais, de m'avoir encouragé, soutenu, félicité, fait relativiser. Tu m'as fait me rendre compte de ce qui était vraiment important :) !

Contents

Résumé	i
Abstract	iii
Remerciements	v
Introduction	xi
I State of the art	1
I.1 Flow at low Reynolds numbers: theoretical framework	2
I.1.1 The Reynolds number	2
I.1.2 The Stokes equations	3
I.1.3 Sedimentation of a sphere	3
I.1.4 The Stokeslet	4
I.2 Sedimentation of an isolated fiber: coupling between the particle configuration and its trajectory	4
I.2.1 Slender body theory	5
I.2.2 Sedimentation of straight fibers in a quiescent fluid	6
I.2.3 Sedimentation of slender objects with complex geometries	7
I.3 Effect of confinement by bounding walls	9
I.3.1 Confinement due to top and bottom walls	10
I.3.2 Effects of lateral walls	13
I.4 Flexible fibers	16
I.4.1 The Euler-Bernoulli equation	16
I.4.2 The elasto-viscous number	18
I.4.3 Sedimentation of flexible fibers	18
I.4.4 Flexible fibers in confined geometries	21
I.4.5 Shear and compressive flows	22
I.5 Conclusion	23
II Materials and methods	25
II.1 Fiber fabrication	26
II.1.1 Particle fabrication principle	26
II.1.2 Fabrication protocol	27
a) The experimental setup	27
b) Channel geometry	28

c)	Mask design	29
d)	Optical focusing	29
e)	Oligomer solutions	29
II.1.3	Particle geometry	30
a)	Two-dimensional geometry	30
b)	Three-dimensional geometry	31
II.2	Flow control	33
II.3	Data acquisition and image analysis	34
II.3.1	Image acquisition	34
II.3.2	Fiber shape and position	34
II.3.3	Velocity measurements	34
II.4	Mechanical characterization	35
II.4.1	Young's modulus of PEGDA hydrogels	36
II.4.2	Measurement techniques	37
a)	<i>In situ</i> characterization	37
b)	Cantilever experiment	40
c)	Microindentation method	41
d)	Compression tests	42
III	Novel <i>in situ</i> techniques to measure mechanical properties	43
III.1	Measurements of Young's modulus	44
III.1.1	Description of the method	44
III.1.2	Modelling	45
III.1.3	Experimental results	48
III.1.4	Conclusion	52
III.2	Characterization of the Poisson's ratio of the hydrogels	53
III.2.1	Experimental protocol	53
III.2.2	Analysis	55
III.2.3	Results and discussions	56
a)	Validation of the method	56
b)	Limitations	57
c)	Transient regime.	59
d)	Dependence of the Poisson's ratio to solvent composition	60
III.3	Opening and conclusive remarks	60
IV	Bending of a flexible fibers transported in a confined viscous flow	63
IV.1	Observations	64
IV.2	Experimental setup and geometrical arrangement	65
IV.3	Physical mechanisms and scaling arguments	66
IV.4	Influence of the side walls	68
IV.5	Fabrication of flexible fibers	68
IV.6	Modeling	70
IV.6.1	3D model	70
IV.6.2	2D depth-averaged model	71
IV.6.3	Boundary conditions	74
IV.6.4	Numerical implementation	74

IV.6.5 Model validation and assessment	75
IV.7 Results	76
IV.7.1 Mechanism of fiber deformation	76
IV.7.2 Fiber deflection as a function of the elasto-viscous number	80
IV.7.3 Effect of the confinement	81
IV.8 Conclusion	84
V Buckling instability of a freely transported fiber in a micro-channel	87
V.1 Observations	88
V.2 Presentation of the experimental setup	88
V.3 Results	89
V.3.1 Spatio-temporal evolution	89
V.3.2 Wavelength characterization	90
V.3.3 Amplitude dynamics	93
V.3.4 Angular frequency and phase velocity	95
V.4 Modeling	96
V.4.1 A naive approach	96
V.4.2 A more realistic model	100
V.4.3 Linear stability analysis	102
V.5 Conclusion and perspectives	103
VI Controlling transport dynamics of confined asymmetric fibers	107
VI.1 Motivation and experimental observations	108
VI.2 Problem formulation and methods	110
VI.3 Results	112
VI.3.1 Dynamics in laterally unbounded channel	112
VI.3.2 Equilibrium orientation angle and drift angle	115
VI.3.3 Trajectories and impact of the lateral walls	118
VI.4 Conclusion	121
VII Conclusion	123
A Microfluidic channel fabrication	129
A.1 Fabrication of the channel mold	129
A.2 Fabrication of the all-PDMS microfluidic channels	130
B Cantilever experiment	131
C Convergence of numerical simulations	133
D Velocity of a freely transported parallel fiber	135
D.1 Presentation of the system	135
D.2 Pressure force acting on the fiber	135
D.3 Force on the top and bottom of the fiber	136
D.4 Force on the lateral sides of the fiber	136
D.5 Determination of the fiber velocity	136

Bibliographie

Introduction

Fibers and suspensions of fibers have been a paramount source of interest since many thousands of years, as they are omnipresent in nature and of broad use in industry. Paper fabrication [1] is the older of these industries. The invention of paper - thin sheets fabricated from plantlike fibers - is attributed to China during 140 to 87 B.C. Papermaking knowledge moved out from China to the Arabic world and arrived in Europe through Sicily and Spain in the XIIth century. Figure 0.1 shows the entangled structure of fibers of a paper sheet observed with scanning electron microscopy. The oil industry also makes extensive use of fibers, from fiber suspensions used to seal leaks in rock fractures to single optical fibers introduced into these rock fractures as *in situ* probes. In this case, confinement due to the shallow structure of the fractures plays an important role in fiber dynamics during insertion and during removal from the fracture. This situation of confined geometries is also relevant to a broad range of fields. For example, in industries where injection processes in porous media are needed [2] or in biomedical sciences where there is a lot of interest in the locomotion of microorganisms such as sperm cells [3] in soils or in medical conduits.

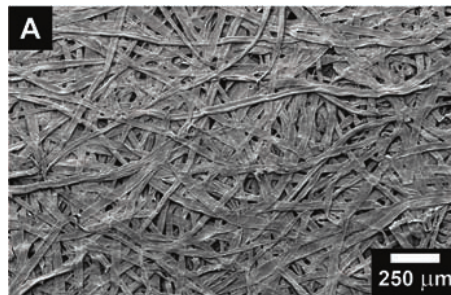


Figure 0.1: Scanning electron micrograph of ordinary paper made from wood pulp fiber. Figure extracted from [4].

Situations where an object interacts with a flow are called fluid-structure interaction problems: the flow makes the object, here a fiber, reorient, rotate or change its shape if flexible and in return the presence of the object in the fluid has an impact on the flow. The richness of fluid-structure interaction problems emerges from the non-trivial coupling between the object reorientation or deformation and the flow perturbation.

These topics, of very fundamental interest, have also many practical applications: one of those is, for instance, the sorting of particles which is of major importance in the

biomedical field or in the food industry. To answer these particular questions, in the last decade, a lot of effort have been put onto the design of microfluidic tools (hydraulic channels of characteristic height of the order of tens to hundreds of microns) aiming to sort particles according to their shapes or flexibility [5, 6, 7].

In this thesis, we primarily focus on fluid-structure interaction problems in confined viscous flows (i.e. where inertia is negligible). Our work benefited from the rich literature on the dynamics of isolated fibers in viscous flows. Such investigations started with Jeffery [8], who described in 1922 the motion of an elongated object in a shear flow (more details are given in chapter I). This work has been followed by studies on the dynamics of sedimenting fibers in viscous fluids, which have largely profited from the slender-body theory [9, 10] developed in the 70's. This theory is used to approximate the flow field around an elongated object and hence the force exerted by the fluid on the body (see section I.2.1 of chapter I). However, little is known on the transport of isolated fibers in confined geometries. Semin *et al.* studied the interactions of a fixed cylinder confined between two parallel walls. They focused on the calculation of the drag force exerted on the fiber as a function of its orientation parallel or perpendicular to the flow [11, 12]. This work has been followed by the investigations of Berthet *et al.* [13, 14] on free rigid fibers transported in confined microchannels by an external viscous flow. Similar to Semin *et al.*, Berthet *et al.* focused on the two simple configurations of fibers oriented parallel or perpendicular to the flow direction. Both of these works shed light on the role of the fiber confinement on its dynamics. Confinement, here, needs to be understood in two ways, firstly the flow is nearly two dimensional as it takes place in a channel of Hele-Shaw geometry (channel of height much smaller than width). Secondly, the fiber occupies almost all the channel height and is thus confined by the channel top and bottom walls.

The work of Berthet *et al.* performed at PMMH has been enabled by the development in the group of Patrick S. Doyle of an *in situ* technique of fabrication of hydrogel particles directly inside a microchannel [15, 16]. This technique enables the fabrication of objects of different and well controlled shapes and allows for a good control of the particle position and orientation.

Uspal *et al.* [17] used this experimental technique to study the impact of the shape of a particle on its transport dynamics in confined geometries. Using particles composed of two disks bridged to each other, they showed that the particle trajectory is controlled by the symmetry properties of the object. Up to our knowledge, this study is the first investigation of the coupling between geometry and trajectory of particles transported by an external flow in a confined geometry.

Here, starting from the study of Berthet *et al.* [13, 14], we ask how the transport dynamics are perturbed when going from an initially straight and rigid particle to a more complex object. Two directions have been studied here: we either add flexibility to the object and focus our investigations on the deformations of perpendicular and parallel fibers during their transport by an external viscous flow in confined geometry. Complementary, we also choose to change the shape and study the trajectory and the transport dynamics of rigid "L-shaped" fibers.

The first chapter of this manuscript reviews past studies on isolated fibers evolving in

viscous flows or fluids. Bridging the gap between the flow dynamics of a single fiber to collective fiber behavior is outside the scope of this work. We will thus restrict this review on the dynamics of individual fibers. First, we introduce a dimensionless number which compares viscous forces and inertia, named Reynolds number, and we present some basic properties of flows at low Reynolds number i.e. flow where inertia is negligible. Among the rich literature on fibers in flows, we choose to review studies on the sedimentation of rigid fibers with different shapes, in the second section of the chapter. This allows us to introduce important notions such as drag anisotropy and to discuss the impact of the geometry of a particle on its trajectory. We then present investigations on fibers interacting with a viscous flow in a confined geometry. In the last section of the chapter, we introduce the theoretical framework used to describe the flexibility of an elongated object. We show that in any system where a flexible fiber interacts with a viscous flow the fiber deformation scales with a dimensionless parameter - the elasto-viscous number - comparing the viscous forces to restoring elastic forces. Finally, we present studies on the dynamics of flexible fibers sedimenting in quiescent fluids and investigations of the deformation, by an external flow, of a fixed fiber in confined geometries. We also briefly discuss the buckling of flexible fibers in compressive flows.

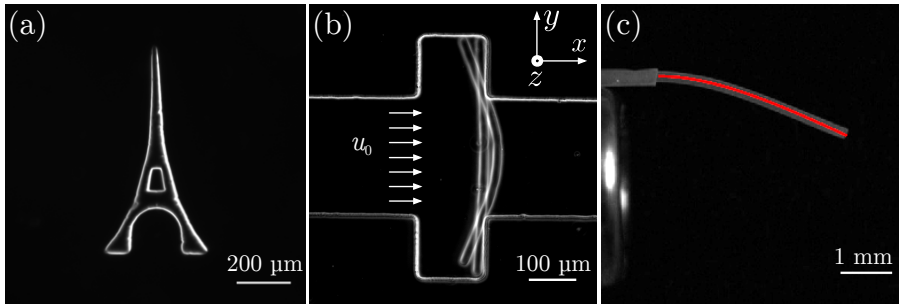


Figure 0.2: (a) Picture of an Eiffel tower particle fabricated into the microchannel using a photolithography technique. (b) and (c): Characterization of Young's modulus using an *in situ* technique (b), or a cantilever experiment (c).

The second chapter is dedicated to the description of the technique used to fabricate our fibers directly inside micro-fluidic channels. The principle of the technique and the experimental protocols are detailed, followed by a description of the geometrical characteristics of the hydrogel particles. To give an indication of the strength of the versatility/accuracy of the particle synthesis, we created a particle resembling the Eiffel tower (Figure 0.2 (a)). We then discuss the mechanical properties of these particles, present the method chosen to tune their Young's modulus and describe four different experimental techniques to measure these Young's moduli (two of them are shown in Figures 0.2 (b) and (c)). For each technique we discuss pros and cons. We show that it is very difficult to measure the Young's modulus of very soft hydrogels without extracting them to a dry environment. As a consequence, the role of the surrounding fluid and possible swelling effects cannot be taken into account. This highlights the need of a novel measurement method of Young's moduli of very soft hydrogels in the presence of a surrounding fluid.

The third chapter, is divided in two sections. The first section describes a novel mea-

surement technique allowing for *in situ* determination of the Young's modulus of very soft particles. A trapezoidal particle is pushed through a constriction by means of an external flow and eventually reaches an equilibrium position (while the flow is still on). In the constriction the particle is compressed by the channel's lateral walls. Measuring its geometry before and during compression enables us to derive its Young's modulus. Figure 0.3 (a) shows a superposition of pictures of an undeformed and deformed trapezoidal particle. In the second section of the chapter, we describe another independent technique allowing for the determination of the Poisson's ratio of the hydrogels. We use rectangular particles fabricated in a wide channel that we compress uni-axially by moving them to a narrower region of the channel. Again, measurements of the deformation enable us to determine the Poisson's ratio of the particle. Figures 0.3 (b) and (c) illustrate the experiment. This technique is used to characterize hydrogels of different compositions.

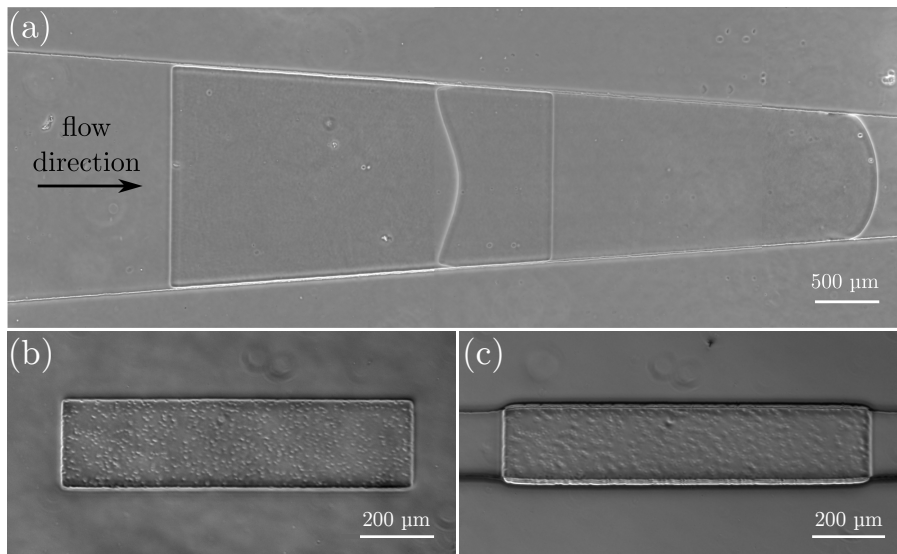


Figure 0.3: Mechanical characterization of the hydrogels. (a) Superposition of a trapezoidal particle just after fabrication and when pushed through the constriction and compressed by the lateral walls. This experiment is used to determine the Young's modulus of the hydrogel. (b) and (c): Picture of a rectangular particle in its undeformed (b) and deformed (c) state. From the deformation of the particle one can derive the Poisson's ratio of the hydrogel.

In the fourth chapter, we study the deformation of a free, flexible fiber transported by an external viscous flow in a confined geometry. We focus on the simple configuration of a fiber oriented perpendicular to the flow direction. Figure 0.4 illustrates the transport and the deformation of a flexible fiber. Due to the finite length of the fiber and the resulting edges effects, it experiences a non-homogeneous drag force. The variations of the drag force along the fiber deforms the latter. Combining well controlled experiments using our microfluidic tools together with numerical simulations - based on the resolution of the Brinkman equation supplemented with a gap flow model - we characterized the deformation of the fiber and we quantitatively describe the impact of the confinement.

The study presented in this chapter has been published in [18].

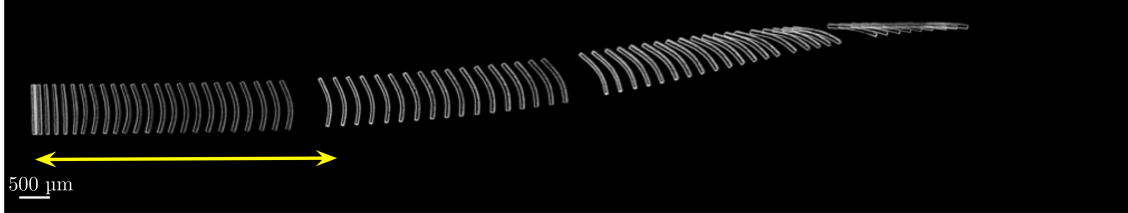


Figure 0.4: Chronophotography of a transported and deformed flexible fiber initially oriented perpendicular to an external flow. The yellow arrow indicates the bent state of a deformed fiber perpendicular to the flow. The fluid flows from left to right.

The fifth chapter describes the transport dynamics of flexible fibers oriented parallel to the flow direction. We show that under certain experimental conditions fibers deform into a wavy sine shape that flattens out towards the fiber ends (see Figure 0.5). This instability is observed only for very long fibers (the length must be almost one order of magnitude larger than the observed wavelength). We characterize the shape of the fiber and we extract, from the temporal evolution of the amplitude of the deformation, the characteristic growth time of the perturbation for different fiber geometries, flow strengths, and mechanical properties of the fiber. Other dynamical quantities such as the angular frequency of the wave and its phase velocity are also characterized experimentally. In the last section of the chapter we present models aiming to describe the origin of the instability and predict the wavelength.

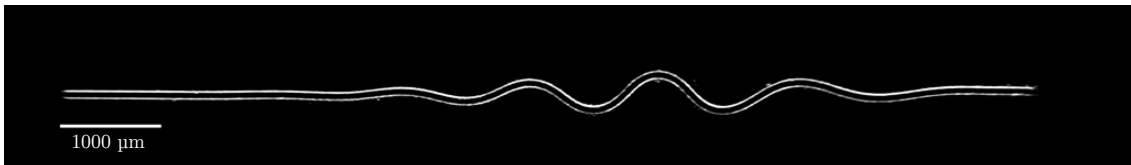


Figure 0.5: Picture of a parallel fiber transported in a confined geometry by an external flow. The fluid flows from left to right.

In the sixth chapter, we study the impact of the shape of a particle on its trajectory. We investigate geometries with different properties of symmetry: straight fibers, T-fibers and L-fibers. We primarily focus on the most complex shape: the L-fibers which do not have any axis of symmetry. Experimental chronophotographies of L-fibers transported by an external flow in confined geometries are shown in Figure 0.6. The particle rotates, until it reaches an equilibrium orientation and then drifts toward one of the walls of the channel. We characterize the dynamics of this rotation and the equilibrium configuration, both numerically - using again the modified Brinkman equation - and experimentally, for very wide channels. We then focus on the interaction of the particle with the lateral walls of the channel and show that straight fibers oscillate laterally, T fibers are either pushed toward the channel center or toward the lateral walls (depending on the lateral confinement) and L-fibers are always captured by the lateral walls. The study led to the

publication [19].

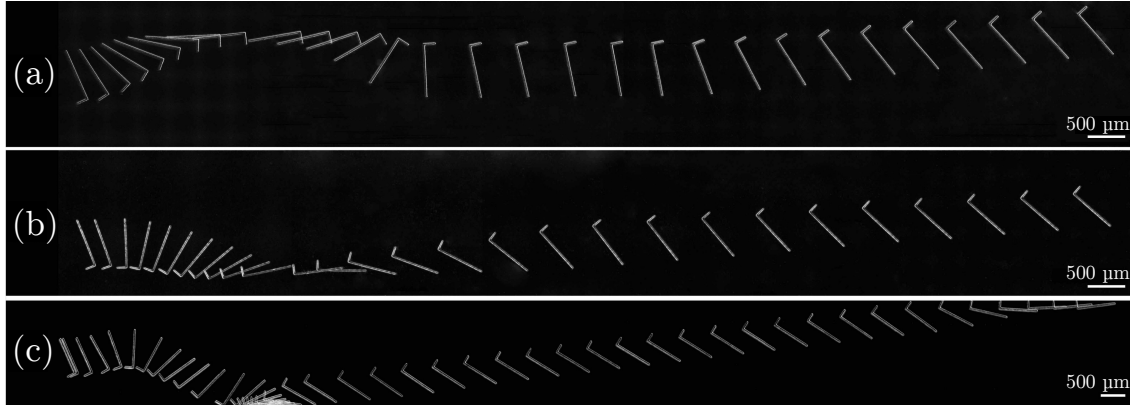


Figure 0.6: Experimental chronophotographies of transported L-fibers fibers of different geometries and initial configurations. The fluid flows from left to right.

The last chapter concludes this thesis. We give a general conclusion of the work presented in the manuscript and the main results obtained in each project. This discussion is followed by a presentation of the different outlooks that emerge from our work.

Experimental and numerical methods are detailed in appendices [A](#) and [C](#). And the appendices [B](#) and [D](#), present analytical calculations.

Collaborations

All the experiments presented in this study have been done in close collaboration with Camille Duprat from LadHyX (Polytechnique, Palaiseau).

The numerical simulations and discussions presented in chapters [IV](#) and [VI](#) have been performed in collaboration with François Gallaire and Mathias Bechert from LFMI (EPFL, Lausanne). Close discussions with them, also, enabled the study presented in chapter [V](#). The experiments presented in chapter [III](#) have been carried out together with Vincent d’Herbement, intern in the group, and the experiments of chapter [VI](#) are the results of a collaboration with Marine Daïeff, former PhD student in the group.

Chapter I

State of the art

In this chapter we give a review of some of the important studies on the transport dynamics of objects in viscous flows or fluids that are relevant for our study.

We start this review with a quick presentation of the flow at low Reynolds numbers, introducing the theoretical framework used in our studies.

We then focus on the coupling between the shape of a rigid particle and its trajectory. The example of sedimentation is used to present important notions such as the drag anisotropy for an elongated object and the impact of the symmetries of a particle on its trajectory.

The discussion is followed by a presentation of studies on the dynamics of confined particles i.e. particles confined by the top and bottom walls of a microfluidic channel. This situation shares some similarities with sedimentation. Indeed, in confined geometries one also observes a drag anisotropy with all its consequences, as for instance the drift of a fiber or the reorientation of an asymmetric particle.

In the last part of the chapter we discuss the role of the flexibility of a slender object on its dynamics. We present the Euler-Bernoulli theory used to describe the fiber deformation. We introduce the elasto-viscous number, a dimensionless parameter that compares the effects of hydrodynamic forces and the effects of restoring elastic forces. We finish the review with the presentation of studies on the dynamics of flexible fibers in these two flow geometries: quiescent fluids (sedimentation) and plug flow (confined geometry) and we also briefly touch on the discussion of fibers evolving in a shear flow.

I.1 Flow at low Reynolds numbers: theoretical framework

The velocity field \mathbf{u} and the pressure p in a Newtonian fluid (a fluid with constant viscosity μ for any shear rates), incompressible and of homogeneous density ρ can be described by the continuity and the Navier-Stokes equations [20]:

$$\nabla \cdot \mathbf{u} = 0 \quad \text{and} \quad \rho \left(\frac{\partial \mathbf{u}}{\partial t} + \mathbf{u} \cdot \nabla \mathbf{u} \right) = -\nabla p + \mu \nabla^2 \mathbf{u} + \rho \mathbf{f}_b, \quad (\text{I.1})$$

where \mathbf{f}_b is an external body force per unit mass. For instance, this force per unit mass can be due to gravity and in that case $\mathbf{f}_b = \mathbf{g}$. The continuity equation (equation on the left) describes the incompressibility of the flow and the Navier-Stokes equation (equation on the right) corresponds to the conservation of momentum. In the Navier-Stokes equation all terms have the dimension of a force per unit volume. The left hand side of the Navier-Stokes equation corresponds to inertial terms and the terms on the right hand side correspond, from left to right, to pressure forces, viscous forces and external body forces.

These two equations form a system of coupled, non-linear, partial differential equations which does not have any general solution. It is generally required to use numerical simulations to solve this system, however, in some cases, the equations can be simplified and analytical solutions can be found. These situations correspond, for example, to the case of inviscid flows or the case of flow at low Reynolds number. In the following we will focus on this last case.

I.1.1 The Reynolds number

The Reynolds number (R_e) is a dimensionless number which compares the magnitude of inertial and viscous terms in the Navier-Stokes equation.

We consider the flow of a Newtonian fluid of viscosity μ , density ρ , characteristic velocity u , and typical dimension ℓ . According to equation I.1 the inertial term scale as $\rho u^2/\ell$ and the typical magnitude of the viscous term is $\mu u/\ell^2$. Thus the Reynolds number is given by [21]:

$$R_e = \frac{\text{inertial term}}{\text{viscous term}} = \frac{\rho u^2/\ell}{\mu u/\ell^2} = \frac{\rho u \ell}{\mu}. \quad (\text{I.2})$$

The Reynolds number can also be interpreted as a comparison of time scales [21]:

$$R_e = \frac{\text{characteristic time of viscous diffusion}}{\text{characteristic time of convection}} = \frac{\ell^2/\nu}{\ell/u}, \quad (\text{I.3})$$

where $\nu = \mu/\rho$ is the kinematic viscosity of the fluid and has the dimension of a diffusion coefficient.

As can be seen in equation I.3 the Reynolds number characterizes the relative importance of the transport of momentum over a distance ℓ by convection and by viscous

diffusion. The fastest mechanism will be the dominant one and will impose the characteristics of the velocity field.

At low Reynolds number, $R_e \ll 1$, transport by viscous diffusion is much faster than transport by convection. Inertia being negligible, the flow results from an equilibrium between viscous forces and pressure gradients. According to the expression of the Reynolds number, low Reynolds number flows occur for low velocities, in systems of small size or for very viscous fluids.

I.1.2 The Stokes equations

For low Reynolds number flow, $R_e \ll 1$, equations I.1 simplify to the continuity and Stokes equations [20]:

$$\nabla \cdot \mathbf{u} = 0 \quad \text{and} \quad \mathbf{0} = -\nabla p + \mu \nabla^2 \mathbf{u} + \rho \mathbf{f}_b. \quad (\text{I.4})$$

The Stokes equation is a linear partial differential equation. Since the equation is linear there is a unique solution for given boundary conditions, and it is possible to apply the principle of superposition. Moreover, a consequence of the time-independence of the Stokes equation is the kinematic reversibility. Kinematic reversibility can be understood as follows [22]: if we reverse time in the boundary condition ($t \rightarrow -t$), in a flow due to the movement of the boundaries (as for instance in a Couette flow), we reverse the sign of \mathbf{u} and p ($\mathbf{u} \rightarrow -\mathbf{u}$ and $p \rightarrow -p$). Due to the linearity and the time-independence of the Stokes equation, $-\mathbf{u}$ and $-p$ are still solutions of the equation. Using the uniqueness of the solution, reversing time implies that the flow field is exactly reversed i.e. the streamlines are not modified but the direction of the flow along these streamlines is reversed.

I.1.3 Sedimentation of a sphere

Let us consider the situation of a flow induced by a sedimenting sphere at low Reynolds number in a quiescent fluid. We denote \mathbf{V} the velocity of the sphere and a its radius. In the frame of reference of the translating sphere the continuity and the Stokes equations are given by equations I.4 with $\mathbf{f}_b = 0$ and the boundary conditions are $\mathbf{u}(r = a) = 0$ and $\mathbf{u}(r \rightarrow \infty) = -\mathbf{V}$. The solutions are given by [20]:

$$p - p_\infty = \frac{3}{2} \mu a \frac{\mathbf{V} \cdot \mathbf{r}}{r^3} \quad \text{and} \quad \mathbf{u} = \frac{3}{4} a \mathbf{V} \cdot \left(\frac{\mathbf{I}}{r} + \frac{\mathbf{r}\mathbf{r}}{r^3} \right) + \frac{1}{4} a^3 \mathbf{V} \cdot \left(\frac{\mathbf{I}}{r^3} - \frac{3\mathbf{r}\mathbf{r}}{r^5} \right), \quad (\text{I.5})$$

with \mathbf{I} the identity tensor and $\mathbf{r}\mathbf{r}$ the dyadic tensor.

The hydrodynamic force \mathbf{F}^H is given by:

$$\mathbf{F}^H = \int_S \mathbf{n} \cdot \boldsymbol{\sigma} dS, \quad (\text{I.6})$$

with S the surface of the sphere, \mathbf{n} the unit normal vector directed from the sphere surface to the fluid and $\boldsymbol{\sigma} = -p\mathbf{I} + \mu (\nabla \mathbf{u} + (\nabla \mathbf{u})^T)$ the stress tensor. The result is $\mathbf{F}^H = -6\pi\mu a \mathbf{V}$ and is known as the Stokes drag force.

An important consequence of the absence of inertia is that any object evolving in a viscous fluid or flow at low Reynolds number will be subject to zero total force and zero total torque. Hence, in the case of a sedimenting sphere of density ρ_s in a fluid of density ρ , the net gravitational force $\mathbf{F}^{ext} = (4\pi a^3/3)(\rho_s - \rho)\mathbf{g}$ is balanced by the viscous drag $\mathbf{F}^H = -6\pi\mu a\mathbf{V}$. Thus, the velocity of the sedimenting sphere reads

$$\mathbf{V} = \frac{2a^2(\rho_s - \rho)\mathbf{g}}{9\mu}. \quad (\text{I.7})$$

The velocity is proportional to a^2 , thus if the radius of the sphere is doubled the velocity is multiplied by a factor four. Moreover, \mathbf{V} is proportional to \mathbf{g} and the sphere sediments following a vertical line. The situation changes when two spheres interact hydrodynamically. Depending on their initial configuration, the spheres can drift and their velocity is altered. For instance, the velocity of two spheres close to each other, in a vertical or a perpendicular configuration, is larger than the velocity of an isolated sphere. This simple result will be used later in section I.4.

I.1.4 The Stokeslet

We now consider that the radius of the sphere $a \rightarrow 0$. As a consequence this new situation corresponds to a flow due to a point force \mathbf{F}^{ext} . In this situation the continuity and the Stokes equations read

$$\nabla \cdot \mathbf{u} = 0 \quad \text{and} \quad \mathbf{0} = -\nabla p + \mu \nabla^2 \mathbf{u} + \mathbf{F}^{ext} \delta(\mathbf{r}). \quad (\text{I.8})$$

The solution of these equations $\{p, \mathbf{u}, \sigma\}$ - named Stokeslet - is [23]:

$$p = \frac{\mathbf{F}^{ext} \cdot \mathbf{r}}{4\pi r^3}, \quad \mathbf{u} = \frac{\mathbf{F}^{ext}}{8\pi\mu} \left(\frac{\mathbf{I}}{r} + \frac{\mathbf{r}\mathbf{r}}{r^3} \right), \quad \sigma = -\frac{3\mathbf{F}^{ext}}{4\pi} \frac{\mathbf{r}\mathbf{r}}{r^5}, \quad (\text{I.9})$$

with $\sigma = -p\mathbf{I} + \mu (\nabla \mathbf{u} + (\nabla \mathbf{u})^T)$ the stress tensor.

The determination of the flow due to a point-force is of major interest since it paves the way for the determination of flows due to more complex forces. For instance the flow caused by a sedimenting elongated object will be presented in the next section.

I.2 Sedimentation of an isolated fiber: coupling between the particle configuration and its trajectory

A fiber is an elongated object whose geometry can be fully characterized by the shape of its cross section and the ratio between length and thickness (aspect ratio). Slender objects such as fibers are ubiquitous in nature and industry and, from the flagella of a bacteria or a sperm cell to optical fibers, their characteristic length and aspect ratio can vary over several orders of magnitude.

Here, we focus on the sedimentation of isolated fibers in viscous fluids. First, we present a powerful theoretical framework: the slender body theory, which is particularly

adapted for the description of very elongated objects evolving in viscous flows. This theory is then used to describe the sedimentation of a rigid and straight fiber. Secondly, we review studies on the sedimentation of particle of complex shapes and we primarily focus on the coupling between the particle symmetries and its trajectory. The sedimentation of slender structures is used, here, to introduce important notions and observations which bear similarities to what is obtained in confined geometry.

I.2.1 Slender body theory

The slender body theory relies on the approximation of the flow field around an elongated body using asymptotic techniques justified by its slenderness [9, 10]. For a cylinder of radius a and length ℓ the aspect ratio is $\epsilon = \ell/a$. The slender body theory approximation applies whenever $\epsilon \gg 1$. It gives a relation between the translation speed of the slender object with respect to the surrounding fluid and the force per unit length exerted by the fluid on the body.

The simplest form of the slender body approximation is the resistive force theory. It assumes that locally the fluid motion is the same as the flow past a cylinder with a hydrodynamic force per unit length different if tangential or normal to the local body axis. If we call the velocity of the body in the tangential and normal directions, respectively \mathbf{v}_{\parallel} and \mathbf{v}_{\perp} , the force per unit length on the body reads

$$\mathbf{f}^{\mathbf{H}} = -\xi_{\parallel}\mathbf{v}_{\parallel} - \xi_{\perp}\mathbf{v}_{\perp}, \quad (\text{I.10})$$

where the resistance coefficients ξ_{\parallel} and ξ_{\perp} depend on the aspect ratio of the slender body ϵ and the fluid viscosity μ [20]

$$\xi_{\parallel} = \frac{2\pi\mu}{\ln(\epsilon) - \frac{1}{2}} \quad \text{and} \quad \xi_{\perp} = \frac{4\pi\mu}{\ln(\epsilon) + \frac{1}{2}}. \quad (\text{I.11})$$

This approximation is purely local and, consequently, the force per unit length at a given location cannot depend in any way on the velocities at other positions along the slender object.

Note that for $\epsilon \gg 1$, $\xi_{\perp} \approx 2\xi_{\parallel}$ i.e. an elongated object with a motion perpendicular to its orientation experiences an hydrodynamic resistance almost twice as big as the one experienced by an elongated object with a motion parallel to its orientation.

We can also notice that the force per unit length only weakly depends on the aspect ratio of the slender structure, which appears as the argument in the logarithm. The total force on the particle can be approximated by the force per unit length multiplied by the particle length ℓ .

One can derive similar formulas using the results presented in section I.1: the disturbance created by the elongated object is equivalent to that due to a line of point forces \mathbf{f}^{ext} (forces per unit length) distributed along its length. Thus, the velocity field around the slender structure at a position \mathbf{r} corresponds to the integral of Stokeslets along the centerline [23]:

$$\mathbf{u}(\mathbf{r}) \approx \frac{1}{8\pi\mu} \int_{-\ell/2}^{\ell/2} \mathbf{f}^{\text{ext}} \left(\frac{\mathbf{I}}{\mathbf{r} - \mathbf{r}'(s)} + \frac{(\mathbf{r} - \mathbf{r}'(s))(\mathbf{r} - \mathbf{r}'(s))}{|\mathbf{r} - \mathbf{r}'(s)|^3} \right) ds, \quad (\text{I.12})$$

with $\mathbf{r}'(s)$ the position on the centerline and s the curvilinear abscissa.

Assuming the external force per unit length does not depend on s we obtain the velocity \mathbf{v} of the elongated object

$$\mathbf{v} = \frac{1}{4\pi\mu} \ln(\epsilon) (\mathbf{I} + \lambda\lambda) \mathbf{f}^{\text{ext}}, \quad (\text{I.13})$$

with λ a unit vector indicating the orientation of the centerline. Inverting equation I.13 we obtain:

$$-\mathbf{f}^{\text{ext}} = \mathbf{f}^{\mathbf{H}} = -\frac{4\pi\mu}{\ln(\epsilon)} \left(\mathbf{I} - \frac{1}{2} \lambda\lambda \right) \mathbf{v}. \quad (\text{I.14})$$

We notice that equation I.14 is equivalent to equations I.10 and I.11 up to leading order in $\ln(\epsilon)$.

I.2.2 Sedimentation of straight fibers in a quiescent fluid

For a sedimenting rigid fiber the external force per unit length is $\mathbf{f}^{\text{ext}} = \mathbf{F}_g/\ell$ (with \mathbf{F}_g the gravitational force) and the translation speeds of vertical and perpendicular fibers are given respectively by $\mathbf{v}_{\parallel} = \frac{\mathbf{F}_g}{\ell\xi_{\parallel}}$ and $\mathbf{v}_{\perp} = \frac{\mathbf{F}_g}{\ell\xi_{\perp}}$. Both cases are sketched in Figures I.1 (a) and (b). An important consequence of the anisotropy of the velocities is that a fiber neither horizontal nor vertical drifts with a constant angle (see Figure I.1 (c)). According to the principle of reversibility of Stokes flows the fiber cannot rotate and its velocity has a constant drift angle θ .

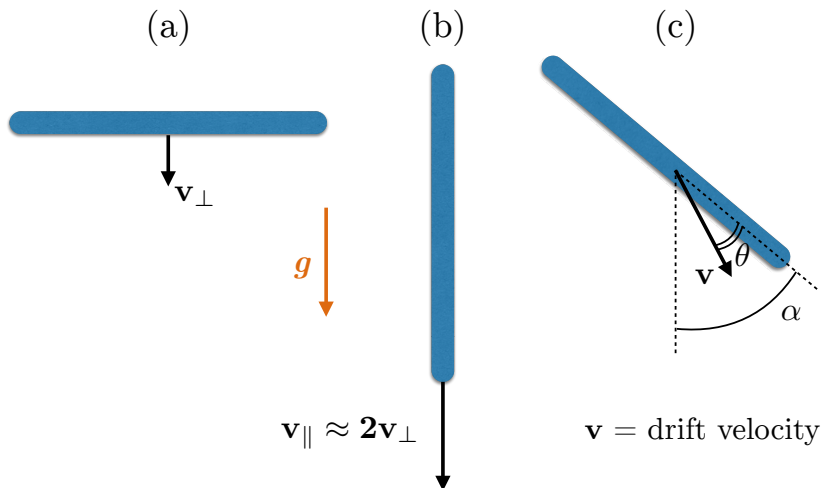


Figure I.1: Sedimentation of fibers with different orientations: perpendicular fiber (a), parallel fiber (b), fiber oriented with an angle α with respect to gravity (c). As a consequence of the velocity anisotropy the translation velocity in (c) is oriented at an angle $\alpha - \theta$ with respect to gravity.

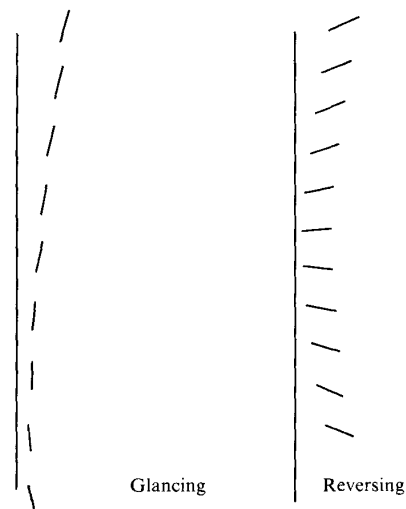


Figure I.2: Chronophotographs of a rod sedimenting close to a wall. Depending on the initial orientation of the fiber two cases are possible: glancing for an initially almost vertical fiber and reversing for an initially almost horizontal fiber. Figure extracted from [24].

As discussed by Russel *et al.* in [24] the situation changes if the fiber approaches a wall: a rotation occurs, the drift angle varies and the fiber eventually escapes from the wall. This experimental study together with the slender body theory and the mirror image method - which model the interaction of the fiber with the wall - yields results on the orientation, position and velocity of the rod. Depending on the initial orientation of the fiber two different trajectories are possible: glancing (for an initially almost vertical fiber) and reversing (for an initially almost horizontal fiber). The positions and orientations of a slender particle sedimenting close to a wall experiencing glancing and reversing are shown, respectively, in Figures I.2 (a) and (b). During glancing the fiber first rotates until it aligns with the wall, when vertical its drift angle changes sign and the fiber escapes from the wall. On the contrary, during reversing the fiber rotates until perpendicular to the wall, at this stage the sign of the drift angle inverts and the fiber moves away from it. Note that, due to the principle of reversibility, the orientation of the fiber escaping from the wall is the symmetric with respect to the wall axis of the orientation that the fiber had when approaching the wall.

I.2.3 Sedimentation of slender objects with complex geometries

The examples of the sedimenting sphere and fiber presented in sections I.1.3 and I.2.2 show that, at low Reynolds numbers, the trajectory of a particle highly depends on its geometry. A sphere, an object with an infinite number of symmetry axes, sediments

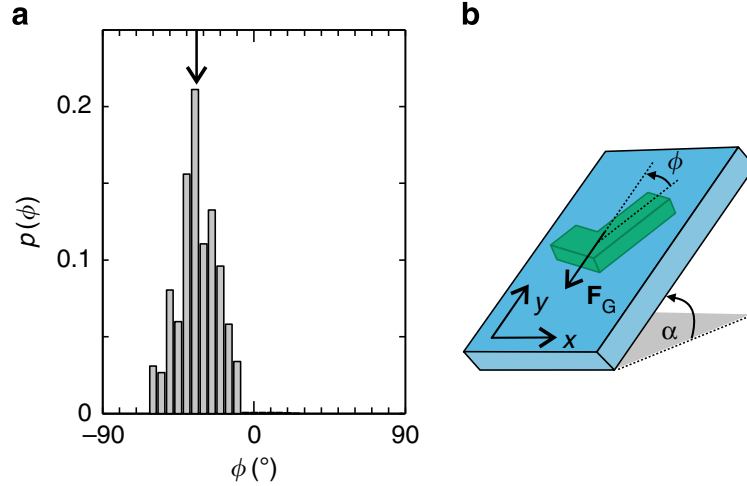


Figure I.3: (a) Measured probability distribution $p(\phi)$ of the orientation angle ϕ of a passive L-shaped particle during sedimentation. (b) Sketch of the particle geometry and angles definitions. Figure extracted from [25].

vertically. On the contrary, a straight fiber, with two axes of symmetry, drifts if oriented neither parallel nor perpendicular to gravity and cannot rotate unless it approaches a wall.

The complexity of the object geometry can be even further increased by releasing one of the symmetries of the straight fiber: for instance by adding a second arm to the fiber giving an "L-shaped" object. Ten Hagen *et al.* have investigated the sedimentation of such L-shaped fibers both experimentally and theoretically [25]. It appears that the asymmetric particle rotates until it reaches an equilibrium orientation and then slowly drifts while maintaining this orientation. Figure I.3 (a) shows the experimental results of the probability distribution of the orientation angle ϕ of a L-shaped particle (see Figure I.3 (b)). The data shows a clear maximum of the orientation angle corresponding to the situation where the shorter arm of the fiber is at the bottom and the orientation angle is close to $\phi \sim -45^\circ$. The authors demonstrate that the selection of an equilibrium orientation is due to the asymmetry of the particle, and they were able to derive the equilibrium angle by applying the slender body theory on the two arms of the particle.

Decreasing the number of symmetries of the particle even further leads to the work of Tozzi *et al.* [26]. In this study, the authors investigated, both experimentally and numerically, the relation between the trajectory of a particle and its shape. The 3D trajectory of a particle, tracked using a set of two synchronized cameras, shows that, after a transient reorientation, the particle reaches an asymptotic motion that depends on the geometry of the particle. Some examples are given in Figure I.4. Particle (a) has two axes of symmetry but its center of hydrodynamic resistance (point where the total sum of the hydrodynamic forces act on a body) does not coincide with its center of mass. As a consequence a torque is applied on the particle. The particle rotates until the torque vanishes i.e. when the direction defined by the two centers aligns with gravity. Then the particle sediments keeping its equilibrium orientation and no drift is observed. The

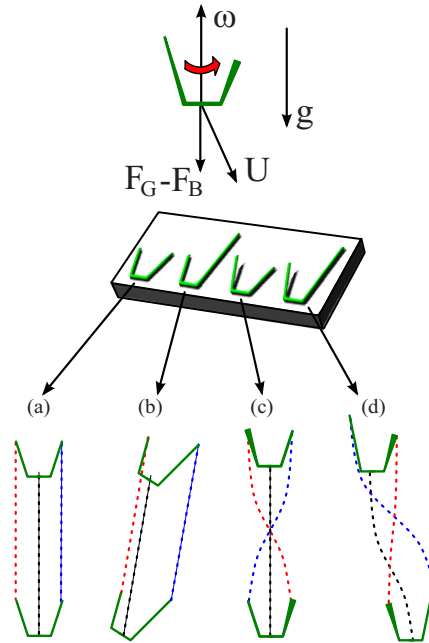


Figure I.4: Qualitative motion of fibers having different types of symmetry. After a transient regime of reorientation, particles can follow various types of asymptotic motion. Particles (a) and (b) have no translation-rotation coupling, and they do not achieve a rotational motion as they sediment. For particles (a) and (c), the translational velocity does not have a horizontal component, so they attain a state where their center of mass moves in a vertical fashion. Fiber (b), on the contrary, tends to drift sideways, sedimenting with a diagonal trajectory. Fiber (d) is similar to (b), but additionally it has translation-rotation coupling, and therefore the diagonal fall is accompanied with a rotational motion, resulting in a helical trajectory. Figure extracted from [26]

particle (b) shows one plane of symmetry and, as observed for L-shaped fibers, the particle reorients toward an equilibrium orientation before drifting. Particles (c) and (d) don't have any axis or plane of symmetry, i.e. they are chiral objects. After a transient regime they reach an helical trajectory resulting from a translation-rotation coupling. Similarly, according to [27], helicoidal particles - which are as well chiral objects - experience also helical trajectories. This observation can be generalized to any chiral objects sedimenting in a viscous fluid.

I.3 Effect of confinement by bounding walls

We have seen that the interaction of a fiber with a boundary can lead to rich dynamics (see section I.2.2). Here, we review studies where a fiber is confined between the top and bottom walls of a channel and we primarily focus on the role of confinement on the particle trajectory and dynamics.

I.3.1 Confinement due to top and bottom walls

Semin and co-authors [11, 12] investigated, both experimentally and numerically, the influence of confinement by top and bottom walls on the drag force acting on a cylinder held at a fixed position in a viscous flow.

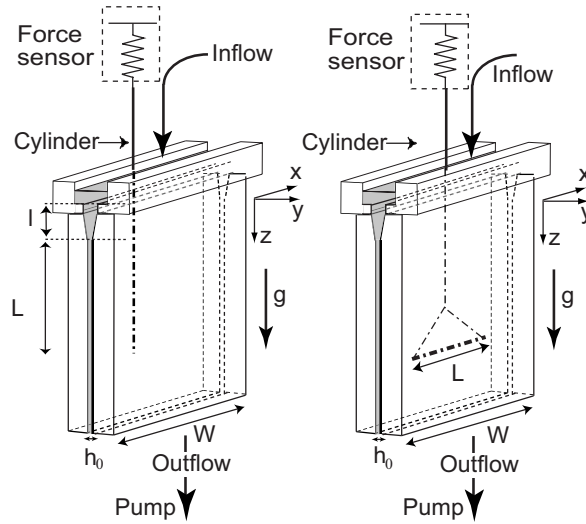


Figure I.5: Experimental setup used for the study of confined fibers between two parallel walls. Left and right panels correspond to the configuration where the fiber is respectively parallel and perpendicular to the flow direction. Figure extracted from [11].

In these studies a cylinder is placed in a rectangular slit either parallel or perpendicular to an external viscous flow. Figure I.5 illustrates the flow geometry. The slit of height h_0 is made from two vertical walls of width W . h_0 being much smaller than W the flow is plug-like. The cylinder has a diameter d and the authors define the confinement of the system β as the ratio d/h_0 .

Additionally to the experimental investigation of the parallel fiber 2D numerical simulations are performed. In these simulations the fiber is considered as infinitely long. However, for a perpendicular fiber a 3D numerical simulation is necessary to account for the experimental results. Indeed, 2D simulations which assume a uniform flow along the fiber length cannot describe the flow between the cylinder edges and the lateral walls which have an important impact on the drag forces. As expected for a low Reynolds number flow, the drag force exerted on the cylinder is proportional to the flow velocity and the viscosity of the fluid allowing the drag coefficient to be defined. The evolution of the drag coefficient for parallel and perpendicular fibers as a function of the confinement is shown in Figure I.6. In both cases the drag coefficient increases for an increasing confinement. For a parallel cylinder this evolution is linear, whereas, for a perpendicular cylinder the increase is exponential and eventually diverges for a confinement $\beta \rightarrow 1$. At Reynolds numbers larger than 20, the central position of the fiber between the two confining walls becomes unstable and the fiber starts to oscillate between them [28]. A similar observa-

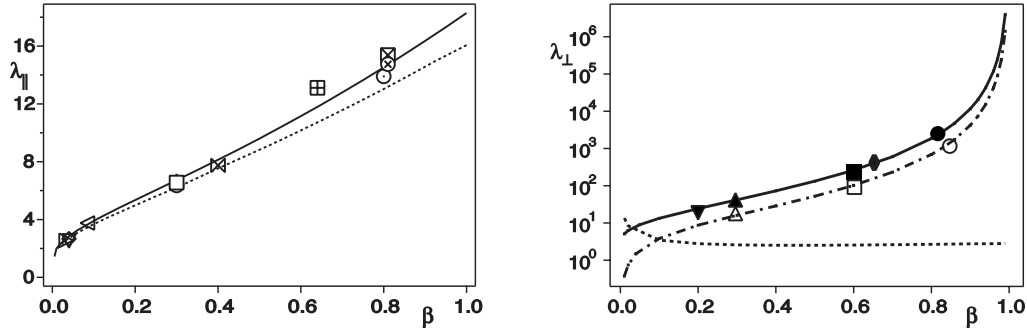


Figure I.6: Experimental (symbols) and numerical (lines) results of the evolution of the drag coefficient as a function of the confinement β for the parallel fiber (left) and for the perpendicular fiber (right). β is defined as $\beta = d/h_0$ where d is the cylinder diameter and h_0 the channel height. In the two cases the drag coefficient increases with the confinement. For the parallel configuration this evolution is linear. For the perpendicular configuration the increase is exponential and eventually diverges for $\beta = 1$. Figure extracted from [11].

tion has been made for fibers, free to rotate and to move vertically in an upward flow, in a confined geometry [29]. The authors of [29] reported a critical Reynolds number of 30.

The understanding of the effect of the confinement on the dynamics of single fibers was also the main purpose of the studies of Berthet and co-authors [13, 14]. They investigated the transport of free fibers confined by top and bottom walls and transported by an external viscous flow in microfluidic channels. As in the work of Semin *et al.* [11, 12], they focus their study on two situations: a fiber oriented parallel to the flow direction and a fiber oriented perpendicular to the flow direction. These two situations are shown in Figure I.7.

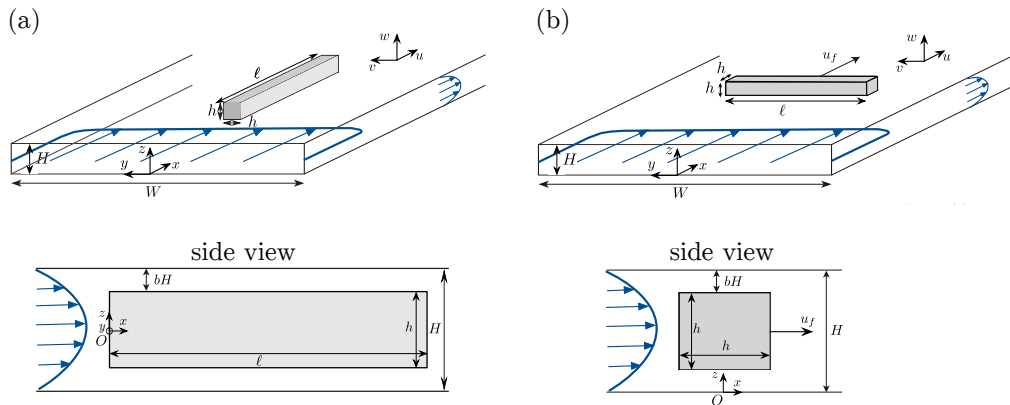


Figure I.7: Geometries of the system for the parallel fiber (a) and perpendicular fiber (b). Due to the Hele-Shaw geometry of the channel the flow in the Oxy plane is plug-like except in the direct vicinity of the fiber and the lateral walls and Poiseuille-like in the plane Oxz .

In these studies the fibers have square cross sections of width and height $h \sim H$, with H being the channel height, and are always located in the middle of the channel height. The confinement of the system is $\beta = h/H$. Due to the Hele-Shaw geometry of the channel, the flow in the (Oxy) plane is plug-like and Poiseuille-like in the (Oxz) plane.

When an external flow is imposed, the fiber is transported at a velocity V_{fiber} proportional to the mean velocity of the external flow V_{mean} . The viscous friction occurring in the gaps between the fiber and the channel top and bottom walls slows down the fiber. Its velocity is thus always smaller than the maximal flow velocity $\frac{3}{2}V_{\text{mean}}$. Moreover, the fiber acts as a moving obstacle and it impacts the external flow differently as a function of its orientation. A perpendicular fiber deforms the streaklines over a distance ℓ (the length of the fiber), whereas a parallel fiber deforms the streaklines over a typical distance h (the width of the fiber). As a consequence, the ratio between the fiber velocity and the mean flow velocity $V_{\text{fiber}}/V_{\text{mean}}$ strongly depends on the fiber orientation. Figure I.8 shows the evolution of this ratio for the two situations - parallel and perpendicular fibers - as a function of the confinement. The results shown are obtained experimentally and using 2D and 3D numerical simulations based on finite element methods.

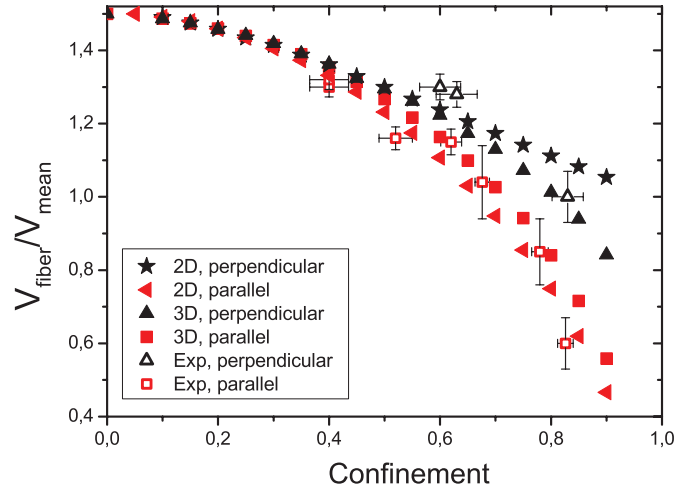


Figure I.8: Experimental (open symbols) and numerical (filled symbols) rescaled fiber velocity as a function of the confinement for parallel (red) and perpendicular fibers (black). Figure extracted from [13].

For parallel fibers, 2D and 3D descriptions yield similar results, whereas, for perpendicular fibers, the two simulations show discrepancies for large confinements. The origin of these differences is the same as in the study of Semin *et al.* [11]: 2D simulations which assume that the fiber is infinitely long (i.e. that the flow is uniform along the fiber length) cannot describe the flow around the fiber edges.

Figure I.8 shows that for the two configurations the fiber velocity decreases nonlinearly with the confinement. Here, contrary to sedimentation, the velocity of a perpendicular fiber is larger than the velocity of a parallel fiber. Note that for low confinements the fiber velocity is the same for both orientations and equal to the maximum velocity of the

flow $\frac{3}{2}V_{\text{mean}}$.

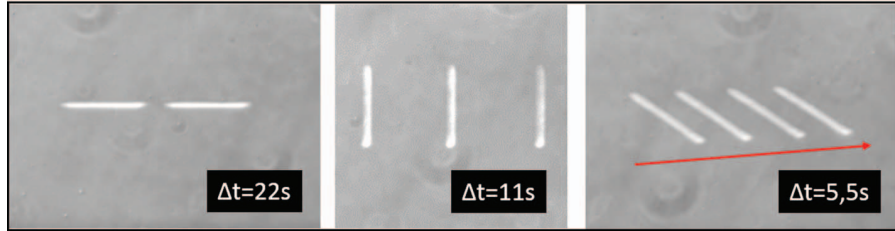


Figure I.9: Superposition of successive images for a parallel fiber (left), a perpendicular fiber (middle) and a fiber oriented at 45° to the flow direction (right). The confinement is $\beta = 0.8$. The fiber is $200\mu\text{m}$ long. Figure extracted from [13].

Similarly to sedimentation, the velocity anisotropy leads to drift of a fiber that has an arbitrary orientation with the flow direction. But as the velocity anisotropy is inverted compared to sedimentation (here $V_{\parallel} < V_{\perp}$ whereas $V_{\parallel} > V_{\perp}$ in sedimentation), the direction of the drift will be the opposite compared to the one observed for a sedimenting fiber. The velocity anisotropy and the resulting drift of a transported fiber are visible in Figure I.9.

In our work, we use the same flow geometry as Berthet *et al.* [13]. Hence, we largely inspire ourself from reference [13] to describe the flow around transported fibers in confined geometries.

I.3.2 Effects of lateral walls

As previously mentioned, the presence of the fiber induces strong flow perturbation over distances that can be comparable to the fiber length. Thus, one expects the lateral walls to interact hydrodynamically with the fibers. Such interactions of the channel lateral wall with the fibers transported in confined microchannels have been investigated experimentally and numerically by Nagel *et al.* [30].

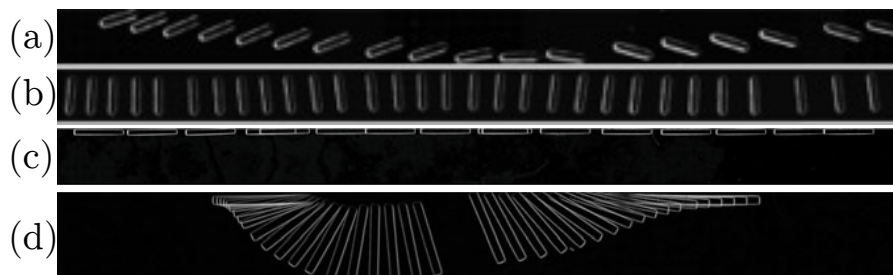


Figure I.10: Experimental chronophotographies of fiber trajectories exhibiting (a) glancing, (b) reversing, (c) wiggling and (d) pole vaulting. The external flow is directed from left to right. Figures (a) and (b) are extracted from [19], and Figures (c) and (d) are taken from [30].

Figure I.10 shows four different families of trajectories. The trajectories presented in Figures I.10 (a) and (b) correspond, respectively, to glancing and reversing of a fiber approaching a wall. These two trajectories are very similar to the ones observed for a sedimenting fiber approaching a wall and, here as well, the observation of either glancing or reversing is related to the initial orientation of the fiber. If the angle between the flow direction and the orientation of the fiber in the middle of the cell is small (case (a)) the fiber mostly exhibits glancing. Whereas, if the fiber is almost perpendicular to the flow direction (case (b)), it exhibits reversing. Here, due to the presence of two lateral walls, the fiber first drifts toward one wall, interacts with it, escapes from the wall vicinity, drifts and approaches the other wall. The sequence is repeated leading to oscillations of the fiber inside the microchannel. If the fiber is placed horizontally ($\theta \sim 0$) in the direct vicinity of a wall it can exhibit other kinds of trajectories: wiggling and pole-vaulting as shown in Figures I.10 (c) and (d). For these two types of trajectories the fibers enter the boundary layer very close to the lateral walls.

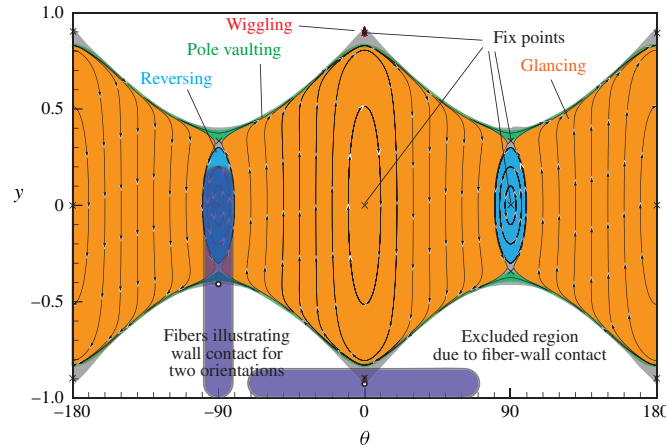


Figure I.11: Trajectory map in the configuration space spanned by orientation angle θ and lateral position y . The physical accessible space is shaded in color. Figure extracted from [30].

The full state diagram, spanned by the orientation angle relative to the flow direction θ and the lateral position of the center of mass of the fiber y , is represented in Figure I.11. It shows the four kinds of trajectories described above (orange: glancing, blue: reversing, red: wiggling and green: pole-vaulting). This diagram has been obtained using a 2D numerical simulation based on the resolution of the Brinkman equation and a model flow profile in the gap between the fiber and the channel top and bottom walls. One obtains the Brinkman equation by averaging the Stokes equation over the channel height. It is particularly adapted for the description of porous media or confined flows. The flow profile in the gaps is assumed to be a Couette-Poiseuille flow. The model used by Nagel *et al.* has been used at many occasions in our work and is extensively explained in chapter IV.

The study of Nagel *et al.* [30] can be compared to the work of Uspal *et al.* [17]. Here, the authors investigated both experimentally and theoretically the trajectories of

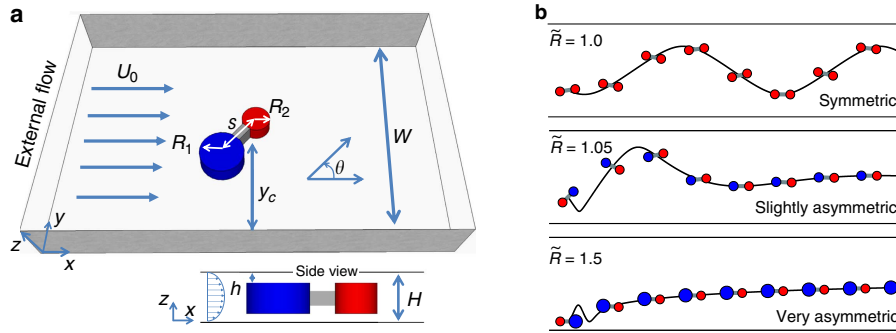


Figure I.12: (a) Geometry of the channel and the particle. (b) Trajectories of particles of varying symmetries. A symmetric particle oscillates between side walls. When the symmetry is slightly broken, these oscillations are damped and the particle aligns with the flow on the centerline on the channel. For a very asymmetric particle no oscillations are visible (overdamped regime). Figure extracted from [17].

"dumbbell" particles (see Figure I.12) transported by an external viscous flow in a confined geometry. They bring to light that a symmetric dumbbell - a dumbbell composed of two identical discs - which has one axis of symmetry oscillates along the channel similarly to straight fibers. The same dynamics are also observed for contacting droplets transported in confined geometries [31]. For asymmetric dumbbells, these oscillations are damped and the object reorients toward an equilibrium orientation corresponding to the particle aligned with the flow direction and in the center of the channel. The geometry of the system and the particle trajectories are shown in Figure I.12 (a) and (b). To model the system, the authors used a two dimensional description of the flow supplemented by a model of Couette flow in the gap between the particle and the channel top and bottom walls. Lateral confinement has been taken into account by the mirror image technique [32, 33].

More recently Bet and co-authors studied numerically the trajectories of fully asymmetric particles composed of three disks of different diameters in the same channel and flow geometry [34]. The study focusses on the temporal dynamics of the orientation and position of the particle and on the trajectories of particles of different geometries (see Figures I.13 (a) and (b)). Figure I.13 (a) shows that, after a transient regime, the particle eventually reaches an equilibrium orientation. The fixed points visible in Figure I.13 (b) are signatures of these equilibrium orientations and also indicate that when the equilibrium orientation is reached the particle does not drift i.e. the particle also reaches an equilibrium lateral position.

This last observation is in contradiction with the study of Ten Hagen *et al.* [25], previously mentioned, which shows that a sedimenting asymmetric L-shaped particle exhibits a drift when it reaches its equilibrium orientation. Similarly to reference [25], we will see in chapter VI that an asymmetric fiber transported in a confined viscous flow never reach any equilibrium lateral position.

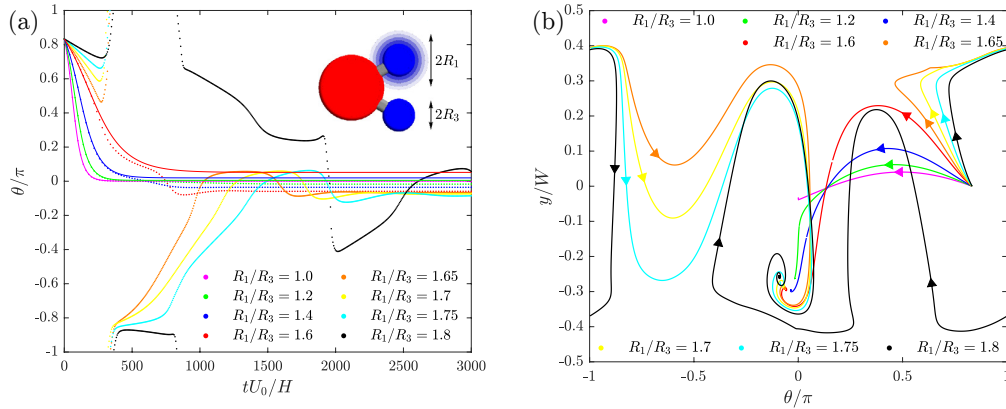


Figure I.13: (a) The orientation θ as a function of time t , for different particles geometry. In the inset: sketch of the particle geometry. (b) Particle trajectories in the (θ, y) phase space for different trimers geometries. Figure extracted from [34].

I.4 Flexible fibers

In the last two sections, we presented studies on rigid particles sedimenting in a quiescent fluid or transported in a confined geometry and we emphasized the coupling between the shape of a particle and its trajectory. In the following section, we will focus on flexible objects that can change shape while interacting with the flow.

I.4.1 The Euler-Bernoulli equation

The Euler-Bernoulli equation describes the deformation of a beam on which external forces are applied. In the Euler-Bernoulli beam theory the beam is taken as a one-dimensional object. The theory relies on two important assumptions [35, 36]: first, any section of the beam that was plane before deformation remains plane after the deformation and any section that was perpendicular to the neutral axis before deformation remains perpendicular to the neutral axis after the deformation. Second, deformations remain small i.e. the variation of the amplitude of deformation $\Delta\delta$ over a distance Δx verifies $\Delta\delta/\Delta x \ll 1$. It is important to note that the expression of the Euler-Bernoulli equation given in the following is only valid at leading order in deformation.

For the case, sketched in Figures I.14 (a) and (b), of a beam centered along the x -axis and subject to a distributed load (force per unit length) $f_y(x)$ perpendicular to its axis, the Euler-Bernoulli equation writes [35]

$$\frac{\partial^2}{\partial x^2} \left(EI \frac{\partial^2 \delta(x)}{\partial x^2} \right) = f_y(x), \quad (\text{I.15})$$

where $\delta(x)$ denotes the beam deflection, E is the Young's modulus and $I = \iint z^2 dydz$ is the moment of inertia of the beam. For a beam of rectangular cross section of height h and width w (see Figure I.14 (c)), the moment of inertia is $I = wh^3/12$.

Often, the product EI , called flexural rigidity or bending modulus, is constant and equation I.15 reads

$$EI \frac{\partial^4 \delta(x)}{\partial x^4} = f_y(x). \quad (\text{I.16})$$

The Euler-Bernoulli equation is a linear fourth order differential equation. As a consequence, the solution of the equation needs four boundary conditions. If the beam end is free then $\delta''' = 0$ and $\delta'' = 0$, if it is clamped then $\delta = 0$ and $\delta' = 0$, if it is subject to a point force F orthogonal to the beam axis $\delta''' = F/EI$ and to a point torque M $\delta'' = M/EI$.

The situation where the beam is subject to a load transverse to its longitudinal axis, is called bending. In this case, the deflection of the beam is proportional to the amplitude of the load.

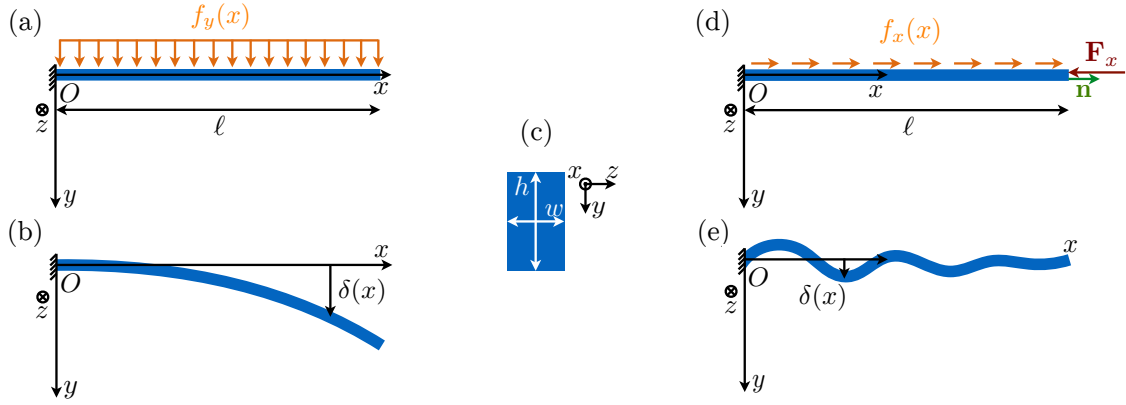


Figure I.14: (a) and (b): bending of a fiber under a transversal load $f_y(x)$. (a) Initial configuration and sketch of the external load. (b) Sketch of the deformed beam. (c) Rectangular cross section of the beam. (d) and (e): buckling of a beam subject to a longitudinal load $f_x(x)$ and a longitudinal point force \mathbf{F}_x . (d) Initial configuration and sketch of the load and point force. (e) Sketch of the buckled beam.

When the beam is subject to a distributed longitudinal load $f_x(x)$ and/or a point force oriented parallel to its axis \mathbf{F}_x , the deformation of the beam occurs only for large enough loads and is due to an instability named buckling. This situation is sketched in Figures I.14 (d) and (e). In this case, the Euler-Bernoulli theory reads [35]

$$\frac{\partial T}{\partial x} + f_x(x) = 0, \quad (\text{I.17})$$

$$EI \frac{\partial^4 \delta(x)}{\partial x^4} - \frac{\partial}{\partial x} \left(T(x) \frac{\partial \delta(x)}{\partial x} \right) = 0, \quad (\text{I.18})$$

with $T(x)$ a scalar quantity, named tension, corresponding to an internal force within the beam. It is a Lagrange multiplier ensuring the length conservation of the beam. The

boundary condition needed to determine the tension is given by the projection of the longitudinal forces applied on the beam tip \mathbf{F}_x on \mathbf{n} , the outer-pointing normal vector at the tip surface. In the case sketched in Figures I.14 (d) and (e), $T(x = \ell) = -\|\mathbf{F}_x\|$. Negative values of the tension correspond to situations where the beam is compressed, whereas positive values result in a stretched beam. Buckling only occurs for negative values of the tension and for ratios $-T_0\ell^2/EI$, with T_0 the typical magnitude of the tension, larger than a critical value (instability threshold), which depends on the force distribution and on the boundary conditions.

I.4.2 The elasto-viscous number

We now consider an elastic fiber subject to viscous forces. As we have seen in section I.2.1, the viscous forces per unit length are proportional to μv with μ the viscosity of the fluid and v the typical velocity of the fiber. Their exact form, $\tilde{\mathbf{f}}\mu v$, with $\tilde{\mathbf{f}}$ a dimensionless vector, will depend on the specific geometry of the flow. On the other hand, the elastic force per unit length scales with EI/ℓ^3 , where E , I and ℓ are respectively the Young's modulus, the moment of inertia and the length of the fiber. Thus, one can define a dimensionless number $\tilde{\mu}$, called elasto-viscous number, which compares the viscous forces and the elastic restoring force

$$\tilde{\mu} = \frac{\mu v \ell^3}{EI}. \quad (\text{I.19})$$

Another definition gives the elasto-viscous number as a function of the shear rate $\dot{\gamma} \propto v/\ell$

$$\tilde{\mu} = \frac{\mu \dot{\gamma} \ell^4}{EI}. \quad (\text{I.20})$$

According to equation I.20 the elasto-viscous number can also be interpreted as the ratio between the characteristic relaxation time of the fiber $\tau = \mu\ell^4/(EI)$ and the characteristic time of the flow $\dot{\gamma}^{-1}$.

In the case where there are only transverse viscous forces (bending), the larger the elasto-viscous number the larger the deformation. Thus, to increase the deformation of a fiber one can either increase the fiber length, the flow velocity or the fluid viscosity or decrease the fiber width, its height or its Young's modulus.

If the fiber is subject to longitudinal compressive forces, there is a negative tension inside the fiber and, as previously mentioned, buckling occurs if the quantity $-T_0\ell^2/EI$ is larger than an instability threshold. According to equation I.17, $\|T_0\| \propto v\mu\ell$, and $-T_0\ell^2/EI \sim v\mu\ell^3/EI = \tilde{\mu}$. Thus for small elasto-viscous numbers the fiber remains undeformed, and for large enough elasto-viscous numbers the fiber buckles.

I.4.3 Sedimentation of flexible fibers

When a flexible fiber sediments in a quiescent fluid, a competition between viscous forces and elastic forces leads to a complex deformation and reorientation of the object impacting

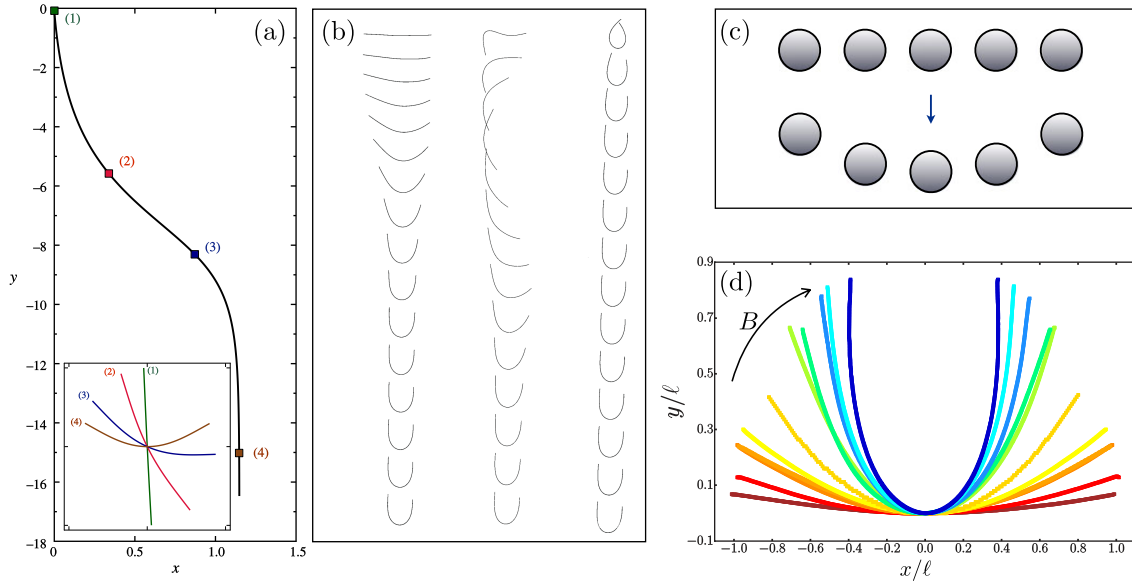


Figure I.15: Sedimentation of flexible fibers. (a) Trajectory of the center of mass of a fiber. The fiber shape during sedimentation is shown in the inset. Extracted from [37]. (b) Chronophotographies of a flexible fiber released with different initial conditions. Extracted from [38]. (c) Sketch illustrating the origin of bending. Extracted from [37]. (d) Final shape of the fiber for different values of the elasto-gravitational number B ($B = F_g \ell^2 / (EI)$ with F_g the gravitational force). The elasto-gravitational number is a dimensionless parameter which compares the gravitational force and the elastic restoring forces. Extracted from [38].

its trajectory. In the following section we review studies on the sedimentation of flexible fibers.

The first investigation on sedimenting flexible fibers has been done theoretically by Xu *et al.* [39] in 1994. This work has been followed by a numerical study by Li *et al.* describing the fiber deformation and its trajectory using the slender body theory [37]. Surprisingly, to our knowledge, the first experiments on sedimenting flexible fibers have been published only recently [38]. As already discussed for rigid fibers, as the object evolves at low Reynolds number, its weight is perfectly balanced by the viscous drag. But, because of the finite length of the fiber, this viscous drag varies along the object i.e. edges effects lead to inhomogeneous hydrodynamic force distributions along the fiber. This causes deformation and rotation of the fiber. Moreover, as already discussed, a consequence of the drag anisotropy is a coupling between orientation and drift. Thus, as the fiber rotates and deforms, this coupling leads to complex trajectories (see Figure I.15 (a)). The fiber rotates and deforms and eventually reaches an equilibrium configuration. This configuration corresponds to a bent fiber, whose shape is symmetric about the gravity axis, sedimenting at constant velocity. As we can see in Figure I.15 (b) the final configuration of the fiber does not depend on the initial configuration.

The equilibrium shape of the fiber can be understood qualitatively as follows: let us model the fiber as composed by an assembly of spheres. As previously mentioned in

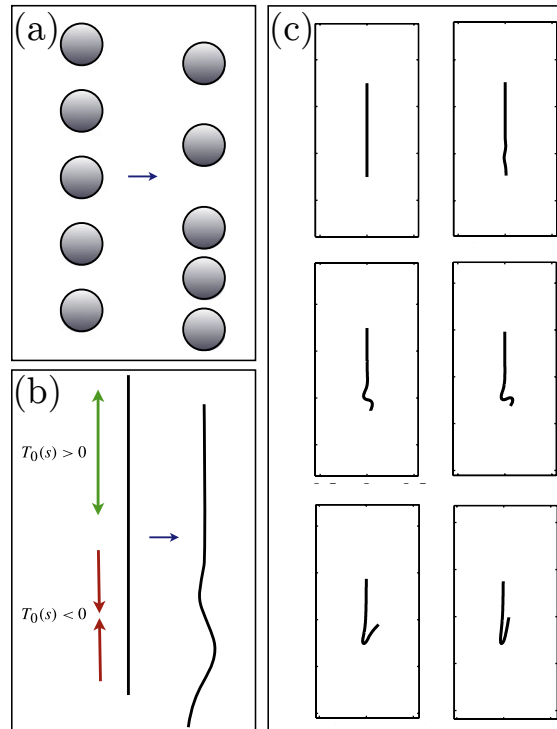


Figure I.16: (a) Sketch illustrating the origin of the tension and buckling in the vertically oriented fiber. (b) Illustration of the tension distribution in the filament: the front half of the fiber is compressed and the rear half of the fiber is stretched. If the fiber is flexible enough compression leads to buckling. (c) Numerical chronophotographies of a buckling fiber. (a) (b) and (c) are extracted from [37].

section I.1, two spheres sedimenting close to each other are faster than an isolated sphere. Thus, we expect the spheres on the edges, which have fewer neighbors, to be slower than the spheres in the middle. As a consequence, the fiber bends. This idea is sketched in Figure I.15 (c).

At each moment the drag force balances the gravitational force, and it is thus appropriate to define the gravitational number, $B = F_g \ell^2 / (EI)$ with F_g the gravitational force, as the control parameter. Figure I.15 (d) shows the increase of the amplitude of the deformation for increasing B . For large B the deflection of the fiber reaches a maximal value close to half the fiber length.

The case of a vertical fiber sedimenting in a quiescent fluid is very different. In order to gain insights on the dynamics of this system, Li and co-authors [37] proposed to model the fiber as a column of spheres (see Figure I.16 (a)). Again, the spheres placed in the middle of the fiber are faster than the spheres on the edges of the fiber and one expects the fiber to be compressed in the leading part and stretched in the rear part. The fiber is thus subject to an inhomogeneous drag leading to an inhomogeneous tension. If the elasto-gravitational number B is large enough, the tension leads to a buckling of the fiber in its leading half. Figure I.16 (b) shows the tension distribution in the fiber and its

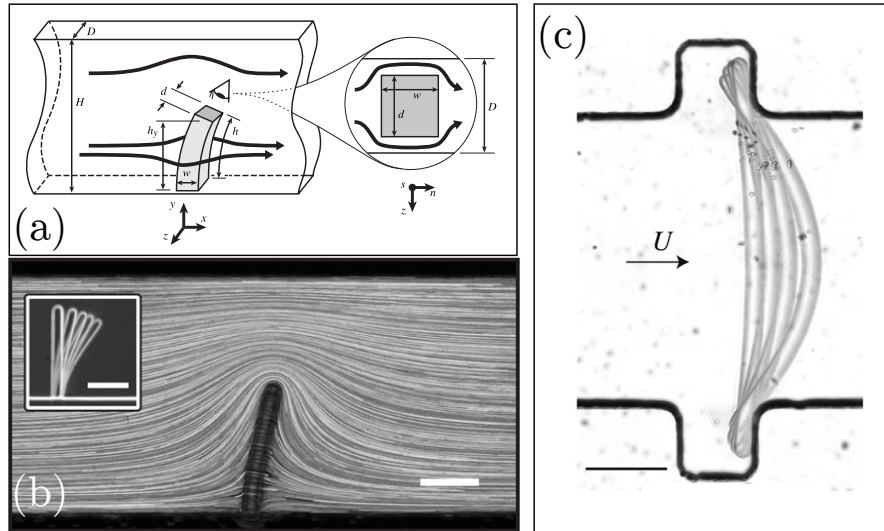


Figure I.17: (a) Sketch illustrating the channel and fiber geometry. (b) Visualization of the flow pathlines around a bent fiber. Scale bars are $100 \mu\text{m}$. Figures (a) and (b) are extracted from [40]. (c) Superposition of images showing a flexible fiber deformed by an external viscous flow of varying velocity. The higher the velocity of the flow, the larger the deformation. Scale bars is $100 \mu\text{m}$. Figure (c) is extracted from [41].

buckled shape. It is an unstable state and buckling is followed by a fast reconfiguration of the fiber through the previously described equilibrium configuration (see Figure I.16 (c)).

I.4.4 Flexible fibers in confined geometries

In the following section we review two studies investigating the deformation of flexible fibers in a confined geometry [40, 41]. The fibers are confined by top and bottom walls i.e. they occupy almost all the channel height.

Figure I.17 (a) shows the geometry of the system studied by Wexler and co-authors [40]. A flexible fiber is clamped at one edge and free at the other. Upon application of an external viscous flow, the fiber bends. A picture of the bent fiber is shown in Figure I.17 (b). In this system, the flow around the particle is complex and its three dimensional nature is visible in Figures I.17 (a) and (b). Part of the flow goes through the gaps between the fiber and the channel top and bottom walls while another part of the flow circumvents the obstacle. The authors observed that in the limit of low flow velocity, the deformation of the fiber evolves linearly with the external flow velocity. To explain their observations and to derive the deflection of the fiber as a function of the flow velocity they used a two dimensional model. In the model, the fiber is considered as a porous object allowing the flow to pass through the fiber. The flow around the fiber is modeled as a Hele-Shaw flow.

The study of Duprat *et al.* [41] investigates, both experimentally and theoretically,

the deformation by an external flow of a fiber whose both ends are simply supported. A picture of the experiment is shown in Figure I.17 (c): a flexible fiber is placed in two slots, an external flow is imposed, which deforms the object. The amplitude of the deformation is observed to be proportional to the elasto-viscous number $\tilde{\mu}$. The authors model the flow around the fiber using the lubrication theory which enables them to derive the forces per unit length applied on the fiber. Using Euler-Bernoulli theory Duprat *et al.* obtained a very good prediction of the shape of the bent fiber and its deflection amplitude. This situation is used as a measurement method to characterize the Young's modulus of hydrogels. This last point will be developed further in chapter II.

I.4.5 Shear and compressive flows

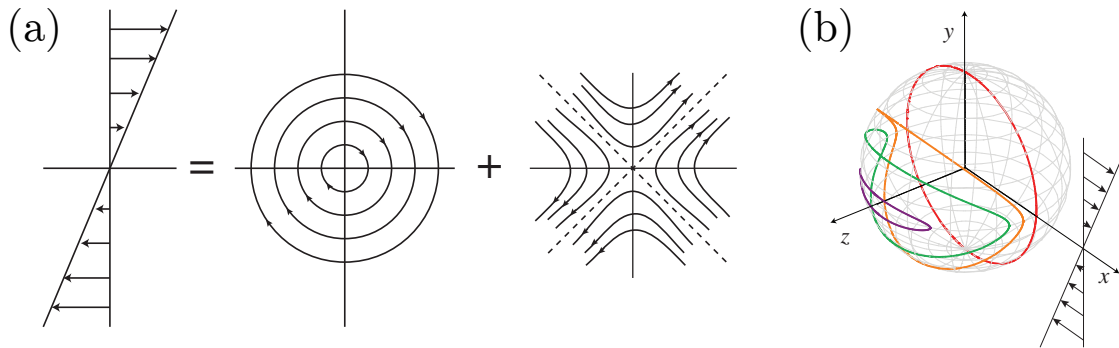


Figure I.18: (a) Decomposition of a simple shear flow into a rotating flow and a pure straining flow oriented at 45° with the flow direction. (b) Jeffery orbits in a shear flow. The colored lines correspond to the trajectory of one edge of an elongated object during a Jeffery orbit. Depending on the initial orientation of the elongated object it will have in-plane rotation (red curve) or will exhibit a "kayaking" motion (orange, green and purple curves). Extracted from [20].

We primarily focused our literature review on the evolution of particles in quiescent fluids or in plug flows, but other flow geometries lead to very interesting particle dynamics as well. Let us take the example of the simple shear flow. It can be decomposed into a rotating flow and a pure straining flow oriented at 45° with respect to the flow direction (see Figure I.18 (a)). When an elongated object is placed in a simple shear flow, it translates with its center of mass flowing at the velocity of the fluid. At the same time it experiences periodic rotations and its tips follow orbital trajectories called "Jeffery orbits". These trajectories are named after George Barker Jeffery who gave a mathematical description of these motions in 1922 [8]. The rotating flow, together with the drag anisotropy of an elongated object, are at the origin of these "Jeffery orbits". The trajectories of the fiber tips, for different initial orientations of the fiber, are shown by the colored lines in Figure I.18 (b). If the fiber is perpendicular to the axis of vorticity of the flow (Oz in Figure I.18 (b)) it will rotate in the plane (Oxy) (see the red curve), but if the fiber axis is neither perpendicular nor parallel to the vorticity axis it will exhibit a "kayaking" motion (see orange, green and purple orbits). Generalizations of these results

in more complex flow geometries have been done in the cases of shear flows and Poiseuille flows near a boundary [42, 43].

When the particle is oriented at 45° with the flow direction, it experiences a compression from the straining flow, which can lead to buckling (see Figure I.19). The situation presented here is very different from the situations encountered in our studies where we deal with Hele-Shaw flow geometries and thus have a plug-like flow in the (Oxy) plane and a Poiseuille-like flow in the (Oxz) plane (see Figure I.7). Thus, we do not detail this argument. Curious readers are invited to refer themselves to the extensive bibliography on the phenomenon of buckling of flexible fibers in simple shear flow [45, 46, 47, 48, 44].

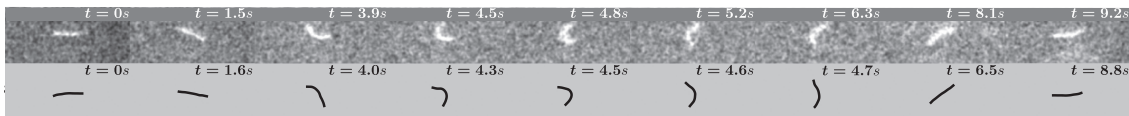


Figure I.19: Buckling of an actine filament in a simple shear flow. Top: experiments, bottom: numerical simulations. Figure extracted from [44].

I.5 Conclusion

In this chapter, we reviewed studies on the dynamics of isolated rigid or flexible fibers evolving in viscous fluids and flows. A lot of work has already been performed to describe and model the transport of rigid fibers by an external viscous flow in confined geometries [13, 14, 30]. The role of the flexibility has, however, not clearly been addressed. Investigations on the deformations of flexible fibers in such geometries mainly dealt with fibers held at a fixed position [40, 41]. Thus, in our study, we will focus on the situations of freely transported flexible fibers oriented either perpendicular or parallel to the flow direction. Contrary to Berthet *et al.* [13] and Nagel *et al.* [30], in our investigations we will look at force distributions along the fiber length and not only at integrated quantities.

When flexible fibers are transported in confined geometries, their shapes change and, as we have seen in this review, these shape variations impact the trajectories. Thus, another aspect of our work will focus on the coupling between the shape of a model rigid fiber and its trajectory. In our studies, motivated by the fact that no experiments have been carried out on the dynamics of fully asymmetric fibers transported in confined geometries, we will primarily investigate the dynamics and the trajectories of "L-shaped" particles.

Chapter II

Materials and methods

The aim of this work is to study the dynamics of isolated fibers transported by an external flow in a confined geometry. Special focus is laid on the investigation of the role of the shape and of the flexibility of the fibers, facing the necessity of using fibers of well-defined and reproducible shape and mechanical properties.

The introduction of microsized objects into microchannels faces different difficulties. Indeed, besides the low variety of commercial micro-particles, the introduction of such an object into a microfluidic channel can lead to clogging of the setup in regions where constrictions are present. Moreover, the manipulation of single particles of this size to place them in the desired position and orientation can be extremely difficult.

In this work we use a technique developed in the group of Patrick Doyle at MIT [15, 16], that consists in creating the particles directly *in situ* using a photolithography technique, which is already well mastered in our group [13]. It allows for an excellent control on the particle geometry, orientation and position inside the microchannel. In this chapter, we describe the experimental method of fabrication of the fibers, the different options chosen to flow them and the protocol used to tune their mechanical properties in order to obtain very flexible fibers.

II.1 Fiber fabrication

II.1.1 Particle fabrication principle

In order to control the position, shape and mechanical properties of the hydrogel particle, we use the so called "stop-flow microscope-based projection photo-lithography method" [15, 16]. A schematic of this technique is shown in Figure II.1 (a).

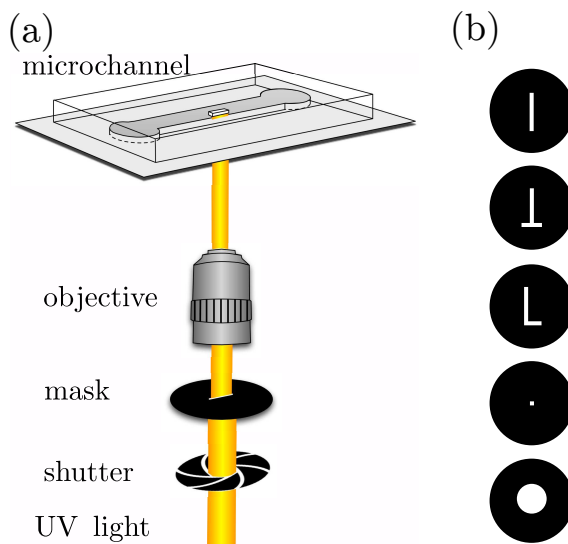


Figure II.1: (a) *In situ* fabrication of fibers using a microscope-based projection lithography technique. UV-light is projected into the channel through a fiber-shaped mask, polymerizing the photosensitive solution inside the channel. (b) Examples of lithography masks.

With an inverted microscope equipped with a UV-source, we expose a polydimethylsiloxane (PDMS) channel filled with a photosensitive solution, composed of an oligomer and a photo-initiator, by flashes of controlled duration. The wavelength emitted by the source needs to match the excitation wavelength of the photo-initiator in order to get crosslinking. A mask, consisting of a black disk with any 2D shape drawn in transparency (see Figure II.1 (b)), is placed in the path of the UV-light, in the field stop position of the microscope. Hence, by focusing the UV-light in the center of the channel an hydrogel particle is fabricated.

The polymeric fibers are fabricated at zero flow rate and we can control the geometry of the hydrogel particle using two different methods. The first one simply consists in using a mask with the desired 2D shape of the particle drawn on it. The second one takes advantage of a motorized stage that can be controlled using a Labview program: a long pulse of UV-light pass trough a dot shaped mask while the microscope stage moves and literally draws the particle. In order to obtain particles with homogeneous mechanical properties with this process, we ensure a constant velocity of the stage during the fabrication of the fiber. Hence, each portion of the fiber is illuminated for the same amount of time. This method is well adapted for the fabrication of long particles of simple geometries, whereas the first technique allows for the fabrication of objects of

more complex shapes but smaller dimensions.

As we project the image of a 2D object in a 3D channel the hydrogel particle has a rectangular cross section.

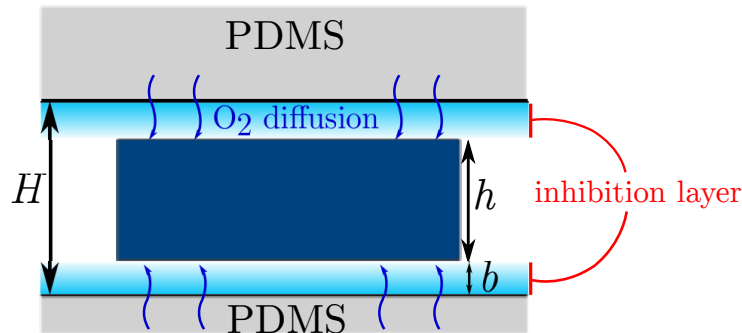


Figure II.2: Sketch of the cross section of the microfluidic chip and the hydrogel particle. The microchannel is entirely made of PDMS. PDMS is porous to oxygen, which diffuses through the channel. As a result, two layers saturated in oxygen appear on the top and on the bottom of the channel. Because the oxygen inhibits the cross-linking reaction the hydrogel does not occupy all the channel height. The height of the inhibition layer is constant and equal to $6 \pm 1.6 \mu\text{m}$.

Due to the permeability of PDMS to oxygen, which inhibits the polymerization, a non-polymerized inhibition layer of constant thickness is left along the top and bottom walls of the channel [16]. These layers are illustrated in Figure II.2. The presence of the inhibition layers is particularly important to our purpose: first, it allows us to flow the particle in the channel (there is no adhesion between the particle and the channel top and bottom walls), and second, because of their constant thickness, it allows us to tune the height of the fiber by changing the channel height. The mask being fixed, we control the particle position by adjusting the position of the channel on the microscope stage.

Figure II.3 shows different geometries of particles created using the stop-flow microscope-based projection photo-lithography method. The long fibers shown in the center of Figure II.3 are fabricated using the second method (moving stage method) and the others using the first method (fixed stage method).

Note that in order to fabricate very long fibers one can also use the technique presented in references [49, 50, 51] which works by illuminating a jet of photosensitive solution with a continuous and fixed UV-spot.

II.1.2 Fabrication protocol

a) The experimental setup

We adapt the stop-flow microscope-based projection photo-lithography method on our setup using an inverted microscope Zeiss Axio Observer equipped with a UV-light source (Lamp HBO 130W) and a $\times 5$ EC Plan NEOFLUAR objective or a $\times 10$ ULTRAFUAR objective. The exposure time is precisely controlled using an electronic shutter (V25, Uniblitz) coupled to an external generator (Agilent 33220A). The mechanical response

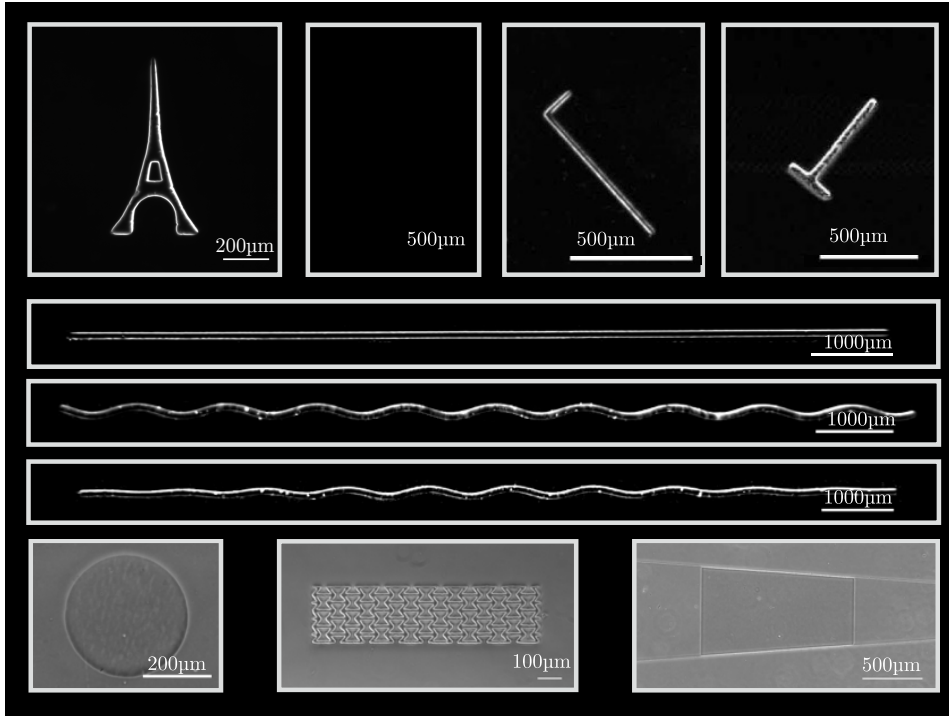


Figure II.3: Examples of particles fabricated using the stop-flow microscope-based projection photo-lithography method. All the particles are fabricated in the absence of flow inside the channel. The different shapes are obtained using different masks or by moving the microscope stage in different ways.

time of the shutter is 10 ms. A band pass filter (11004v2 Chroma) centered at $\lambda = 365\text{nm}$ with a bandwidth of 10 nm is placed in the path of the UV-light just before the lithography mask.

Microchannels are made with polydimethylsiloxane (PDMS, Sylgard 184, Corning) and produced from molds fabricated using a micro-milling machine (Minitch Machinery) or traditional soft lithography technics. They are bonded to a cover slide, spin-coated with a thin layer of PDMS, in order to ensure identical boundary conditions on the four walls. The fabrication protocol of the channels is detailed in the appendix A. The channel is then placed on the motorized stage of the microscope (ASI MS-2000-500).

b) Channel geometry

We use rectangular cross section channels of height much smaller than width. The aspect ratio, width over height, is between 10 and 100. The channel height is a few tens of micrometers, whereas the width is typically one millimeter. The length of the channel is a few centimeters. Such a shallow geometry of the channel is imposed by the particle fabrication technique. Indeed, the particle geometry is highly dependent on the channel height: whereas the geometry of the fiber in the plane of observation is independent of the channel dimensions, the height of the fiber, as we have seen previously, is solely determined by the channel height.

c) Mask design

We design the masks using Clewin or Adobe Illustator softwares. They are printed with the highest resolution available (2400 dpi) at FGN Espace Numérique or at Institut Pierre Gilles de Gennes. The masks are black circles of 2.5 cm diameter with the particle geometry drawn in transparency in its center. Examples of particle masks are shown in Figure II.1 (b).

d) Optical focusing

The fabrication method requires focusing UV-light onto the channel. Due to the chromatic aberration of the optics the focusing distance is different for visible light and UV-light. Practically, the channel will appear out of focus when UV-light is in focus. The "defocusing" distance is found by fabricating particles in test channels with varying focus until the edges of the particle appear sharp.

e) Oligomer solutions

In this work we use different photosensitive solutions which are all composed of the three following elements:

- the oligomer: polyethyleneglycol diacrylate (PEGDA, Sigma). We vary the chains length using two different PEGDA mean number-average molecular weights: $M_n=700$ g/mol and $M_n=575$ g/mol.
- the photoinitiator (PI): Darocur 1173 (2-hydroxy-2-methylpropiophenone, Sigma).
- the solvent: either water or a solution of polyethyleneglycol (PEG, $M_n=1000$ g/mol, Sigma, PEG₁₀₀₀) and water at the ratio 2:1 in volume.

The nature of the photoinitiator has been carefully chosen in order to match the light source wavelength with the photoinitiator excitation wavelength. In all the photosensitive solutions used in this work, we kept a constant ratio of PI, of 10% in volume, to keep the height of the inhibition layers constant [16].

The mechanical properties of the hydrogel particle directly depend on the nature of the photosensitive solution. We vary the relative quantities of oligomer and solvent in order to tune the properties of both the fluid (viscosity, density...) and the hydrogel (Young's modulus, Poisson's ratio...).

The viscosity of the different photosensitive solutions has been measured with an Anton Paar rheometer Physica MCR501, using a cone/plate geometry of 0.5° angle and 60 mm diameter. As illustrated in Figure II.4, all the tested photosensitive solutions are Newtonian fluids i.e. the viscosity is constant for varying shear rates. The shaded region corresponds to sets of parameters where the resolution of the rheometer is low.

The measured viscosities for the different solutions used in our work are summarized in table II.1.

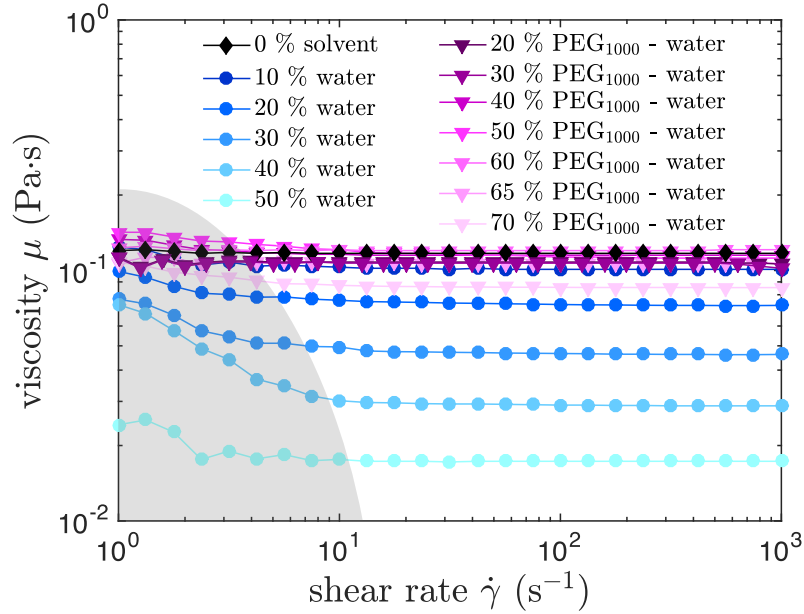


Figure II.4: Viscosity of the photosensitive solutions used in the following studies as a function of the shear rate. No solvent (black diamond) and different solvents (water (circles) and a solution of PEG₁₀₀₀-water at the ratio 2:1 in volume (triangles)) have been used in different quantities. The region corresponding to a low resolution of the rheometer is shaded in grey. In all the cases viscosity is constant as a function the shear rate evidencing the Newtonian character of these fluids.

Volume fraction of solvent	water	PEG ₁₀₀₀ -water (2:1 in volume)
0%	$\mu = 117 \pm 3 \text{ mPa}\cdot\text{s}$	$\mu = 117 \pm 3 \text{ mPa}\cdot\text{s}$
10%	$\mu = 101 \pm 3 \text{ mPa}\cdot\text{s}$	—
20%	$\mu = 73 \pm 3 \text{ mPa}\cdot\text{s}$	$\mu = 108 \pm 3 \text{ mPa}\cdot\text{s}$
30%	$\mu = 46 \pm 3 \text{ mPa}\cdot\text{s}$	$\mu = 107 \pm 3 \text{ mPa}\cdot\text{s}$
40%	$\mu = 29 \pm 3 \text{ mPa}\cdot\text{s}$	$\mu = 116 \pm 3 \text{ mPa}\cdot\text{s}$
50%	$\mu = 17 \pm 3 \text{ mPa}\cdot\text{s}$	$\mu = 112 \pm 3 \text{ mPa}\cdot\text{s}$
60%	—	$\mu = 121 \pm 3 \text{ mPa}\cdot\text{s}$
65%	—	$\mu = 107 \pm 3 \text{ mPa}\cdot\text{s}$
70%	—	$\mu = 85 \pm 3 \text{ mPa}\cdot\text{s}$

Table II.1: Viscosities of the different photosensitive solutions used in this work. — symbols correspond to unmeasured viscosities.

II.1.3 Particle geometry

a) Two-dimensional geometry

The size of the particle depends not only on the size of the drawing on the mask but also on the chosen objective. The objective makes the image of the mask into the microchannel, hence the higher its magnification the smaller the particle.

For all the objectives used in our studies we measure the linear relation between the mask dimension and the particle dimension. The reduction factor (mask length over particle length), the numerical aperture (NA) and the theoretical resolution (D) of the $\times 5$ and $\times 10$ objectives are given in table II.2.

Objectives	$\times 5$ EC Plan NEOFLUAR	$\times 10$ ULTRAFUAR
Reduction factor	1.9	3.9
Numerical aperture (NA)	0.16	0.2
Theoretical resolution (D)	1.1 μm	0.91 μm

Table II.2: Properties of the different objectives used for the fabrication of the hydrogel particles. The wavelength (λ) used for the calculation of the resolution is 365 nm. Resolution (D) is determined using the equations provided by the microscope objectives manufacturer (Zeiss): $D = \lambda / (2 NA)$, with NA the numerical aperture of the objective.

It is easier to work with low magnification objectives, because they have a larger depth of field, simplifying the focus of UV-light. Moreover, the depth of field of the objective should be large enough to ensure homogeneous mechanical properties along the height of the particle, orienting the user to prefer small magnification objectives.

We observe that the minimum achievable particle size is around 5 to 10 μm . Smaller particles are not homogeneous and break when transported in the channel. The maximal size of the particles depends on the choice of the method. If the microscope stage is immobile during fabrication, the maximal size is determined by the width of the light beam at the mask position, which is measured to be 3 mm. Thus, the maximal length of a particle is for instance 1.5 mm using the $\times 5$ EC Plan NEOFLUAR objective. The method that consists in moving the microscope stage during illumination allows for the fabrication of much longer particles. Their sizes are thus only limited by the channel length and width.

An example of particle fabricated using a combination of the two techniques is shown in Figure II.5. The sine shape is fabricated by moving the microscope stage in a controlled way and the vertical lines are fabricated by illuminating the photosensitive solution through a mask on which a vertical rectangle is drawn in transparency. The vertical lines are 1.5 mm long and the sine shaped part is around 4 mm long.

b) Three-dimensional geometry

As we have seen in section II.1.1, the 3D geometry of the particle is determined by the presence of inhibition layers close to the channel walls. Hence, the knowledge of the height of these layers is of paramount importance for the control of the height of the particle. According to Dendukuri *et al.* [16], the height of these thin regions is determined by a competition between the rate of diffusion of oxygen in the photosensitive solution, the rate of production of free radicals and the rate of reaction of the oxygen with radicals. The inhibition layer thus depends on experimental parameters such as light intensity or photoinitiator concentration but not on the channel height. In our experiments, we choose to use a constant concentration of PI (10% in volume) and a constant light intensity in order to have always the same thickness of inhibition layer.

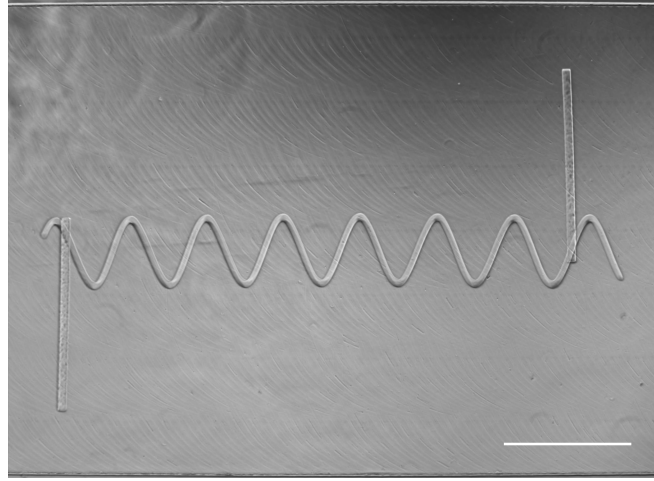


Figure II.5: Hydrogel representing the PMMH logo fabricated using the stop flow microscope-based photolithography method. Two techniques have been used to fabricate the particle. The vertical lines have been fabricated using a mask on which a vertical fiber was drawn in transparency and the sine shape has been fabricated using a dotted mask and moving the microscope stage in a controlled way. Scale bar is 1000 μm .

The thickness of the inhibition layer is measured by the following method: we use a channel of known height H , measured using an optical profilometer with a measurement uncertainty smaller than one micrometer. In this channel, we fabricate a fiber whose width is smaller than its height. If we then apply an external flow, we observe that the fiber rotates until it turns on its side. In this configuration, the fiber height, h , can be measured. Figure II.6 (a) shows a fiber just after fabrication, and Figure II.6 (b) shows the same fiber after rotation. The height of the inhibition layer b is derived using the formula $b = \frac{H-h}{2}$.

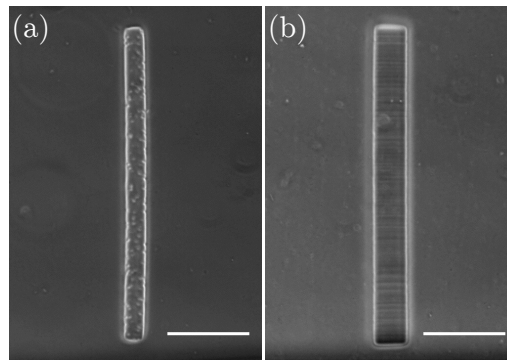


Figure II.6: Two pictures of the same fiber, (a) just after fabrication and (b) after it turned on its side. We adjusted the dimensions of the fiber-shaped mask so that the fiber height is larger than its width. The initial position (a) of the fiber is unstable and a small perturbation makes the fiber rotate (b). Picture (b) allows for a direct measurement of the fiber height h . Knowing the channel height H we derive the height of the inhibition layer $b = \frac{H-h}{2}$. Scale bars are 200 μm .

In our setup we measured a constant inhibition layer of $b = 6 \pm 1.6\mu\text{m}$, both for the $\times 5$ and $\times 10$ magnification objectives.

The knowledge of the inhibition layer thickness allows us to control one key parameter of our studies, the confinement β , defined as the ratio h/H . Since the height of the inhibition layer is constant the confinement is solely defined by the channel height. Thus, we vary the confinement by changing the channel height. As sketched in Figure II.7, an increase (decrease) of the channel height leads to an increase (decrease) of the confinement.

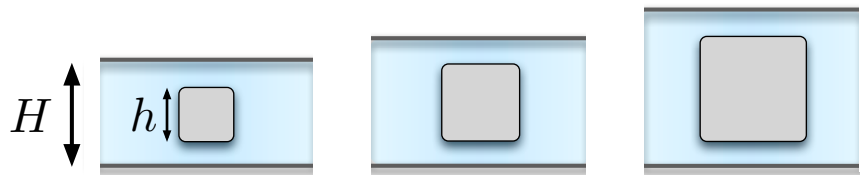


Figure II.7: Sketch of the cross section of the microfluidic chip and the hydrogel particle highlighting the impact of the channel height, H , on the confinement, $\beta = h/H$. From left to right the confinement increases.

In rare situations we wanted to tune the height of the inhibition layers. This can be achieved by changing the protocol of the channels fabrication. If a plasma treatment is used to bind the upper part with the bottom part of the channel, the concentration of oxygen in the PDMS is decreased as well as the height of the inhibition layer. By using this strategy we manage to reduce the inhibition layer height to a minimum of three micrometers.

II.2 Flow control

Once the particles are fabricated, an external flow is imposed and the particles are transported in the channel. In the fluid-structure problems we aim to study, the control of the flow is of crucial importance. We choose to use either a syringe pump or a pressure controller to impose the flow. The main advantage of a syringe pump is the direct control of the the flow velocity by setting the flow rate. The range of flow rate used in our studies varies from a few nL/s to a few hundreds of nL/s. To accurately deliver such low flow rates we use a Nemesys (Cetoni) syringe pump. The pressure controller allows us to impose a pressure difference between the inlet and the outlet of the channel. The main hydraulic resistance is due to the shallow channel and we assume that the inlet tubing and outlet tubing lead to negligible pressure drops. Hence, the pressure difference is mainly applied across the channel. This second method does not allow for a precise control of the flow rate, but has much faster response time than the syringe pump systems.

The outlet of the channel is connected to a reservoir. In rare cases we measure the flow rate by placing the reservoir on a precise scale and monitoring the evolution of the weight.

II.3 Data acquisition and image analysis

II.3.1 Image acquisition

We use dark field microscopy for the image visualization. This technique takes advantage of the fact that the particle and the surrounding fluid do not have the same refractive index, which allows for a visualization of the interface between the particle and the fluid. An Hamamatsu Orca-flash 4.0 camera at a frame rate of few images per second (5 to 10 images per second) is used to record the particle transport. The microscope stage is moved by hand to keep the particle in the field of view of the camera.

II.3.2 Fiber shape and position

The particle shape and position are obtained using standard image treatment procedures (with ImageJ [52] and Matlab) and recorded as a function of time. The grey-level images are binarized and we extract the centerline of the fibers using a skeletonization method. An example of the picture of a bent fiber and its skeletonized shape extracted using our MatLab routine is shown in Figure II.8.

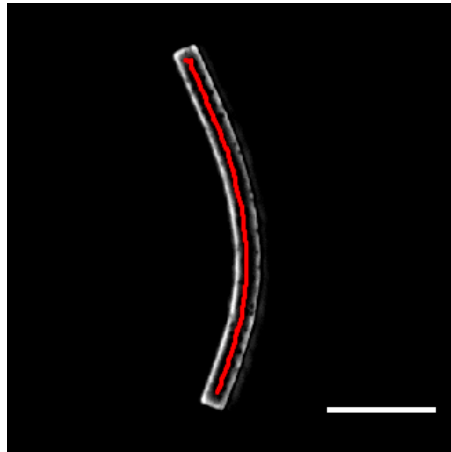


Figure II.8: Superposition of a picture of a deformed fiber and its skeletonized shape (red line) obtained using standard image treatment procedures with ImageJ [52] and Matlab. Scale bar is 200 μm .

II.3.3 Velocity measurements

Streaklines and velocity fields around a moving object can be gathered from experiments. We place a suspension of beads into the photosensitive solution and keep the object in the field of view of the camera while it moves. Figure II.9 (a) shows the streaklines around an hydrogel particle. It is a reconstructed image built from processing several successive snapshots of the flow with suspended latex particles of 1 μm diameter, all superimposed while keeping the fiber in the center of the image. The velocity field around the fiber, shown in Figure II.9 (b), is obtained using particle-tracking velocimetry (PTV) techniques in the frame of reference of the fiber. Velocity is calculated by averaging

the particles velocities on 64×64 pixels windows, and once the system has reached its stationary regime, by averaging over time. The $10\times$ ULTRAFUAR objective used for these measures allows us to image the full channel depth, the flow field obtained thus corresponds to the depth-averaged velocity of the fluid.

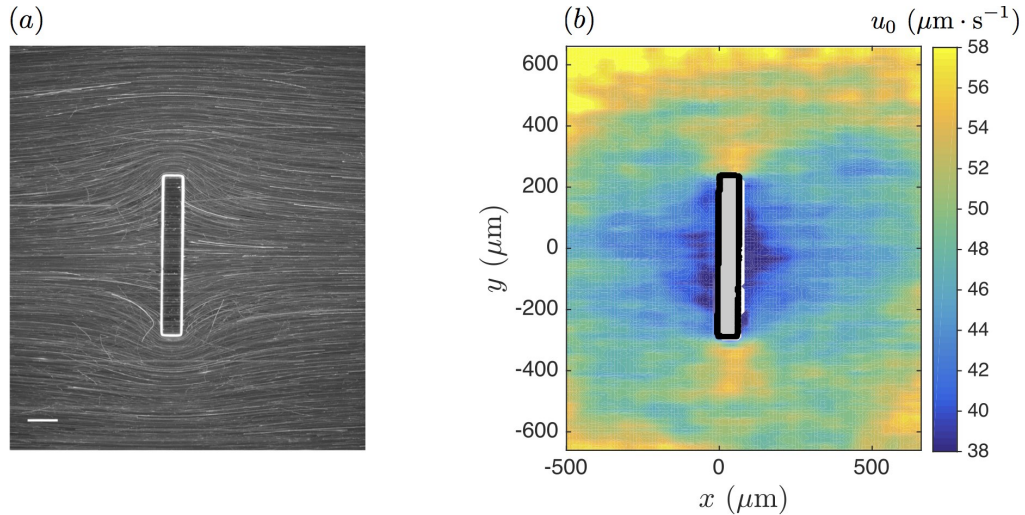


Figure II.9: (a) Streaklines of the flow around a rigid fiber transported by an external flow of velocity u_0 in the reference frame of the fiber. The mean fluid velocity is $u_0 = 48 \mu\text{m} \cdot \text{s}^{-1}$ and the fiber dimensions are $\ell = 528 \pm 5 \mu\text{m}$, $w = 67 \pm 5 \mu\text{m}$, and $h = 49 \pm 3 \mu\text{m}$. Confinement is $\beta = 0.82$. Streaklines are obtained by visualizing $1 \mu\text{m}$ diameter latex beads flowing around the fiber with a $10\times$ objective. Scale bar is $100 \mu\text{m}$. (b) Depth-averaged velocity field around the fiber obtained from the particle tracking by averaging the particles velocities on time and on 64×64 pixel windows. The constant velocity of the fiber has been added to get the velocity field in the reference frame of the laboratory. The noise on the edges of the window field results from lack of data in these regions.

II.4 Mechanical characterization

In the previous sections, we have seen how to fabricate confined objects directly inside microfluidic channels with an excellent control of their shape, orientation and position using the stop flow microscope-based photo-lithography method. Once the particles are created, it becomes important to characterize their mechanical properties. A major technical challenge of our study is to develop a robust protocol to fabricate flexible fibers. In order to tune the bending modulus of a fiber there are two options: either playing with its geometry (width, height) or with its Young's modulus. In our study, we explored both directions: section II.1 already explained how to control and vary the geometry of the particle and this section aims to explain how to tune and measure the Young's modulus of the particle.

II.4.1 Young's modulus of PEGDA hydrogels

In order to decrease the Young's modulus of the hydrogel we based our investigations on the results presented in the paper of Duprat *et al.* [41]. In this study the authors presented an experimental measurement technique of the Young's modulus of fibers fabricated from an oligomer solution composed of PEGDA $M_n = 575$ g/mol and P.I. directly inside a microchannel.

In their article Duprat *et al.* [41] showed that the Young's modulus of an hydrogel depends on different parameters such as the exposure time t_{UV} and the photo-initiator concentration [PI].

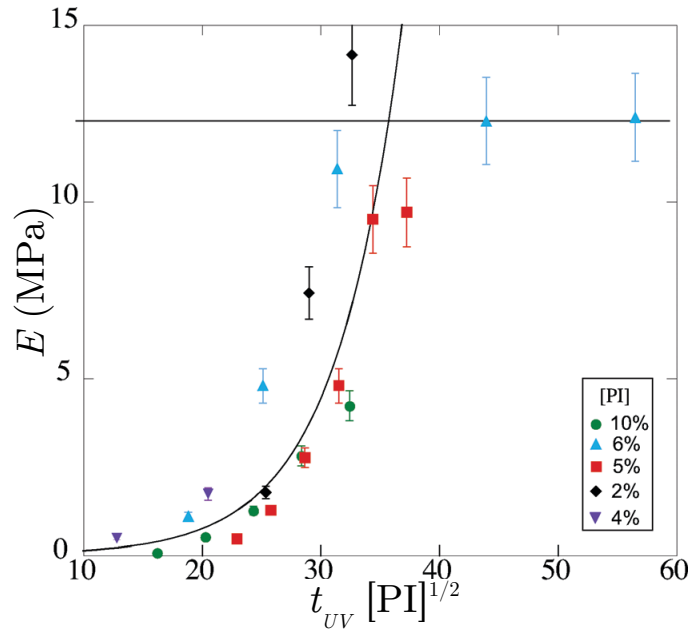


Figure II.10: Evolution of the Young's modulus as a function of the rescaled exposure time $t_{UV}[\text{PI}]^{1/2}$ for various [PI] concentrations (2, 4, 6, 8, 10 vol%). The increasing black line is a fit of the experimental datas with an exponential function $E \simeq Ae^{\frac{t_{UV}[\text{PI}]^{1/2}}{B}}$. The horizontal black line corresponds to the value $E_{\text{plateau}} = \frac{3\rho RT}{M_n}$, where R is the ideal gas constant, T the temperature (in Kelvin), ρ the density, and M_n the number average molecular weight. From Duprat *et al.* [41].

Figure II.10 shows the evolution of the Young's modulus as a function of the rescaled exposure time $t_{UV}[\text{PI}]^{1/2}$ for different exposure times t_{UV} and different photo-initiator concentrations [PI]. All the experimental measurements of the Young's modulus rescale to a master curve. For low exposure time the Young's modulus evolves exponentially with $t_{UV}[\text{PI}]^{1/2}$ until it reaches a plateau. The value of the plateau is given by $E_{\text{plateau}} = \frac{3\rho RT}{M_n}$, where R is the ideal gas constant, T the temperature (in Kelvin), ρ the density, and M_n the number average molecular weight.

According to Figure II.10, different options are possible to vary the Young's modulus of the hydrogel. For instance, a decrease of the photo-initiator concentration [PI] or of the exposure time t_{UV} leads to a decrease of the Young's modulus.

II.4.2 Measurement techniques

Different techniques have been used to characterize the Young's modulus of the hydrogels. Here we briefly present them and focus on their advantages and their limitations.

a) *In situ* characterization

The *in situ* measurement of Young's modulus has been developed by Duprat and coworkers [41].

The principle of the measurement is illustrated in Figure II.11: in a channel with regularly spaced slots (see Figure II.11 (a)), the stop flow photo-lithography method is used to fabricate a rectangular cross section beam inside a notch of the channel (see Figure II.11 (a) and (b)). When an external flow is imposed, the beam is pushed to the notch edges. The liquid flows around the fiber and the resulting hydrodynamic forces (viscous and pressure forces) deform the beam (II.11 (c)). The elasticity of the beam opposes to the deformation. Due to the competition between these two forces (hydrodynamic forces and elastic forces) the fiber will eventually reach an equilibrium deformation. A measure of the beam deflection δ (see Figure II.11 (d)) allows for a direct access to its bending modulus and thus its Young's modulus. The main advantage of this technique relies on the fact that the beam is surrounded by the photosensitive solution and thus the measurement of the Young's modulus takes into account the swelling of the hydrogel.

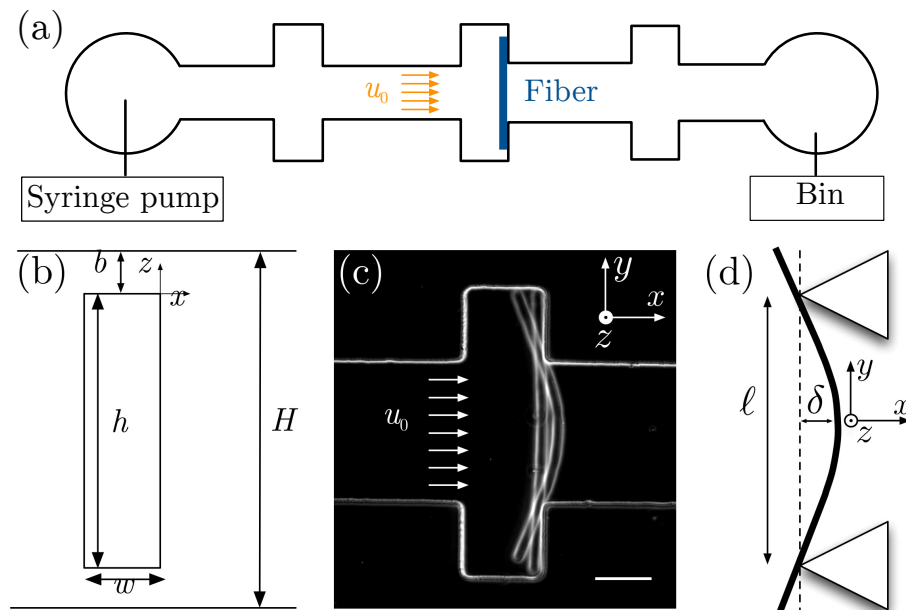


Figure II.11: *In situ* characterization of Young's modulus technique: (a) Sketch of the straight channel presenting regularly spaced notches. (b) Side view of the channel and the fiber. The fiber has a rectangular cross section and is highly confined by top and bottom walls. (c) Superposition of pictures showing the deformation of the beam as the flow is turned on. Scale bar is $100 \mu\text{m}$. (d) The fiber is supported on both edges and bent due to hydrodynamic forces with a maximum deflection δ located at its center.

To derive the force per unit length acting on the fiber, Duprat *et al.* assume the flow to be invariant to translation in the y -direction and they use the lubrication approximation to describe the flow in the gaps between the fiber and the channel top and bottom walls. The deformation is then determined using the Euler-Bernoulli equation (I.15) which is well adapted for slender structures ($w, h \ll \ell$). The maximum deflection of the fiber is given by:

$$\delta = \frac{\mu}{E} u_0 \Lambda, \quad (\text{II.1})$$

with E the Young's modulus, μ the viscosity of the solution, u_0 the mean flow velocity imposed in the channel, and $\Lambda = \frac{15H(h+H)\ell^4}{4hw^2(H-h)^3}$ a factor uniquely dependent on the fiber and channel dimensions.

Note that the deformation reads

$$\frac{\delta}{\ell} = \tilde{\mu} \Lambda', \quad \text{with} \quad \Lambda' = \frac{15}{48} \frac{H}{w} \frac{h^2(h+H)}{(H-h)^3} \quad (\text{II.2})$$

In equation II.2 the deflection δ is proportional to the elasto-viscous number $\tilde{\mu}$, previously introduced in chapter I. This result was expected since the deflection of the fiber is due to a competition between viscous drag and elasticity.

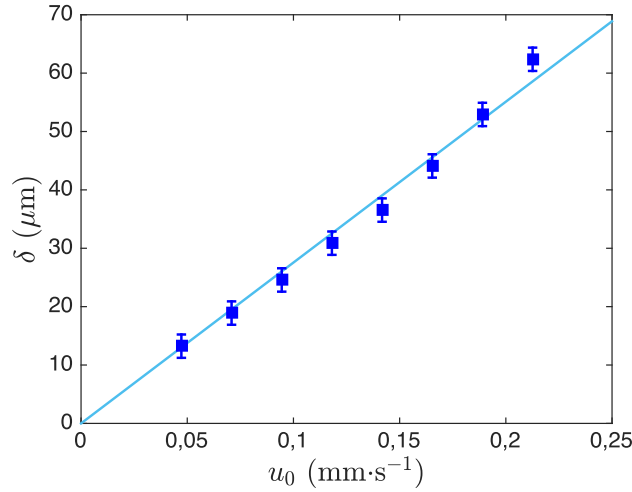


Figure II.12: Maximum deflection δ as a function of the external flow velocity for a beam fabricated from a solution of 90 % of PEGDA $M_n = 700$ g/mol and 10% of P.I. illuminated during $t_{UV} = 300$ ms through a $\times 5$ objective. The dark blue dots correspond to experimental measurements and the light blue line is a linear fit. The corresponding Young's modulus is $E = 6.5$ MPa \pm 2.0 MPa.

Figure II.12 shows the evolution of the deflection δ , as a function of the flow velocity u_0 . As expected from equation II.1, δ varies linearly with u_0 . The linear fit is represented in light blue, and the slope of the curve gives directly the quantity $\mu/E\Lambda$. E is then determined after the measurement of Λ and of the viscosity of the solution μ .

We use this method to measure the Young's modulus of gels fabricated from different oligomer solutions. The hydrogels are created by illuminating the photosensitive solution

during 600 ms, ensuring the Young's modulus to have reached its maximal value i.e. ensuring that the Young's modulus is in the plateau regime shown in Figure II.10.

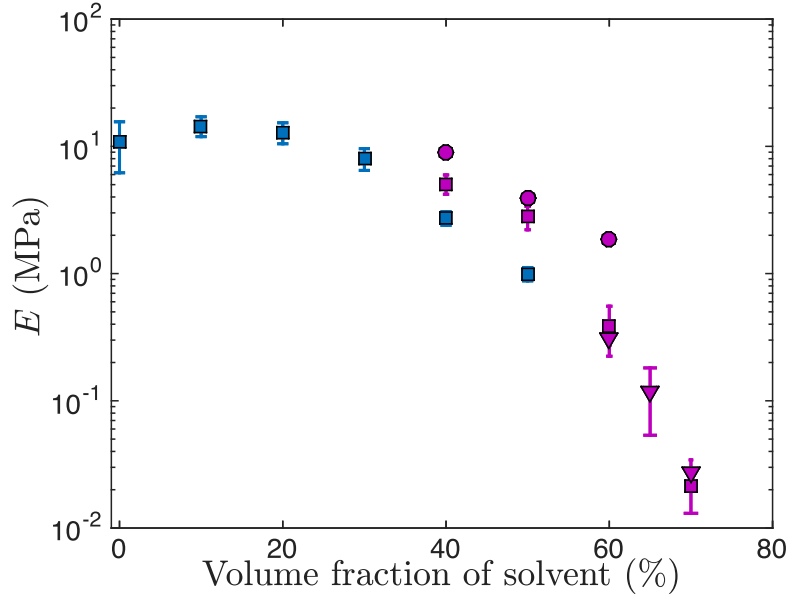


Figure II.13: Evolution of the Young's modulus as a function of the percentage of dilution in the photosensitive solution. Blue and purple symbols correspond respectively to dilution with water and with a solution of PEG₁₀₀₀-water (ratio 2:1 in volume). Measurements are obtained using the *in situ* method [41] and are completed with macroscopic measurements: cantilever experiment (triangles) and micro-indentation experiments (circles).

Figure II.13 shows the evolution of the Young's modulus as a function of the volume fraction of solvent in the photosensitive solution. Two solvents are used: the blue points correspond to a dilution with water and the purple points correspond to a dilution with a solution of PEG₁₀₀₀ - water (ratio 2:1 in volume). For a dilution with more than 50% of water, the oligomer solution starts to be biphasic and no hydrogel can be fabricated.

As visible in Figure II.13, the larger the dilution, the smaller the Young's modulus. Dilution with solvents is thus an efficient way to decrease the Young's modulus of our hydrogels. For instance, diluting PEGDA $M_n = 700$ g/mol with 70% of solvent decreases by almost three orders of magnitude the Young's modulus of the hydrogel.

Note that for very low Young's modulus (dilution with 60% and 70% of solvent) the uncertainty of the measure is quite large. Indeed, such measures are very difficult to carry out. The fiber, being extremely flexible, deforms a lot and eventually escapes from the notches even for low flow velocities. Thus, only few measurements of the deflection as function of the flow velocity are accessible, leading to inaccurate determination of the Young's modulus. The two points corresponding to dilution with 60% and 70% of solvent have been obtained using a suspension of tracer beads of 1 μm diameter in the solution in order to measure the mean flow velocity. Such an external measurement is required since

at low flow velocity the flow rate imposed by the syringe pump can be slightly different than the set point.

b) Cantilever experiment

To supplement the *in situ* measurements presented previously, we carried out cantilever experiments.

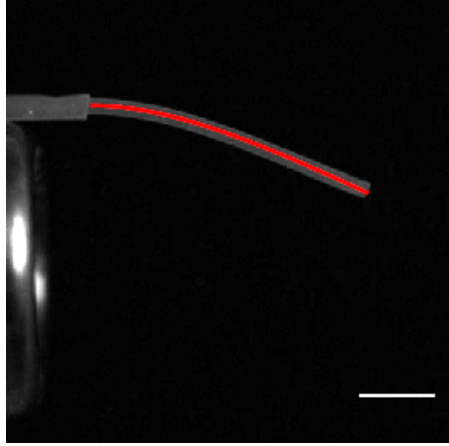


Figure II.14: Superposition of a picture of a filament fabricated from the 60% PEG₁₀₀₀-water solvent bent by its own weight and a fit (red line) of its shape using equation II.3. Scale bar is 1 mm.

The experiment relies on the study of the shape of a clamped-free cylindrical cantilever beam bent under its own weight. This method allows for a direct measurement of the bending modulus of the fiber, from which we can extract the Young's modulus. We fit the shape of the beam, as it is illustrated in Figure II.14, by the theoretical equation [53, 54]:

$$\delta(x) = \frac{2}{3} \frac{\rho g}{E d^2} (x^4 - 4\ell x^3 + 6\ell x^2), \quad (\text{II.3})$$

with δ the deflection of the fiber, E the Young's modulus, ρ the density of the gel, g the gravitational acceleration, d the diameter of the beam and ℓ its length.

The derivation of equation II.3 is detailed in appendix B.

We use the numerical least squares method, with the Young's modulus E as a unique fitting parameter, to fit the shape of the beam.

The measurements of the Young's modulus of hydrogels fabricated from solutions with 60%, 65% and 70% of PEG₁₀₀₀-water solvent are shown in Figure II.13 (triangles). Each point corresponds to an average value of the Young's modulus obtained from experiments in which we varied the filament length and its diameter. The error bars correspond to the standard deviation of the different measurements.

Figure II.13 shows an excellent agreement between the *in situ* (squares) and the cantilever (triangles) measurements.

The main advantage of this technique compared to the previous one stands on its simplicity. Indeed, if the Young modulus is low, one can always decrease the filament

length to ensure small deformations and apply the measurement method successfully. But on the other hand, this technique does not take into account the swelling of the gel. As the hydrogel is dry the impact of the solvent on the mechanical properties of the hydrogel cannot be evaluated.

c) Microindentation method

A third measurement method - based on micro-indentation - has been used to verify our results. These measurements have been done in the FAST laboratory with the help of Ludovic Pauchard and Camille Duprat following the experimental protocol described in reference [55]. Using a micro-indentation technique, sketched in Figure II.15 (a), we determine the Young's modulus of our hydrogels: a spherical tip of radius R initially in contact with the hydrogel surface is driven inside the sample. The applied normal force F is measured as a function of the penetration depth p . Figure II.15 (b) shows indentation force-displacement (F - p) responses for an hydrogel obtained from a solution of 50% PEG₁₀₀₀-water solvent.

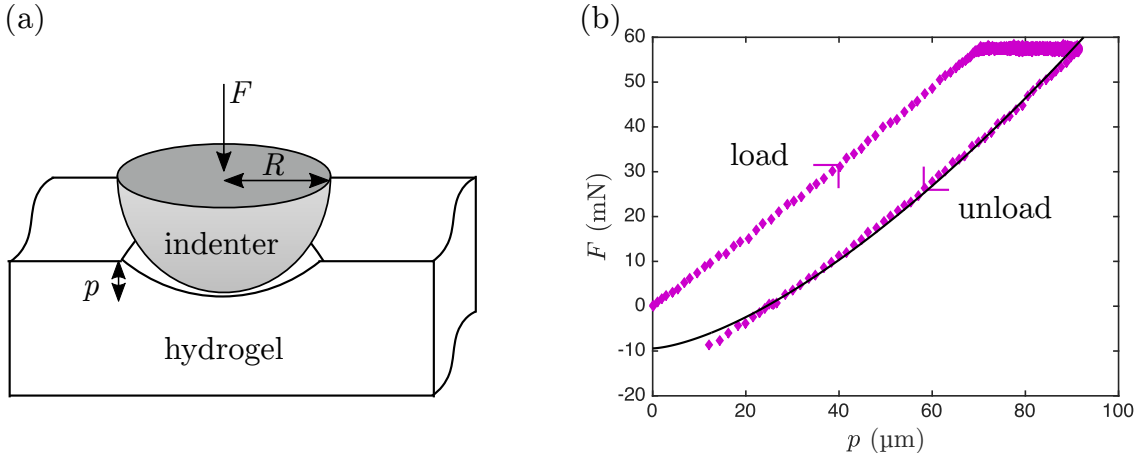


Figure II.15: (a) Sketch of the indentation method. (b) Indentation force-displacement response of an hydrogel obtained from a solution of 50% PEG₁₀₀₀-water solvent. The black curve correspond to a fit of the unloading part of the curve by the Hertz formula (equation II.4).

Measurements of the applied indentation force as a function of the penetration depth are well described by the Hertz contact theory. The Young's modulus is extracted by fitting the force-displacement response in the unload regime using the Hertz formula:

$$F = \frac{4}{3} \frac{E}{1 - \nu^2} p^{3/2} \sqrt{R}, \quad (\text{II.4})$$

with F the loading force, E the Young's modulus, ν the Poisson's ratio, p the penetration depth and R the radius of the indenter.

For the fit shown in Figure II.15 (b) we use the Poisson's ratio determined experimentally in chapter III. We followed the same protocol for gels obtained from solutions diluted with 40% and 60% of PEG₁₀₀₀-water. We do not have measurements of the Poisson's ratio of the hydrogel obtained from a dilution of the solution with 60% of PEG₁₀₀₀-water

and we took a value $\nu_{60\%} = 0.16$. The derived Young's moduli are represented by circles in Figure II.13. Good agreements with the other techniques are obtained for the gels diluted with 40% and 50% of PEG₁₀₀₀-water. For the dilution with 60 % of solvent the measured Young's modulus is larger than the ones measured with the *in situ* and with the cantilever techniques. This is due to low number of experimental points available in the unloading regime. Indeed, the hydrogel being very soft, large penetration depths p were obtained even for low normal forces F and the force probe was not sensitive enough to have reliable measurements. For the hydrogel created from a solution diluted with 70% of PEG₁₀₀₀-water solvent the indentation method was not conclusive, no normal force measurements were achievable even for large penetration depths.

d) Compression tests

A last technique, relying on compression tests, has been used for the measurement of the Young's moduli of our hydrogels. We place a cylindrical sample of gel on the stage of a rheometer and we impose a compression using a plate-plate geometry of 25 mm diameter. The rheometer (Anton Paar Physica MCR501) cannot measure normal force larger than 40N corresponding to normal stress of $\sigma = 81$ kPa thus only low Young's modulus can be measured using this tool.

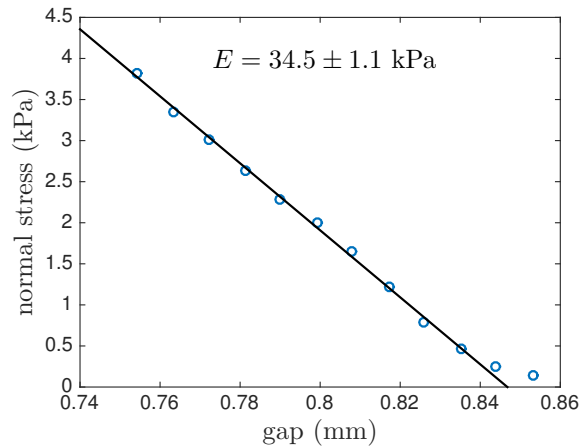


Figure II.16: Compression test. Normal stress as a function of the gap size between the two plates of a rheometer.

We impose the gap, wait for 30 minutes until the normal force converges to its final value and measure the normal force. Figure II.16 shows the evolution of the normal stress (normal force divided by the area of contact between the hydrogel and the indenter) as a function of the gap height for an hydrogel fabricated from a solution diluted with 70% PEG₁₀₀₀-water solvent. The slope of the curve is proportional to the Young's modulus and a linear fit of the measurements yields to a Young's modulus $E_{70\%}^{\text{comp}} = 35 \pm 1$ kPa. A fair agreement is obtained between this measurement and the measurements obtained with the *in situ* technique $E_{70\%}^{\text{in situ}} = 21 \pm 8$ kPa and with the cantilever technique $E_{70\%}^{\text{cantilever}} = 27 \pm 7$ kPa.

Chapter III

Novel *in situ* techniques to measure mechanical properties

In the previous chapter, we presented the experimental technique used to fabricate hydrogel particles of well-defined shapes, positions and orientations. We also discussed one of the major advantage of the technique which relies on the possibility to tune the mechanical properties of these hydrogels. The discussion was followed by a presentation of the different experimental techniques used to measure the Young's modulus of the hydrogels. We have seen that the measurement of low Young's modulus faces many difficulties: low flow velocities are needed for the *in situ* method, and in this regime the flow rate imposed by a syringe pump is not reliable. A way to overcome this problem is to accurately measure the flow velocity by particle tracking techniques. Such technique implies the use of tracers (small beads of radius 1 μm) that can impact the flow. This is especially true in the gaps between the particle and the channel top and bottom wall which have a typical size of 6 μm . The other techniques, such as the compression tests and the cantilever experiments, allow for the measure of small Young's modulus but do not take into account swelling effects due to the presence of the uncured solution surrounding the hydrogel particle as the hydrogel needs to be taken out of the channel in order to carry out the experiments.

To solve these experimental issues, we developed with Vincent D'Herbement, master 1 intern in the group, a novel *in situ* technique to measure low Young's modulus directly inside the microchannel. This technique is inspired by the work of Wyss *et al.* [56] and Li *et al.* [57, 58] who measured Young's modulus from the deformation of hydrogel spheres pushed into conical constrictions. Here we adapt this idea to geometries with rectangular cross sections. This technique is used to measure the Young's modulus of very soft hydrogels.

To completely describe the elasticity of a material, one needs the measure of two quantities among the shear modulus, bulk modulus, Young's modulus, Lamé's first parameter and Poisson's ratio. In this study, in addition to the measure of the Young's modulus, we develop an *in situ* measurement technique of the Poisson's ratio that we apply to different hydrogels.

III.1 Measurements of Young's modulus

III.1.1 Description of the method

The determination of the Young's modulus of the hydrogel relies on the following experiment: a trapezoidal particle is pushed through a constriction by applying a pressure difference ΔP (using a pressure controller). The particle moves into the constriction, is compressed by the lateral walls of the channel and eventually reaches an equilibrium position given by the competition of the elastic forces and the hydrodynamic forces (ΔP being maintained constant). Figure III.1 shows a superposition of images of an initially undeformed trapezoidal particle and the same particle pushed through the constriction by the external flow.

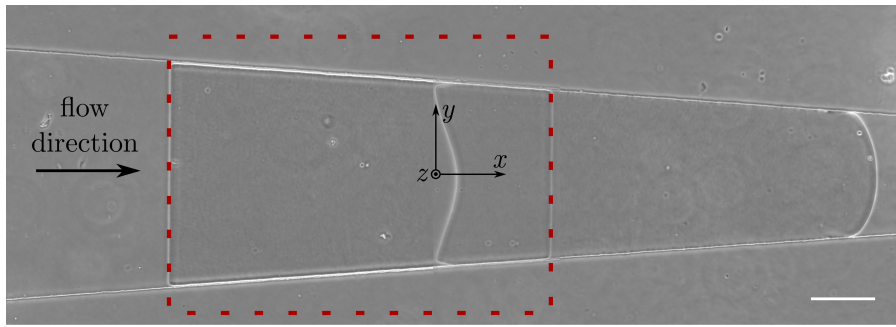


Figure III.1: Superposition of pictures of a trapezoidal particle just after fabrication and when pushed through the constriction and compressed by the lateral walls. The red dotted frame corresponds to the image of the mask used to fabricate the particle. Scale bar is 500 μm .

When the equilibrium is reached, knowing the forces applied by the flow (viscous forces and pressure forces) and measuring the compression of the particle in the y -direction we can determine the Young's modulus of the particle. We study one trapezoidal particle taking a movie (one frame per second) of its displacement during at least 1000 s. Once the particle has reached its equilibrium position, a last image is taken and then we flow the particle out of the channel and start again the experiment. In some cases, at the end of the experiment (i.e. after 1000 s), the particle is still moving but at very low velocity (typically $0.05 \mu\text{m}\cdot\text{s}^{-1}$) and we consider this velocity to be zero.

For the sake of simplicity, we directly fabricate trapezoidal particles in the channel by using a rectangular mask larger than the channel width (see the red dotted frame in Figure III.1). This fabricates particles that have the exact same geometry as the channel: symmetry towards the x -axis and same inclination angle θ as the channel. Note that the lateral wall being in PDMS there exists inhibition layers at the lateral sides of the trapezoidal particle.

We use channels of height $H = 57 \pm 3 \mu\text{m}$ or $H = 103 \pm 3 \mu\text{m}$ and of small constriction angle ($\theta < 10^\circ$). As described in chapter II the inhibition layer (gap between the particle and the channel top or bottom walls) has a constant height $b = 6 \pm 1.6 \mu\text{m}$. Thus, the two channels lead respectively to particle heights $h = 45 \pm 3 \mu\text{m}$ or $h = 97 \pm 3 \mu\text{m}$. We then systematically vary the imposed pressure difference ΔP and the constriction angle

and study the resulting deformation of the particle.

III.1.2 Modelling

The geometries of the channel and of the particle just after fabrication, are sketched in Figures III.2 (a) and (b) (dark blue particle). The particle is fully characterized by its larger width y_0 , length x_0 and height h . When an external flow is imposed, the trapeze advances in the channel over a distance Δx until it reaches its equilibrium position. At equilibrium, the particle being compressed by the lateral walls, its geometry changes leading to a new width y_f , length x_f and height h_{eq} (light blue particle). Note that for usual hydrogels the Poisson's ratio is larger than zero. As a consequence h_{eq} is expected to be larger than h and the gap height at equilibrium b_{eq} is expected to be smaller than b . The flow in the gap between the particle and the channel top wall is sketched in Figure III.2 (c).

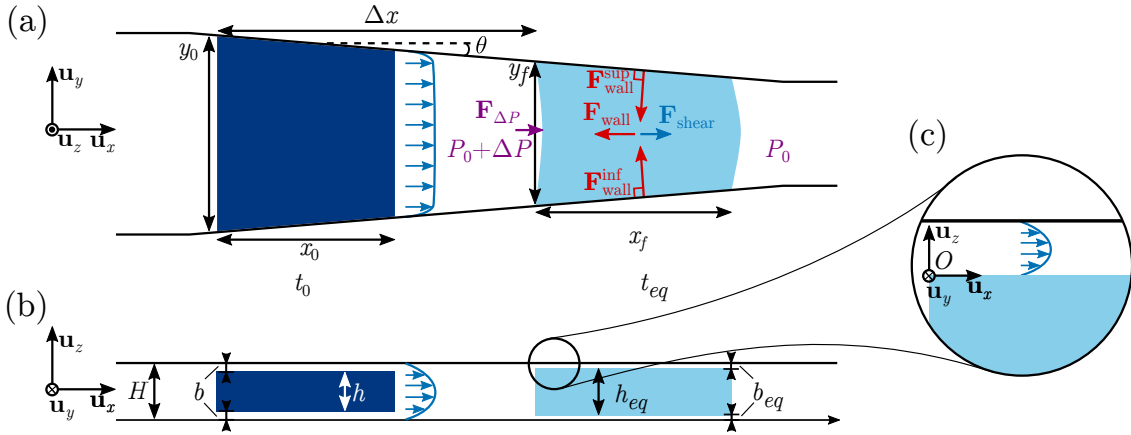


Figure III.2: Sketch of the experiment. (a) top view. (b) side view. (c) is a zoom of the gap between the particle and the channel top wall. At equilibrium the flow in the gap is Poiseuille-like. The particle just after fabrication is represented in dark blue, and the particle at equilibrium is represented in light blue.

When the particle reaches its equilibrium position, it is subject to different forces: a pressure force due to the difference of pressure between the front and the back of the particle ($\mathbf{F}_{\Delta P}$), a force due to the shear stress resulting from the flows in the gaps between the particle and the channel top and bottom walls ($\mathbf{F}_{\text{shear}}$) and the force ($\mathbf{F}_{\text{wall}} = \mathbf{F}_{\text{wall}}^{\text{sup}} + \mathbf{F}_{\text{wall}}^{\text{inf}}$) due to the walls normal reaction. The particle being subject to a zero total force, these three forces, sketched in Figure III.2, balanced:

$$\mathbf{F}_{\Delta P} + \mathbf{F}_{\text{shear}} + \mathbf{F}_{\text{wall}} = \mathbf{0}. \quad (\text{III.1})$$

Note that we neglect friction forces between the particle and the channel lateral walls due to the zero velocity of the particle. In other words we assume that there is no solid friction between the hydrogel and the walls but only friction dependent on the particle velocity [59, 60, 61].

Due to the low constriction angle θ , we assume that the front and the back of the particle have the same width. Thus, the pressure force $\mathbf{F}_{\Delta P}$ reads

$$\mathbf{F}_{\Delta P} \sim \Delta P y_f h_{eq} \mathbf{u}_x, \quad (\text{III.2})$$

with ΔP the difference of pressure across the object and \mathbf{u}_x the unit vector in the x -direction.

Assuming Poiseuille flows (see Figure III.2 (c)) and a linear decrease of the pressure in the gaps between the particle and the top and bottom walls ($\frac{\partial P}{\partial x} = -\frac{\Delta P}{x_f}$) we obtain the flow profile [21]

$$\mathbf{u}(z) = \frac{b_{eq}^2}{2\mu} \frac{\Delta P}{x_f} \left(\frac{z}{b_{eq}} - \frac{z^2}{b_{eq}^2} \right) \mathbf{u}_x. \quad (\text{III.3})$$

Thus, if the constriction angle θ is small, $\mathbf{F}_{\text{shear}}$ can be approximated by:

$$\mathbf{F}_{\text{shear}} \sim 2y_f x_f \mu \left. \frac{\partial \mathbf{u}}{\partial z} \right|_{z=0} = b_{eq} y_f \Delta P \mathbf{u}_x. \quad (\text{III.4})$$

Let us now look at the orders of magnitude. As seen previously, $h_{eq} \gtrsim h$ and $b_{eq} \lesssim b$. Moreover, as mentioned in chapter II, the fabrication technique used here implies $h \gg b$. Hence, $h_{eq} \gg b_{eq}$ and $\Delta P y_f b_{eq} \ll \Delta P y_f h_{eq}$. As a consequence one can neglect the shear force $\mathbf{F}_{\text{shear}}$ with respect to the pressure force $\mathbf{F}_{\Delta P}$ and equation III.1 can be simplified to

$$\mathbf{F}_{\Delta P} + \mathbf{F}_{\text{wall}} = \mathbf{0}. \quad (\text{III.5})$$

By symmetry the y -component of \mathbf{F}_{wall} is zero.

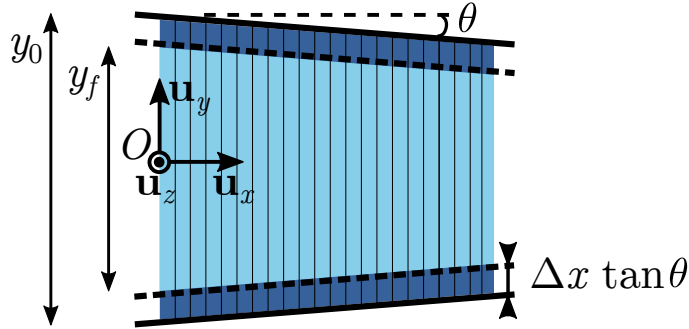


Figure III.3: Sketch of the equivalent system. The trapeze particle is decomposed in an assembly of columns of varying heights compressed by two tilted planes. The undeformed particle is represented in dark blue, and the compressed particle is represented in light blue.

In order to derive the x -component of \mathbf{F}_{wall} , we consider an equivalent system consisting in a trapeze particle decomposed in an assembly of columns of varying heights compressed by two tilted planes. The situation is sketched in Figure III.3. When compression occurs, each column is subject to a stress σ_{yy} (stress in the y -direction, normal

to the y -surface) and experiences a strain ϵ_{yy} (strain in the y -direction, normal to the y -surface). Since each column has a different initial height, ϵ_{yy} and σ_{yy} are functions of the position x .

A displacement of the particle over a distance Δx leads in the equivalent system to a compression of each column of $\Delta y = -2\Delta x \tan \theta$. As a consequence, a column placed in x , which had an initial height $y_{\text{init}}(x) = y_0 - 2x \tan \theta$ has a final height $y_{\text{fin}}(x) = y_0 - 2x \tan \theta - 2\Delta x \tan \theta$. Hence, the strain ϵ_{yy} reads

$$\epsilon_{yy}(x) = -\frac{y_{\text{init}}(x) - y_{\text{fin}}(x)}{y_{\text{fin}}(x)} = -\frac{2\Delta x \tan \theta}{y_0 - 2x \tan \theta}. \quad (\text{III.6})$$

On the other hand, assuming that the hydrogel is an isotropic elastic material we can write the stress-strain relations [62]:

$$\epsilon_{xx} = \frac{1}{E}[(1 + \nu)\sigma_{xx} - \nu(\sigma_{xx} + \sigma_{yy} + \sigma_{zz})], \quad (\text{III.7})$$

$$\epsilon_{yy} = \frac{1}{E}[(1 + \nu)\sigma_{yy} - \nu(\sigma_{xx} + \sigma_{yy} + \sigma_{zz})], \quad (\text{III.8})$$

$$\epsilon_{zz} = \frac{1}{E}[(1 + \nu)\sigma_{zz} - \nu(\sigma_{xx} + \sigma_{yy} + \sigma_{zz})], \quad (\text{III.9})$$

with ϵ_{ij} , σ_{ij} being respectively the strain and the stress in the particle in the i direction and normal to the j surface.

We introduce, here, a new quantity Π_{wall} : the stress due to the normal reaction of the wall in the direction normal to the wall. It is related to σ_{yy} by the following equation:

$$\Pi_{\text{wall}} = -\frac{\sigma_{yy}}{\cos \theta}. \quad (\text{III.10})$$

This quantity allows for a simple expression of the x -component of the force due to the walls normal reaction

$$F_{\text{wall}}^x = -h_{eq} \int_{x_f} 2\Pi_{\text{wall}} \sin \theta \frac{dx}{\cos \theta}. \quad (\text{III.11})$$

In order to derive σ_{yy} or Π_{wall} from equations III.8 and III.6 one needs to know the expressions of σ_{zz} and σ_{xx} .

First, we suppose that the top and bottom of the particle are free, i.e. that there is no contact between the particle and the channel top and bottom walls. It yields

$$\sigma_{zz} = 0. \quad (\text{III.12})$$

This assumption will be verified for each experiment by calculating the deformation of the particle in the z -direction - once the Poisson's ratio is known - and by comparing it to the height of the channel.

Second, we assume a linear decrease of the stress in the x -direction, matching the two boundary conditions $\sigma_{xx}(0) = \Delta P$ and $\sigma_{xx}(x_0) = 0$:

$$\sigma_{xx} = -\Delta P \left(1 - \frac{x}{x_0}\right). \quad (\text{III.13})$$

Using equations III.10, III.12 and III.13, equation III.8 becomes:

$$\epsilon_{yy} = \frac{1}{E} \left[-\Pi_{wall} \cos \theta + \nu \Delta P \left(1 - \frac{x}{x_0}\right) \right]. \quad (\text{III.14})$$

From equations III.6 and III.14 we derive the stress applied by the wall on the particle Π_{wall} :

$$\Pi_{wall} = \frac{1}{\cos \theta} \left[\nu \Delta P \left(1 - \frac{x}{x_0}\right) + \frac{2E\Delta x \tan \theta}{y_0 - 2x \tan \theta} \right]. \quad (\text{III.15})$$

Equation III.11 together with equation III.15 lead to

$$F_{wall}^x = h_{eq} \int_{x_f} \frac{2 \tan \theta}{\cos \theta} \left[\nu \Delta P \left(1 - \frac{x}{x_0}\right) + \frac{2E\Delta x \tan \theta}{y_0 - 2x \tan \theta} \right] dx, \quad (\text{III.16})$$

$$F_{wall}^x = h_{eq} \frac{2 \tan \theta}{\cos \theta} \left[\nu \Delta P \left(x_f - \frac{x_f^2}{2x_0}\right) + E\Delta x \ln \left(\frac{y_0}{y_0 - 2x_f \tan \theta}\right) \right]. \quad (\text{III.17})$$

Using equations III.2 and III.17, the projection on the x -axis of the zero force condition (equation III.5) reads

$$\Delta P y_f = \frac{2 \tan \theta}{\cos \theta} \left[\nu \Delta P \left(x_f - \frac{x_f^2}{2x_0}\right) + E\Delta x \ln \left(\frac{y_0}{y_0 - 2x_f \tan \theta}\right) \right]. \quad (\text{III.18})$$

The larger width of the compressed trapeze y_f is related to the distance travelled by the particle Δx as follows $y_f = y_{in}(x=0) = y_0 - 2\Delta x \tan \theta$.

Introducing the two quantities $\Lambda = 1 - 2 \tan \theta \left[\frac{\Delta x}{y_0} + \nu \frac{x_f}{y_0 \cos \theta} \left(1 - \frac{x_f}{2x_0}\right) \right]$ and $\Gamma = -\frac{2 \tan \theta \Delta x}{y_0 \cos \theta} \ln \left(1 - \frac{2 \tan \theta x_f}{y_0}\right)$ we eventually obtain:

$$\Delta P \Lambda = E \Gamma. \quad (\text{III.19})$$

Λ and Γ depend only on the distance traveled by the particle until the equilibrium is reached (Δx) and on the particle geometries at rest and at equilibrium. Thus, according to equation III.19, measurements of these parameters for varying pressure differences ΔP lead directly to the determination of the Young's modulus of the particle.

III.1.3 Experimental results

Monitoring the displacement of the trapezoidal particle through the constriction we measure the evolution of Δx - which is directly linked to the strain in the y -direction - as a function of time.

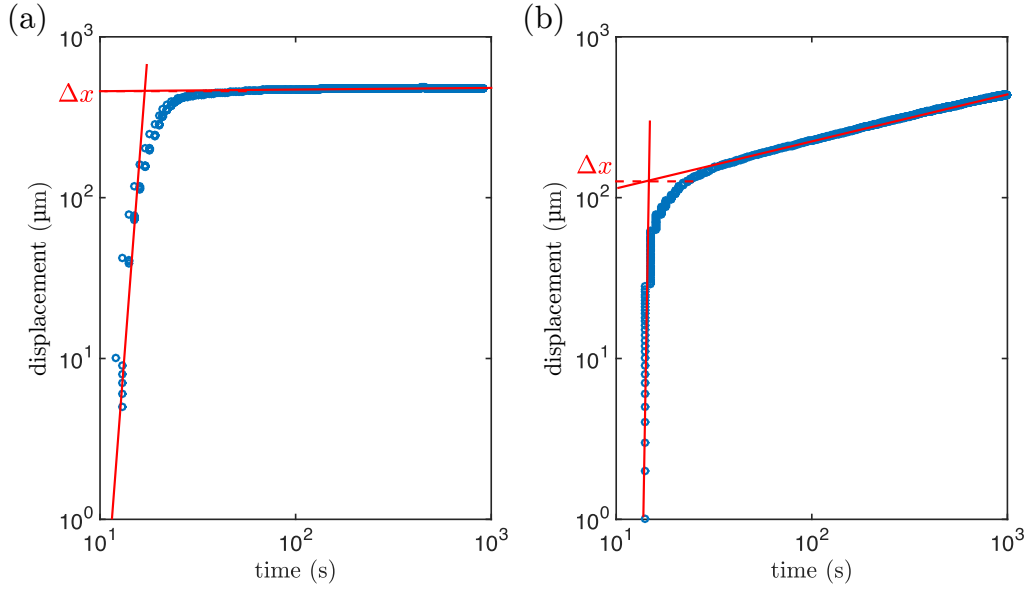


Figure III.4: Two examples of the displacement of the trapezoidal particle as a function of time. Two regimes highlighted by the red lines are visible. The first regime corresponds to a fast increase of the displacement as a function of time due to the elastic compression of the particle. This first regime is followed by a long time evolution regime that can be different from one experiment to the other. In (a) the displacement remains constant in the second regime corresponding to a stop of the particle in the constriction whereas in Figure III.4 (b) the elastic regime is followed by a slow displacement of the particle through the constriction which can be due to a creep of the particle. We consider the equilibrium displacement Δx as the value at the end of the elastic regime where the two red lines cross each other.

Two examples are given in Figure III.4 (a) and (b). In each example, two different regimes are visible. The first one corresponds to a fast increase of Δx as a function of time, which is a signature of the elastic deformation of the trapeze. It is followed by a second regime where the evolution of Δx is different in the two examples. In Figure III.4 (a), Δx does not evolve anymore after the elastic regime corresponding to a complete stop of the particle in the constriction whereas in Figure III.4 (b) the elastic regime is followed by a slow displacement of the particle through the constriction which can be due to a creep of the particle. Aiming to determine the Young's modulus of the hydrogels we primarily focus on the elastic regime and consider the equilibrium displacement as the value at the end of the elastic regime i.e. where the two slopes - highlighted by the red lines in each situations - cross each other.

We measure the equilibrium displacement for different values of ΔP , as shown in Figure III.5 (a) and (b), for different experimental conditions. Figure III.5 (a) shows the evolution of ΔP as a function of Δx for a gel fabricated from a photosensitive solution composed by 65% PEG₁₀₀₀-water solvent, 25% of PEGDA $M_n=700$ g/mol and 10 % P.I.. Figure III.5 (b) corresponds to different series of measurements for a gel fabricated from a photosensitive solution composed by 70% PEG₁₀₀₀-water solvent, 20% of PEGDA $M_n=700$ g/mol and 10 % P.I.. The different series correspond to different trapeze geometries and constriction angles.

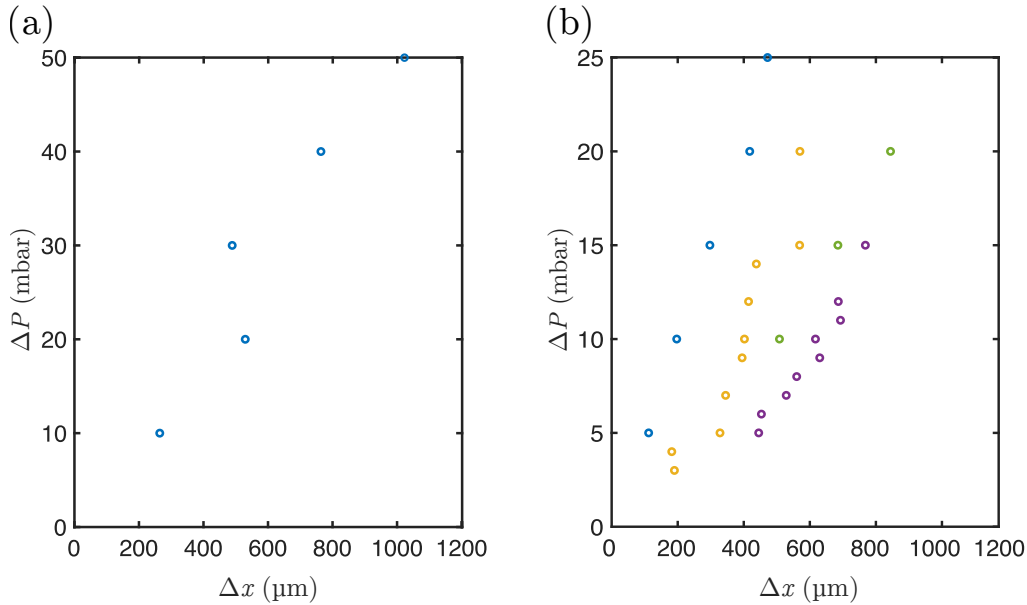


Figure III.5: Evolution of the pressure difference ΔP as a function of the particle equilibrium displacement Δx for two different hydrogels. (a) hydrogel obtained from a solution composed by 65% PEG₁₀₀₀-water solvent, 25% of PEGDA $M_n=700$ g/mol and 10 % P.I. and (b) hydrogel obtained from a solution composed by 70% PEG₁₀₀₀-water solvent, 20% of PEGDA $M_n=700$ g/mol and 10 % P.I.. In (b) the different colors correspond to four different sets of measurements with different constriction angles (θ) and particle geometries (x_0 and y_0).

It can be noticed that all these curves seem to evolve linearly, which is, at first sight, surprising if we compare to equation III.19. It is actually due to the fact that Δx , x_f and y_0 are of the same order of magnitude and θ is small (always smaller than 10°). As a consequence, the second term of Λ is small compared to unity and can be neglected, with this simplification the equation III.19 shows a linear relation between ΔP and Δx with a slope depending on the particle geometry and the Young's modulus of the hydrogel.

A more straightforward way to determine the Young's modulus of the hydrogels consists in looking at the evolution of $\Delta P\Lambda$ as a function of Γ , as shown in Figure III.6 (a) (65% of solvent solution) and (b) (70% of solvent solution). According to equation III.19, the Young's modulus of the hydrogel corresponds to the slope of these curves. The determination of Λ and Γ needs the measurement of the particle geometries and the knowledge of the Poisson's ratio of the hydrogel. The last quantity can be measured by a complementary experiment detailed in section III.2. The value of the Poisson's ratio has a small impact on the determined Young's modulus, as it appears in the right term of Λ which is small compared to unity and which can be neglected in a first approximation. For the two gels used in this study, we take a Poisson's ratio $\nu = 0.16$ corresponding to the value measured for poorly cross-linked hydrogels (see section III.2).

Figures III.6 (a) and (b) show good correlation between the different points of each series of experiments. However, systematic errors seem to be present since all the points

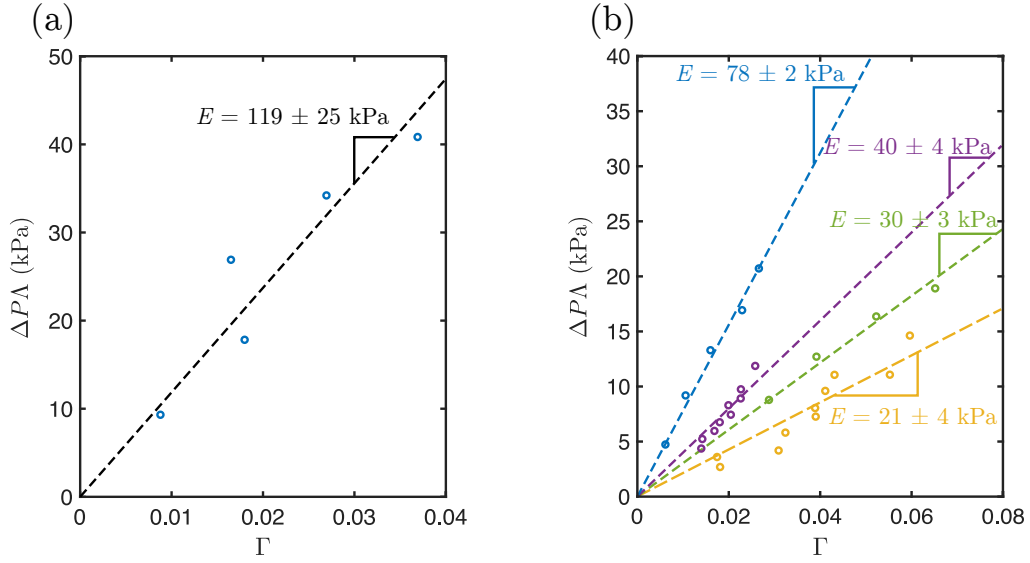


Figure III.6: Evolution of the ΔPA as a function of Γ for two different hydrogels. (a) Hydrogel obtained from the 65% solvent solution and (b) hydrogel obtained from the 70% solvent solution. In (b) the different colors correspond to four different sets of measurements with different constriction angles (θ) and particle geometries (x_0 and y_0).

do not collapse to a master curve and each series leads to a different value of the Young's modulus (see Figure III.6 (b)). Different sources of errors can be proposed:

- The measurement of Δx needs an excellent determination of the initial moment when the trapeze touches the lateral walls of the channel which is far from being easy to achieve. As already mentioned, when the hydrogel is fabricated, there is an inhibition layer between the trapeze and the lateral walls of size b and the particle needs to move over a distance $\delta_x = b/\sin \theta \sim 50 - 100 \mu\text{m}$ from its fabrication position in order to first touch the wall. Δx takes into account this displacement, but small errors on the determination of the constriction angle θ lead to large errors on δ_x and thus systematic error on the measurements of Δx . Moreover, if a residual flow is present just after the formation of the particle it may slightly move (typically of few microns or tens of microns) leading to inaccurate determination of the fabrication position.
- As shown in Figure III.4, the elastic regime is followed by a regime of long time evolution of Δx . The slope, in log-log scale, of this regime varies from one experiment to the other leading to errors in the determination of the equilibrium displacement. Note that the set of measurements yielding the larger, and more different, value of the Young's modulus (blue curve of Figure III.6 (b)) corresponds to experiments where the slopes of this second regime were large.

The resulting Young's modulus of the two hydrogels, measured from Figure III.6 (a) and (b) are summarized in table III.1. The table also compare these Young's modulus values with the measurements obtained from the *in situ* technique (see chapter II).

Volume fraction of solvent	65% of PEG ₁₀₀₀ -water	70% of PEG ₁₀₀₀ -water
$E^{\text{constriction}}$	119 ± 25 kPa	42 ± 13 kPa
$E^{\text{cantilever}}$	117 ± 64 kPa	27 ± 7 kPa
$E^{\text{in situ}}$	not measured	21 ± 8 kPa

Table III.1: Young’s modulus measurements for two hydrogels fabricated from photosensitive solutions diluted with 65% and 70% of PEG₁₀₀₀-water solvent. The second, third and fourth lines of the table correspond, respectively, to measurements obtained using the constriction method the cantilever experiment and the *in situ* technique (see chapter II).

In table III.1, $E_{70\%}^{\text{constriction}}$ is the mean value of the Young’s modulus obtained from the four different series of experiments (see Figure III.6 (b)), and the error corresponds to the standard deviation of the measurements. For the determination of $E_{65\%}^{\text{constriction}}$ there is a unique set of experiments and the value corresponds to the result of the fit.

The method presented here leads to results similar to the ones obtained with cantilever and the *in situ* techniques (see chapter II).

III.1.4 Conclusion

The experimental technique of determination of the Young’s modulus of soft hydrogels relies on the compression of trapezoidal particles pushed through a constriction by means of an external flow. Using a simple mechanical model we are able to determine their Young’s modulus and the results obtained are comparable to what was measured with other methods presented in chapter II. The main advantage of this methods relies on the fact that Young’s moduli as small as a few tens of kPa can be measured directly inside the channel in the presence of a surrounding fluid.

We notice that during the compression of the particle, it experiences two different dynamics: a first regime, of fast dynamics, which corresponds to an elastic compression is followed by a second regime, of slow dynamics, that could be a signature of a creep. As a perspective, it would be interesting to carry out further experiments confirming the creep of our hydrogel and which would allow us to gain a better understanding of the variation of this phenomenon from one experiment to the other. Moreover, for the gel obtained from a photosensitive solution diluted with 70% of PEG₁₀₀₀-water we noticed important systematic errors in our measurements: different series of experiments lead to different Young’s modulus measurements. An investigation on the origins of the second regime could be, as well, of great interest in order to achieve a better determination of Δx and consequently of the Young’s modulus. In addition, systematic measurements for varying experimental parameters, as the angle of the constriction or the size of the particle, would be useful to determine the cause of these errors. The determination of the Young’s modulus of the hydrogel fabricated from the 65% solvent solution, relies on an unique set of experiments. A repetition of the experiment is thus needed to quantify the reproducibility of the measurements.

III.2 Characterization of the Poisson's ratio of the hydrogels

In a compressive/tensile test of an elastic specimen, the Young's modulus is linked to the compression/elongation whereas the Poisson's ratio relates the strain in the extensional direction to the strain in the transverse direction. It quantifies the compressibility of a material and varies, for an isotropic material, from 0.5 (incompressible material) to -1. Negative values of Poisson's ratio are obtained for auxetics metamaterials [63]. Due to their peculiar structure, when stretched (compressed) these materials become thicker (thinner) in the direction perpendicular to the applied force. For usual isotropic materials the Poisson's ratio varies from 0.5 to 0.

Different techniques have been developed to measure Poisson's ratio. The most straightforward method relies on the measure of the strain in two orthogonal directions during a compressive/tensile test. Yet, this method usually requires a macroscopic specimen, and thus large amount of material. Moreover, to carry out this experiment the sample often needs to be dried in order to be fixed onto the stretching machine [64]. To overcome these limits, Wyss *et al.* [56] proposed a simple measurement method of the Poisson's ratio of a soft particle relying on the measurement of the bulk modulus $K = E/(3(1 - 2\nu))$ together with the Young's modulus. But the determination of the Poisson's ratio via two separate experiments, leading each to measurement uncertainties, faces problems of precisions that is an important issue since the Poisson's ratio evolves in a very small interval. Other techniques, such as micropipette aspirations experiments [65, 66], atomic force microscopy (AFM) techniques [67], have been used to measure Poisson's ratio with very high accuracy. But, they probe the material very locally at the surface and not in bulk. Dynamic mechanical tests using acoustic waves are also available [68]: From the speed of sound waves passing through the sample, in our case the hydrogel, one can access to the elastic properties of the material. Usually the frequency of the waves vary from 0.5 to 5.0 MHz, and the measured elastic constant at these frequencies may be different than the static one. Finally, optical techniques such as small angle X-ray scatterings [69] also enable the measure of Poisson's ratio but require costly infrastructures.

Here we propose a simple, novel, and direct method to measure the Poisson's ratio of soft hydrogels directly inside a micro-channel. We use a microfluidic setup where hydrogel particles are fabricated and subsequently transported in a channel whose width is smaller than the particle width (see Figure III.7). After the full entry of the particle into the narrow channel, the external flow is stopped and the particle is only submitted to an uniaxial compression by the lateral walls. This geometry is well adapted to have access to the Poisson's ratio by measuring the deformation of the particle in the direction of the uniaxial compression and the perpendicular one. Here, we detail this method, discuss its limitations and give the Poisson's ratio of PEGDA hydrogels for different solvent compositions. As, in this method, the measurement is done *in situ*, no drying step is necessary ensuring no modification of the structure of the material.

III.2.1 Experimental protocol

The channels have a rectangular cross section and a constant height (either $H = 57 \pm 3 \mu\text{m}$ or $H = 103 \pm 3 \mu\text{m}$). They are composed of three regions: two linear channels

with different widths (a large one in the order of mm and a small one in the order of a few hundreds of micrometers) are connected by a constriction with a small angle (5 to 10 degrees). The channel geometry is sketch in Figure III.7. The inlet of the channel is connected to a reservoir, and a pressure controller is used to control the flow in the channel. Once the channel is filled with the photosensitive solution, the flow is stopped and a particle is fabricated.

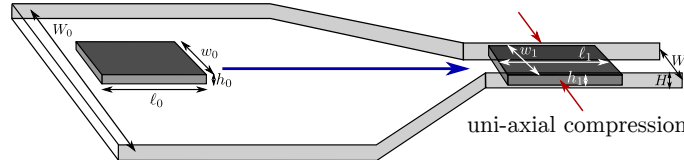


Figure III.7: Geometry of the system and experimental protocol. An hydrogel particle surrounded by the uncured solution is pushed through a constriction by applying an external flow. When the particle has completely entered the narrow region of the channel, the flow is stopped and the particle experiences uni-axial compression. Measurements of the particle geometry before and during compression allows for the determination of its Poisson's ratio.

The first picture of the particle gives a precise measure of the dimensions before deformation. Then the particle is pushed through the constriction to the narrow channel by a flow, which is turned off once the particle has entirely entered the narrow region. There, the particle experiences uniaxial compression from the channel's lateral walls and its shape changes. A new picture of the particle, in its deformed state, is acquired when equilibrium is reached i.e. when its length and width do not evolve any more with time (see Figure III.8). At the end of the experiment, the particle is ejected from the channel by imposing again an external flow. We repeat this procedure at least 10 times for each condition.

PEGDA	PI	water	PEG ₁₀₀₀ -water (ratio 2:1 in volume)	name
90%	10%	0%	0%	pure PEGDA
80%	10%	10%	0%	PW ₁₀
70%	10%	20%	0%	PW ₂₀
60%	10%	30%	0%	PW ₃₀
50%	10%	40%	0%	PW ₄₀
40%	10%	50%	0%	PW ₅₀
80%	10%	0%	10%	PP ₁₀
70%	10%	0%	20%	PP ₂₀
60%	10%	0%	30%	PP ₃₀
50%	10%	0%	40%	PP ₄₀
40%	10%	0%	50%	PP ₅₀
30%	10%	0%	60%	PP ₆₀
20%	10%	0%	70%	PP ₇₀

Table III.2: Volume fraction of each component of the different photosensitive solutions used in this study.

In this study we used different photosensitive solution composed of an oligomer PEGDA $M_n = 700$ g/mol, a photoinitiator (PI) and a solvent. The solvent can be either pure water or a mixture of water and PEG₁₀₀₀ in a proportion of 1:2. While the proportion of solvent varies, the proportion of photoinitiator is kept constant at 10%. The volume fraction of water varies from 0% to 50%. Indeed, as previously mentioned in chapter II, above 50% the solution becomes biphasic and no particle can be fabricated. The maximal dilution with the PEG₁₀₀₀-water mixture is 70%. The table III.2 shows the composition of the different solutions used in this study.

For most of the photosensitive solutions experiments have been carried out on two different days to ensure reproducibility.

We vary the particle height ($h_0 = 45 \pm 3\mu\text{m}$ and $h_0 = 91 \pm 3\mu\text{m}$), width ($w_0 = 205 - 470\mu\text{m}$) and the narrow channel width ($W = 175 - 370\mu\text{m}$). We keep the length of the particle constant and equal to $\ell_0 = 960 \pm 8\mu\text{m}$.

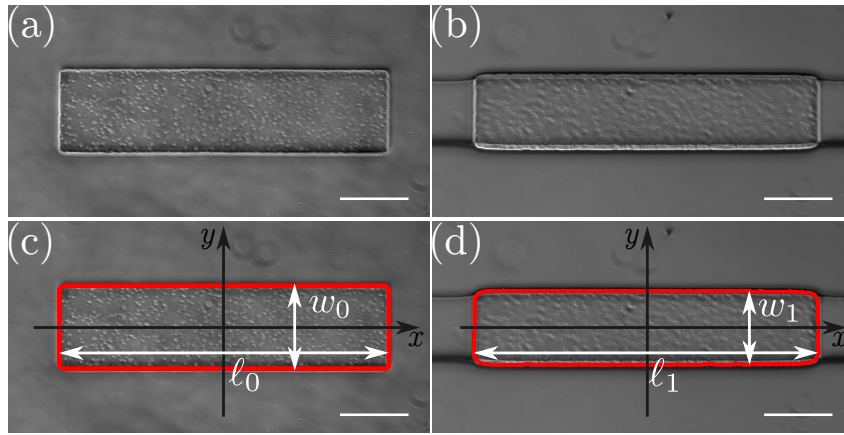


Figure III.8: Pictures of the slab in the wide (left column) and in the narrow (right column) region of the channel. Top row corresponds to direct observations of the undeformed (a) and deformed (b) particle. In (b) the dark region around the particle correspond to the channel walls. Bottom row shows the superposition of the raw images (a) and (b) with the shape extracted using MatLab. Scale bar are $200\mu\text{m}$.

Using standard image treatment procedures (with ImageJ [52] and MatLab), we extract the shape of the particle before and after deformation and measure the particle width w_i , and length ℓ_i , with $i = 0(1)$ before (after) deformation (see Figure III.8). As can be seen in Figure III.8 (b), the narrow channel is deformed by the presence of the particle. We thus chose not to consider the width of the deformed particle to be equal to the width of the narrow channel but rather to measure w_1 for each experiment even if they only slightly differ. This difference depends on to the ratio of the Young's modulus of the PDMS and the hydrogel.

III.2.2 Analysis

After the full entry of the particle into the narrow channel, the external flow is stopped and the particle is only submitted to an uniaxial compression by the lateral walls. As in the previous section III.1, we assume that the hydrogel is isotropic and homogeneous and

thus stress-strain relationship are given by equations III.7, III.8 and III.9.

The particule being submitted to an uniaxial compression in the y -direction, one can write $\sigma_{yy} = -P_{wall}$, with P_{wall} a constant pressure applied by the PDMS walls on the particle, and $\sigma_{xx} = 0$. Assuming that the the deformed particle does not touch the top and bottom walls (*i.e.* $h_1 < H$ and $h_0\epsilon_{zz} < 2b$) there is no stress in the z -direction and $\sigma_{zz} = 0$. This last assumption has to be verified *a posteriori* by evaluating the strain in the z -direction.

Equations III.7, III.8 and III.9 then become:

$$\epsilon_{xx} = \frac{\nu}{E}\sigma_{yy}, \quad \epsilon_{yy} = \frac{1}{E}\sigma_{yy} \quad \text{and} \quad \epsilon_{zz} = \frac{\nu}{E}\sigma_{yy} \quad (\text{III.20})$$

The strains ϵ_{xx} and ϵ_{yy} are directly related to the changes of particle length and width

$$\epsilon_{yy} = \ln\left(\frac{w_1}{w_0}\right), \quad \epsilon_{xx} = \ln\left(\frac{\ell_1}{\ell_0}\right) \quad (\text{III.21})$$

And the Poisson's ratio is directly given by their ratio:

$$\nu = -\frac{\epsilon_{xx}}{\epsilon_{yy}} = -\frac{\ln(w_1/w_0)}{\ln(\ell_1/\ell_0)} \quad (\text{III.22})$$

III.2.3 Results and discussions

a) Validation of the method

As it is visible in Figures III.8 (a) and (b), when the particle is compressed by the channel walls both its length and its width change compared to the situation where the particle is free (in the wide region). According to equations, III.21 and III.22 a measure of the width and length before and after the deformation is necessary to estimate the Poisson's ratio of the hydrogel. Figures III.8 (c) and (d) show the determination of the slab geometry used to derive its length and its width.

Figure III.9 summarizes experiments where particles have been created in PW₃₀ solution, with different initial width w_0 and compressed in a channel of width $W = 175 \pm 0.7\mu\text{m}$. The dimensions of the deformed particles are measured after the particle has reached its equilibrium. Note that the temporal evolution will be discussed in section c). Figures III.9 (a) and (b) show the increase of the width w_1 and the length ℓ_1 of deformed particles as a function of w_0 . While the increase of ℓ_1 is a consequence of the compressibility of the material and will be used in the following to measure Poisson's ratio, the increase of w_1 is due to the deformation of the channel and depends on the ratio of the elastic modulus of the two materials. The Young's modulus of the particle used here ($E = 8.0 \pm 1.6 \text{ MPa}$, see chapter II) is larger than the Young's modulus of PDMS ($E_{\text{PDMS}} \sim 2 \text{ MPa}$, [70]), thus the channel deforms more than the particle does. For the largest value of $w_0 = 300\mu\text{m}$ shown in this figure, this competition between deformation of the particle and deformation of the walls could lead to the buckling of the slab as the buckling threshold decreases when width increases. This buckling is the reason why ℓ_1 saturates and measured *Poisson's ratio* drops at large w_0/W .

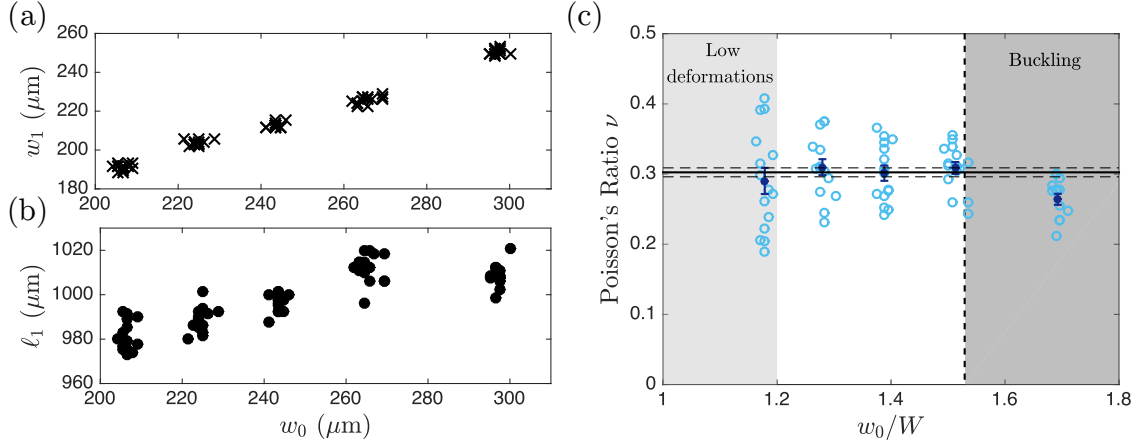


Figure III.9: Direct measurements and derivation of the Poisson's ratio. Results are shown for the hydrogel PW_{30} in a channel of width $W = 175 \pm 0.7 \mu\text{m}$ and height $H = 103 \pm 3 \mu\text{m}$. Width (a) and length (b) of the deformed particle at equilibrium as a function of the initial width w_0 . (c) Evolution of the ratio $-\epsilon_{xx}/\epsilon_{yy}$ as a function of the horizontal confinement w_0/W . Each light blue dot corresponds to a single experimental measurement, and dark blue markers correspond to the average and standard deviation of the measurements. The light (dark) gray region corresponds to particle width that are too small (large) to ensure good precision of the Poisson's ratio. The vertical dotted line corresponds to the limit between linear compression and buckling (see text). Horizontal black lines correspond to the average and standard deviation of all points except the dark grey region ($w_0/w_1 \geq 1.53$). The measure of the Poisson's ratio is $\nu_{30\%} = 0,302 \pm 0,007$ for the photosensitive solution PW_{30} .

Figure III.9 (c) shows the evolution of the ratio $-\epsilon_{xx}/\epsilon_{yy}$ as a function of the confinement w_0/W for PW_{30} hydrogel as an example. As can be seen on the figure, if the particle is not too narrow nor too wide, the measured Poisson's ratio is independent on the particle width as expected for a material property.

b) Limitations

For small w_0 ($w_0/W \leq 1.2$, light grey region), particle deformations are too small to be accurately measured. For large w_0 ($w_0/w_1 \geq 1.53$, dark grey region), the particle is wide enough to buckle preventing any precise measurement to be performed. The critical stress to induce buckling of a thick plate is given by $|\sigma_{yy}^{crit}| = \alpha \pi^2 \frac{E}{12(1-\nu^2)} \left(\frac{h_0}{w_0}\right)^2$ [71, 72]. The correction factor α depends on the ratio w_0/h_0 and takes into account the shear deformation in the height. According to [72] $\alpha = 2.11$ for $w_0/h_0 = 2$ and $\alpha = 1.03$ for $w_0/h_0 = 10$. This critical stress is compared to the actual stress exerted by the lateral walls $\sigma_{yy} = \epsilon_{yy}E$ via the dimensionless number

$$N = \frac{12(1-\nu^2)}{\alpha \pi^2} \left(\frac{w_0}{h_0}\right)^2 |\epsilon_{yy}| \quad (\text{III.23})$$

If $N > 1$ the particle buckles and, on the contrary, if $N < 1$ the particle deforms linearly. The black vertical dotted line in Figure III.9 (c) corresponds to $N = 1$ and a good

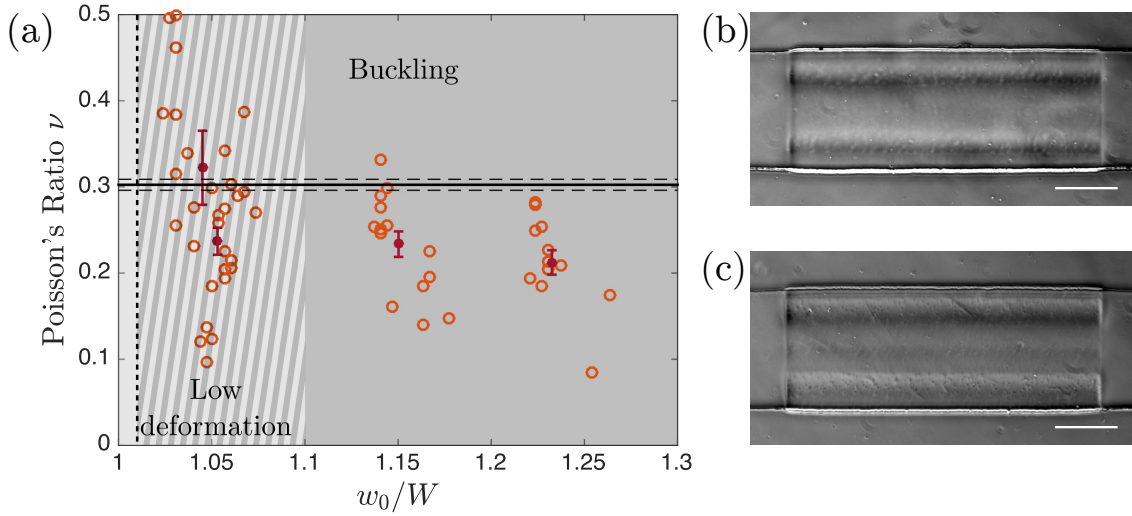


Figure III.10: Limitations of the method: (a) Evolution of the ratio $-\epsilon_{xx}/\epsilon_{yy}$ as a function of the confinement w_0/w_1 for a hydrogel particle created with the PW₃₀ photosensitive solution in a channel of width $W = 370 \pm 1\mu\text{m}$ and height $H = 57 \pm 3\mu\text{m}$. Open circles represent the results of single experiments and dark red markers represent average values of the different experiments. The light and dark gray regions of Figure III.9 (c) overlap for this example. Note that here also the measured ratio $-\epsilon_{xx}/\epsilon_{yy}$ is lower than the Poisson's ratio when the particle buckles. Images of buckled particles are shown in (b) and (c), at least two wavelengths are visible in (b), three in (c). They correspond respectively to $w_0/W = 1.23$ and $w_0/W = 1.36$.

agreement between the buckling threshold and the experimental observations of buckling - drops of the ratio w_1/w_0 - is obtained.

Our model relies on the assumption that the deformation in the vertical direction is small enough that the particle does not touch the channel top and bottom walls. This means that $\sigma_{zz} = 0$, which can be verified experimentally by comparing the height of the compressed particle to the channel height. The height of the deformed particle is $h_1 = h_0 \exp(\epsilon_{zz}) \sim h_0(1 - \nu\epsilon_{yy})$ and the condition $\sigma_{zz} = 0$ is true if $-h_0\nu\epsilon_{yy} < 2b$. As a consequence the assumption is more likely to be true for particles of small height and for small deformations. In all our experiments we verify *a posteriori* that the $\sigma_{zz} = 0$ assumption is valid and disregard experiments where this is not the case.

Increasing the channel width will increase the resolution on the deformation and thus one could think that the range of measurements will be increased. However, increasing the width will also decrease the buckling threshold on w_0/W and may reduce this range. An illustration of this situation can be found in Figure III.10 (a). In this figure, the photosensitive solution is the same as the one used in Figure III.9 but for a wider and thinner channel ($W = 370 \pm 1\mu\text{m}$ and $H = 57 \pm 3\mu\text{m}$). The resolution on the deformation is, as expected, better, and the light grey region limit is pushed to a lower value of w_0/W (≈ 1.1 to be compared to ≈ 1.2 in Figure III.9). However, these particles are more prone

to buckle and the limit of the dark grey region is decreased to smaller value of w_0/W (≈ 1.01 to be compared to ≈ 1.53 in Figure III.9). As can be seen on the figure, the two grey regions overlap meaning that this channel geometry does not allow for Poisson's ratio measurements. In the pictures of Figures III.10 (b) and (c), buckling is clearly visible through the modulation of the grey intensity along the particle width.

The comparison of the Figures III.9 and III.10 shines light on the compromise that have to be done between increasing the resolution on the deformation and avoiding particle buckling. While designing the channel for such measurements, one has to keep in mind these two opposite effects and choose the best geometry based on the knowledge of the Young's modulus E which sets the value of w_1 .

c) Transient regime.

Figure III.11 (a) shows the temporal evolution of the length, $\ell_1(t)$, for different hydrogel compositions after the flow has been turned off. The length of the particles fabricated in presence of solvent (colored curved) decreases with time whereas particles fabricated in absence of solvent (grey curve) increases. As the walls are slightly deformable, when pressure difference is turned to zero, they will relax and increase the compression on the particle. This effect is probably the reason why pure PEGDA particles further deform after stopping the flow. Analyzing $\ell_1(t)$ in this case gives the typical relaxation time of the channel and has been found to be $\tau_{\text{channel}} = 95 \pm 3$ s here.

In the presence of solvent, flow of solvent molecules through the mesh of the hydrogel takes place and this poroelastic effect depends on the porosity of the hydrogel and the viscosity of the liquid [73, 74]. Exponential fits on the evolution of $\ell_1(t)$ (black curves in Figure III.11 (a)) give characteristic times τ for the different hydrogels. The different photosensitive solutions used in this study have comparable viscosity (see table II.1 in chapter II). On the contrary, the mesh size decreases with dilution as the polymer chains are further apart during reticulation in presence of solvent molecules. This is in good agreement with the tendency shown in Figure III.11 (b) in which τ decreases when the solvent fraction increases. Note that as poroelasticity depends also on the dimensions of the hydrogel [73, 74], the timescales for micron-scale particles like ours are much smaller than for macroscopic ones. In all our measurements we wait long enough (1200s) to measure the length of the particles after the poroelastic phenomenon has stopped.

Finally, we also observe a dependence on the velocity at which the particle enter in the constriction for certain hydrogel compositions. One example is given in Figures III.11 (c) and (d) which show pictures, taken 1200s after the passage through the constriction, of two hydrogels fabricated with the same photosensitive solution (PP₇₀) and with the same geometry but with slow (a) or fast (b) dynamics. The length of the deformed particle ℓ_1 is smaller for slow dynamics (the particle velocity is approximately one particle length per minute) than for fast passage (particle velocity larger than one particle length per second). A possible reason of this observation can be found in the viscoelastic properties of the gel and/or the complex friction between the hydrogel and the lateral channel walls [59]. In such situation, we consider that the measurement of the Poisson's ratio can not been achieved properly. Hydrogels fabricated from the PP₆₀ solution show similar behaviors.

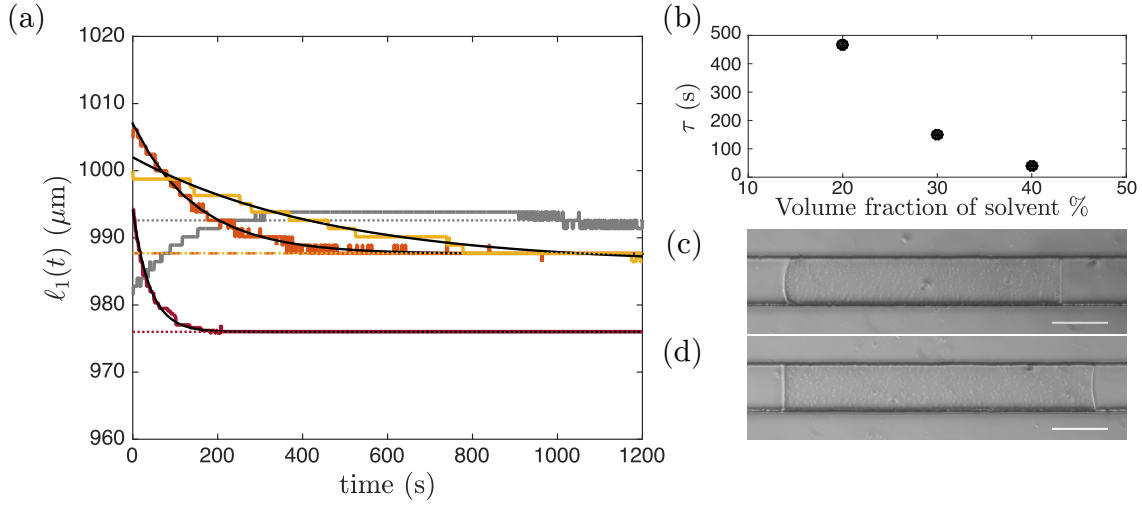


Figure III.11: (a) Evolution of the length of the deformed particle as a function of time. The grey, yellow, orange and red curves correspond to hydrogel fabricated respectively from the pure PEGDA, the PP₂₀, the PP₃₀ and the PP₄₀ solutions. The black lines correspond to exponential fit of the experimental curves for PP₂₀, PP₃₀ and PP₄₀. For the four temporal evolutions we represent with the dotted lines the value of l_1 after 1200 s, when equilibrium is reached. (b) Characteristic time scale of the length temporal evolution as a function of the volume fraction of PEG₁₀₀₀-water solvent. The characteristic time scale are obtained from the exponential fits shown in (a). (c) and (d) correspond to pictures of a deformed hydrogel after (c) a slow passage through the constriction (particle velocity of the order of magnitude of one particle length per minute) and (d) a fast passage through the constriction (velocity larger than one particle length per second). Different dynamics of passage through the constriction lead to different length of the compressed particle. Scale bars are 200 μm .

d) Dependence of the Poisson's ratio to solvent composition

We measured the Poisson's ratio of hydrogel fabricated from different photosensitive solution compositions with different solvent nature and amount. Figure III.12 shows the measured Poisson's ratio for dilution of PEGDA $M_n = 700$ g/mol with water (blue points) and with a PEG₁₀₀₀-water (ratio 2:1 in volume) solution (purple points). In the absence of solvent the hydrogel is nearly incompressible ($\nu_{0\%} = 0.50 \pm 0.01$), which is in agreement with the literature [75]. The Poisson's ratio decreases with the dilution but for the same dilution, it is always smaller in PEG₁₀₀₀-water than in water. This result may be surprising at the beginning, but may be understood in the light of the work of Lee and co-authors [76], who showed that the presence of long chains of PEG in a solution of PEGDA $M_n = 700$ g/mol leads to the formation of hydrogel of larger porosity. One can thus assume that the hydrogel microstructure depends on the nature of the solvent. In water, the lower value that we measured $\nu_{50\%} = 0.255 \pm 0.009$. In PEG₁₀₀₀-water the Poisson's ratio reaches a plateau corresponding to a value of $\nu = 0.165 \pm 0.002$.

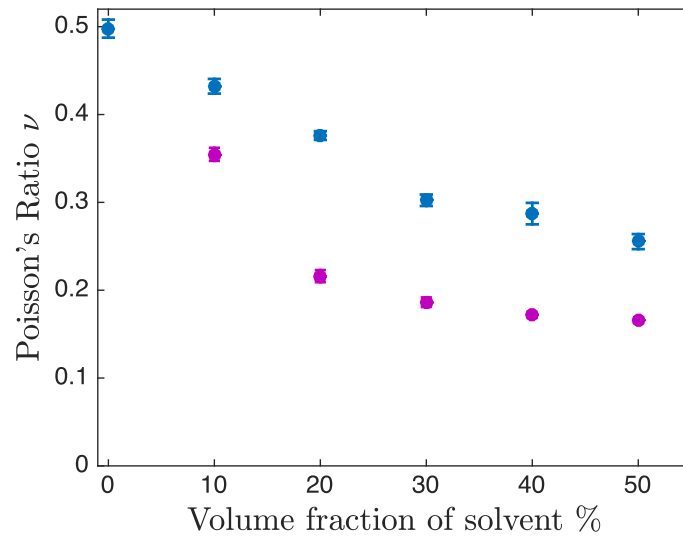


Figure III.12: Evolution of the Poisson's ratio of hydrogels fabricated from different photo-sensitive solutions as a function of the solvent volume fraction. Two different solvents are shown: water (blue markers) and a solution of PEG₁₀₀₀ g/mol -water at a ratio 2:1 in volume (purple markers).

III.3 Opening and conclusive remarks

Until now we have considered homogenous materials and shown that our experimental technique is well-suited to determine the Poisson's ratio of the material they are made of. Figure III.13 shows the extension of our technique to metamaterials in which the geometry of the structure changes the mechanical properties. In this example, an auxetic particle has been fabricated using a specific design of the structure [63]. The superposition of the shapes of this particle before (grey) and after (black) introduction into the narrow channel shows that the particle is slightly shorter when compressed which is the signature of a negative Poisson's ratio.

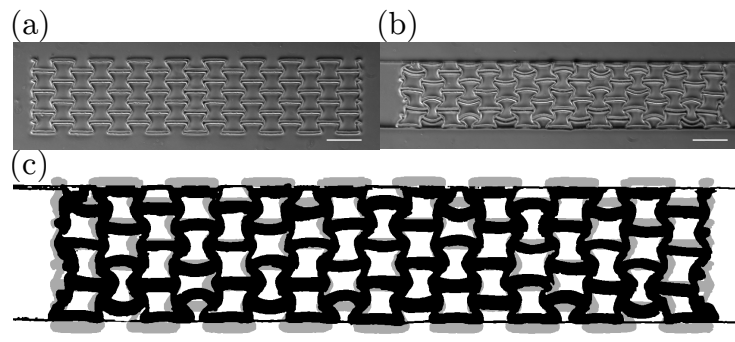


Figure III.13: Auxetic metamaterial fabricated from a pure PEGDA solution. (a) Before compression, (b) submitted to an uniaxial compression, (c) superposition of the undeformed and deformed shape. The particle width as well as its length decrease while compressed, signature of a negative Poisson's ratio.

In this section we have presented a new technique of measurement of the Poisson's ratio of micrometric soft hydrogels. We successfully used this approach to measure Poisson's ratio of different hydrogels and show that this Poisson's ratio varies on a large range of values (from 0.165 to 0.5). We discussed, here, the limitations of the methods and we showed how channel and particle geometries should be chosen to accurately measure the Poisson's ratio. Compared to other approaches an important advantage of our method is that it is done *in situ* directly in the surrounding fluid and does not require any drying of the sample. Another advantage as compared to other experiments, as for instance atomic force microscopy (AFM) or micropipette aspirations experiments, which probe the mechanical properties at nanometer scale is the determination of the Poisson's ratio of the entire hydrogel particle. Thanks to these advantages and because of its simplicity, we think, this method could be used for the characterization of the Poisson's ratio of many different soft objects from nature or industry.

Chapter IV

Bending of a flexible fibers transported in a confined viscous flow

In the Chapters II and III, we have seen how to fabricate fiber with very good control on their shape, position, orientation and mechanical properties. Here, we focus our study on the dynamics and the deformation of a flexible fiber transported in a confined viscous flow.

When transported in confined geometries, rigid fibers show interesting transport dynamics induced by friction with the top and bottom walls (see section I.3.1 of chapter I or references [13, 30]). As we have seen in chapter I, fiber flexibility causes an additional coupling between fiber deformation and transport, and is expected to lead to more complex dynamics. A first crucial step for their understanding is the characterization of the deformed fiber shape. Here, we characterize this shape for a fiber transported in a confined plug flow, perpendicular to the flow direction using a combination of microfluidic experiments (presented in chapter II) and numerical simulations that we present in the following.

We show that a perpendicular fiber bends while transported. This bending is due to the finite length of the fiber and the resulting non-homogeneous force distribution acting on the elongated object. When the fiber is confined, friction occurring in the gap between the fiber and the channel top and bottom walls slows down the fiber. Because its velocity is smaller than the velocity of the surrounding fluid, the object acts as a moving obstacle. As a consequence, a maximum of the pressure difference (between the front and the back of the fiber) is observed in the middle of the slender object, which leads to a C-shape deformation. We show that the amplitude of the deformation is proportional to an elasto-viscous number (introduced in chapter I), which compares viscous to elastic forces. We also quantitatively characterize the influence of the confinement on the fiber deformation. The precise understanding of the deformation of a flexible fiber in a confined geometry can also be used in the future to understand the deformation and transport of more complex deformable particles in confined flows, as for example vesicles or red blood cells [77, 78, 79].

The study presented in this chapter has been done in collaboration with François Gallaire and Mathias Bechert and have been published in Physical Review Fluids in 2019 [18]. The chapter is constituted by the slightly reorganized manuscript of the article.

IV.1 Observations

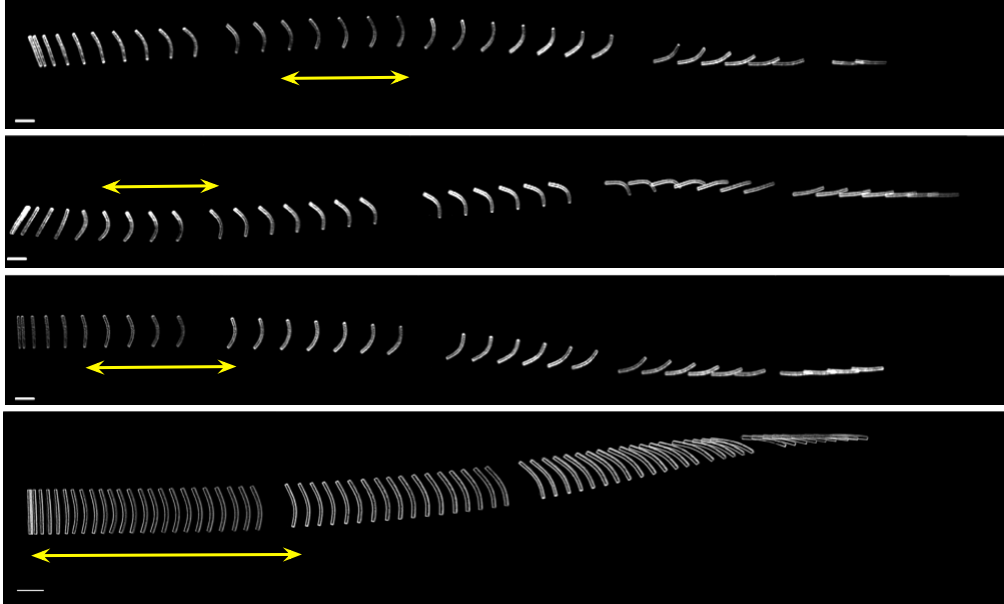


Figure IV.1: Superposition of pictures of a transported and deformed flexible fiber for different initial orientations. The height of the channel is $65 \mu\text{m}$ and the confinement is around 0.81. The length of the fiber is $800 \pm 10 \mu\text{m}$, its height is $54 \pm 3 \mu\text{m}$ and its width is $57 \pm 3 \mu\text{m}$. Scale bar are $500 \mu\text{m}$. The mean velocity of the flow is $0.62 \text{ mm}\cdot\text{s}^{-1}$. The yellow arrow indicates the bent state of a deformed fiber perpendicular to the flow.

An example of trajectory of a flexible fiber transported in a pressure driven flow in a Hele-Shaw like geometry is shown in Figure IV.1. The fiber is strongly confined by the top and bottom walls (fiber width and height are comparable to the channel height), whereas the channel width is much larger than the fiber length.

During downstream transport there is a coupling between fiber deformation and re-orientation. Depending on the initial orientation of the fiber, different dynamics are observed, involving in most cases a deformation to a bent state where the fiber is close to a perpendicular orientation to the flow as highlighted by the yellow arrows in Figure IV.1. This perpendicular orientation is not stable and, in all cases, the fiber finally aligns with the flow and is advected downstream without deformation or rotation. Reaching the final position involves, in some cases, oscillations of the fiber with respect to the lateral walls similarly to the dynamics expected of a rigid fiber interacting with the channel lateral walls [30].

The deformation of a freely transported fiber at low Reynolds number in a homogeneous plug flow is at first glance surprising. However, due to friction with the top and bottom walls, the fiber acts as a moving obstacle when pushed down the channel, leading to a strong flow perturbation (see section I.4 of chapter I or references [13, 30]). Despite the fact that the total force acting on the fiber is equal to zero, the deformation indicates that the force distribution is non-homogeneous along the fiber.

A first step in understanding these complex dynamics is to understand the fiber deformation occurring for a fiber oriented perpendicular to the flow, and in particular to identify the mechanisms leading to a non-homogeneous force distribution responsible for the observed shape.

IV.2 Experimental setup and geometrical arrangement

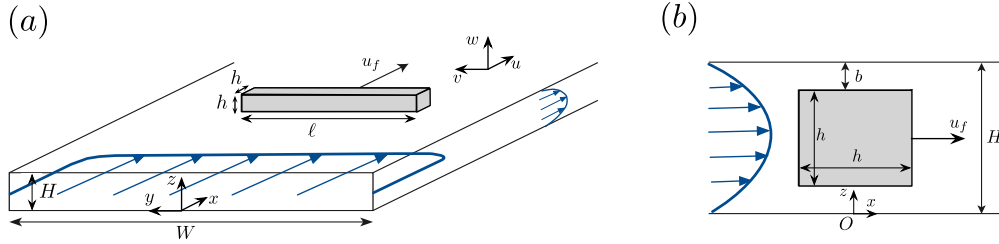


Figure IV.2: (a) Geometry of the perpendicularly oriented fiber and the confining channel. The pressure-driven flow is sketched in blue and defined by a mean velocity u_0 , while the fiber is moving with a velocity u_f so that the total force on the fiber surface becomes zero. (b) Cross section view of the channel and of a perpendicular fiber. The height of the gap b is determined by the confinement $\beta = 1 - 2b/H$.

The fibers used in the experiments are elongated objects of square cross section with height (and width) h and length ℓ , so that the aspect ratio $a = \ell/h$ is large (19 to 25). The choice of square cross section has been motivated by two aspects: it allows us to reduce the number of parameters of the study and, more importantly, it avoids the fiber to rotate around its long axis while it is transported (see Figure II.6 in chapter II). Typical fiber dimensions vary from $19 \mu\text{m}$ to $74 \mu\text{m}$ for width and height and from 0.5 mm to 1.5 mm for the length. The channel is rectangular, of constant height H , width W and length L with $W, L \gg H$. Typically $W=3500 \mu\text{m}$, L is a few centimeters and the channel height H varies from 30 to $85 \mu\text{m}$. Performing particle tracking velocimetry experiments, with suspensions of $1 \mu\text{m}$ diameter latex beads, we assess the variation of the channel height via measurements of the mean flow velocity at different channel locations. We verified that the channel height does not vary more than $3 \mu\text{m}$ along the its width or length, even if the aspect ratio W/H is very large.

The fiber is fabricated using the stop-flow photo-lithography method (detailed in chapter II) and is located at the center of the channel. The confinement $\beta = h/H$ quantifies the influence of the top and bottom channel walls on the fiber dynamics and the height of each gap above and below the fiber is given by b , with $2b = H(1 - \beta)$. The fiber is transported at a velocity u_f by an external pressure-driven flow characterized by its mean velocity u_0 . The velocity field is denoted by $\mathbf{u} = (u, v, w)$, with u , v and w the velocity components in x , y and z direction, respectively. The pressure field is denoted by p . The fiber evolves in a Newtonian liquid (uncured oligomer solution see chapter II) with constant shear viscosity μ . Due to the Hele-Shaw geometry of the channel, the flow in the xy -plane is a plug flow, except close to the side walls and in the vicinity of the fiber. In the z direction the flow is Poiseuille like.

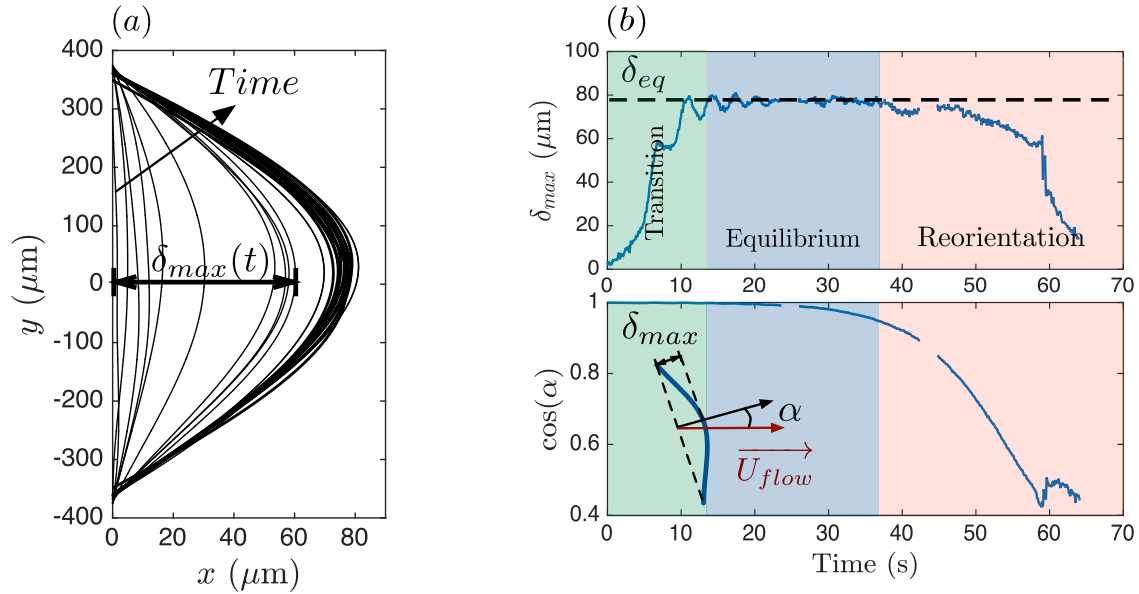


Figure IV.3: Evolution of fiber deformation with time. The data corresponds to the experiment shown on the bottom row of Figure IV.1. (a) Fiber shape evolution. The time step between two lines is 1s. (b) Top: Evolution of the maximum deflection of the fiber δ_{max} as a function of time. The equilibrium deflection δ_{eq} corresponds to the value of the plateau. Bottom: evolution of the angle α between the fiber and the flow as a function of time. $\cos(\alpha) = 1$ corresponds to a perpendicular orientation of the fiber.

Once the fibers are fabricated inside the channel, the flow is turned on using a syringe pump and fiber transport is monitored with a camera. The microscope stage is displaced by hand to keep the fiber in the field of view. Using MatLab routines (see chapter II for more details), we extract the fiber shape as a function of time together with the maximum deflection δ_{max} (Figure IV.3 (a)). Figure IV.3 (b) shows that, after a transition period (green area), the maximum fiber deflection and orientation remain almost constant over a given time (purple area). During this equilibrium state the fiber remains perpendicular to the flow and translates along the x -axis only. However, this equilibrium is not stable and small perturbations lead to a change in fiber orientation and a decrease of fiber deformation. The maximum deflection of a perpendicular fiber, δ_{eq} , is measured during the equilibrium regime.

IV.3 Physical mechanisms and scaling arguments

The shape of an elastic fiber interacting with a viscous flow is given by a balance between drag, i.e. pressure and viscous forces, and elastic restoring forces [80]. In the specific situation of a freely transported fiber in a viscous flow, the total force acting on the fiber is zero and fiber deformation can only occur due to a non-homogeneous force distribution acting on the fiber. This force distribution can, for example, result from the straining part

of a shear flow [80]. However, here the fiber is transported in a plug flow (see Figure IV.2 (a) and (b)), and in this case the viscous and pressure force distributions result from the disturbance flow occurring around the fiber. Thus in order to characterize the fiber deformation we need to determine the disturbance of the flow induced by the fiber.

The fiber shape is determined by first evaluating the flow around a rigid fiber. The transport velocity of a rigid fiber is given by the balance between the pressure and viscous forces pushing the fiber and the viscous friction occurring in the small gaps between the moving fiber and the fixed top and bottom walls. The equilibrium velocity u_f is then obtained by imposing a force-free condition on the fiber surface. Note that, as previously mentioned in chapter I, all previous analyses considering rigid fibers in confined geometries have investigated only total force and torque balances [81, 29, 13, 30]. Here we need to determine the force distribution per unit length along the fiber $f(y)$ resulting from pressure and viscous friction to explain the deformation of the flexible fiber. Finally, the fiber deflection δ caused by this force distribution is calculated employing the linear Euler-Bernoulli beam equation:

$$EI \frac{\partial^4 \delta}{\partial y^4} = f(y), \quad (\text{IV.1})$$

with flexural rigidity EI , E being the material Young's modulus and $I = h^4/12$ being the areal moment of inertia. For an homogeneous slender rod, the flexural rigidity is independent of y . Resolving this equation requires the use of appropriate boundary conditions, which will be discussed in section IV.6.3.

In the following, we assume the hydrodynamic force $f(y)$ to be invariant to small fiber deflections, as the symmetry of the fiber with respect to the flow is preserved under bending and the effect of a small fiber deformation on the surrounding flow is considered negligible. This enables us to calculate the fiber deflection using exclusively the force on a straight, perpendicular fiber.

We scale x , y , z and δ by the fiber length ℓ , the velocity components by u_0 , the pressure and stress tensor components by $\mu u_0/\ell$ and the forces per unit length f , consequently, by μu_0 . This scaling leads to the dimensionless geometry

$$\tilde{\ell} = 1, \quad \tilde{h} = \frac{1}{a} \quad \text{and} \quad \tilde{H} = \frac{1}{a\beta}. \quad (\text{IV.2})$$

Note that all dimensionless variables are denoted by a tilde throughout this chapter. Equation IV.1 transforms to

$$\frac{\partial^4 \tilde{\delta}}{\partial \tilde{y}^4} = \tilde{\mu} \tilde{f}(\tilde{y}), \quad (\text{IV.3})$$

with

$$\tilde{\mu} = \frac{\mu u_0 \ell^3}{EI}, \quad (\text{IV.4})$$

referred to as the elasto-viscous number (see section I.4.2 of chapter I or references [80, 82, 83]). With the drag force on the fiber being proportional to u_0 , $\tilde{\mu}$ compares viscous drag to elasticity, which are the main forces controlling the dynamics provided that the

effect of inertia and Brownian motion is negligible. As already mentioned in chapter I and according to equation IV.3, the scaled fiber deflection is expected to depend linearly on the elasto-viscous number. While the drag force is proportional to the mean velocity of the surrounding fluid, its exact form $f(y)$ also depends on the confinement β . The dependence of the fiber deformation on $\tilde{\mu}$ and β is one of the main questions investigated in the rest of this chapter.

IV.4 Influence of the side walls

In order to determine the impact of the confinement due to the side walls, we systematically measure the maximal deflection of the fiber for different lateral confinement $\xi = \ell/W$. Figure IV.4 shows such evolution of δ_{eq} as a function of ξ . One can see that up to $\ell/W \gtrsim 0.6$ the fiber deflection is independent of the lateral confinement. Only above this threshold the influence of the lateral walls becomes noticeable and the deflection is observed to decrease with increasing confinement. Hence, in the following the fiber length ℓ is always kept smaller than $0.43W$ in order to neglect the influence of the side walls.

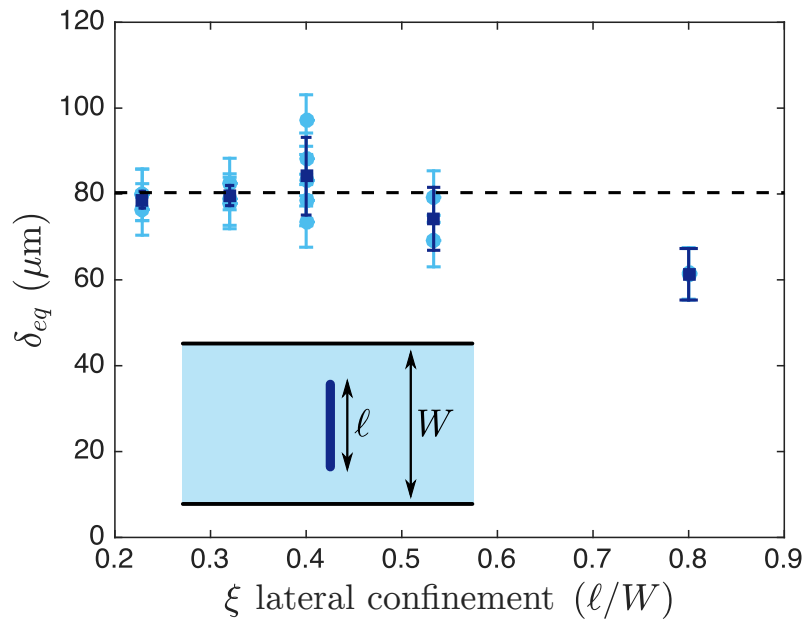


Figure IV.4: Evolution of the equilibrium deflection of flexible fiber for different lateral confinements. The lateral confinement is defined as $\xi = \ell/W$. Each light blue point corresponds to one single experiment and each dark blue point corresponds to the mean value and standard deviation of the repetition of experiments for one given lateral confinement.

IV.5 Fabrication of flexible fibers

Compared to other situations studied previously (see chapters I, II and publications [41, 40, 84]), where a flexible fiber is held fixed in the channel, the fiber studied here is free

and the deformations induced by the fluid are rather small. In order to obtain significant deformation we work with highly flexible fibers, i.e. fibers with large aspect ratio a or small elastic modulus, thus small flexural rigidity. The aspect ratio is limited by the maximum fiber length possible in our set-up (see section II.1 of chapter II) and we thus attempt to fabricate fibers of low modulus with good accuracy and reproducibility.

As seen in section II.4 of chapter II the Young's modulus can be tuned either by varying the composition of the photosensitive mixture or by adjusting the UV exposure time [41, 85], the latter influencing the Young's modulus exponentially until a plateau is reached for large times [41]. As the control over the exposure time is not accurate enough even with the high-precision shutter we use, we choose to perform all experiments in the plateau regime using a constant exposure time of 600 ms. We tune the Young's modulus by diluting the PEGDA with water or with a mixture of water and PEG₁₀₀₀.

As presented in section II.4 of chapter II, the Young's modulus is measured using the *in situ* technique developed by Duprat *et al.* [41] and we complemented the measures using cantilever and micro-indentation experiments.

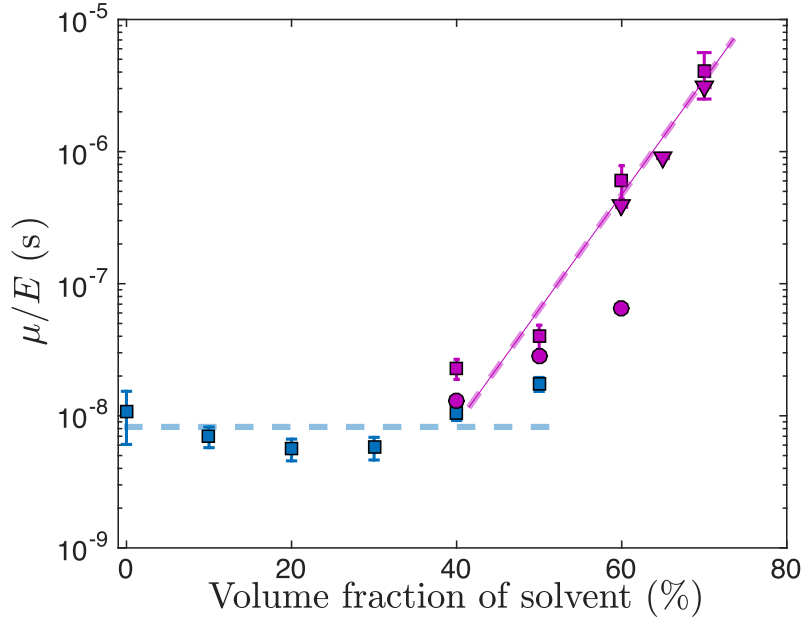


Figure IV.5: Evolution of the ratio of viscosity to Young's modulus as a function of dilution. Blue and purple symbols correspond, respectively, to dilution with water and with a solution of PEG₁₀₀₀-water (ratio 2:1 in volume). While the change in viscosity cancels the influence of solvent fraction on μ/E for a dilution with water, the quantity can be tuned within several orders of magnitude by diluting with PEG₁₀₀₀-water.

In our experiments, the fibers are surrounded by the uncross-linked photosensitive mixture. Diluting the photosensitive mixture affects not only the Young's modulus of the fiber but also the viscosity of the surrounding fluid. The value of interest is actually the ratio μ/E as the elasto-viscous number $\tilde{\mu}$ is proportional to μ/E according to equation IV.3. We plot this ratio as a function of the dilution fraction in Figure IV.5. Diluting PEGDA with water leads to a decrease of the elastic modulus E of the crosslinked fiber (see Figure II.13 in section II.4 of chapter II), but the ratio μ/E remains constant: the

gain in flexibility is cancelled out by the loss of viscosity. Diluting PEGDA with the more viscous PEG₁₀₀₀-water mixture on the contrary leads to a variation of μ/E over three orders of magnitude allowing for larger deformations.

In the following, we use fibers with bending moduli ranging from $5.6 \cdot 10^{-16} \text{ N}\cdot\text{m}^2$ to $8.4 \cdot 10^{-14} \text{ N}\cdot\text{m}^2$. These values are large compared to typical biological fibers such as motile cilia or flagella ($EI \sim 10^{-21} \text{ N}\cdot\text{m}^2$) [86], bacterial flagella ($EI \sim 10^{-22} \text{ N}\cdot\text{m}^2$ - $10^{-23} \text{ N}\cdot\text{m}^2$) [87] microtubules ($EI \sim 10^{-23} \text{ N}\cdot\text{m}^2$) [88] or actin filaments ($EI \sim 10^{-26} \text{ N}\cdot\text{m}^2$) [88], but small compared to cellulosic paper fibers ($EI \sim 10^{-11} \text{ N}\cdot\text{m}^2$) [89].

IV.6 Modeling

In the following we present two models which have been developed, in collaboration with Mathias Bechert and François Gallaire of the Laboratory of Fluid Mechanics and Instabilities at EPFL, to characterize the disturbed flow around the fiber.

We start with introducing a 3D model to calculate the flow around a rigid, perpendicularly oriented fiber and the resulting forces on the fiber surfaces. This model will mainly serve as a reference for the reduced 2D simplified model introduced in section IV.6.2 and largely inspired by the work of Nagel *et al.* [30].

IV.6.1 3D model

The scaled velocity and pressure fields are determined by the well-known continuity and Stokes equations (see chapter I),

$$\nabla \cdot \tilde{\mathbf{u}} = 0, \quad (\text{IV.5a})$$

$$-\nabla \tilde{\mathbf{p}} + \Delta \tilde{\mathbf{u}} = 0. \quad (\text{IV.5b})$$

We impose slip conditions on the lateral walls of the channel to simulate an infinite channel width and additionally no-slip conditions on the top and bottom walls. The fiber velocity $\tilde{u}_f \mathbf{e}_x$ is prescribed on the surface of the fiber. The inlet velocity is defined to have a Poiseuille profile in z with unit mean velocity and a normal flow and constant pressure are specified at the outlet. The forces imposed by the flow on the fiber surfaces are determined by integrating along the x and z axes, leading to forces per unit length in x -direction on the fiber front and back, denoted by \tilde{f}_{front} and \tilde{f}_{back} , respectively, as well as to the cumulated force on top and bottom of the fiber \tilde{f}_{gap} and the total force on the edge surfaces \tilde{F}_e . As we are restricting the analysis to fibers with perpendicular orientation, only the force components in x -direction are relevant, which are given as

$$\tilde{f}_{\text{front}}(\tilde{y}) = - \int_{\tilde{b}}^{\tilde{H}-\tilde{b}} d\tilde{z} \tilde{\sigma}_{xx}|_{\tilde{x}=-\tilde{h}/2}, \quad (\text{IV.6a})$$

$$\tilde{f}_{\text{back}}(\tilde{y}) = \int_{\tilde{b}}^{\tilde{H}-\tilde{b}} d\tilde{z} \tilde{\sigma}_{xx}|_{\tilde{x}=\tilde{h}/2}, \quad (\text{IV.6b})$$

$$\tilde{f}_{\text{gap}}(\tilde{y}) = \int_{-\tilde{h}/2}^{\tilde{h}/2} d\tilde{x} \left(\tilde{\sigma}_{xz}|_{\tilde{z}=\tilde{H}-\tilde{b}} - \tilde{\sigma}_{xz}|_{\tilde{z}=\tilde{b}} \right), \quad (\text{IV.6c})$$

$$\tilde{F}_e = \int_{\tilde{b}}^{\tilde{H}-\tilde{b}} d\tilde{z} \int_{-\tilde{h}/2}^{\tilde{h}/2} d\tilde{x} \left(\tilde{\sigma}_{xy}|_{\tilde{y}=0.5} - \tilde{\sigma}_{xy}|_{\tilde{y}=-0.5} \right), \quad (\text{IV.6d})$$

with the stress tensor components

$$\tilde{\sigma}_{ij} = -\tilde{p} \delta_{ij} + (\partial_i \tilde{u}_j + \partial_j \tilde{u}_i). \quad (\text{IV.7})$$

The signs in equations IV.6 are determined by the orientation of the surface normal vectors. The fiber will move exclusively in x -direction with constant speed \tilde{u}_f , which is determined by the condition of zero total force \tilde{F}_{tot} , i.e.,

$$\tilde{F}_{\text{tot}} = \int_{-1/2}^{1/2} d\tilde{y} \left(\tilde{f}_{\text{front}}(\tilde{y}) + \tilde{f}_{\text{back}}(\tilde{y}) + \tilde{f}_{\text{gap}}(\tilde{y}) \right) + \tilde{F}_e = 0. \quad (\text{IV.8})$$

With the Stokes equations IV.5 being linear, it is possible to determine \tilde{u}_f by superposition of two independent solutions [30]. In particular, the flow and the total force are calculated for two configurations, a fiber fixed in a flow $\{\tilde{u}_0^{(1)} = 1, \tilde{u}_f^{(1)} = 0\}$ and a fiber moving in a quiescent fluid $\{\tilde{u}_0^{(2)} = 0, \tilde{u}_f^{(2)} = 1\}$. The equilibrium velocity fulfilling the force-free condition IV.8 can then be calculated to

$$\tilde{u}_f = -\frac{\tilde{F}_{\text{tot}}^{(1)}}{\tilde{F}_{\text{tot}}^{(2)}}, \quad (\text{IV.9})$$

where the superscripts indicate the configuration.

IV.6.2 2D depth-averaged model

As the calculations for the 3D model require a lot of computational power, we also introduce a refined version of the depth-averaged 2D model proposed by [30]. This model is based on the Brinkman equations,

$$\nabla \cdot \bar{\mathbf{u}} = 0, \quad (\text{IV.10a})$$

$$\left(\nabla^2 \bar{\mathbf{u}} - \frac{12}{\tilde{H}^2} \bar{\mathbf{u}} \right) - \nabla \bar{\mathbf{p}} = 0. \quad (\text{IV.10b})$$

We use a bar above the variables to indicate averaging across the height of the channel and the differential operators correspond consequently to a two-dimensional space. The 2D flow is then calculated by defining a composite particle containing the fiber and the fluid in the gap between the fiber and the top and bottom channel walls. A constant flow velocity in x -direction \bar{u}_p is imposed on the surface of the composite particle and slip conditions are set on the lateral walls to simulate an infinite channel width. Moreover, a plug flow profile with unit velocity at the inlet and a normal flow with constant pressure at the outlet are prescribed.

In a second step, the forces imposed by the flow on the fiber surfaces are determined. In contrast to the 3D model, only the height-integrated forces per unit length in x -direction on the fiber front and back, \tilde{f}_{front} and \tilde{f}_{back} , respectively, and the total force on the edge surfaces \tilde{F}_e are directly given by

$$\tilde{f}_{\text{front}}(y) = -\tilde{h} \bar{\sigma}_{xx}|_{\tilde{x}=-\tilde{h}/2} \quad \text{for } -1/2 \leq \tilde{y} \leq 1/2, \quad (\text{IV.11a})$$

$$\tilde{f}_{\text{back}}(y) = \tilde{h} \bar{\sigma}_{xx}|_{\tilde{x}=\tilde{h}/2} \quad \text{for } -1/2 \leq \tilde{y} \leq 1/2, \quad (\text{IV.11b})$$

$$\tilde{F}_e = \tilde{h} \int_{-\tilde{h}/2}^{\tilde{h}/2} d\tilde{x} \left(\bar{\sigma}_{xy}|_{\tilde{y}=1/2} - \bar{\sigma}_{xy}|_{\tilde{y}=-1/2} \right). \quad (\text{IV.11c})$$

In order to evaluate the forces on top and bottom of the fiber, an additional model for the flow in the gap has to be proposed. As we are considering fibers perpendicular to the flow, the composite particle and thus the fiber are moving only in the x -direction, and it is possible to extend the gap flow profile as introduced by [30] to account for variations along the fiber length \tilde{y} . This leads to a total velocity profile of the composite particle $\bar{\mathbf{u}}_{\mathbf{p}} = \bar{u}_p q(\tilde{y}, \tilde{z}) \mathbf{e}_{\mathbf{x}}$, where the gap flow profile $q(\tilde{y}, \tilde{z})$ has to fulfill the normalization condition

$$\frac{1}{\tilde{H}} \int_{-1/2}^{1/2} d\tilde{y} \int_0^{\tilde{H}} d\tilde{z} q(\tilde{y}, \tilde{z}) = 1. \quad (\text{IV.12})$$

Following [30], $q(\tilde{y}, \tilde{z})$ is assumed to be of Couette–Poiseuille type in \tilde{z} , but now has an additional \tilde{y} -dependence, i.e.,

$$q(\tilde{y}, \tilde{z}) = \begin{cases} q_1(\tilde{y}, \tilde{z}) = C_1(\tilde{y}) \left(\frac{\tilde{z}}{\tilde{H}}\right)^2 + C_2(\tilde{y}) \frac{\tilde{z}}{\tilde{H}} & \text{for } 0 \leq \tilde{z} \leq \tilde{b}, \\ q_2(\tilde{y}, \tilde{z}) = \frac{\tilde{u}_f}{\tilde{u}_p} & \text{for } \tilde{b} < \tilde{z} < \tilde{H} - \tilde{b}, \\ q_3(\tilde{y}, \tilde{z}) = C_1(\tilde{y}) \left(1 - \frac{\tilde{z}}{\tilde{H}}\right)^2 + C_2(\tilde{y}) \left(1 - \frac{\tilde{z}}{\tilde{H}}\right) & \text{for } \tilde{H} - \tilde{b} \leq \tilde{z} \leq \tilde{H}, \end{cases} \quad (\text{IV.13})$$

where the no-slip condition at the channel walls, $q(\tilde{y}, 0) = q(\tilde{y}, \tilde{H}) = 0$ was already applied. Note that the gap flow profile presented by [30] is identical to the reduced profile $\int_{-1/2}^{1/2} d\tilde{y} q(\tilde{y}, \tilde{z})$. $C_1(\tilde{y})$ and $C_2(\tilde{y})$ are determined by the no-slip condition assumed on the fiber surface, $q(\tilde{y}, \tilde{b}) = q(\tilde{y}, \tilde{H} - \tilde{b}) = \tilde{u}_f / \tilde{u}_p$ and by applying the Stokes equation in the gap, which introduces the pressure gradient $\partial_{\tilde{x}} \bar{p}$. Unlike the model proposed by [30], here, $C_1(\tilde{y})$ and $C_2(\tilde{y})$ are no longer constants and take into account the variation of the pressure gradient along the fiber length. Due to symmetry and for the sake of simplicity, we will restrict the rest of the analysis to the bottom gap flow q_1 , which can finally be written as

$$q_1(\tilde{y}, \tilde{z}) = \frac{1}{\tilde{u}_p} \left[-\frac{\tilde{H}^2}{2} \partial_{\tilde{x}} \bar{p} \left(\frac{\tilde{b} - \tilde{z}}{\tilde{H}} \right) \frac{\tilde{z}}{\tilde{H}} + \tilde{u}_f \frac{\tilde{z}}{\tilde{b}} \right]. \quad (\text{IV.14})$$

Note that the only dependence of $q_1(\tilde{y}, \tilde{z})$ on y is hidden in the pressure gradient $\partial_{\tilde{x}} \bar{p}$. For a rigid particle only the mean value of the forces along the fiber contributes to the movement. The correlation between fiber velocity \bar{u}_f and composite particle velocity \bar{u}_p remains thus identical to the one obtained from the model of [30] and [13] and can be written as

$$\bar{u}_f = \frac{3(1 + \beta)}{2(1 + \beta + \beta^2)} \bar{u}_p. \quad (\text{IV.15})$$

The average of $\partial_{\tilde{x}} \bar{p}$ along the fiber is implicitly given by equation IV.12 and can be expressed employing equation IV.14 by

$$\langle \partial_{\tilde{x}} \bar{p} \rangle = \int_{-1/2}^{1/2} d\tilde{y} \partial_{\tilde{x}} \bar{p} = -\frac{12 \bar{u}_p}{\tilde{H}^2 (1 - \beta^3)}. \quad (\text{IV.16})$$

The equality in equation IV.16 was separately verified for various values of β as shown in Figure IV.6. The latter compares the values obtained by numerical calculation to the

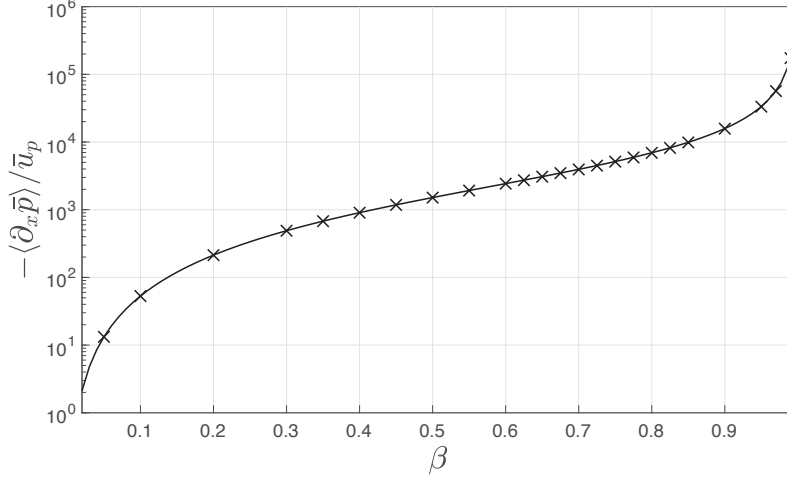


Figure IV.6: Verification of condition IV.16. The single points are calculated based on the numerical simulation while the solid line corresponds to $12\beta^2 a^2 / (1 - \beta^3)$ and thus depends only on β and a , the latter being equal to 21.

prescribed dependence on β and reveals perfect coincidence. This ensures that the presented model is a consistent extension of the one introduced by [30], where only averaged values of the forces are used.

Approximating the pressure gradient along the fiber by

$$\partial_{\bar{x}} \bar{p} \approx \frac{\bar{p}|_{\bar{x}=\tilde{h}/2} - \bar{p}|_{\bar{x}=-\tilde{h}/2}}{\tilde{h}}, \quad (\text{IV.17})$$

the force per unit length in x -direction on top and bottom of the fiber \tilde{f}_{gap} can thus be calculated, using equation IV.16, to

$$\tilde{f}_{\text{gap}}(\tilde{y}) = -2\tilde{h} \bar{\sigma}_{xz}|_{\tilde{z}=\tilde{b}} = -\frac{12\beta^2}{1-\beta^3} \bar{u}_p - \frac{\beta(1-\beta)}{2} \tilde{H}^2 \Delta_{\partial_{\bar{x}} \bar{p}}, \quad (\text{IV.18})$$

with the pressure gradient variation

$$\Delta_{\partial_{\bar{x}} \bar{p}} = \partial_{\bar{x}} \bar{p} - \langle \partial_{\bar{x}} \bar{p} \rangle. \quad (\text{IV.19})$$

The factor 2 in equation IV.18 is needed to account for both the bottom and the top gap and the negative sign originates from the direction of the surface normal vector. The first term on the right-hand side of equation IV.18 is identical to the gap force resulting from the model of [30]. The second term directly derives from the consideration of the variation of the flow velocity around its mean value in the gap. The composite particle velocity \bar{u}_p is determined by the condition of zero total force on the composite particle, which is equivalent to setting the total force on the fiber \tilde{F}_{tot} to zero, i.e.,

$$\tilde{F}_{\text{tot}} = \int_{-1/2}^{1/2} d\tilde{y} \left(\tilde{f}_{\text{front}} + \tilde{f}_{\text{back}} \right) + \tilde{F}_e + \frac{12\beta^2}{1-\beta^3} \bar{u}_p = 0. \quad (\text{IV.20})$$

Only the first two terms on the left-hand side of equation IV.20 are calculated from the numerical simulation, while the third term, i.e., the gap force, can be determined analytically once \bar{u}_p is set. As for the 3D model, it is possible to exploit the linearity of

the Brinkman equations to determine the composite particle velocity by the superposition of two reference configurations [90]. The fiber velocity \bar{u}_f is then directly given by equation IV.15.

It is important to note that the proposed extension of the gap flow is only valid for perpendicular fibers moving exclusively in x -direction. In the more general case of lateral motion, the y -dependence of the gap flow cannot be separated from the composite particle velocity in a straightforward manner. For this reason, the contribution of the pressure gradient variation along the fiber on the total force distribution is evaluated in section IV.7.3, so that possible errors by neglecting this effect can be estimated for future studies.

IV.6.3 Boundary conditions

As already introduced in section IV.3, once the viscous and pressure forces are determined we derive the fiber deformation from the Euler-Bernoulli equation IV.3. Because of the fiber being symmetric along \tilde{y} at $\tilde{y} = 0$, it is sufficient to consider half of it. The force applied on the two edges of the fiber \tilde{F}_e is taken into account via the boundary conditions,

$$\tilde{\delta}(\pm 1/2) = 0, \quad \partial_{\tilde{y}}\tilde{\delta}(0) = 0, \quad \frac{1}{\tilde{\mu}} \partial_{\tilde{y}\tilde{y}}\tilde{\delta}(\pm 1/2) = 0, \quad \frac{1}{\tilde{\mu}} \partial_{\tilde{y}\tilde{y}\tilde{y}}\tilde{\delta}(\pm 1/2) = \frac{\tilde{F}_e}{2}. \quad (\text{IV.21})$$

The first condition arbitrarily sets the deflection to be zero at the edges as reference point. The second condition is due to the symmetry of the fiber and the last two conditions represent, respectively, the bending moment and the shear force due to the viscous forces applied on the edges of the fiber. The deflection is obtained by multiple numerical integration of one half of the obtained force distribution, leading directly to the maximum deflection $\tilde{\delta}_{\text{eq}}$.

IV.6.4 Numerical implementation

Because we are assuming symmetry at $\tilde{y} = 0$ and $\tilde{z} = 0$, it is sufficient to simulate only a quarter of the channel in the 3D model and half of the channel in the 2D model. The fiber constitutes a hole in the channel. Figure IV.7 shows the corresponding geometry and marks the channel domain Ω_c as well as the lateral and top channel boundaries, denoted by $\omega_{w,1}$ and $\omega_{w,2}$, respectively, the symmetry planes $\omega_{s,1}$ and $\omega_{s,2}$, the inlet and outlet, denoted by ω_i and ω_o , respectively, and the fiber surface ω_f . For both models, the dimensionless channel length and width are set to $\tilde{L} = 9$ and $\tilde{W} = 8$, while the remaining lengths are defined by equations IV.2.

We impose a slip condition on $\omega_{w,1}$, a no-slip condition on $\omega_{w,2}$ and a constant velocity, \bar{u}_p in the 2D simulation and \tilde{u}_f in the 3D simulation, on ω_f . At the inlet ω_i , a constant flow velocity $\tilde{u}_0 \mathbf{e}_x$ (2D) or, respectively, a Poiseuille profile in z (3D), i.e., $3/2 (1 - (2\tilde{z} a \beta)^2) u_0 \mathbf{e}_x$, are prescribed, while the pressure is fixed to $\tilde{p} = 0$ at the outlet ω_o together with a normal outflow condition. The channel domain Ω_c is meshed with tetrahedral (3D) or triangular (2D) elements with maximum element size $\tilde{H}/2$ (3D) or $\tilde{\ell}/5$ (2D) and maximum element growth rate of 1.2. In addition, the number of elements on the fiber edges is fixed to m_h elements per \tilde{h} , $m_h = 60$ for the 2D model and $m_h = 50$ for the 3D model, and for the 3D simulation, the maximum element size on ω_f is fixed

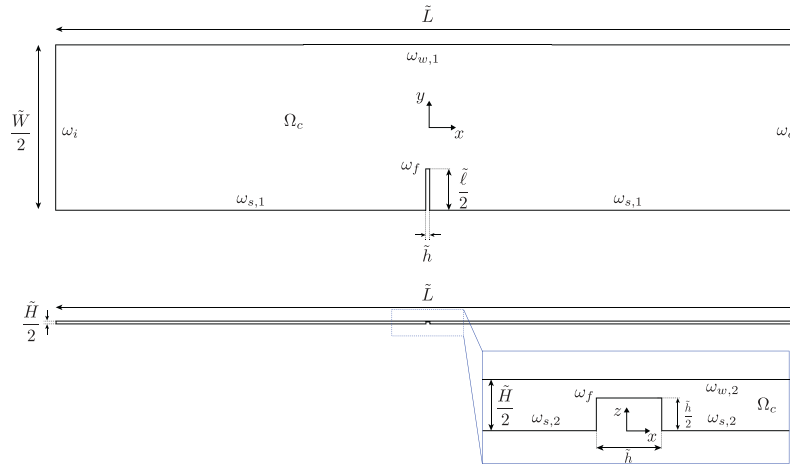


Figure IV.7: Geometry of the 2D and 3D simulations: channel domain Ω_c , lateral channel boundary $\omega_{w,1}$, symmetry plane $\omega_{s,1}$, inlet ω_i , outlet ω_o and fiber surface ω_f . Exploiting symmetry, only half of the domain in y - and z -direction is modeled. Top: Geometry of the 2D simulation and xy plane view of the 3D simulation. Bottom: xz plane view of the 3D simulation with additional top channel boundary $\omega_{w,2}$ and symmetry plane $\omega_{s,2}$.

to $3m_h/\tilde{h}$ together with a maximum element growth rate of 1.2. For both 2D and 3D simulations, the direct solver PARDISO of COMSOL MULTIPHYSICS software is utilized. For 2D simulation results are verified by separate calculations with the ULAMBATOR [91]. Convergence for both models was checked with respect to \tilde{u}_f , or, respectively, \bar{u}_f , and $\tilde{\delta}_{\text{eq}}$, details are given in the appendix C.

IV.6.5 Model validation and assessment

We validate our models against the results from [13] and [30] by comparing the calculated fiber velocities for a rigid fiber as a function of the confinement β for an aspect ratio $a = 10$, as shown by Figure IV.8. The fiber velocity is observed to decrease monotonically with increasing confinement β due to the increasing friction between the fiber and the top and bottom channel walls. Our results from both the 3D and the depth averaged 2D numerical simulations coincide very well with the existing results in literature, indicating the reliability of the present implementations. We have also displayed results for an aspect ratio of 21, the value primarily used in the present work, and for $\beta > 0.8$ they differ only slightly from the ones for $a = 10$. In both configurations, the 2D model reproduces the results of the 3D model with high accuracy.

In the following, we will use our models mainly to predict the force distribution \tilde{f} and the fiber shape, including the maximum deflection $\tilde{\delta}_{\text{eq}}$. The validity of our two models to predict these quantities will be discussed in detail in section IV.7.1, where we will show that both models lead to similar results. As the 2D model offers a significantly higher flexibility and reduction of computational power and as the deviations from the 3D model are in the same range as the experimental error, we will primarily employ this model and provide additional results from the 3D model when appropriate.

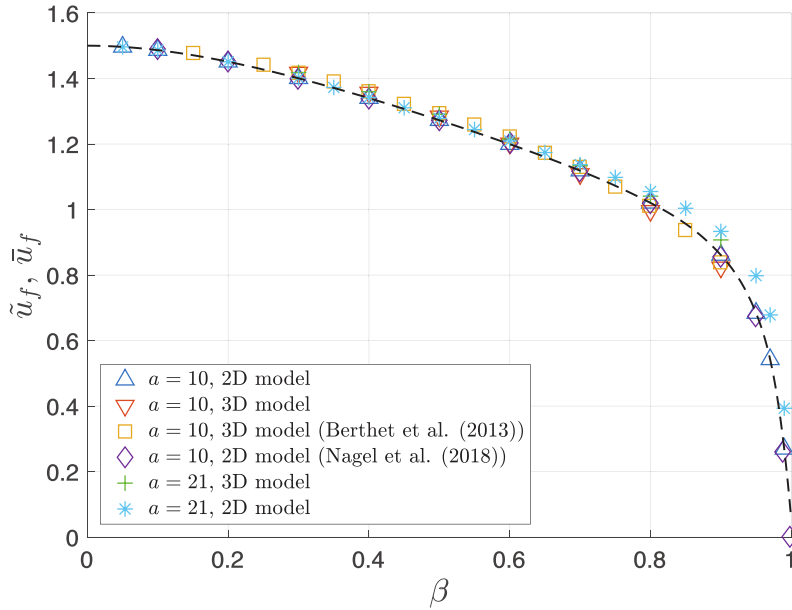


Figure IV.8: Validation against literature values: Dependency of the rigid fiber velocity \tilde{u}_f on the confinement β at force-free conditions for the 2D and 3D models for an aspect ratio $a = 10$ and $a = 21$ together with the data presented by Berthet *et al.* [13] and Nagel *et al.* [30].

IV.7 Results

IV.7.1 Mechanism of fiber deformation

Typical experimental observations can be seen in Figure IV.1 showing the successive positions and shapes of a flexible fiber during its transport along the microchannel. Here we are interested in the deformed equilibrium shape of fibers of perpendicular orientation as indicated by the yellow arrows. We investigate the maximum deflection δ_{eq} , as well as the corresponding fiber shapes, as a function of different parameters as the mean velocity of the surrounding fluid u_0 , the fiber length ℓ , or the confinement β .

As previously said, the fiber deformation results from the inhomogeneous distribution of the drag force along the fiber due to its finite length. While being transported downstream, the flow pushes the fiber along the flow direction against the viscous friction, but it also flows around it. This leads to a specific flow profile and thus a specific pressure distribution around the fiber. Figure IV.9 (a) shows an experimental visualization of the flow around a fiber in the reference frame of the fiber. Figure IV.9 (b) shows the corresponding velocity field averaged over the channel height and Figure IV.9 (c) the pressure distribution. The pressure field is calculated from the experimental velocity field using the Brinkman equation. To distill the part of the pressure field causing a deformation of the fiber, we subtract the linear pressure field corresponding to a channel flow without fiber. The precise image and data treatment to obtain these results is described in the chapter II. Similar results are obtained from numerical simulations of the 2D model as shown by Figure IV.9 (d) and (e) for identical conditions. From these pictures two effects

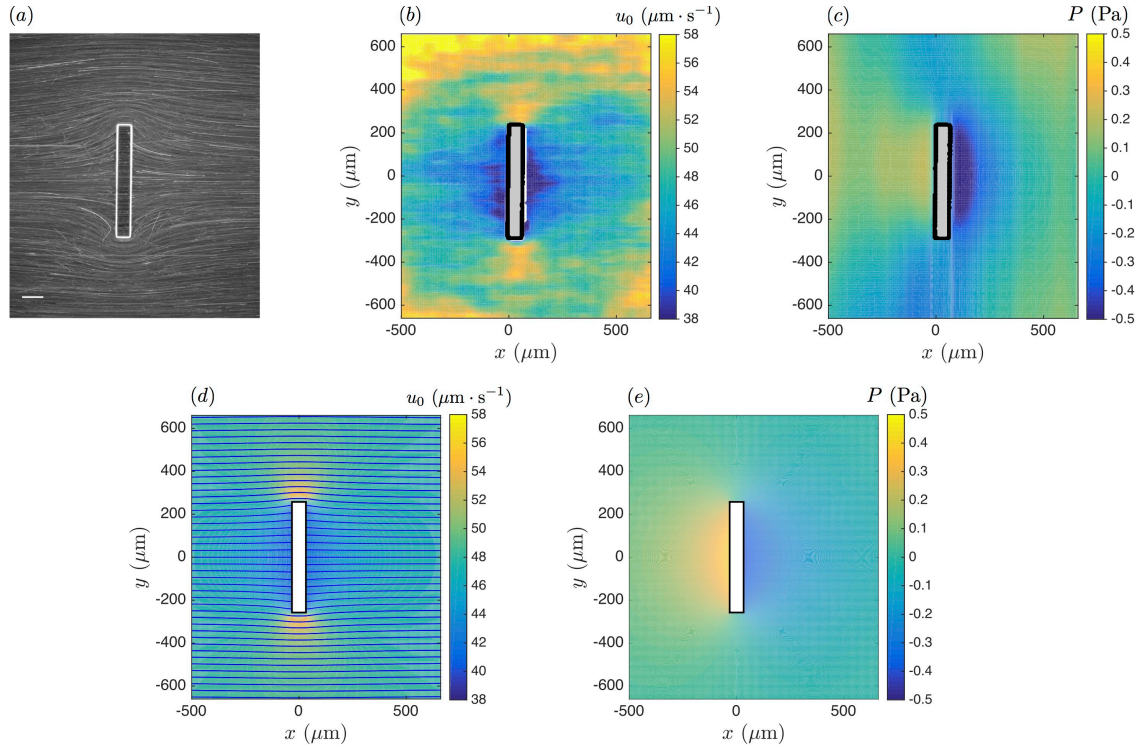


Figure IV.9: Experiments: (a) Streaklines of the flow around a rigid fiber in the reference frame of the fiber. The mean fluid velocity is $u_0 = 48 \mu\text{m}\cdot\text{s}^{-1}$, and the fiber dimensions are $\ell = 528 \pm 5 \mu\text{m}$, $w = 67 \pm 5 \mu\text{m}$, and $h = 49 \pm 3 \mu\text{m}$. Confinement is $\beta = 0.82$. Streaklines are obtained by visualizing $1 \mu\text{m}$ diameter beads flowing around the fiber with a $\times 10$ objective. Scale bar is $100 \mu\text{m}$. (b) Depth averaged velocity field around the fiber obtained from the particle tracking by averaging the particle velocity on time and on 64×64 pixels windows. The constant velocity of the fiber has been added to get the velocity field in the frame of the laboratory. The noise on the edges of the window field results from the lack of data in this regions. (c) Pressure distribution minus the constant gradient in the (Ox) direction. It is obtained from the velocity field using the 2D Brinkman equation. Simulations: (d) Velocity field obtained numerically from the 2D model, the fiber dimension are length $\ell = 525 \mu\text{m}$, width $w = 65 \mu\text{m}$ and height $h = 49 \mu\text{m}$. Confinement is $\beta = 0.82$. In order to compare with experimental data the mean flow velocity is set to $48 \mu\text{m}\cdot\text{s}^{-1}$. (e) Pressure field obtained from simulation with the same fiber geometry and confinement. The viscosity is set to $\mu = 67.4 \text{ mPa}\cdot\text{s}$.

can be seen clearly: a non-homogeneous pressure distribution along the fiber length with a maximum pressure difference between the fiber front and back located at the middle of the fiber, and an increase of the flow velocity close to the edges of the fiber. These two effects have opposite consequences on the fiber deflection: the pressure field leads to a maximum deformation of the fiber at the middle, whereas the velocity field leads to a maximum deformation of the fiber at the edges in the opposite direction.

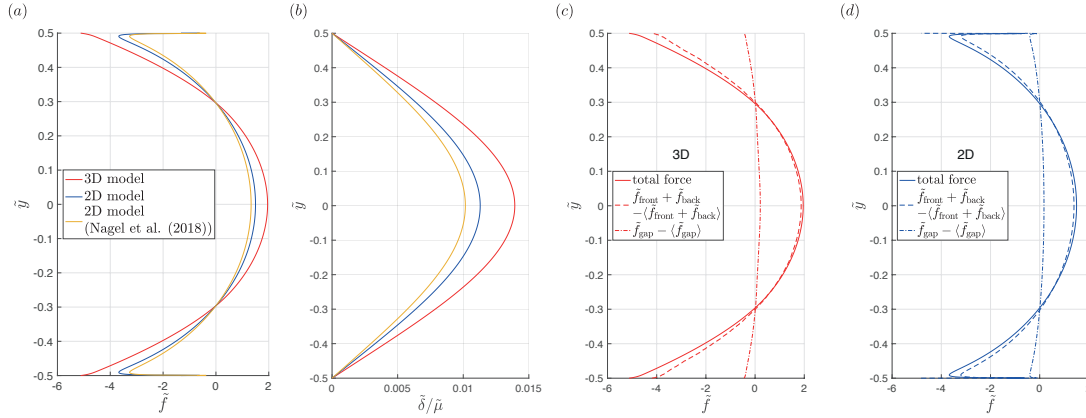


Figure IV.10: (a) Force distributions and (b) resulting normalized fiber deflections obtained from the 2D and 3D models. A smoothing function has been applied to the 3D data. For comparison the results from the model by [30] have been added. The confinement is $\beta = 0.8$ and the aspect ratio is $a = 21$. (c) and (d) Decomposition of the force distributions into the force on fiber front and back and the force on fiber top and bottom for the 3D and 2D model, respectively. The mean values are subtracted for the sake of comparison.

From the non-homogeneous pressure and velocity distribution observed experimentally and numerically we expect a non-homogeneous force distribution along the fiber length. An example of such a force distribution is shown in Figure IV.10 (a) for $\beta = 0.8$ and $a = 21$ for the 2D and 3D models. For the sake of completeness, the results from the model by [30] are shown as well. In all cases a maximum is observed at the center of the fiber, as indicated by the pressure distribution. This shows that the system is dominated by pressure effect as one would expect from the confined geometry. It can also be seen that while all three models lead to similar results, the force is slightly underestimated by the 2D models. Our refined 2D model, however, leads to a correction towards the 3D results, and constitutes therefore an improvement compared to the model of [30].

Figure IV.10 (b) shows the corresponding fiber shapes. Note that the non-zero shear force at the edges \tilde{F}_e , resulting from the increased flow velocity around the latter, is taken into account through the boundary conditions IV.21. All models lead to the characteristic C-shape obtained in experiments, with a slightly varying amplitude for the different models. Figures IV.10 (c) and (d) show for the 3D and 2D model, respectively, the decomposition of the force distribution into the contributions of the pressure difference at fiber front and back and the viscous shear forces on top and bottom. The mean values (subtracted from the force distributions in Figures. IV.10 (c) and (d)) of both $\tilde{f}_{\text{front}} + \tilde{f}_{\text{back}}$ and \tilde{f}_{gap} are significant and almost equal in absolute value, as expected from the zero

force condition and as the edge force \tilde{F}_e is rather small. However, the variation around these mean values, which leads to the deflection of the fiber, is clearly more pronounced for the pressure difference than for the gap force. This reveals that the shape of the fiber is primarily determined by the pressure distribution and also comforts the use of an averaged 2D model. Nevertheless, it can be seen from this decomposition that while the force distributions predicted by the 2D and 3D models coincide very well in the gap, the amplitude of the force distribution calculated with the 2D model is smaller than the one obtained from the 3D model. This is caused by the implicit assumption used in the averaged 2D model that the force distribution on the composite particle is equally distributed in z .

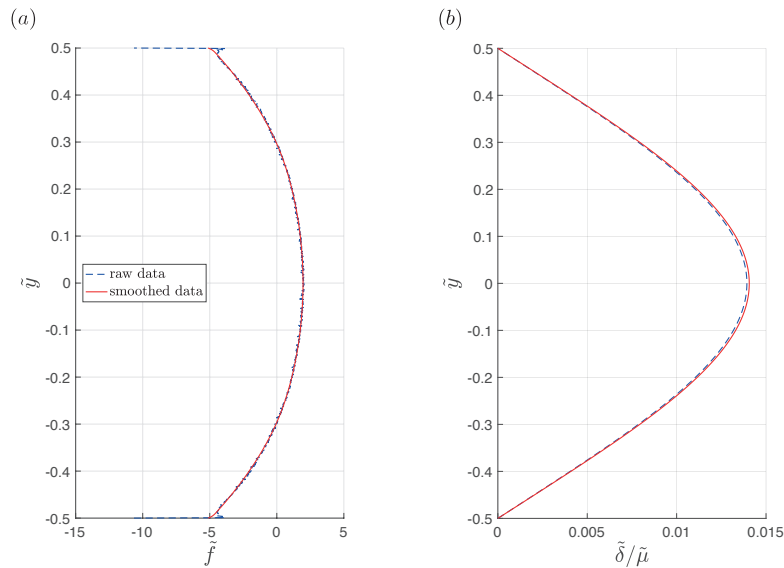


Figure IV.11: Influence of smoothing the force distribution for the 3D model for $\beta = 0.8$. (a) Raw and smoothed force distributions. (b) Resulting fiber deflections.

Note that the presence of sharp edges and corners of the fiber in the numerical implementations of both the 2D and the 3D model leads to fluctuations in the force distributions. For the 2D results, this can be seen at the edges of the force distribution in Figures IV.10 (a) and (d), which seems to diverge. While this effect is clearly visible in the force distributions, the calculated deflections were not found to be significantly influenced by it. This is demonstrated in Figure IV.11 for the 3D model for $\beta = 0.8$. Here, the force distribution appears to be scattered along the fiber, which is caused by averaging across the height and thus including the effect of the top and bottom edges. The magnitude of variation of the force around zero is rather small compared to the absolute forces at the fiber surfaces. As a consequence, small fluctuations can already lead to visible uncertainties in the data. We, therefore, smooth the data additionally, which implies truncating the apparent divergencies at $\tilde{y} = \pm 0.5$, as depicted by Figure IV.11 (a). The resulting calculated deflections visualized by Figure IV.11 (b) exhibit no significant differences.

In the following, we will quantitatively discuss the fiber shape and maximum deflection from experiments and simulations as a function of the control parameters of the system.

IV.7.2 Fiber deflection as a function of the elasto-viscous number

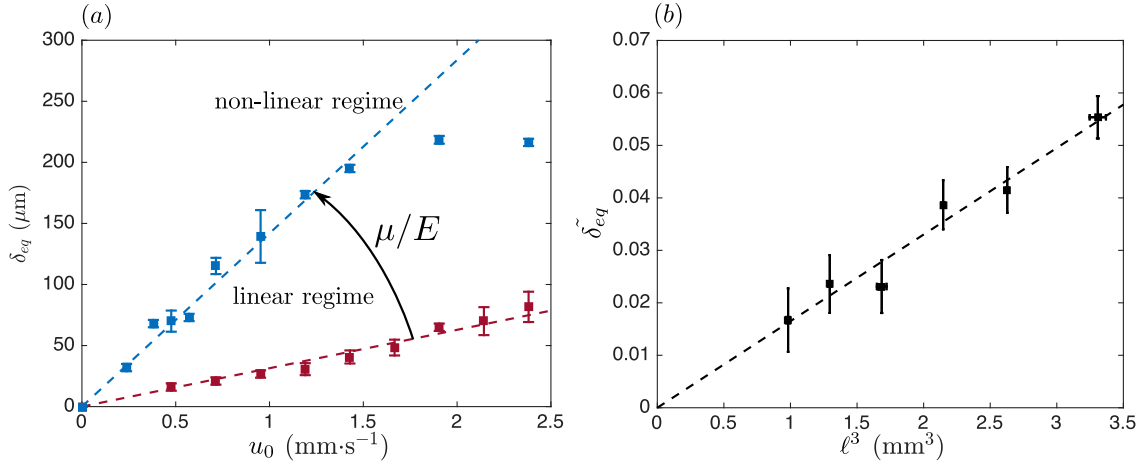


Figure IV.12: Equilibrium deflection for a given confinement $\beta = 0.8$. (a) Evolution of the equilibrium deflection as a function of the fluid mean velocity for a given fiber length $\ell = 1300 \mu\text{m}$ and for two different ratios $\mu/E = 3.14 \pm 0.08 \mu\text{s}$ (blue) and $\mu/E = 0.911 \pm 0.026 \mu\text{s}$ (red). (b) Evolution of the dimensionless equilibrium deflection as a function of fiber length to the power three for a given flow velocity $u_0 = 0.41 \text{ mm}\cdot\text{s}^{-1}$. Each point corresponds to two to four measurements.

As already mentioned in chapter I and as given by equation IV.3, for small deformations we expect the scaled deformation $\tilde{\delta}_{eq}$ to be proportional to the elasto-viscous number $\tilde{\mu}$. We first test the dependence on the fluid velocity by performing several sets of experiments keeping all other parameters constant. Figure IV.12 (a) illustrates that δ_{eq} increases indeed linearly with the fluid velocity as long as the deformation remains small. For deformations larger than 20%, deviations from the linear behavior are observed. All the following experiments have been performed in the linear regime. Figure IV.12 (a) also shows that with increasing ratio μ/E , the deflection increases for identical flow velocities. Figure IV.12 (b) shows a series of experiments where the fiber length was modified and all other parameters were kept constant. As expected, $\tilde{\delta}_{eq} \propto \ell^3$. Note that the range of length available is small (the length varies from $990 \pm 10 \mu\text{m}$ to $1490 \pm 10 \mu\text{m}$), as for too short fibers the deflection is too small to be measurable and for too long fibers the influence of the lateral channel walls can no longer be neglected (Section IV.4).

Figure IV.13 regroups experiments performed for different flow velocities, ratios μ/E and several fiber geometries for a constant confinement $\beta = 0.80 \pm 0.06$. It represents the scaled deflection $\tilde{\delta}_{eq}$ as a function of $\tilde{\mu}$. The data points of Figure IV.13 align very well on a straight line, proving that $\tilde{\mu}$ indeed controls the amplitude of fiber deflection linearly. Here, each point corresponds to the average value over several experiments and the large error bars are mainly due to the uncertainties on the determination of the Young's modulus (see chapter II). While the Young's modulus is accurately controlled, i.e. similar fabrication conditions lead to identical fibers, its absolute value is determined with an error. The large error bar reflects this determination error but the alignment of

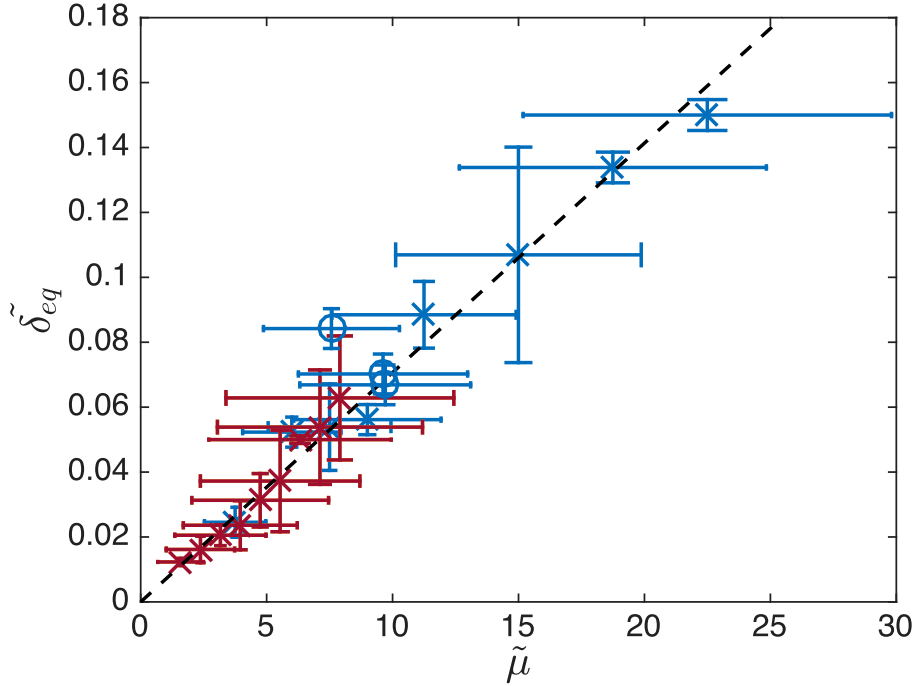


Figure IV.13: Evolution of the dimensionless equilibrium deformation as a function of the elasto-viscous number $\tilde{\mu}$. The cross markers correspond to the data shown in Figure IV.12 (a) and circles are obtained with a smaller fiber, $\ell = 985 \pm 10 \mu\text{m}$ for fluid velocities varying from $0.46 \text{ mm}\cdot\text{s}^{-1}$ to $0.69 \text{ mm}\cdot\text{s}^{-1}$. The color code is the same as for Figure IV.12 (a) and distinguishes the different ratios μ/E . Dotted lines correspond to linear fits.

the data points indicate the good accuracy in the mechanical properties. This remark is also true for all the figures representing data normalized by the elasto-viscous number.

IV.7.3 Effect of the confinement

Previous studies, presented in chapter I, have shown that the confinement tunes the flow perturbation around the fiber and as a consequence the drag forces applied on the fiber [13, 30]. We thus expect the fiber deformation to strongly depend on the confinement. Figure IV.14 (a) shows snapshots of fibers transported in channels of different confinement. A variation of the confinement implies a homothetic variation of the fiber width and length in order to keep a constant aspect ratio and a square cross section. Despite the fact that the scaled deflection is normalized by $\tilde{\mu}$ in Figure IV.14 (b), in order to compensate for the geometrical variations, different amplitudes of deflection are observed for different confinements. In the following we will discuss the influence of the confinement experimentally and numerically.

The force distribution along the fiber length, obtained numerically using the 2D model, is shown in Figure IV.15 (a) for confinements varying from $\beta = 0.1$ to $\beta = 0.9$. The

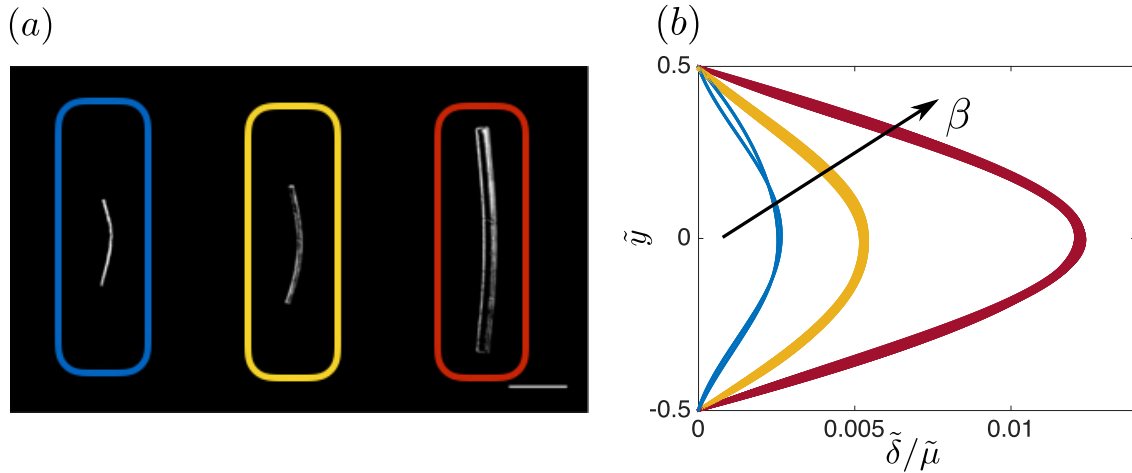


Figure IV.14: Role of confinement. (a) Pictures of deformed fiber for confinements of 0.6 ± 0.1 (blue), 0.73 ± 0.08 (yellow) and 0.86 ± 0.04 (red). Fibers dimensions are: $h = 18 \pm 3 \mu\text{m}$, $w = 24 \pm 5 \mu\text{m}$, $\ell = 614 \pm 10 \mu\text{m}$ (blue), $h = 29 \pm 3 \mu\text{m}$, $w = 35 \pm 5 \mu\text{m}$, $\ell = 788 \pm 10 \mu\text{m}$ (yellow), $h = 73 \pm 3 \mu\text{m}$, $w = 79 \pm 5 \mu\text{m}$, $\ell = 1482 \pm 10 \mu\text{m}$ (red). Scale bar is $500 \mu\text{m}$. (b) Dimensionless fiber shapes. $\tilde{\delta}$ has in addition been normalized by $\tilde{\mu}$. The color code is the same as for (a). Several fiber shapes for identical conditions have been superimposed.

amplitude of \tilde{f} increases with increasing confinement. Figure IV.15 (b) shows the related fiber shape and clearly indicates that the amplitude of fiber deflection also increases with confinement, as it was observed in experiments. The last panel of this figure shows the fiber shapes normalized by the maximum deflection, and reveals no significant change in the deflection shape. This means that the confinement mainly modifies the amplitude of the force and not its distribution, i.e., the fiber deflection is fully characterized by $\tilde{\delta}_{\text{eq}}$. Similarly, normalized experimental fiber shapes for different confinements collapse onto a single shape, coinciding with the numerical result, as shown in the inset of Figure IV.16.

Finally, we quantitatively discuss the amplitude of deflection $\tilde{\delta}_{\text{eq}}$ as a function of the confinement by comparing experimental results to numerical calculations obtained from both 2D and 3D models. Figure IV.16 superimposes the experimental (blue diamonds) and the numerical results obtained from the 2D (red squares) and the 3D (black circles) models. Each experimental point corresponds to 2–30 measurements for different fluid velocities, Young’s moduli and fiber dimensions. The results obtained from the 3D simulations predict slightly stronger deformations compared to the results obtained from the 2D model. This was already visible from Figure IV.10 (c) and (d). In particular for high confinements, the results from the different models differ only slightly, confirming again the validity of the simplified 2D model which offers a significantly higher flexibility and reduction of computational power. In all cases, the differences in predictions of both models are in the same range as the experimental error and both are found to be in good agreement with the experimental data.

Even though both model predictions lie in the experimental error range, Figure IV.16 suggests a small overprediction of the deflection, as most of the experimental mean val-

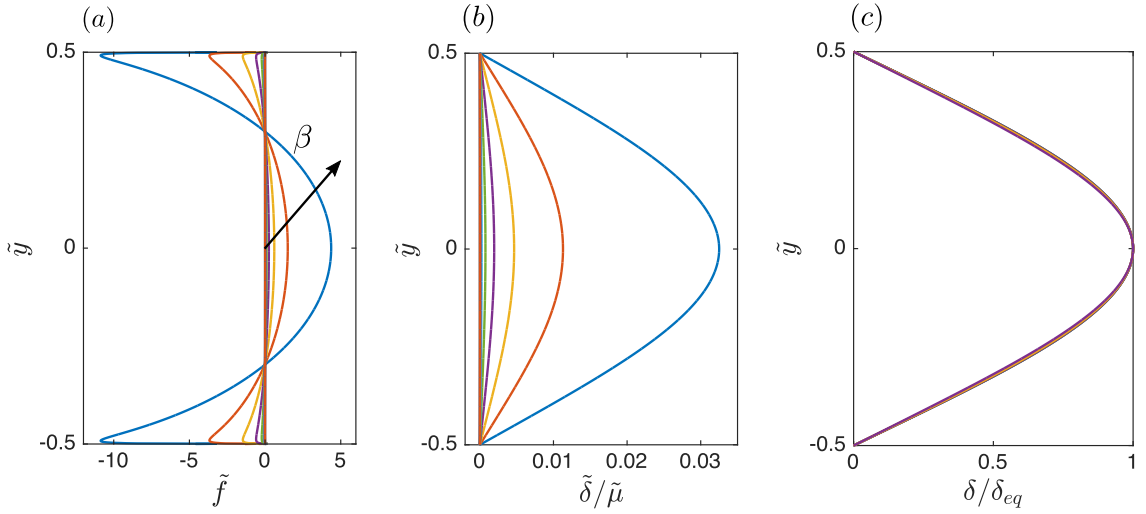


Figure IV.15: Influence of confinement using the 2D model. (a) Evolution of the force distribution along the fiber length for confinements varying from $\beta = 0.1$ to $\beta = 0.9$ for a fiber with a squared cross section and an aspect ratio $a = 21$ transported in a confined channel without lateral walls. (b) Resulting normalized fiber deflections. (c) Fiber shapes normalized by δ_{eq} for different confinements.

ues lie below the numerical lines. A possible cause for this is the assumption that the deflected fiber leads to the same force distribution as a straight fiber. However, for high confinements and thus larger deflections, the effective force on the fiber might change due to the change in fiber shape and the resulting equilibrium state might exhibit a smaller deflection. An other source of error lies in the beam model we used, we did not consider any tension among the fiber which is expected to decrease the deformation. But the current results still exhibiting a good agreement between experiment and theory and the simplicity of the current approach is nevertheless considered to be more valuable than the possibly gained accuracy of more complex model refinements.

The deflection is observed to increase strongly with the confinement for $\beta \geq 0.6$. For less confined fibers, only a weak dependence can be observed. A similar observation had been made for the transport velocity of rigid fibers in confined channels (see Figure IV.7), where, for confinements above 0.6, a strong decrease of the transport velocity is observed, whereas, for smaller confinements, only a small influence is present.

Figure IV.17 compares the determined maximum normalized deflection for various values of the confinement β as obtained from the 3D and 2D models as well as from the 2D model from Nagel *et al.* [30], which can be obtained by setting $\Delta_{\partial_{\tilde{x}}\tilde{p}} = 0$ in equation IV.18, i.e. by considering a constant force per unit length in the gap. While the 2D models systematically underestimate the maximum deflection, this effect decreases with increasing confinement. The difference between the two 2D models decreases as well with increasing confinement and is almost negligible for $\beta \geq 0.8$.

For a perpendicular fiber, the complexity of the calculations is not increased by including the gap force variations and they have thus been taken into account in the present work. However, the extension of the gap flow model is only possible for perpendicular

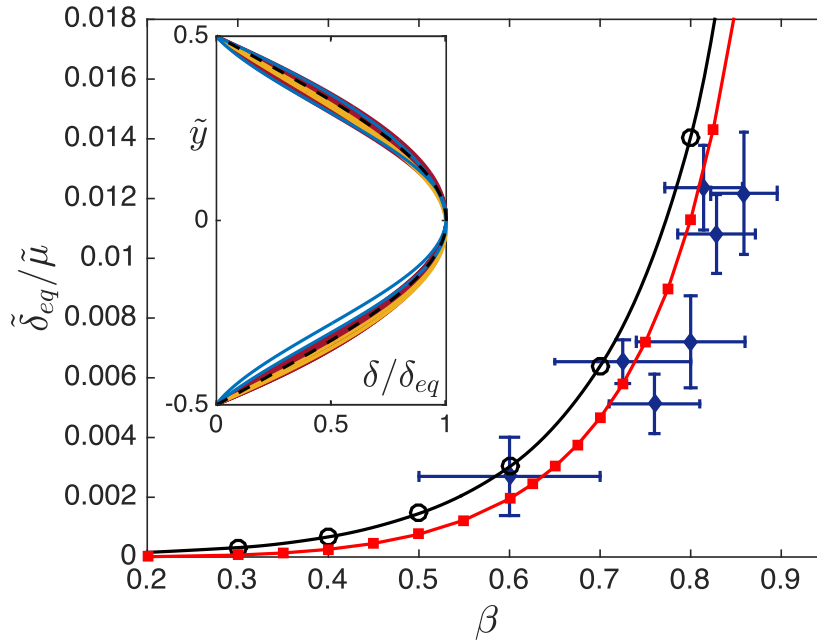


Figure IV.16: Evolution of the normalized deflection of the fiber $\tilde{\delta}/\tilde{\mu}$ as a function of the confinement $\beta = h/H$ for a fiber of aspect ratio $a = 21$. The blue diamonds show experimental data, each point corresponding to an average over the normalized deflection for varying $\tilde{\mu}$. The red squares show the prediction of the 2D model and the black circles correspond to the 3D model. Red and black lines are guidelines. The inset shows experimental fiber shapes normalized by $\tilde{\delta}_{eq}$ for different confinements (Blue: $\beta = 0.60 \pm 0.10$, yellow: $\beta = 0.73 \pm 0.08$, red: $\beta = 0.86 \pm 0.04$). The black dashed line indicates the shape obtained from the 2D numerical simulations for a confinement $\beta = 0.8$.

fibers and approximating the gap force by its mean value as done by [30] can be advantageous for future studies on inclined fibers.

IV.8 Conclusion

In this chapter we have shown that flexible fibers transported in a plug flow deform when confined by the top and bottom walls. Fibers transported perpendicularly to the flow direction exhibit a C-shape, directly reflecting the nonuniform force distribution imposed on the fiber. The fiber acts as a moving obstacle when pushed by the flow against the friction with top and bottom walls along the channel. This leads to a perturbation of the flow and thus to non-homogeneous pressure and force distributions along the fiber, while the total force remains zero due to negligible inertia. We have seen that the variations in fiber deflection can be rationalized with an elasto-viscous number $\tilde{\mu}$ and that the force distribution strongly depends on the confinement as reflected by a sharp increase of the deflection with increasing confinement. This last point can be understood as follows: the system is dominated by the pressure force distribution since it takes place in a confined

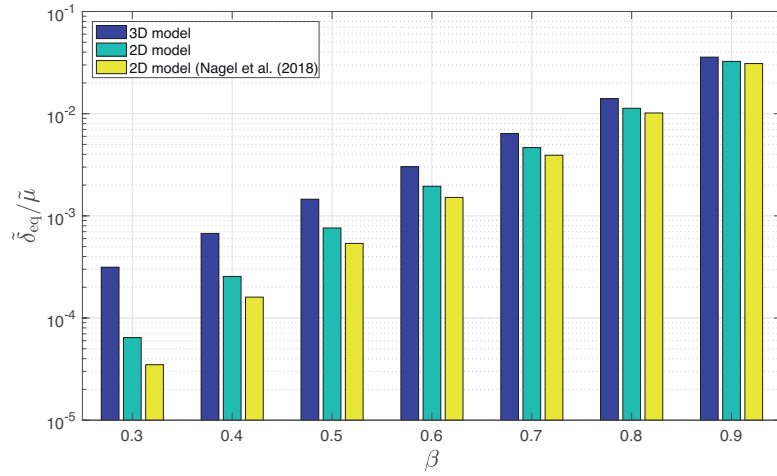


Figure IV.17: Comparison of the normalized maximum deflection $\tilde{\delta}_{\text{eq}}/\tilde{\mu}$ as calculated using the 3D and 2D models.

geometry. Thus the larger the confinement, the larger the pressure difference between the front part and the back part of the fiber, and this leads to larger deformations of the fiber.

The interaction between deformation and transport of such flexible fibers leads to interesting dynamics and in particular to a reorientation towards an orientation parallel to the flow direction. The observed dynamics bear some similarities to the dynamics of sedimenting flexible fibers, which, however, reach a stable final position perpendicular to the direction of sedimentation. A stability analysis of the equilibrium state can shed light on this issue and is left here for future studies. Understanding these dynamics is of importance for the controlled transport of flexible fibers in confined geometries, such as in enhanced oil recovery or fiber optics. It could also provide insight in the deformation and transport of more complex deformable particles in confined geometries, such as vesicles or red blood cells. In addition, as it was shown here that the deflection of the fiber can directly be linked to the force distribution, flexible fibers could be used as microfluidic sensors.

Chapter V

Buckling instability of a freely transported fiber in a micro-channel

In this chapter, we use the same flow geometry as in the previous chapter and we focus on the transport dynamics of flexible fibers oriented parallel to the flow direction. We show that, under certain conditions, fibers deform into a sine shape that flattens out towards the fiber ends (see Figure V.1). Such deformation is triggered by a competition between viscous and elastic forces and is observed only for very long fibers, almost one order of magnitude larger than the observed wavelength. We characterize this deformation experimentally and show that the wavelength of the deformation does not depend on the fiber length and is proportional to an elasto-viscous length. Furthermore, we study the growth rate of the instability for different fiber geometries, flow strengths, and mechanical properties of the fibers and we evidence the existence of an instability threshold. Other dynamical quantities such as the angular frequency of the wave and its phase velocity are characterized experimentally. In the last section of the chapter, we aim at understanding the origin of the instability using simple fluid-structure interaction models.

V.1 Observations

Typical experimental observations can be seen in Figure V.1 which shows the shape of a flexible fiber during its transport along the microchannel at different times. A fiber, initially straight, deforms in a sine shape with a very well defined wavelength modulated by an envelope that flattens out at the fiber edges. The dynamics of the deformation is very rich: the amplitude of the deformation increases with time, the envelope spreads along the fiber and, comparing the last two images of Figure V.1, one can see the perturbation wave traveling along the fiber from back to front.

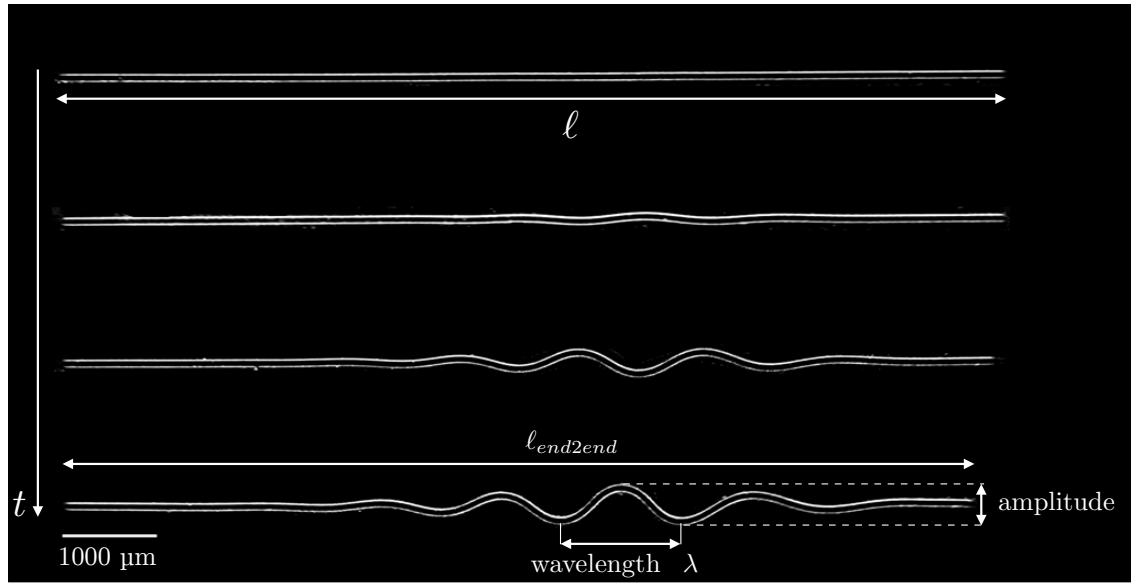


Figure V.1: Chronophotographies of a parallel fiber transported in a confined geometry by an external flow. Time increases from top to bottom. The external flow of velocity $u_0 = 0.65 \text{ mm}\cdot\text{s}^{-1}$ is oriented from left to right. The fiber has a length $\ell = 10130 \pm 15 \text{ }\mu\text{m}$, width $w = 75 \pm 3 \text{ }\mu\text{m}$, height $h = 73 \pm 3 \text{ }\mu\text{m}$, Young's modulus $E = 27.2 \pm 7.1 \text{ kPa}$. The viscosity of the fluid is $85 \pm 3 \text{ mPa}\cdot\text{s}$. Confinement is $\beta = 0.86 \pm 0.04$. We define the amplitude of the deformation by the distance between the maximum and the minimum of the deformation. ℓ_{end2end} is the end to end distance of the fiber. Scale bar is $1000 \text{ }\mu\text{m}$.

Note that contrary to what was observed in the case of a perpendicular fiber, the parallel configuration is stable i.e. the fiber remains parallel to the flow direction even after deformation.

V.2 Presentation of the experimental setup

The channel and fiber geometries are depicted in Figure V.2 (a) and (b). We use the same channel geometry as in chapter IV in order to have a plug flow in the (Oxy) plane and a Poiseuille flow in the (Oxz) plane. The channel width W is varied from $W = 1000 \text{ }\mu\text{m}$ to $W = 3500 \text{ }\mu\text{m}$, and its height is varied from $H = 42 \text{ }\mu\text{m}$ to $H = 85 \text{ }\mu\text{m}$.

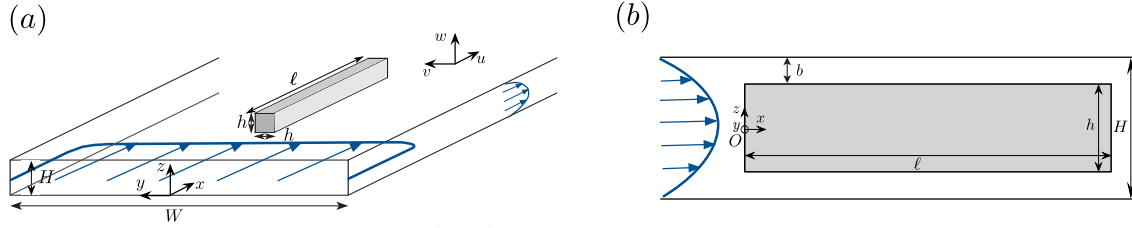


Figure V.2: (a) Geometry of the parallel fiber and the confining channel. The pressure-driven flow is sketched in blue. (b) Cross section view of the channel and of a parallel fiber.

The straight polymeric fibers are fabricated at zero flow rate using the stop-flow microscope-based projection photo-lithography method developed by Dendukuri *et al.* [16], which was previously presented in chapter II. In order to obtain very elongated object, we use the "moving stage" method together with the $\times 5$ EC Plan NEOFLUAR objective.

Apart from one experiment where we vary the width of the fiber, we adjust the mask geometry as a function of the channel height in order to fabricate squared cross section fibers. On the other hand, the length of the fiber is set through the choice of the distance over which the stage is displaced. Typical fiber dimensions vary from $30\ \mu\text{m}$ to $74\ \mu\text{m}$ for width and height and from $9174\ \text{mm}$ to $15000\ \text{mm}$ for the length. The height of the gap between the fiber and the channel top and bottom walls is, as previously mentioned in chapter II, $b = 6.0 \pm 1.6\ \mu\text{m}$.

According to the discussion in chapters II on the control of the Young's modulus of the hydrogel, we move the microscope stage at a constant velocity, $120\ \mu\text{m}\cdot\text{s}^{-1}$, and illuminate through a rectangular mask of length $38\ \mu\text{m}$ (the image in the channel has a length of $72\ \mu\text{m}$) in order to illuminate each portion of the fiber during $600\ \text{ms}$. It allows us to have a reproducible and constant Young's modulus along the fiber. In this study we use very soft hydrogels fabricated from photosensitive solutions diluted with 65% or 70% PEG₁₀₀₀-water solvent.

Once the fibers are fabricated inside the channel, flow is turned on by means of a syringe pump. The fiber shape is recorded using a X2.5 EC Epiplan-Neofluar or a X1 EC Epiplan-Neofluar objective and a Hamamatsu Orca-flash 4.0 camera at a frame-rate of 10 images per second. We monitor its evolution by moving the microscope stage by hand to keep the fiber in the field of view of the camera.

V.3 Results

V.3.1 Spatio-temporal evolution

Figure V.3 corresponds to the spatio-temporal evolution of the deformation of the fiber shown in Figure V.1 in the frame of reference of the fiber (origin being set at the trailing edge of the fiber).

This spatio-temporal evolution shows the spreading of the perturbation envelope with

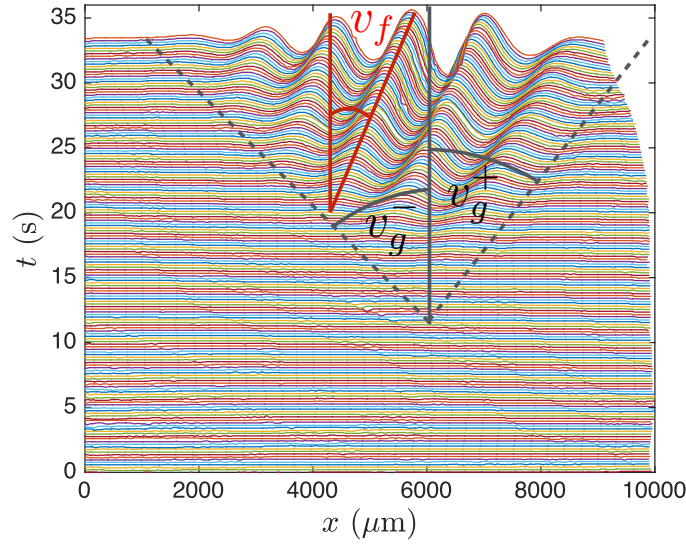


Figure V.3: Spatio-temporal evolution of a flexible fiber transported by an external flow in a confined microchannel. The geometry of the fiber is the same as in Figure V.1.

time, the increase of the amplitude and the phase velocity of the traveling wave v_f . Moreover, in the frame of reference of the fiber, the velocity of the receding front is negative $v_g^- < 0$ and the perturbation travels upstream. This is a signature of an absolute instability. Here, even if it is difficult to accurately determine the abscissa of the point where the perturbation starts, the perturbation seems to appear close to the center of the fiber. Note that, due to the finite length of the fiber, when the fiber deforms the end to end distance $\ell_{end2end}$ decreases.

V.3.2 Wavelength characterization

Taking all the fiber shapes shown in Figure V.3, renormalizing their amplitude by their maximal amplitude and placing the point of maximal deformation at abscissa $x = 0$ we obtain Figure V.4. This figure shows that the wavelength of the perturbation is constant over time. Again the spreading of the envelope is visible at the edges of the fiber.

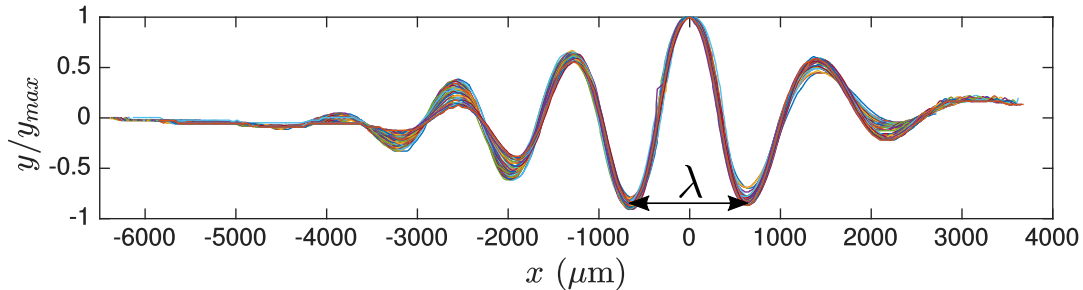


Figure V.4: Superposition of fiber shapes at different times renormalized by their maximal amplitude. The point of maximal amplitude have been placed at $x = 0$.

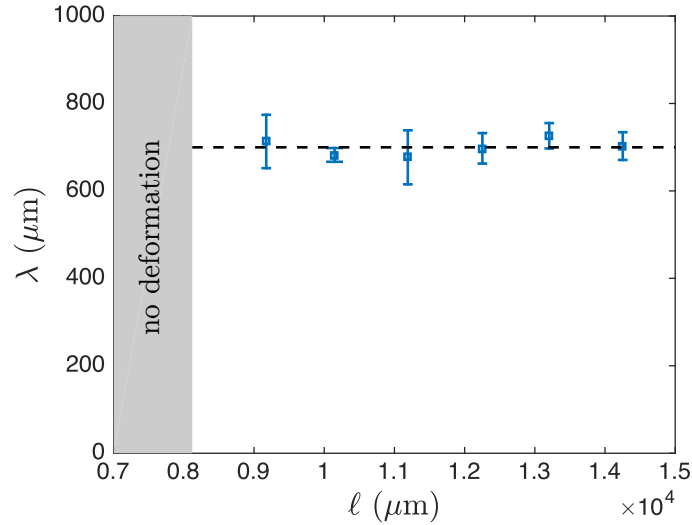


Figure V.5: Evolution of the wavelength as a function of the length of the fiber. The fiber has a Young's modulus estimated at 201 ± 111 Pa, a width $w = 65 \pm 3$ μm and a height $h = 73 \pm 3$ μm . The confinement is $\beta = 0.86 \pm 0.04$.

Using standard Fourier transform of the shape, we measure the wavelength of the perturbation and investigate its evolution as a function of different experimental parameters, such as the fiber length ℓ , the mean velocity of the surrounding fluid u_0 , the Young's modulus E and the width w of the fiber.

Figure V.5 shows the evolution of the wavelength of the perturbation as a function of the length of the fiber. The grey area corresponds to experiments where the fiber remains straight while transported.

Surprisingly the wavelength does not depend on the fiber length, but for small fiber lengths no perturbations are observable. In order to see a perturbation, the fiber needs to be almost one order of magnitude larger than the expected wavelength.

As the length of the fiber does not impact the wavelength, it is not the relevant length scale of the system. Thus, another length-scale needs to be built from the physical parameters of the system such as the flow velocity u_0 , the fluid viscosity μ , the bending modulus of the fiber EI , its width w and its height h .

Figure V.6 (a) shows the variation of λ as a function of the imposed mean flow velocity u_0 for two different Young's moduli ($E = 117 \pm 64$ kPa and $E = 27.2 \pm 7.1$ kPa), different channel widths ($W = 3640 \pm 10$ μm , $W = 3500 \pm 10$ μm and $W = 1000 \pm 10$ μm) and different fiber lengths ($\ell = 15636 \pm 471$ μm and $\ell = 10187 \pm 25$ μm). Flow velocity and Young's modulus have opposite impacts on the wavelength: increasing the flow velocity decreases the wavelength, whereas increasing the Young's modulus increases the wavelength. Moreover, Figure V.6 (a) shows that the wavelength is independent of the channel width; for a given Young's modulus (see red, dark blue and light blue markers), no differences on the evolution of λ as a function of u_0 are observed for the different channel widths.

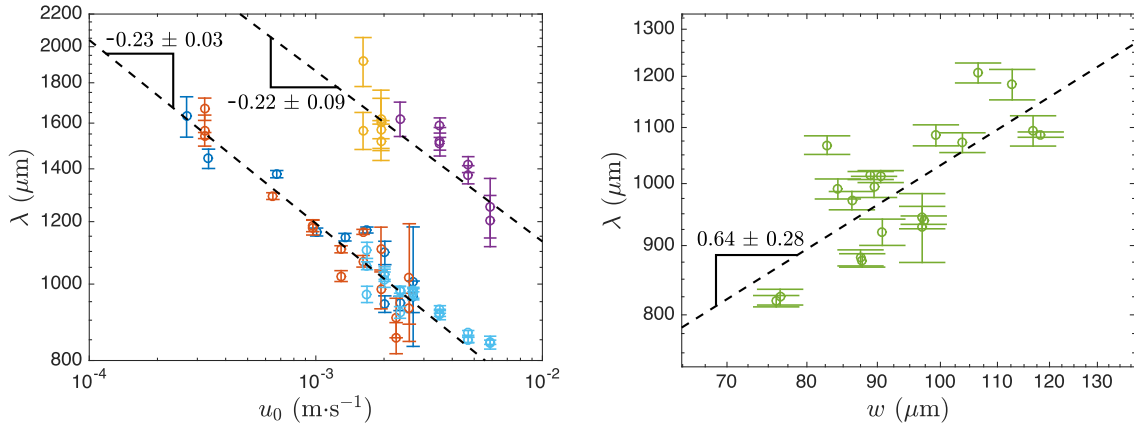


Figure V.6: Wavelength characterization. (a) Evolution of the wavelength as a function of the mean velocity of the external flow for two different fiber moduli and lengths: $E = 117 \pm 64$ kPa, $\ell = 15636 \pm 471$ μm (yellow and purple markers) and $E = 27.2 \pm 7.1$ kPa, $\ell = 10187 \pm 25$ μm (red, dark blue and light blue markers). Different colors correspond to different channel width: $W = 3640 \pm 10$ μm (red), $W = 3500 \pm 10$ μm (dark blue and yellow) and $W = 1000 \pm 10$ μm (light blue and purple). The two sets of measurements are obtained with fibers of width $w = 75 \pm 9$ μm , height $h = 73 \pm 3$ μm and for a confinement of $\beta = 86 \pm 0.04$. Dotted black lines correspond to fits of the measurements by a power law. (b) Evolution of the wavelength as a function of the width w of the fiber for a given fiber Young's modulus $E = 27.2 \pm 7.1$ kPa, length $\ell = 10233 \pm 78$, height $h = 73 \pm 3$ μm and for a confinement of $\beta = 86 \pm 0.04$.

The evolutions of the of the wavelength as a function of the flow velocity are well fitted by a power law $\lambda \propto u_0^\alpha$. For both Young's moduli fits lead to comparable results: $\alpha = -0.22 \pm 0.09$ ($E = 117 \pm 64$ kPa) and $\alpha = -0.23 \pm 0.03$ ($E = 27.2 \pm 7.1$ kPa).

The impact of the fiber width on the wavelength is shown on Figure V.6 (b) which illustrates that the wavelength increases with increasing fiber width. Measurements are fitted with a power law $\lambda \propto w^{\alpha_w}$, which gives a coefficient $\alpha_w = 0.6 \pm 0.3$.

Using the power laws obtained experimentally, one can build another length scale of the problem. As in chapter IV, the deformation is due to a competition of viscous and pressure forces which tend to deform the particle and elastic forces which oppose to the deformation. Thus, one expects that a characteristic elasto-viscous length comparing these two effects is the pertinent length to look at. Such a length can be defined as [92]:

$$\Lambda = \left(\frac{EI}{\mu u_0} \right)^{1/3}. \quad (\text{V.1})$$

This elasto-viscous length is proportional to the velocity at a power $-1/3$ and to the width of the fiber (through $I = hw^3/12$) at a power 1. It is in fair agreement with what we measured experimentally. Indeed, the experimental determination of α relies on experiments where u_0 varies over less than two decades and because of the small exponent α the range of values of λ is rather small. Thus, it is very difficult to have a reliable evaluation of α and to differentiate a value $\alpha = -1/3$ from a value $\alpha = -1/4$. This

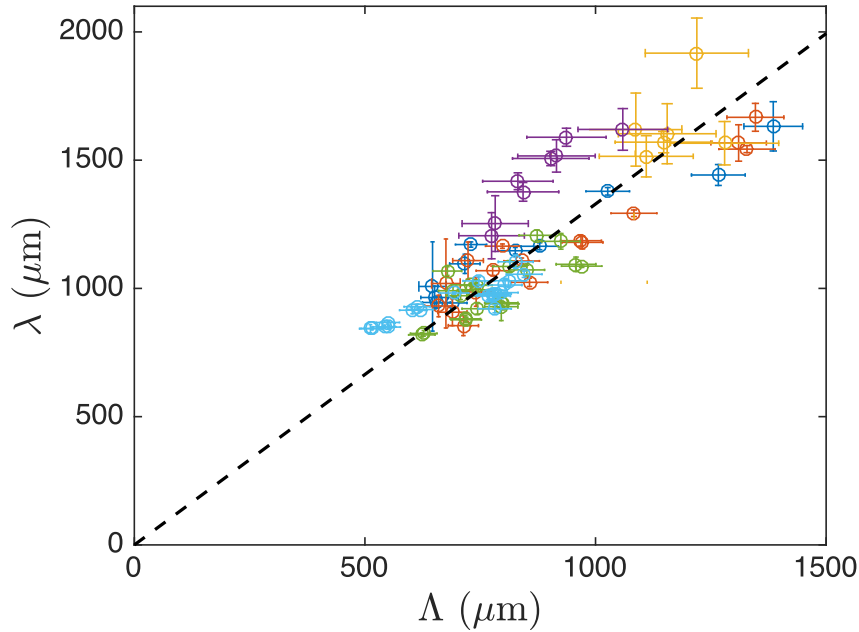


Figure V.7: Evolution of the wavelength as a function of the elasto-viscous length Λ . The color code is the same as in Figure V.6 (a) and (b).

remark holds also for α_w ; the low range of values of w achievable experimentally does not allow to distinguish a power law with a coefficient equal to unity from a power law with a coefficient equal to $2/3$.

Figure V.7 shows that the measured wavelengths obtained for the different experimental parameters presented above collapse onto a single linear curve when plotted as a function of Λ . This confirms Λ is the correct length-scale of the system.

V.3.3 Amplitude dynamics

As shown in Figure V.8 (a), the amplitude of the perturbation, measured at the position along the fiber where it is largest (Figure V.1), varies with time. Note that our definition of the amplitude which is based on the fiber shape, does not exactly correspond to the amplitude of the envelope of the wave packet (i.e. if the wavelength of maximal amplitude is not located in the middle of the envelope, our definition of the amplitude is smaller than the amplitude of the envelope). The evolution of the amplitude is well fitted by an exponential function with a characteristic growth time τ . Such a fit is shown by the black dotted line in Figure V.8 (a). This exponential growth indicates a linear instability.

Using this fitting method we measured the growth time of the perturbation for different sets of experimental parameters. Figure V.8 (b) shows the evolution of the amplitude growth time as a function of the simplest characteristic time one can build $\Gamma = \ell/u_0$, for the same series of experiments as in Figure V.6. These measurements are fairly well fitted by a linear law (dotted black curve). For small growth times, $\tau < 3$ s, we observe a large scatter. Note that this typical range of growth times corresponds to the typical response

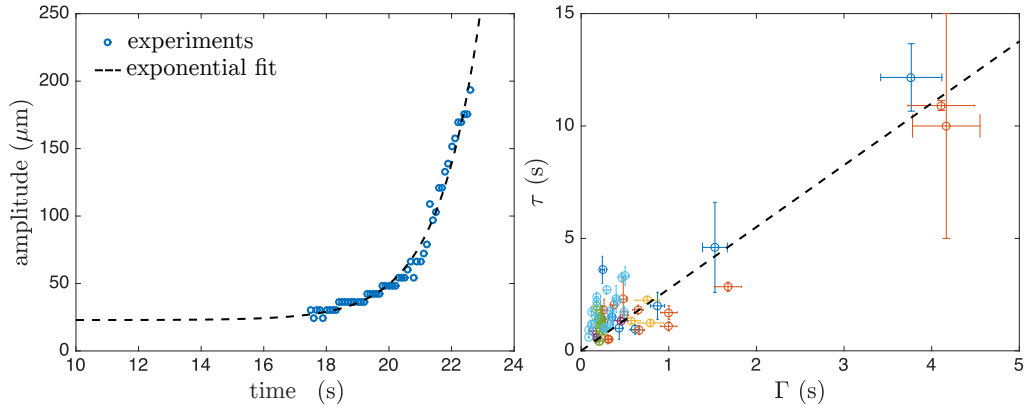


Figure V.8: (a) Evolution of the amplitude as a function of time for the experiments shown in Figure V.1. The experimental measurements are well fitted by an exponential law $\text{amplitude}(t_0) \exp((t - t_0)/\tau)$, with τ the growth time of the perturbation. The exponential fit corresponds to the black dotted line. (b) Evolution of the growth time as a function of the simplest time-scale of the system $\Gamma = \Lambda/u_0$. The black dotted line corresponds to a linear fit of the data. The color code is the same as in Figure V.6.

time of the syringe pump used in the experiments, thus the measured characteristic time could be a superposition of two effects: the actual characteristic time of the amplitude evolution and the time necessary to set the flow.

When the same data is plotted as a function of the dimensionless parameter ℓ/Λ , as in Figure V.9 (a), all the points collapse onto a single curve well fitted by an hyperbolic law. This fit highlights the existence of a critical value $(\ell/\Lambda)_c = 6.6$ for which the growth time goes to infinity, a signature of the existence of an instability threshold.

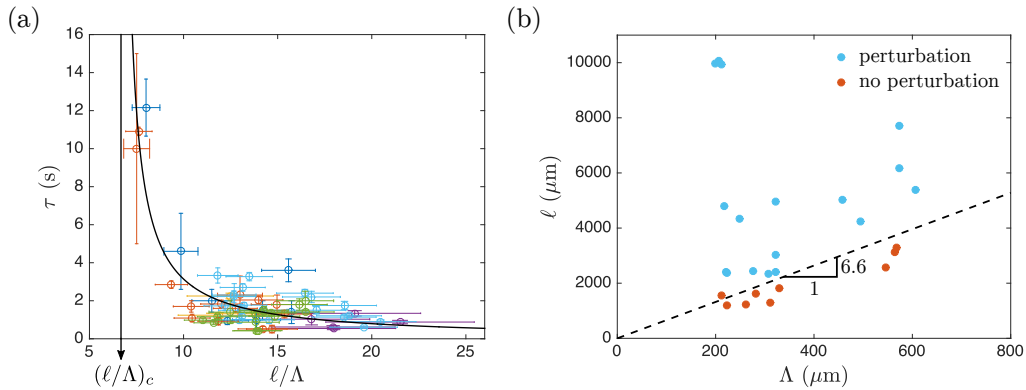


Figure V.9: Instability threshold. (a) Evolution of the growth time as a function of the dimensionless parameter ℓ/Λ . The black line corresponds to an hyperbolic fit of the data. Color code is the same as Figure V.6. (b) Phase diagram ℓ as a function of Λ : experiments where instability occurs are represented with blue markers and experiments where the fiber remains undeformed are represented in orange.

Moreover, this threshold also appears in Figure V.9 (b), phase diagram in the space spanned by ℓ and Λ , in which are represented with blue markers the experiments where instability occurs and with orange markers the experiments where the fiber remains undeformed. Indeed, the linear curve of slope $(\ell/\Lambda)_c = 6.6$ separates the two regions.

V.3.4 Angular frequency and phase velocity

From the temporal evolution of the skeletonized shapes of the fiber shown in Figure V.3, we measure the angular frequency of the waves $\omega = 2\pi/T$, with T the signal period. T corresponds to the oscillatory period of the perturbation at a fixed position on the fiber (as for instance on the vertical grey line shown in Figure V.3).

For the same series of experiments as in Figure V.6, we represent the evolution of the angular frequency as a function of the mean velocity of the external flow u_0 in Figure V.10 (a) and as function of $\Gamma = u_0/\Lambda$ in Figure V.10 (b). Note that no measurements of the angular frequency are achievable for large Young's moduli ($E = 117 \pm 64$ kPa). Indeed, the larger E the larger Λ and, as previously mentioned, in order to observe the instability the fiber needs to be longer than 6.6Λ . Thus the fiber needs to be very large and our experimental setup, even using a $\times 1$ objective, does not enable us to see the total length of the fiber. The edges of the fibers not being visible, the frame of reference of the fiber is not well defined and it is then impossible to look at the time evolution of a specific point on the fiber.

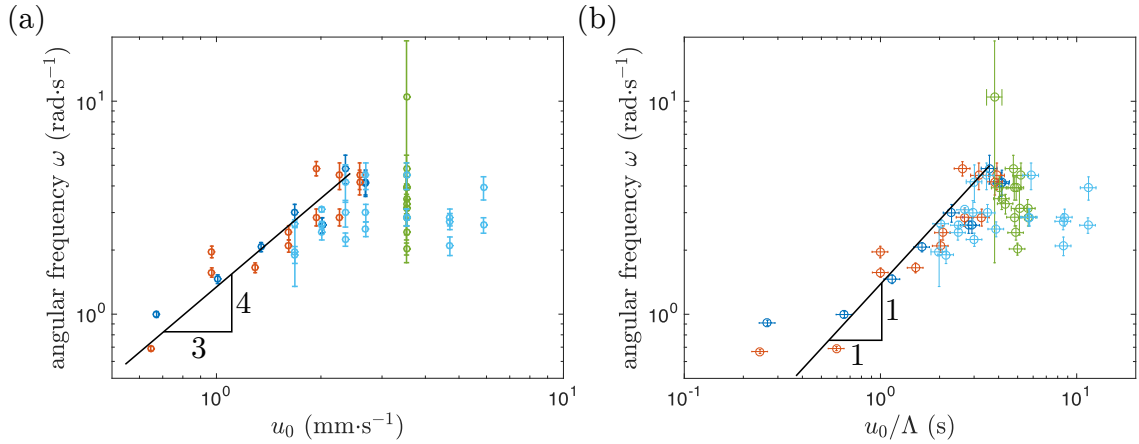


Figure V.10: Angular frequency ω characterization. (a) Evolution of ω as a function of the mean flow velocity u_0 . The black line allows for the visualization of a slope $4/3$. (b) Evolution of ω as a function of u_0/Λ . The black line has a slope 1 . Color code is the same as Figure V.6.

Figure V.10 (a) shows that the evolution of ω as a function of u_0 is divided into two regimes: for low values of u_0 , ω depends on the flow velocity at a power $4/3$ ($\omega \propto u_0^{4/3}$) and for large values of u_0 , it eventually reaches a plateau. This observed power law leads us to represent the evolution of ω as a function of $\Gamma = u_0/\Lambda \propto u_0^{4/3}$ (see Figure V.10 (b)) where in the first regime ω can reasonably be described as being linear in Γ .

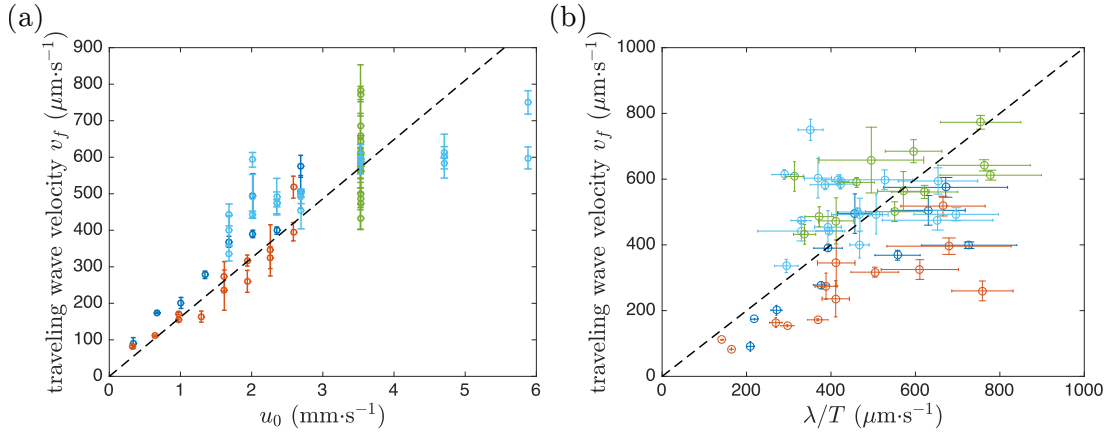


Figure V.11: Characterization of the traveling wave velocity v_f . (a) Evolution of v_f as a function of the mean flow velocity u_0 . The black dotted line is a linear fit of the data. (b) Same data plotted as a function of the phase velocity $v_\phi = \lambda/T$, with λ the wavelength of the perturbation and $T = 2\pi/\omega$ the period of the oscillations. The black line is a linear curve of slope 1. Color code is the same as in Figure V.6.

An additional characteristic parameter of the wave packet has been investigated: the traveling wave velocity v_f (see Figure V.3 for its definition). As shown in Figure V.11 (a), where v_f is plotted as a function of u_0 , the traveling wave velocity is proportional to the external flow velocity. This shows that u_0 is the characteristic velocity scale of the system.

Figure V.11 (b) illustrates the evolution of v_f as a function of the phase velocity $v_\phi = \lambda/T$. The dotted line is a linear curve of slope one which qualitatively recovers the evolution of our measurements. Thus, as expected, v_f corresponds to the phase velocity of the wave. Note that the large scatter visible in Figure V.11 (b) for large v_f ($v_f > 400 \mu\text{m}\cdot\text{s}^{-1}$) is due to the fact that the quantities v_f and T are measured experimentally on short temporal signals (the dynamic being fast, measurements are carried out on just a few points).

V.4 Modeling

In this section, we model the flow around a freely transported parallel fiber and we aim to determine the causes of the observed instability.

V.4.1 A naive approach

We consider a fiber with a square cross section of height h width $w = h$ and length $\ell \gg h$ transported by an external flow of mean velocity u_0 . The channel has a length L , height H and width W , with $H \ll W$ and $W \ll L$. The gap in between the fiber and the top or bottom wall has a height $b = H(1 - \beta)/2$, with $\beta = h/H$ the confinement.

When the fiber is parallel to the flow direction three different forces are acting on the fiber: the pressure force acting on the front and the back of the fiber \vec{F}_p , the viscous forces acting on the lateral sides of the fiber \vec{f}_{lat} and the viscous forces acting on the top

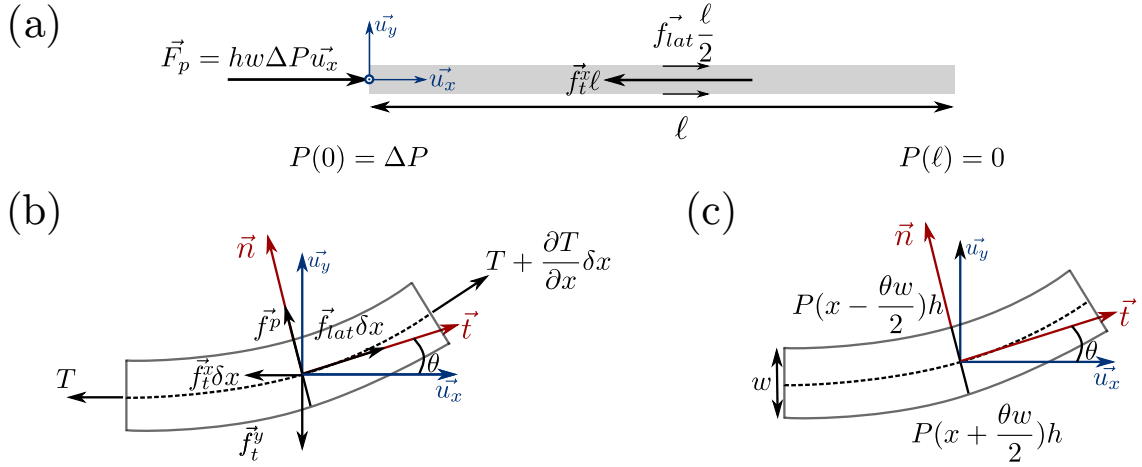


Figure V.12: (a) Geometry of the beam and representation of the pressure force, the lateral viscous force per unit length and the viscous forces per unit length acting on the top and bottom sides of the fiber. (b) Representation of an element of the beam of length δx together with the forces per unit length acting on it. (c) An element of the beam of length δx with a representation of the surrounding pressure. Note that in (b) and (c) only small deformations are considered.

and bottom sides of the fiber \vec{f}_t^x . These forces and forces per unit length are represented in Figure V.12 (a).

The description given here relies on different assumptions:

- We consider small lateral deformations of the beam $y(x, t)$ from its undeformed configuration, which is taken to coincide with the x -direction, and we assume that the angles of incidence, $\theta = \frac{\partial y}{\partial x} \ll 1$. θ is represented in Figures V.12 (b) and (c).
- The presence of the fiber does not impact the flow. Thus, the pressure decreases linearly along the filament,

$$P(x) = \Delta P \left(1 - \frac{x}{\ell}\right), \quad (\text{V.2})$$

with ΔP the pressure drop along the fiber.

- The viscous lateral force per unit length $\vec{f}_{lat} = f_{lat} \vec{t}$ is constant along the filament and is locally tangent to the fiber orientation.
- The viscous force per unit length on the top and bottom sides of the fiber in the x -direction $\vec{f}_t^x = f_t^x \vec{u}_x$ does not vary along the fiber length. Note that for small deformations, at leading order in deformation $\vec{t} = \vec{u}_x + \frac{\partial y}{\partial x} \vec{u}_y$.
- When the fiber starts to deform in the y -direction, a viscous force opposes to this deformation. This viscous force is due to the Couette flows taking place in the gaps which are induced by the fiber motion. This force per unit length can be written $\vec{f}_t^y = -\frac{2\mu w}{b} \frac{\partial y}{\partial t} \vec{u}_y$.

A similar flow description has been used in appendix D to determine the velocity of a parallel fiber.

The forces and moments acting on a small element, δx , of the fiber, which has undergone a small lateral deformation $y(x, t)$, are shown in Figure V.12 (b) and (c). The force balances in the x - and y -directions are (see section I.4.1 of chapter I):

$$\frac{\partial T}{\partial x} + f_{lat} + f_t^x + f_p^x = 0, \quad (\text{V.3})$$

$$-EI \frac{\partial^4 y}{\partial x^4} + f_p^y + f_{lat} \frac{\partial y}{\partial x} + \frac{\partial}{\partial x} \left(T \frac{\partial y}{\partial x} \right) + f_t^y = 0, \quad (\text{V.4})$$

with T the tension inside the fiber and f_p^x and f_p^y , respectively, the force per unit length due to the outer pressure in the x -direction and in the y -direction. In the following we derive the expressions of these two forces.

The pressure force per unit length due to the pressure gradient in the surrounding fluid is [93]:

$$\vec{f}_p = \frac{1}{\Re \theta} \left[-P \left(x - \frac{\theta w}{2} \right) h \left(\Re \theta - \frac{w \theta}{2} \right) + P \left(x + \frac{\theta w}{2} \right) h \left(\Re \theta + \frac{w \theta}{2} \right) \right] \vec{n} \quad (\text{V.5})$$

$$= h \left[-P \left(x - \frac{\theta w}{2} \right) \left(1 - \frac{w}{2\Re} \right) + P \left(x + \frac{\theta w}{2} \right) \left(1 + \frac{w}{2\Re} \right) \right] \vec{n}, \quad (\text{V.6})$$

with \Re the local radius of curvature of the beam defined at leading order in θ as $\frac{1}{\Re} = \frac{\partial \theta}{\partial x}$.

This force per length corresponds to the sum of the pressure forces acting on the left side and on the right side of the fiber. Here, left and right are considered relatively to the x -axis.

The first (second) product in the brackets of equation V.5 corresponds to the pressure in the middle of the left (right) side of the fiber multiplied by the area of the left (right) side. These two terms are divided by the length $\Re \theta$ of the centerline of the element to obtain a force per unit length.

This force per unit length can be developed as follows:

$$\vec{f}_p = \left[\left(P \left(x + \frac{\theta w}{2} \right) - P \left(x - \frac{\theta w}{2} \right) \right) h + \left(P \left(x - \frac{\theta w}{2} \right) + P \left(x + \frac{\theta w}{2} \right) \right) \frac{hw}{2\Re} \right] \vec{n}. \quad (\text{V.7})$$

Using a Taylor expansion of $P \left(x + \frac{\theta w}{2} \right)$ and $P \left(x - \frac{\theta w}{2} \right)$ at first order in θ , one obtains:

$$\vec{f}_p = wh \left[\theta \frac{\partial P}{\partial x} + P \frac{\partial \theta}{\partial x} \right] \vec{n} \quad (\text{V.8})$$

$$= \frac{\partial}{\partial x} \left(whP \frac{\partial y}{\partial x} \right) \vec{n}. \quad (\text{V.9})$$

Projecting \vec{n} over \vec{u}_x and \vec{u}_y ($\vec{n} = \vec{u}_y - \theta \vec{u}_x$ at first order in θ), we obtain

$$f_p^y = \frac{\partial}{\partial x} \left(whP \frac{\partial y}{\partial x} \right) \quad \text{and} \quad f_p^x = O(y^2). \quad (\text{V.10})$$

Note that mathematically f_p^y can be considered as an extra tension term. Thus, equations V.3 and V.4 become at first order in y :

$$\frac{\partial T}{\partial x} + f_{lat} + f_t = 0, \quad (\text{V.11})$$

$$-EI \frac{\partial^4 y}{\partial x^4} + f_{lat} \frac{\partial y}{\partial x} + \frac{\partial}{\partial x} \left((T + hwP(x)) \frac{\partial y}{\partial x} \right) + f_t^y = 0. \quad (\text{V.12})$$

Equation V.12 enables us to define a new "tension":

$$T' = T + hwP(x). \quad (\text{V.13})$$

In order to solve equations V.11 and V.12 one needs to derive the expression of T .

Using the condition of zero force projected on the x -direction on the overall fiber we obtain at leading order in θ

$$hw\Delta P + \ell(f_{lat}\vec{t} \cdot \vec{u}_x + f_t^x) = hw\Delta P + \ell(f_{lat} + f_t^x) = 0, \quad (\text{V.14})$$

with $hw\Delta P = \|\vec{F}_p\|$ the pressure force acting on the front edge of the fiber.

Note that the condition of zero force on the overall fiber at leading order (equation V.14) is the same as the total zero force condition for a straight fiber.

Using equation V.14, equation V.11 writes:

$$\frac{\partial T}{\partial x} = + \frac{hw\Delta P}{\ell}. \quad (\text{V.15})$$

Thus,

$$T(x) = T(0) + hw\Delta P \frac{x}{\ell} = -hw\Delta P \left(1 - \frac{x}{\ell} \right), \quad (\text{V.16})$$

with the boundary condition $T(0) = -hw\Delta P = -\|\vec{F}_p\|$.

Using equations V.13, V.2 and V.16, we find

$$T'(x) = T + hw\Delta P \left(1 - \frac{x}{\ell} \right) = -hw\Delta P \left(1 - \frac{x}{\ell} \right) + hw\Delta P \left(1 - \frac{x}{\ell} \right) = 0, \quad (\text{V.17})$$

and there is no tension inside the fiber.

Consequently equation V.12 becomes

$$-EI \frac{\partial^4 y}{\partial x^4} + f_{lat} \frac{\partial y}{\partial x} + f_t^y = 0. \quad (\text{V.18})$$

According to equation V.18 the fiber cannot buckle. Indeed, the term f_t^y is a stabilizing term, the term $-EI \frac{\partial^4 y}{\partial x^4}$ corresponds to an elastic force per unit length which opposes to the deformation and, as we will discuss further, the term $f_{lat} \frac{\partial y}{\partial x}$ is a term leading to traveling of the perturbation along the fiber (in the x -direction). Thus, there are no destabilizing terms in equation V.18.

As a consequence, the assumptions made are too strong to predict an instability. In order to increase the complexity of our model, in the following, we consider the fact that the forces per unit length vary along the fiber length i.e. we take into account the finite length of the fiber and the resulting edges effects.

V.4.2 A more realistic model

In the following, in order to derive the flow around a rigid fiber of finite length and thus take into account edge effects we use, as in chapter IV, a numerical simulation based on the resolution of the 2D Brinkman equation supplemented with a gap flow model (see chapter IV for more details). In such a way, we derive the forces per unit length acting of the fiber.

We consider variations of the forces per unit length around their mean values and variations of the pressure around its linear decrease. Apart from that, the assumptions made in the previous section remain unchanged i.e. the deformation of the fiber does not impact the flow, \vec{f}_{lat} is locally tangent to the fiber orientation, \vec{f}_t^x is oriented along the x -axis and $\vec{f}_t^y = -2\mu\frac{w}{b}\frac{\partial y}{\partial t}\vec{u}_y$.

These new assumptions lead to the expressions of \vec{f}_{lat} , \vec{f}_t^x and $P(x)$:

$$\vec{f}_{lat} = \left(\langle f_{lat} \rangle + f_{lat}^1 \right) \vec{t}, \quad \vec{f}_t^x = \left(\langle f_t^x \rangle + f_t^{x,1} \right) \vec{u}_x \quad \text{and} \quad P(x) = \Delta P \left(1 - \frac{x}{\ell} \right) + P^1(x) \quad (\text{V.19})$$

We use the $\langle \rangle$ symbol to indicate averaging over the fiber length, and varying quantities are denoted with a ¹. Using this definition the average over the fiber length of f_{lat}^1 and f_t^1 are zero and $P^1(0) = P^1(\ell) = 0$.

Moreover we assume $f_t^{x,1}$ uniformly zero i.e. the local velocity of the fiber in the x -direction is assumed to be constant along the fiber length.

The zero total force condition on the overall fiber in the x -direction is now:

$$\ell (\langle f_t^x \rangle + \langle f_{lat} \rangle) + hw\Delta P = 0, \quad (\text{V.20})$$

with $hw\Delta P$ being, as in the previous section, equal to the pressure force acting on the back edge of the fiber $\|\vec{F}_p\|$ (see Figure V.12 (a)).

And the equations V.11 and V.12 become:

$$\frac{\partial T}{\partial x} + f_{lat}^1 - \frac{hw}{\ell} \Delta P = 0, \quad (\text{V.21})$$

$$-EI \frac{\partial^4 y}{\partial x^4} + f_{lat} \frac{\partial y}{\partial x} + \frac{\partial}{\partial x} \left((T + hwP(x)) \frac{\partial y}{\partial x} \right) + f_t^y = 0 \quad (\text{V.22})$$

Integrating equation V.21 together with the boundary condition $T(0) = -hw\Delta P$, we obtain:

$$T(x) = - \int_0^x f_{lat}^1 dx + hw\Delta P \left(\frac{x}{\ell} - 1 \right) \quad \text{and} \quad T'(x) = - \int_0^x f_{lat}^1 dx + hwP^1(x). \quad (\text{V.23})$$

As already mentioned, to determine the distribution of $T'(x)$ we use a numerical approach based on the resolution of the Brinkman equation, particularly suitable for the resolution of flows in confined geometries.

The "tension" distribution $T'(x)$, represented in Figure V.13, shows that the back part of the fiber is compressed ($T' < 0$) and the front part of the fiber is stretched ($T' > 0$). In between the minimum and the maximum of the tension, the evolution is almost linear.

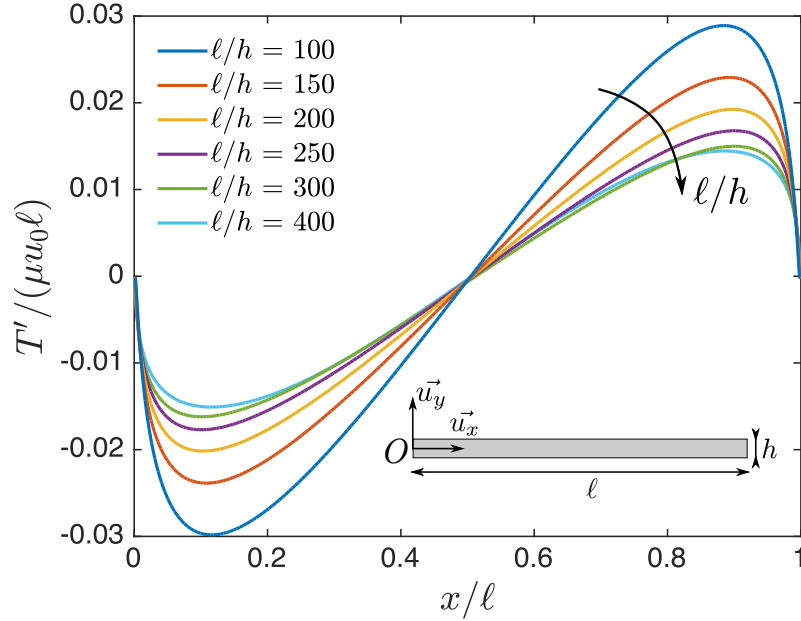


Figure V.13: Tension distribution obtained using ulambator code with a fiber of different aspect ratios ℓ/h and a confinement $\beta = 0.86$.

One can understand qualitatively the evolution of $T'(x)$ as follows: the fiber acts as a moving obstacle and the flow perturbation is primarily localized at the fiber edges. Close to the back tip ($x = 0$) we expect the pressure ($P(0)$) to be larger than in the absence of a fiber ($P_0(0)$). The same remark holds for the front tip ($x = \ell$) where the pressure ($P(\ell)$) is expected to be smaller than in the absence of the fiber ($P_0(\ell)$). On the contrary, the flow on the lateral sides of the fiber remains almost unchanged. Consequently, f_{lat}^1 is expected to be small and the pressure on the lateral sides of the fiber is expected to evolve as $P(x) = (P_0 - P_0(\ell))\frac{x}{\ell} + P_0(0)$.

As a consequence,

$$T \sim hw \left((P(0) - P(\ell))\frac{x}{\ell} + P(0) \right) \quad \text{and} \quad (\text{V.24})$$

$$T' \sim hw \left((P(0) - P(\ell))\frac{x}{\ell} + P(0) \right) - hw \left((P_0 - P_0(\ell))\frac{x}{\ell} + P_0(0) \right). \quad (\text{V.25})$$

By arguments of symmetry $(P(0) - P_0(0)) = -(P(\ell) - P_0(\ell)) = \delta P$ and T' writes

$$T' \sim hw\delta P(2x/\ell - 1). \quad (\text{V.26})$$

Thus, T' is expected to start from a negative value, increase linearly, change sign at $x = \ell/2$ and be symmetric about $x = \ell/2$. The expression of the "tension" T' (equation V.26) recovers most of the features shown in Figure V.13.

However, from this tension distribution one expects the fiber to buckle in the rear region which is not what observed in the experiments.

V.4.3 Linear stability analysis

In order to carry out a linear stability analysis of the system, we simplify the shape of the tension obtained from the numerical simulation to a linear tension $T' = T_0(2x/\ell - 1)$, with $T_0 = \mu u_0 \ell \tilde{T}_0$ and \tilde{T}_0 a dimensionless parameter function of the aspect ratio of the fiber ℓ/w and of the confinement β . Here, we focus on the rear part of the fiber ($x = 0$ to $x = \ell/2$), where buckling is expected to take place as the "tension" T' is negative in this part of the fiber.

Using this simple expression for the "tension" equation V.22 becomes

$$-EI \frac{\partial^4 y}{\partial x^4} + f_{lat} \frac{\partial y}{\partial x} + \frac{\partial}{\partial x} \left((T_0(2x\ell - 1)) \frac{\partial y}{\partial x} \right) = \frac{2\mu w}{b} \frac{\partial y}{\partial t}. \quad (\text{V.27})$$

We normalize lengths by $\ell/2$, forces per unit length by μu_0 , the tension by $\mu u_0 \ell/2$, time by $\frac{w\ell}{bu_0}$ and denote dimensionless quantities by a $\tilde{\cdot}$. Thus, we obtain

$$-8 \frac{EI}{\mu u_0} \frac{1}{\ell^3} \frac{\partial^4 \tilde{y}}{\partial \tilde{x}^4} + \tilde{f}_{lat} \frac{\partial \tilde{y}}{\partial \tilde{x}} + \tilde{T}_0 \frac{\partial}{\partial \tilde{x}} \left((\tilde{x} - 1) \frac{\partial \tilde{y}}{\partial \tilde{x}} \right) = \frac{\partial \tilde{y}}{\partial \tilde{t}}. \quad (\text{V.28})$$

$$(\text{V.29})$$

Developing further we obtain

$$-8 \frac{EI}{\mu u_0} \frac{1}{\ell^3} \frac{\partial^4 \tilde{y}}{\partial \tilde{x}^4} + \tilde{f}_{lat} \frac{\partial \tilde{y}}{\partial \tilde{x}} + \tilde{T}_0 \frac{\partial \tilde{y}}{\partial \tilde{x}} + \tilde{T}_0 (\tilde{x} - 1) \frac{\partial^2 \tilde{y}}{\partial \tilde{x}^2} = \frac{\partial \tilde{y}}{\partial \tilde{t}} \quad (\text{V.30})$$

Following the work of Li *et al.* on the buckling of a sedimenting vertical filament [37], we decompose the deformation y in a countable Fourier basis. The Fourier transform and inverse transform, on this interval, are given by

$$\tilde{y} = \sum_{\tilde{k}=-\infty}^{+\infty} \hat{u}_{\tilde{k}} e^{2i\pi\tilde{k}\tilde{x}}, \quad \hat{u}_{\tilde{k}} = \int_0^1 \tilde{y} e^{-2i\pi\tilde{k}\tilde{x}} d\tilde{x}. \quad (\text{V.31})$$

Inserting these expressions into equation V.30 returns an equation for the perturbation in the Fourier space,

$$-8(2i\pi\tilde{k})^4 \hat{u}_{\tilde{k}} \left(\frac{\Lambda}{\ell} \right)^3 + (\tilde{f}_{lat} + \tilde{T}_0) (2i\pi\tilde{k}) \hat{u}_{\tilde{k}} - \tilde{T}_0 (2i\pi\tilde{k})^2 \hat{u}_{\tilde{k}} + \tilde{T}_0 \hat{u}_{\tilde{k}} = \frac{\partial \hat{u}_{\tilde{k}}}{\partial \tilde{t}}, \quad (\text{V.32})$$

with Λ the elasto-viscous length (c.f. equation V.1), and $\hat{u}_{\tilde{k}}$ the Fourier transform of $\tilde{x} \frac{\partial^2 \tilde{y}}{\partial \tilde{x}^2}$:

$$\hat{u}_{\tilde{k}} = \int_0^1 \tilde{x} \frac{\partial^2 \tilde{y}}{\partial \tilde{x}^2} e^{-2i\pi\tilde{k}\tilde{x}} d\tilde{x} \quad (\text{V.33})$$

$$= \int_0^1 \tilde{x} \left[\sum_{\tilde{m}} (2i\pi\tilde{m})^2 \hat{u}_{\tilde{m}} e^{2i\pi\tilde{m}\tilde{x}} \right] e^{-2i\pi\tilde{k}\tilde{x}} d\tilde{x} \quad (\text{V.34})$$

$$= \frac{1}{2} (2i\pi\tilde{k})^2 \hat{u}_{\tilde{k}} + \sum_{\tilde{m} \neq \tilde{k}} (2i\pi\tilde{m})^2 \hat{u}_{\tilde{m}} \int_0^1 \tilde{x} e^{2i\pi(\tilde{m}-\tilde{k})\tilde{x}} d\tilde{x} \quad (\text{V.35})$$

By integrating by part equation V.35 we find

$$\hat{a}_{\tilde{k}} = \frac{1}{2}(2i\pi\tilde{k})^2\hat{u}_{\tilde{k}} + \sum_{\tilde{m} \neq \tilde{k}} (2i\pi\tilde{m})^2\hat{u}_{\tilde{m}} \frac{1}{2i\pi(\tilde{m} - \tilde{k})}. \quad (\text{V.36})$$

Considering the case of a fiber seeded with a perturbation with a single wavenumber \tilde{k} , assuming that there is no coupling between the Fourier modes, we have

$$\hat{u}_{\tilde{k}}(\tilde{t}) \sim \hat{u}_{\tilde{k}}(0)e^{\tilde{\sigma}\tilde{t}}, \quad (\text{V.37})$$

with $\tilde{\sigma}(k)$ the dimensionless growth rate of the mode \tilde{k} .

Inserting this ansatz into equation V.32 and neglecting the coupling terms, we obtain the growth rate,

$$\tilde{\sigma}(k) = -8 \left(\frac{\Lambda}{\ell} \right)^3 (2i\pi\tilde{k})^4 + (f_{lat} + \tilde{T}_0)(2i\pi\tilde{k}) - \frac{1}{2}\tilde{T}_0(2i\pi\tilde{k})^2. \quad (\text{V.38})$$

The first term on the right hand side of equation V.38 corresponds to a damping of the perturbation due to bending rigidity ($\propto -k^4$), the second term is imaginary and corresponds to the angular frequency of the oscillations (and leads to traveling of the perturbation) and the last term corresponds to a growth of the perturbation due to the filament compression ($\propto +k^2$).

The most unstable wavenumber \tilde{k}^* is given by

$$\left. \frac{\partial \text{Re}(\sigma)}{\partial \tilde{k}} \right|_{\tilde{k}^*} = 0. \quad (\text{V.39})$$

Solving equation V.39, we find

$$\tilde{k}^* = \frac{\tilde{T}_0^{1/2}}{4\pi} \left(\frac{\ell}{2\Lambda} \right)^{3/2}. \quad (\text{V.40})$$

This wavenumber correspond to the wavelength (in dimensional terms),

$$\lambda = 2\pi \sqrt{\frac{\mu u_0}{T_0}} (2\Lambda)^{3/2} = \frac{2\pi}{\sqrt{\tilde{T}_0}} (2\Lambda)^{3/2}. \quad (\text{V.41})$$

According to equation V.41, the most unstable wavelength is proporsionnal to $\Lambda^{3/2}$, and depends on the length of the fiber. These results are in opposition with what found experimentally i.e. $\lambda \propto \Lambda$ and λ independent of the length of the fiber. Thus, this description of the system does not describe our experiments, first it predicts that the instability occurs in the rear part of the fiber which is not what we observe experimentally (see Figure V.1) and second it does not give the measured scaling law for the wavelength.

V.5 Conclusion and perspectives

In this chapter, we have seen that a parallel fiber transported by an external flow in a confined geometry can experience an instability. We were able to monitor the instability

evolution as a function of time and we quantitatively characterized its properties. We have seen that the wavelength of the perturbation is constant with time and does not depend on the length of the fiber. Thus, we introduced another length-scale of the system: the elasto-viscous length Λ which compares elastic and hydrodynamic forces. We have shown that the wavelength is proportional to this elasto-viscous length, which thus, takes into account most of the physical ingredients of the problem. By looking at the evolution of the amplitude of the perturbation, we have shown that it increases exponentially as a function of time, enabling us to define an associated growth time. When this growth time is plotted as a function of (ℓ/Λ) , a critical value $(\ell/\Lambda)_c$ emerges. The closer (ℓ/Λ) to $(\ell/\Lambda)_c$, the larger the growth time, going to infinity when $(\ell/\Lambda) = (\ell/\Lambda)_c$. This is a signature of the existence of an instability threshold. This threshold has been highlighted by another independent experiment (see Figure V.9 (b)). Other quantities, such as the angular frequency of the oscillations and the traveling wave velocity - which corresponds to the phase velocity of the wave packet - have been investigated.

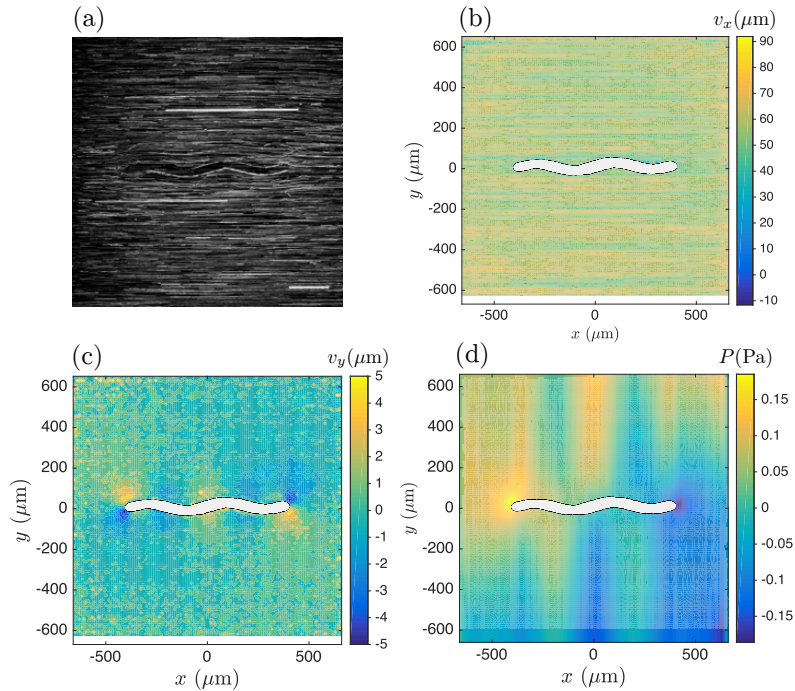


Figure V.14: Flow around a sine shaped rigid particle transported by an external flow of velocity $u_0 = 57 \mu\text{m}\cdot\text{s}^{-1}$. (a) Streaklines. (b) Flow velocity in the x -direction v_x , in the frame of reference of the laboratory. (c) Flow velocity in the y -direction v_y , in the frame of reference of the laboratory. (d) Pressure distribution minus the constant gradient in the (Ox) direction. It is obtained from the velocity field using the 2D Brinkman equation. The confinement is $\beta = 0.76$. Scale bar is $200 \mu\text{m}$.

We, then, attempted to describe the system in order to understand the origin of the instability. The models were set on a major assumption which was that the deformation of the fiber did not impact the flow around it. We started with a very simple model,

where the fiber was considered as infinitely long, and thus the forces per unit length are constant along it, and we showed that in this case there is no tension inside the fiber and consequently no source of instability. We then increased the complexity of the model by taking into account the finite length of the fiber, and we obtained a non-zero tension distribution (see Figure V.13). But once again, the tension distribution did not capture what we observed experimentally. It predicts the instability to occur in the rear half of the fiber, whereas in our experiments it occurs in the middle or slightly in the front part of the fiber. Moreover, the linear stability analysis carried out with this tension distribution gives wrong scalings for the wavelength of the perturbation.

Thus, it seems that our main assumption was too restrictive and we need to consider the impact of the fiber deformation on the flow. As illustrated in Figure V.14, a sinusoidal particle deforms the velocity field and the pressure field around it. Both fields show a sinusoidal perturbation with the same wavelength as the object. As a perspective, in order to couple the fiber deformation and the flow perturbation, we would like to describe the flow using the Brinkman equation and take into account the object deformation through the flow boundary conditions. In this description, the fiber would be considered as infinitely long and subject to a sinusoidal perturbation of wavelength λ . We are currently working on this description, and hope it will lead to a relation of dispersion where the growth rate as a function of λ shows a maximum which is positive resulting in an instability that corresponds to the experimental observations.

Chapter VI

Controlling transport dynamics of confined asymmetric fibers

As described in the previous two chapters, a flexible fiber changes shape while transported in a confined geometry and, as mentioned in chapter I, the coupling between the particle geometry and its dynamics can lead to complex trajectories.

Hence, in this chapter we focus on the role of the particle geometry, or more specifically on the role of its symmetry properties, on its trajectory. Unlike in the previous chapter, we bring our attention to the simple case of rigid fibers of complex shapes which can interact with the lateral walls of a channel in a transversally confined geometry. As mentioned in chapter I, transport properties of rigid particles in confining geometries show very specific characteristics as lateral drift or oscillatory movement between lateral walls. These dynamics result from viscous friction with transversal and lateral channel walls, inducing strong flow perturbations around the particles that act like moving obstacles. In this chapter, we modify the fiber shape by adding an additional, small fiber arm, which leads to T and L shaped fibers with only one or, respectively, zero symmetry axes and investigate their transport properties.

For this purpose, we combine precise microfluidic experiments, as presented in chapter II, and numerical simulations based on modified Brinkman equations (see chapter IV). This study is the results of collaborations with Camille Duprat from LadHyX and Marine Daëff, a former PhD student in the group, for the experiments, and with François Gallaire and Mathias Bechert from EFPL for the simulations.

We will see that, even for small shape perturbations, the transport dynamics change fundamentally and formerly stable configurations become unstable, leading to non-monotonous fiber rotation and lateral drift. Our results show that the fundamental transport dynamics change with respect to the level of fiber symmetry and particles that have different shapes but the same number of axis of symmetry have similar qualitative trajectories.

Thus, tuning the symmetry properties of a particle enables a precise control of particle trajectories which can in the further be used for targeted delivery, particle sorting or capture inside microchannels.

The study presented in the chapter have been published in [19].

VI.1 Motivation and experimental observations

Separating and filtering of particles or micro-organisms as a function of their properties such as flexibility, shape or activity is an important requirement for biomedical or food science applications. Micronscale filters, including micro-pillar arrays [5, 6, 7] are commonly used to sort particles with respect to their size or deformability, but face problems of filter clogging or damaging of deformable particles. Recently microfluidic devices, relying on specific transport properties, have been developed to overcome these difficulties [5]. Inertial [94, 6] or viscoelastic effects [95] can be used to focus particles at specific positions inside channels and flexible particles are known to migrate away from bounding walls, leading for example to a cell free layer as observed in blood flow [96] or migration of flexible fibers in shear gradients [80].

Some microorganisms use passive reorientation mechanisms to move in gradients, either in the gravitational field (gravitaxis)[25] or in a gradient of viscosity (viscotaxis)[97]. In simple unbounded flows, however, when inertia can be neglected, rigid particles migrate across streamlines only when symmetry is broken for example by particle chirality [98].

As we have seen in the chapter I, this situation changes when particles are confined by bounding walls and act as moving obstacles to the flow. The induced strong flow perturbation leads to particle migration, as for example lateral drift observed for rigid fibers even at small Reynolds numbers (see section I.3.1 of chapter I). In particular, it has been shown in section I.3.2 of chapter I, that axisymmetric objects such as fibers or symmetric dumbbells (made of rigid spheres or drops) translate without rotation but drift at a constant angle, and may oscillate between the lateral walls of the channel. Axisymmetric particles with fore-aft asymmetry, such as asymmetric dumbbells, will migrate toward the center of the channel, where they align with the flow [17, 31], while laterally unconfined, asymmetric trimers (chiral particles) rotate to reach an equilibrium angle [34] (see section I.3.2 of chapter I for more details). Flexible fibers may be deformed by the viscous forces and will then rotate and align with the flow as explained in chapter IV. In all these cases, the particle trajectory is strongly affected by the transversal confinement, which tunes the magnitude and distribution of the viscous force.

Note that, as mentioned in chapter I, this situation bears some similarities with sedimenting particles where a drag anisotropy exist as well, in particular, there exists a coupling between translation and rotation that depends on the particle geometry, and particles that possess certain symmetries will exhibit specific motions. For example, axially symmetric objects, such as uniform rods, keep their orientation and merely translate without rotating [10]; an axisymmetric object that presents a fore/aft asymmetry, such as a dumbbell composed of spheres of different sizes, will rotate and align with the flow [99]. An asymmetric particle, as for example an L shaped particle, will rotate until it reaches a stable orientation, at which it will translate without rotating [25]. If in addition the chiral symmetry is broken, the coupling of translational and rotational movement leads to helical trajectories [26, 27].

In the following we investigate these effects in detail by studying a model system consisting of a microfiber with increasing degrees of asymmetry transported in a microchannel. By adding a second arm to an initially straight fiber, we create and analyze,

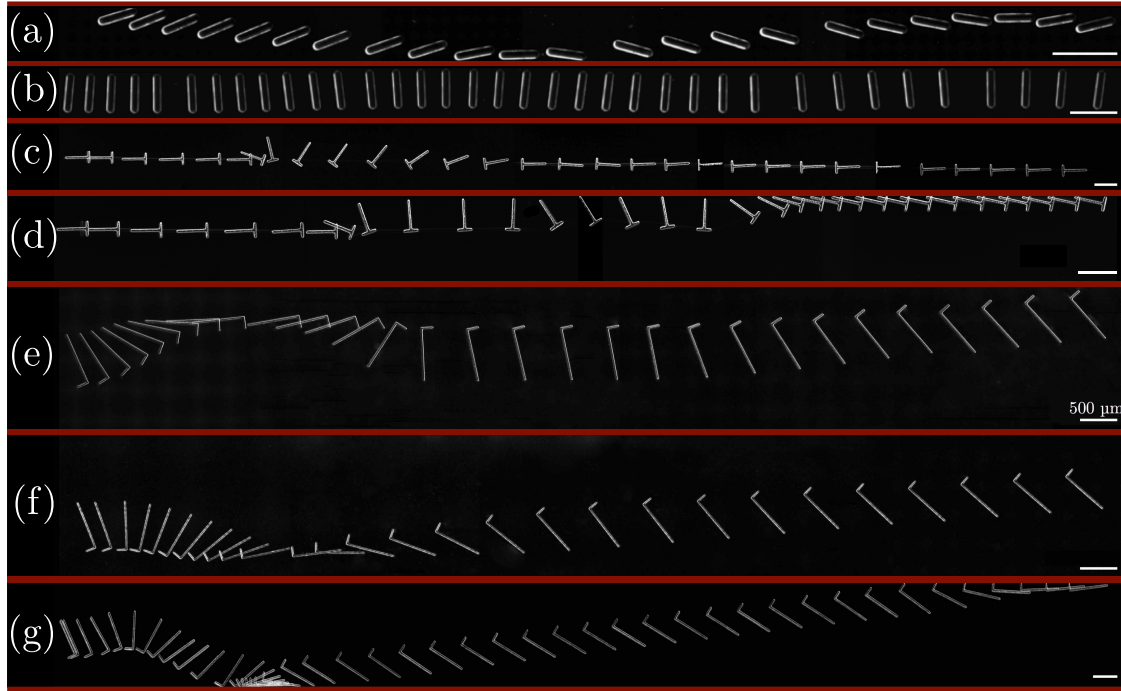


Figure VI.1: Experimental chronophotographies of transported fibers of different geometries. The fluid flows from left to right. The lateral walls are highlight in red. As reported previously, straight fibers oscillate in the channel either through glancing (a) or reversing (b) [30]. T-fibers away from the lateral walls reorient toward a stable orientation parallel to the flow direction (c) or are captured by the wall (d). L-fibers first rotate toward a stable orientation and then drift (e-g) until they are captured by the lateral wall (g). From top to bottom confinements are (a,b) 0.78, (c,d) 0.82, (e-f) 0.76, and (g) 0.72. Scale bars are $500\ \mu\text{m}$. Total length of the channels is typically 4 cm. The time interval between successive snapshots is constant for each panel and varies between 1 s and 7 s (such that the fiber is translated about its length between successive images).

both experimentally and theoretically, T-shaped fibers with fore/aft asymmetry and fully asymmetric L-shaped fibers. Fibers are fabricated using the stop-flow lithography technique presented in chapter II and their dynamics are described using the theoretical model presented in chapter IV. Examples of these fibers and corresponding chronophotographies of their transport dynamics are given in Figures VI.1 (c-g).

As mentioned in chapter I, straight fibers, which we will refer to as "I fibers" throughout this chapter, oscillate between the lateral channel walls while transported downstream (see Figures VI.1 (a,b)). The fiber rotation accompanying the oscillatory movement results from interaction with the lateral walls, i.e., away from these walls, the fiber does not rotate and merely drifts. In contrast, the interplay of the long and short arms of the T and L fibers induces rotation even away from the lateral walls. T fibers rotate in most cases until aligned with the flow, with the small branch at the tail, and remain parallel to the flow while slowly migrating toward the center of the channel (Figure VI.1 (c)). In some cases, due to the lateral confinement, the fiber is captured by the wall while it

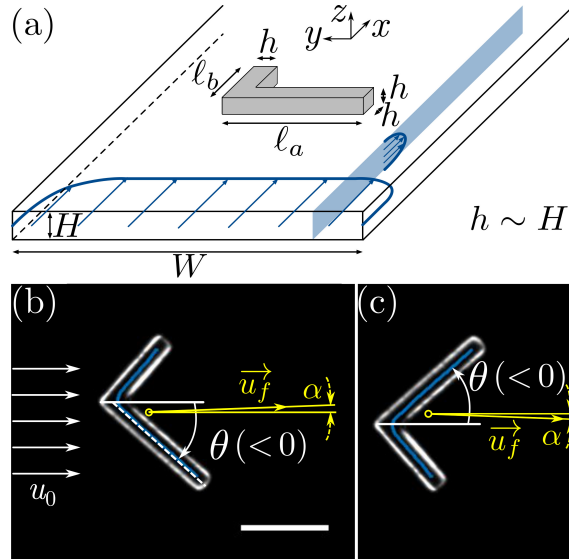


Figure VI.2: (a) Geometry of an L-shaped fiber in the channel. The pressure-driven flow is sketched in blue. (b - c) Image treatment and definition of angles. Using MatLab procedures we derive from the picture of the particle its skeletonized shape (blue) and its center of mass (yellow circle). The orientation angle θ is defined as the angle between the long arm length of the fiber and the flow direction and the drift angle α correspond to the angle between the direction of the particle center of mass velocity and the flow direction. Scale bar is 200 μm . (c) Mirror symmetry: mirror image of the fiber shown in (b).

reorients toward the aligned position (Figure VI.1(d)). L fibers rotate, either clockwise or anti-clockwise, until they reach an equilibrium angle which they keep while drifting toward the lateral wall (Figures VI.1 (e,f)). At the wall, two different scenarii can be observed. Fibers arriving with the sharp edge "rebound" off the wall, i.e. rotate until reaching their equilibrium angle and drift toward the opposite wall. Fibers arriving with the open side impact the wall and remain stuck at the wall (Figures VI.1 (e-g)).

In the following, we will focus on L shaped fibers, being the most asymmetric objects, and then complete the picture by full trajectory diagrams in the configuration space of I, T and L fibers, revealing the fundamental difference between these three types of fibers and symmetries.

VI.2 Problem formulation and methods

Figures VI.2 (a,b) depict the configuration of an L fiber in the channel. As in the previous cases (see: chapter IV and V), the fiber is of square cross section with width and height h , and l_a and l_b denote respectively the lengths of the long and short arms. We will refer to l_a/h and l_b/h as the non-dimensional lengths or aspect ratios of respectively the long and the short fiber arms, and quantify the asymmetry by l_a/l_b . The asymmetry parameter l_a/l_b is bounded by unity ($l_b = l_a$, symmetric fiber with two arms of equal length) and l_a/h ($l_b = h$, I fiber). Starting from $l_a = l_b$, the asymmetry is first enhanced when

decreasing the length of the short arm with respect to the long arm before the symmetry is restored when the short arm vanishes and a straight (I) fiber is attained.

The fiber is fabricated and studied in shallow channels with width W much larger than height H . We varied the aspect ratio of the channel W/H from 15 to 70. The fiber is created at rest in the channel. It is then subject to a pressure driven flow, fully characterized by its mean velocity u_0 . As we have seen in chapter IV and V, due to the Hele-Shaw-like geometry of the channel, the flow in the xy plane is a plug flow, and in the z direction the flow is Poiseuille-like. The transversal and lateral confinements of the fiber are quantified by $\beta = h/H$ and $\xi = \ell_a/W$, respectively. As the channel is assumed to be of infinite length, the state of the fiber is completely described by the lateral position of its center of mass y and the orientation angle θ , together with the corresponding velocities \dot{y} and $\dot{\theta}$. Moreover we define the drift angle α by $\tan \alpha = \dot{y}/\dot{x}$. Note that there exists a mirror symmetry and that the mirror image of the fiber shown in Figure VI.2 (b) corresponds to an opposite fiber chirality, shown in Figure VI.2 (c).

In order to have rigid particles, we used a photosensitive solution made from 90% in volume of PEGDA $M_n = 575$ g/mol and 10% of P.I. Its viscosity is $\mu = 68$ mPa · s. The Young's modulus of the particles is $E \sim 12$ MPa [41]. In the experiments we choose to tune the asymmetry ℓ_a/ℓ_b by changing the length of the long arm ℓ_a/h keeping the short arm length constant.

Due to the low value of the Reynolds number $Re \sim 10^{-3}$, inertia will be neglected implying also that the dynamics does not explicitly depend on the flow velocity.

To derive the equilibrium orientation of L fibers, we first tried to follow the calculations of Ten Hagen *et al.*, who described the situation of a sedimenting L fiber in a quiescent fluid [25] (see chapter I), and use an analogy between the drag anisotropy of a sedimenting fiber and the transport anisotropy of a confined fiber. In confined geometries, the velocity of the fiber is proportional to the velocity of the external flow (see chapter I). The coefficient of proportionality between the perpendicular or parallel velocity of the fiber and the external flow velocity is given by the condition of zero force on the particle. Similarly to Ten Hagen *et al.* [25], we described the L fiber as the sum of two rigid fibers corresponding to its two arms. However, it turns out that the analogy holds for an isolated straight fiber but drops for objects with more complicated shapes. Indeed, here, the zero force condition applies on the all L fiber and not on each of the two arms.

We, thus, chose to use the two-dimensional Brinkman model supplemented by the flow model in the gap between the fiber and the channel top and bottom walls, presented in the chapter IV, to determine the flow around the fiber and the resulting force and torque distribution. But here, contrary to what have been done in chapter IV, we consider that the force in the gaps between the particle and the channel top and bottom walls is constant i.e. the variation of the pressure along the object is not taken into account for the gap force. Note that the velocity vector is uniquely determined by the particular state (y, θ) , as inertial effects are negligible and the problem is thus reversible in time.

VI.3 Results

VI.3.1 Dynamics in laterally unbounded channel

We first focus on the equilibrium positions reached by the fiber far from the lateral walls, i.e. $\xi \rightarrow 0$ (infinitely wide channel). While for an I fiber all orientations are stable, i.e. the fiber keeps a constant orientation and translates without rotating, the L fiber reorients toward a stable orientation, and then drifts at a constant angle (Figures VI.1 (e-f)). We obtain numerically the evolution of the rotation speed $\dot{\theta} \ell_a / u_0$ as a function of θ for an asymmetric L fiber with $\ell_a/h = 10$, $\ell_b/h = 5$, for different transversal confinements $\beta = 0.6$, $\beta = 0.76$ and $\beta = 0.9$ (Figure VI.3 (a)). There are two fixed points separated by 180° : a stable one ($\theta = \theta_s = -47^\circ$) and an unstable one ($\theta = \theta_u = 133^\circ$). For all initial orientations, the fiber rotates monotonously until the stable orientation θ_s is reached. Note that close to the unstable orientation θ_u , a small variation of the angle can change the direction of rotation as depicted in Figures VI.1 (e,f); although both fibers start at very similar configurations ($\theta \simeq 130^\circ$), the first fiber is rotating counter-clockwise while the second is rotating in the opposite direction until they both reach the stable orientation.

The amplitude of $\dot{\theta}$ increases for increasing confinement, i.e., the reorientation of the fiber towards its equilibrium orientation is faster when the transversal confinement increases. For orientation angles close to the stable orientation angle θ_s , the evolution of $\dot{\theta}$ as a function of θ can be approximated by a linear function. The shaded region of Figure VI.3 (a) indicates this linear regime ($|\theta - \theta_s| < 30^\circ$), where the evolution of the orientation angle as a function of time is consequently expected to be exponential.

Figure VI.3 (b) shows the evolution of θ as a function of the dimensionless time tu_0/ℓ_a for three different confinements in the vicinity of the stable orientation angle θ_s . After some time, the orientation angle reaches a plateau, which corresponds to the equilibrium orientation θ_s . For increasing transversal confinement θ_s increases and the equilibrium orientation is reached faster, which can be explained by the higher rotation velocity as shown in Figure VI.3 (a).

The time evolution of the orientation angle can be fitted by an exponential saturation function:

$$\theta(tu_0/h) = (\theta_s - \theta_0) \left(1 - \exp\left(-\frac{tu_0}{\ell_a \tilde{\tau}}\right) \right) + \theta_0, \quad (\text{VI.1})$$

with $\tilde{\tau}$, and θ_s being the two fitting parameters, and initial orientation θ_0 .

Figure VI.3 (b) shows the fit (black curve) of the orientation angle evolution for the lowest confinement. The characteristic dimensionless time $\tilde{\tau}$ characterizes the dynamics of the particle orientation and depends on the fiber lengths ℓ_a/h , ℓ_b/h and on the transversal confinement. These dependencies are shown in Figure VI.3 (c), where $\ell_b = 5h$ in order to remain consistent with the experiments. In particular, we found that increasing the transversal confinement increases the rotation speed $\dot{\theta}$, i.e., the higher (lower) the transversal confinement, the faster (slower) the fiber approaches the stable orientation. On the contrary increasing ℓ_a leads to an increase of the characteristic time and thus slows down the approach of the equilibrium configuration.

We will use these results to determine experimentally θ_s , the stable orientation angle

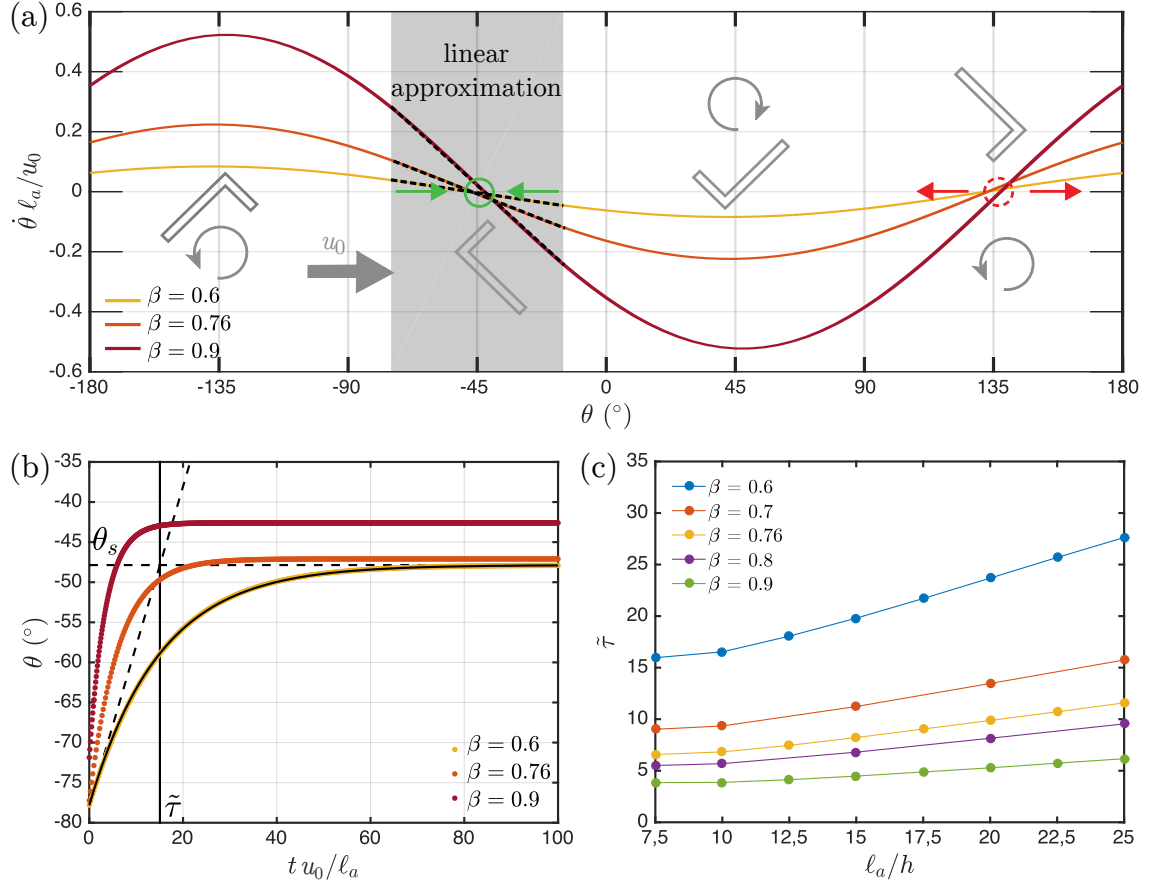


Figure VI.3: (a-b) Dynamics of orientation of an L fiber with $\ell_a/h = 10$ and $\ell_b/h = 5$ for different confinements $\beta = 0.6$ (yellow), $\beta = 0.76$ (orange) and $\beta = 0.9$ (red), as obtained from numerical calculations. (a) Evolution of the dimensionless rotation velocity $\dot{\theta} \ell_a / u_0$ as a function of the angle θ far away from the lateral walls. The green circle indicates a stable fixed point and the red circle an unstable fixed point. In the vicinity of the stable orientation angle θ_s , $\dot{\theta}$ depends approximately linearly on θ . (b) Evolution of the orientation angle as a function of the dimensionless time. The black curve corresponds to an exponential fit of the data using equation VI.1. From the fit one can determine the dimensionless characteristic time of the orientation process $\tilde{\tau}$. (c) Evolution of the dimensionless characteristic time as a function of ℓ_a/h for transversal confinements varying from 0.6 to 0.9. In all cases the short length of the fiber is kept constant $\ell_b = 5h$.

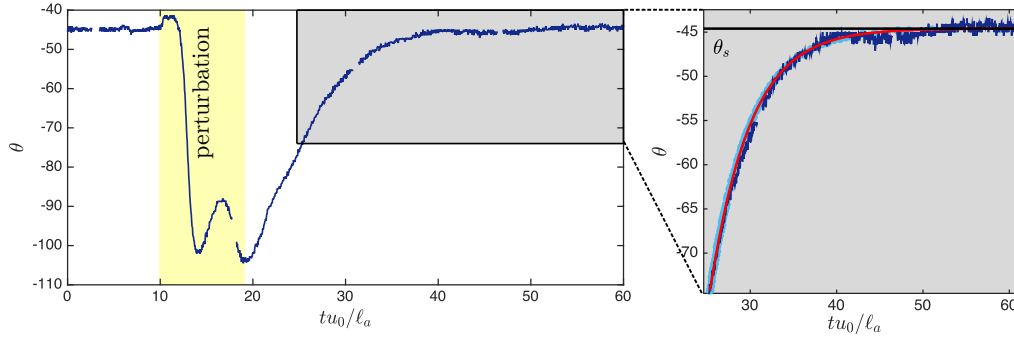


Figure VI.4: Experimentally observed evolution of the orientation angle θ as a function of the dimensionless time (dark blue) for an L fiber with $\ell_a/h = 7.5$, $\ell_b/h = 5$, and $\beta = 0.76$. A fiber initially in its equilibrium orientation hits an obstacle (yellow stripe) and deviates from the equilibrium orientation. It then rotates back to the latter. The reorientation dynamics close to the equilibrium orientation (grey area) are well adjusted by an exponential fit (red curve in the zoom). The calculated dynamics from the simulation is represented in light blue.

of a L fiber transported in an infinitely wide channel, using an exponential fit. For short fibers ($\ell_a/h < 12.5$ and $\ell_b/h = 5$) the influence of the lateral walls is negligible and the transient evolution of the orientation angle exhibits as expected an exponential evolution toward a plateau. For instance, Figure VI.4 shows the evolution of the orientation angle of a short fiber ($\ell_a/h = 7.5$ and $\ell_b/h = 5$) pushed out of the equilibrium orientation by an obstacle in the channel which rotates immediately back to the equilibrium position. The zoom on the left shows the superposition of this evolution obtained experimentally (dark blue curve) and in the simulation (light blue dots), as well as the exponential fit (red curve). The three curves show very good agreement, validating both the numerical results and the pertinence of the exponential fit.

For larger fibers, the orientation angle never reaches a plateau, which makes a direct measurement of the equilibrium angle impossible. Moreover, the fiber reorients with a longer characteristic time as compared to shorter fibers and drifts toward a lateral wall, which impacts the fiber trajectory and the orientation angle evolution. However, knowing the dimensionless characteristic time $\tilde{\tau}$, one can extrapolate the experimental observation of the orientation angle evolution. To distinguish the dynamics caused solely by to the particle shape (and the external flow) from those caused by an interaction with the wall, we fit a portion of the transient evolution of θ , corresponding to the situation where the fibers is far from the walls, by the exponential function (equation VI.1). We keep θ_s as a fitting parameter but set the value of $\tilde{\tau}$ to the one obtained numerically. This one-parameter fitting method allows us to extract the steady orientation angle from the experiments. Note that this procedure shows very good agreement between numerical results and experiments (see Figure VI.4) not only for the equilibrium angle, but also for the transient evolution, i.e., the characteristic time of reorientation $\tilde{\tau}$.

VI.3.2 Equilibrium orientation angle and drift angle

The stable orientation angle θ_s and the corresponding drift angle α_s are uniquely defined by fiber geometry and transversal confinement. Figure VI.5 shows both quantities as determined in the experiment for different lengths of the long arm ℓ_a/h , i.e. for varying asymmetry, and compared to the numerical results. While the drift angle varies only slightly in the examined regime, the stable orientation angle θ_s evolves non-monotonously with increasing length of the long arm ℓ_a/h : it first increases, reaches a maximum at $\ell_a/h \sim 7.5$, and then decreases again. A variation of the transversal confinement impacts both θ_s and α_s , as visualized by the gray shaded regions in Figure VI.5. While the effect of β is almost negligible for low confinement, for $\beta > 0.6$ the orientation and drift angles increase rapidly with increasing confinement.

In order to obtain a general overview of the dependence of θ_s and α_s on the fiber geometry, we systematically compute these quantities in the parameter space $(\ell_a/h, \ell_b/h)$ and visualize the results in a map as shown in Figure VI.6. Due to symmetry, we restrict the space to $\ell_a \leq \ell_b$ and combine the two maps for α_s (top) and θ_s (bottom) in one. The black line corresponds to $\ell_a = \ell_b$, where the fiber is symmetric and is transported with $\theta_s = -45^\circ$ along the flow direction, i.e. $\alpha_s = 0^\circ$. For $\ell_a > \ell_b$ the L fiber is fully asymmetric as long as $\ell_b > h$, and the map of stable orientations θ_s can be divided into two distinct regions. For large values of the aspect ratios ℓ_a/h and ℓ_b/h , the isolines of constant θ_s approach straight lines i.e. θ_s depends on the asymmetry ratio ℓ_a/ℓ_b only and is independent of the fiber height h and thus the fiber aspect ratios. In this region, increasing asymmetry (ℓ_a/ℓ_b decreasing) leads to a decrease of θ_s , as evidenced by the white dots and the corresponding fiber shapes.

At small values of the aspect ratios (≤ 10), the isolines exhibit a different tendency: changing ℓ_a or ℓ_b while keeping ℓ_a/ℓ_b constant leads to different values of θ_s , i.e. θ_s depends not only on the fiber asymmetry, but also on the fiber aspect ratios. Keeping for example ℓ_b/h constant and changing ℓ_a/h (red dots in Figure VI.6), as we did in the experiments shown in Figure VI.5, leads to a non-monotonous evolution of the orientation angle. The crossover between these two regimes can be evidenced by following the isoline for $\theta_s = -46^\circ$ (black dots and corresponding shapes). Along this line, the fiber shape first changes significantly at small fiber arm aspect ratios, but finally reaches an homothetically similar shape at large values of the aspect ratio.

For asymmetric fibers, which form an angle θ_s with the flow direction, there is a lateral drift whose magnitude depends on a combination of both equilibrium angle and asymmetry. For a fixed ℓ_b/h , changing ℓ_a/h (red dots) leads to a small change in drift angle although the orientation angle varies significantly. On the contrary, for a given orientation (black dots), changing the shape leads to a significant change in drift angle. In the limit of large fiber arm aspect ratios, changing the asymmetry ℓ_a/ℓ_b (white dots) leads to significant variations in orientation and drift angle.

These findings demonstrate, at least for small fibers aspect ratios, that it is not possible in general to rationalize the fiber transport using only the fiber asymmetry ℓ_a/ℓ_b , but that the two-dimensional geometry of the fiber has to be taken into account instead of a one-dimensional skeleton.

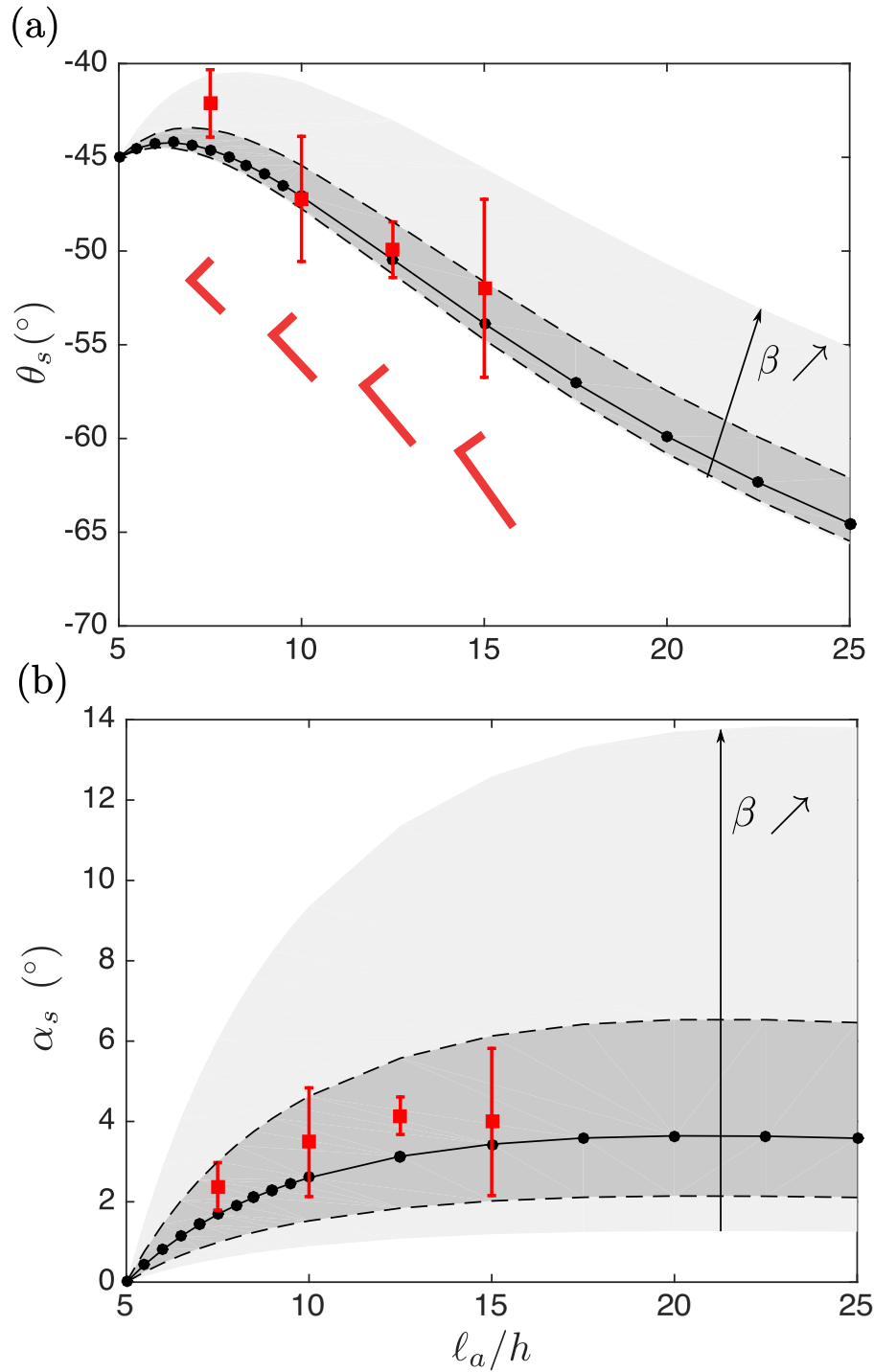


Figure VI.5: Stable orientation angle θ_s (a) and corresponding stable drift angle α_s (b) as a function of the long arm aspect ratio ℓ_a/h , for $\ell_b/h = 5$. Red squares show experimental measurements, black circles correspond to numerical calculation with a transversal confinement of $\beta = 0.76$. The two grey shades correspond to the numerically determined variations for $\beta = 0.76 \pm 0.08$ and $\beta = 0.76 \pm 0.16$ respectively. The error bars correspond to the standard deviation of the measurements.

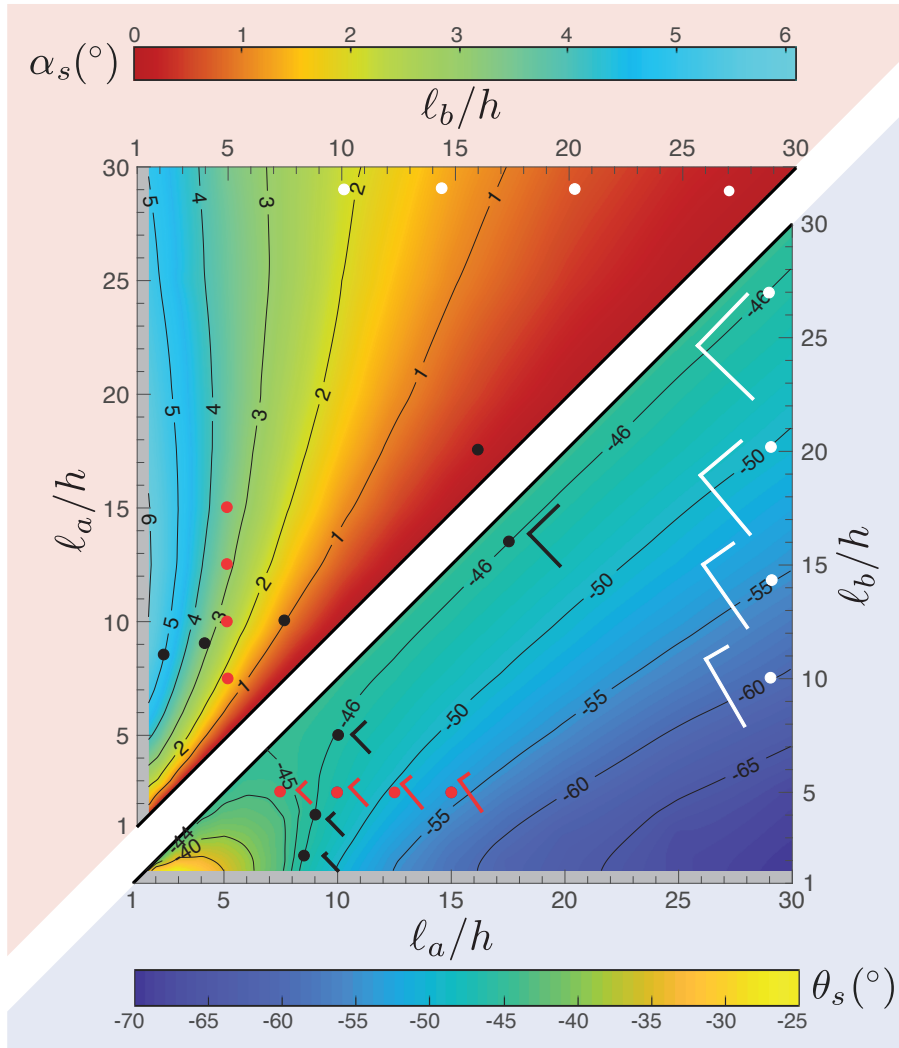


Figure VI.6: Numerically determined isolines of constant stable orientation angle θ_s (bottom right corner) and constant stable drift angle α_s (top left corner) as a function of the fiber arm aspect ratios l_a/h and l_b/h . Both maps are symmetric around the black line defined by $l_a = l_b$, where $\theta_s = 45^\circ$ and $\alpha_s = 0$. Numerically inaccessible regions are shaded in gray.

VI.3.3 Trajectories and impact of the lateral walls

In the presence of lateral walls, the overall fiber trajectories are given by a combination of rotation toward θ_s , drift, and interaction with the lateral walls. For a more global view, we plot the trajectories in the configuration space spanned by θ and y for I, T and L fibers in Figure VI.7. The experiments (right panel) are obtained for a range of parameters (transversal confinement $0.7 \leq \beta \leq 0.8$, lateral confinement $0.12 \leq \xi \leq 0.8$, and long arm aspect ratio $10 \leq \ell_a/h \leq 20$). In the left panel, we present the fiber trajectories obtained numerically for a single set of parameters ($\xi = 0.5$, $\beta = 0.76$ and $\ell_a/h = 10$) for qualitative comparison. The qualitative trends are well reproduced; differences may arise from the different values of the lateral confinement ξ as will be discussed later.

As already discussed in chapter I, I fibers show mostly permanent lateral oscillations, clockwise around the fixed point at $\theta = 0^\circ$ (red trajectory, Figure VI.1(a)) or anti-clockwise around the fixed point at $\theta = \pm 90^\circ$ (green trajectory, Figure VI.1(b)) except if they are located very close to the wall (blue trajectory).

If we reduce the level of symmetry by analyzing a T shaped fiber, the picture changes significantly. The stable fixed points at the center of the channel for $\theta = 0^\circ, \pm 90^\circ, \pm 180^\circ$ are reduced to one at $\theta = 0^\circ$. Apart from trajectories ending at this configuration (red trajectory, Figure VI.1(c)), there are also attracting points at the lateral channel walls (blue and green trajectories, the latter corresponds to Figure VI.1(d)). While approaching these final positions, the T fiber may exhibit non-monotonous lateral movement as it is rotating. Moreover, the interaction with the lateral walls can lead to a change of rotation direction, as two of the four unstable fixed points observed for I fibers are still present (highlighted by red dots in Figure VI.7). The green trajectory (Figure VI.1(d)) corresponds to an example of such a non-monotonous evolution of the orientation angle.

For the fully asymmetric L fibers, the centrally located fixed points finally disappear completely and the only permanent configurations correspond to the fiber being captured by one of the walls, with the sharp edge pointing toward the channel center. Even though there exist trajectories pointing away from this configuration, they finally lead back to it and the fiber cannot escape. The stable and unstable orientations observed without lateral confinement do not appear as fixed points, as they lead to lateral drift, but as ridges with the trajectories either leading away from them (unstable orientation) or attracting to them (stable orientation). In other words, after rotating toward its stable orientation, the L fiber drifts toward the wall where it will remain stuck. In some cases (light red area), the fiber is captured by the opposite wall during the reorientation. We highlight the trajectories of the three cases presented in Figure VI.1 (e-g). The fiber, initially close to the unstable orientation, leaves the orientation by rotating either clockwise (green curve, Figure VI.1 (e)) or anti-clockwise (red curve, Figure VI.1 (f)) to reach equilibrium. When approaching the wall with the sharp edge toward it (blue curve, Figure VI.1 (f)), the fiber is first repelled, rotates until reaching its equilibrium angle, and finally drifts across the channel width to reach the top wall where it will remain. Note that for a mirrored fiber of opposite chirality, there exists a mirror-symmetric diagram where most fibers collect at the opposite wall.

For T and L fibers, we can quantify the percentage of fibers being trapped at one of the channel walls or localized at the channel center. The corresponding sets of initial configurations which end up in the channel center (light green) or at the walls (light red or

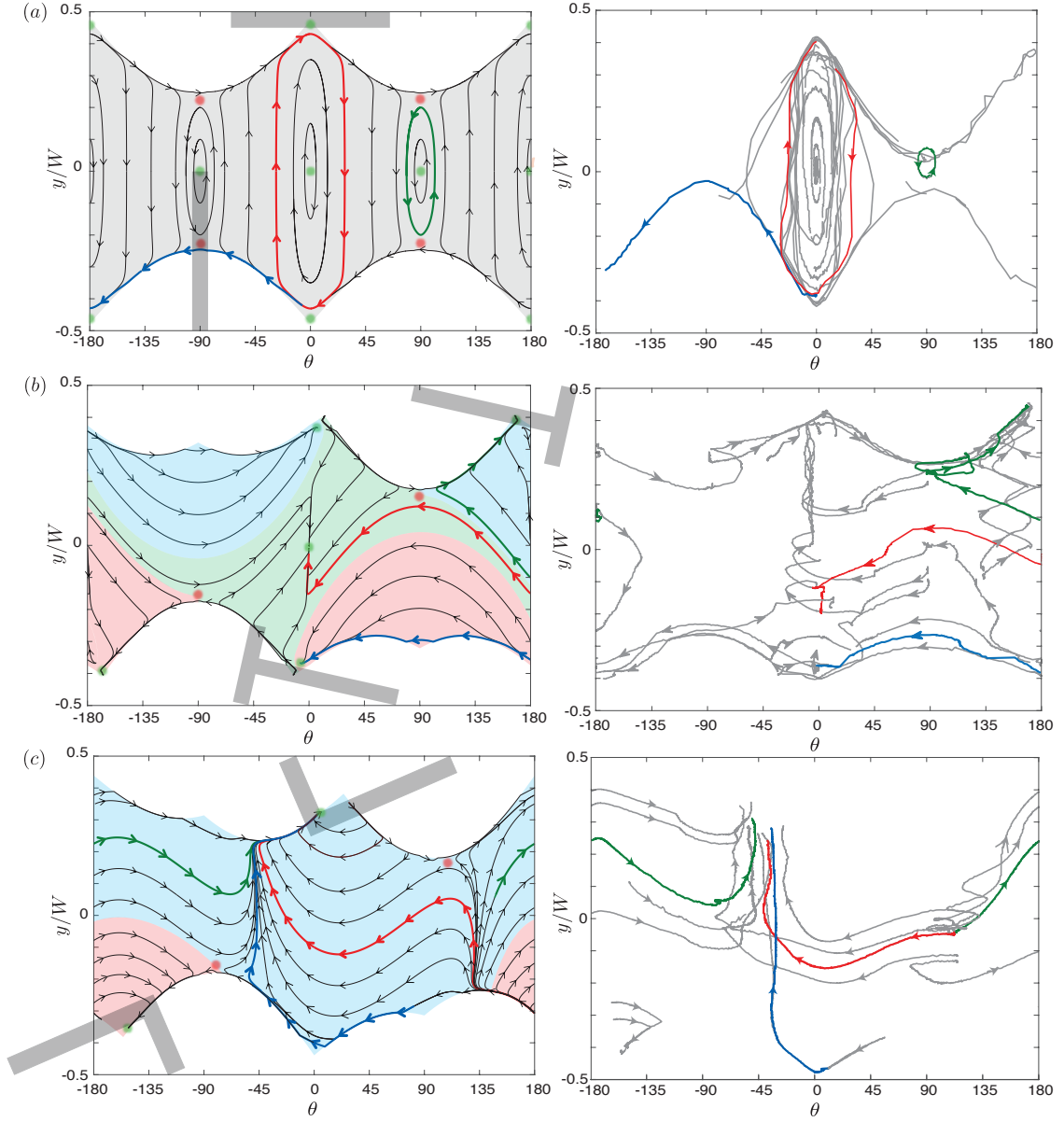


Figure VI.7: Trajectory map in the configuration space spanned by orientation angle θ and lateral position y for (a) an I fiber, (b) a T fiber, and (c) an L fiber for numerics (left) and experiments (right). The physical accessible space is shaded in color. For T fibers, the space of trajectories ending at the channel center is shaded in light green. The space of trajectories ending at the wall at $y = 0.5$ (resp. $y = -0.5$) is shaded in light blue (resp. light red). Stable and unstable fixed points are highlighted in green and red, respectively. Experiments: transversal confinement $0.7 \leq \beta \leq 0.8$, lateral confinement $0.12 \leq \xi \leq 0.8$, and arm lengths $10 \leq \ell_a/h \leq 20$, $\ell_b/h = 5$. Numerics: Long arm aspect ratio $\ell_a/h = 10$, lateral confinement $\xi = 0.5$ and transversal confinement $\beta = 0.76$. The short arms of the T and L fibers have half the length of the long arm, i.e., $\ell_b/h = 5$. Some numerical and experimental trajectories are highlighted for comparison.

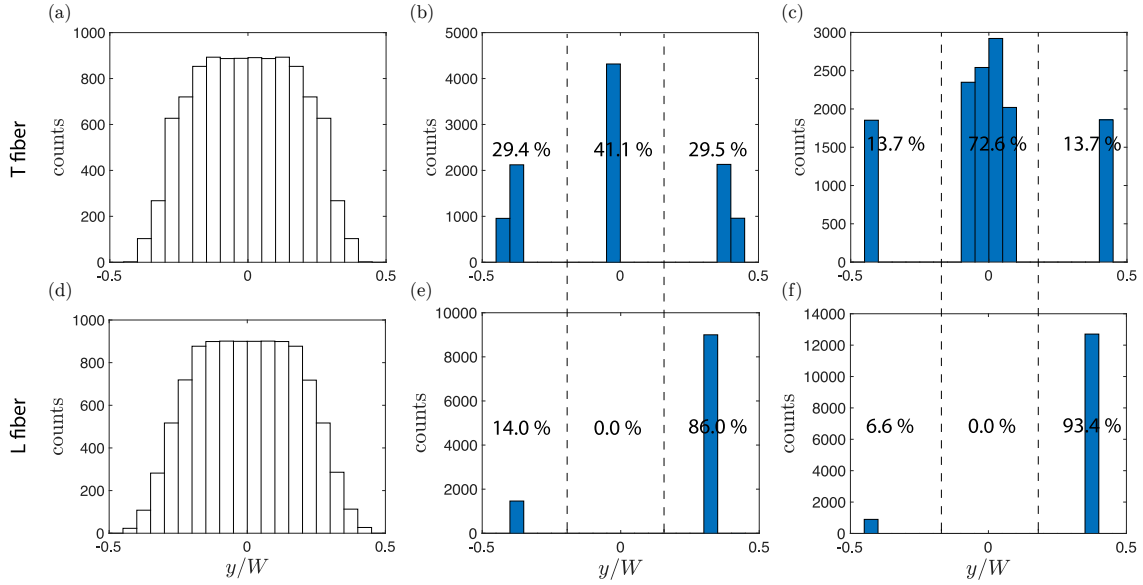


Figure VI.8: Distribution of lateral position in the channel for T ((a)-(c)) and L ((d)-(f)) fibers: Initial distribution for $\xi = 0.5$ (a) and (d), and distribution after $L = 10^3 \ell_a$ for (b) and (e) $\xi = 0.5$ and $\xi = 0.3$ for (c) and (f).

blue) are highlighted in Figure VI.7. Consequently, the areas of these regimes represent the statistical probability of finding a fiber with random initial orientation and lateral position at the channel center or wall.

An other way of quantification of these probabilities sets on the calculation of the trajectories of T and L fibers for at least 10^4 initial configurations equally distributed in the configuration space. Figures VI.8 (a) and (d) show the distribution in lateral position for, respectively, T and L fibers and for a lateral confinement of $\xi = 0.5$. We then analyze the distribution after transportation in a channel of length $L = 10^2 - 10^3 \ell_a$ for lateral confinements $\xi = 0.5$ (Figure VI.8 (b) and (e)) and $\xi = 0.3$ (Figure VI.8 (c) and (f)).

As shown in Figure VI.8 (b), for a lateral confinement of $\xi = 0.5$ (corresponding to the situation of Figure VI.7), approximately 40% of the T fibers end in the channel middle and the rest are captured by the lateral walls. Looking at the trajectories ending at the walls (Figure VI.7 (b)), we can see that they correspond to the case where the fiber is captured by the wall during reorientation toward the central position (Figure VI.1(d)). This means that we can tune this ratio by varying the lateral confinement ξ . In fact, for $\xi = 0.3$, we find approximately 73% of the fibers in the channel center (see Figure VI.8 (c)). Decreasing the lateral confinement thus increases the probability of finding a T fiber in the middle of the channel. It has to be noted, however, that close to the end points at the walls, there exist trajectories which lead away again from the wall. Assuming some experimental noise, this can easily lead to a higher amount of fibers finally ending in the channel center than obtained from a noise-free theoretical study.

By doing the same analysis with L fibers (Figure VI.8 (d): initial configuration for $\xi = 0.5$, (e): final configuration for $\xi = 0.5$, and (f): final configuration for $\xi = 0.3$), we can see that most of them end at the same lateral wall (approximately 86% for $\xi = 0.5$,

light blue area in Figure VI.7 (c)), which is determined by the sign of drift angle at stable orientation of a fiber without lateral confinement. Analogue to the T fiber, the partition of fibers being captured by the opposite wall can be reduced (increased) by decreasing (increasing) the lateral confinement (approximately 93 % fibers at one wall for $\xi = 0.3$).

VI.4 Conclusion

These findings show that it is possible to control the lateral position of fibers transported in confining micro-channels by tuning their geometry, in particular their symmetry properties, and/or the lateral confinement, i.e. the channel width.

As mentioned in the chapter I, I fibers (two axes of symmetry) are mostly laterally oscillating, or tend to end in the channel center due to small imperfections (damped oscillation in the case of small fore/aft asymmetry). Note that these damped oscillations are also observed for flexible perpendicular fibers (see chapter IV). T fibers (left/right symmetry, fore/aft asymmetry) are either pushed toward the channel center or toward the lateral walls, depending on the level of lateral confinement. Similar observations have been reported by Uspal *et al.* for fore/aft asymmetric "dumbbell" particles [17] (see chapter I). On the contrary, L fibers (fully asymmetric) are always captured by the lateral walls. Depending on their chirality being left- or right-handed, most of the fibers end hereby at one or the other wall. This is in contradiction with the numerical study of Bet *et al.* [34], presented in chapter I, where authors state that fully asymmetric particles reach an equilibrium orientation which is not accompanied by a drift.

The reorientation time, i.e., the time needed to reach the equilibrium orientation in the absence of lateral walls, strongly depends on the transversal confinement β but is typically $\tau \sim 10 - 100\ell_a/u_0$ (see Figure VI.3 (c)), indicating that a fiber reaches its equilibrium position after traveling a few tens of its length. For fibers of length $\ell_a \sim 100 \mu\text{m}$, equilibrium is thus reached after a few centimeters. In addition, for laterally confined channels, starting from a broad initial distribution, all fibers have reached the end point of their trajectories (at the wall or at the center of the channel) after $100-1000\ell_a$ (see Figure VI.8). Typically, a channel of length 4 cm is sufficient for fibers to reach their final configuration (Figure VI.1). This dynamics can be tuned by adjusting both transversal (β) and lateral (ξ) confinements. The presented results thus open new doors toward the design of sorting devices or filters as a function of, for example, micro-organism shape. In addition they can be used to design targeted delivery or particle capture applications in microfluidic devices.

Chapter VII

Conclusion

In this thesis, we studied the dynamics of freely transported isolated fibers in a confined geometry. We focused on the dynamics of free flexible particles, whose shape varies while transported and on the role of the geometry of a rigid particle on its trajectory.

These situations correspond to simple model systems, which can be further used, as building blocks, to describe more complex fluid-structure interaction problems where other ingredients, such as activity or complex fluids, are involved.

We hope that the understanding of our model situations can, for instance, help in the description of the dynamics of optical fibers that are introduced into rock fractures as *in situ* probes in the oil industry. Also, the study of the deformation of flexible fibers can shed light on the description of the locomotion and transport of microorganisms in soils or in medical conducts. Moreover, our study provides insights into the sorting of particles based on their shape or flexibility which is of fundamental interest in the biomedical field or in the food industry.

We used a microfluidics system, combining in a single experiment the fabrication and the flow of particles. Recently developed soft-lithography techniques have been used to fabricate microchannels of adjustable geometry with an excellent control of the (laminar) flow. A technique, based on the photo-polymerization of an oligomer, has been used to fabricate hydrogel particles directly inside the micro-channel. This technique enables the fabrication of objects of rectangular cross section in a confined geometry: we used Hele-Shaw-like cells, where a two dimensional flow develops, and the particles are confined by the top and bottom walls. Complementary to the standard "stop-flow lithography technique" we develop a second method of fabrication of particles which takes advantage of the use of a motorized microscope stage. The combination of these two methods allowed us to fabricate particles of very different shapes with an excellent control of their positions, their orientations but also of their mechanical properties. Indeed, we implemented a reliable protocol of fabrication of soft hydrogels: instead of varying the duration of the photosensitive solution illumination, we dilute the oligomer with varying proportions of solvent. We chose either water or a non-reactive oligomer solution as the solvent to be able to adjust the its viscosity. Characterizing the mechanical properties of the hydrogels, we realized that measuring the Young's modulus of soft hydrogels is extremely complicated. We thus decided to develop an *in situ* measurement inspired by compression tests. With this method Young's moduli as low as few tens of kPa can be measured directly inside

the microchannel. We also develop an *in situ* technique of measurement of the Poisson's ratio of hydrogels, and applied it to hydrogels of different compositions. This way, we could show that the Poisson's ratio decreases from 0.5 to 0.165 when diluting the oligomer solution with 0% to 50% of PEG₁₀₀₀-water solvent in volume.

We experimentally and numerically - using a model based on the resolution of the Brinkman equation supplemented with a gap flow model - investigated the transport of an isolated flexible fiber in a confined geometry. A first study focussed on the dynamics of a fiber oriented perpendicular to the flow direction. We showed that while the fiber is transported it bends into a C-shape. This bending is due to the finite length of the fiber and the resulting non-homogeneous force distribution along the slender object. When the fiber is confined, its velocity is smaller than the velocity of the surrounding fluid. As a consequence, the object acts as a moving obstacle and a maximum of the pressure difference (between the front and the back of the fiber) is observed in the middle of the slender object leading to a C-shape deformation. Moreover, we have shown that the amplitude of the deformation is proportional to an elasto-viscous number, which compares the hydrodynamic forces to the elastic restoring forces. We also quantitatively characterized the influence of the confinement on the fiber deformation and evidenced the fact that increasing confinement increases the deflection of the fiber. Indeed, increasing the confinement decreases the height of the gap between the fiber and the channel top and bottom walls and increases the pressure difference leading to larger deformations. We hope the precise understanding of the deformation of a flexible fiber in a confined geometry can pave the way to the understanding of the deformation and transport of more complex deformable particles in confined flows, as for example vesicles or red blood cells. Last, we also noticed that the perpendicular configuration is unstable and the fiber reorients until it aligns with the flow direction.

Then, we studied the situation of a parallel fiber transported in similar flow and channel geometries. Under certain conditions, while the fiber was transported by the external viscous flow, it experienced an instability resulting in a deformation of the fiber in a sine shape flatten at the edges. We were able to monitor the instability, and quantitatively characterize its wavelength, the dynamics of the amplitude, its angular frequency and the velocity of the traveling waves. We have shown that the wavelength does not depend on the length of the fiber and is proportional to an elasto-viscous length, constructed by dimensional analysis. Even if the wavelength does not depend on the length of the fiber, the length triggers the instability onset. Indeed, we highlighted the existence of an instability threshold, expressed as a critical ratio of the fiber's length over the elasto-viscous number. In order to understand the origins of the instability, we tried to model the hydrodynamic forces acting on the fiber. We assumed that these forces were the same as the ones acting on an undeformed fiber, i.e. we did not take into account the impact of the fiber deformation on the flow. However, the model derived did not describe the experimental observations correctly. Thus, it seems that one needs to take the impact of the fiber deformation on the flow into account to describe the instability. We are currently working on a description of the flow around an infinitely long fiber with an sinusoidal perturbation using the Brinkman equation and we hope to be able to correctly capture the local instability.

After studying the dynamics of objects whose shape changed while transported, we focussed our investigations on the impact of the particle geometry on its trajectory. We chose to look at model system consisting of rigid particles of complex shape and we primarily focussed on L fibers, two dimensional chiral objects without any axis of symmetry. The dynamics of such objects are very rich: far from lateral walls the fiber rotates until it reaches an equilibrium orientation and then drifts. We characterized, both experimentally and numerically (using the modified Brinkman equation), the evolution of the equilibrium orientation angle and of the drift angle as a function of the fiber geometry and of the confinement. We also describe the dynamics of rotation of these fibers when they are close to the equilibrium orientation and we showed that the characteristic time of rotation toward the equilibrium configuration is an increasing function of the length of the fiber and a decreasing function of the confinement. We then investigated the dynamics of straight fibers, T fibers and L fibers in laterally confined geometries. The observed trajectories were different for each fiber geometry. A straight fiber, with two axes of symmetry, oscillates along the channel length, a T fiber, with one axis of symmetry, rotates until it aligns with the flow direction in the middle of the channel or is captured at a channel wall during the rotation if the lateral confinement is large and an L fiber is always captured at one of the channel walls. Depending on the chirality of the object, most of the L fibers are captured at one or the other channel wall. A possible application could be the design of a microfluidic tool to sort particles (as for example micro-organisms) based on their symmetries.

This PhD work led to two published papers, one on the transport of flexible perpendicular fibers [18] and one on the dynamics and the trajectory of asymmetric rigid particles [19]. A manuscript on the development of the Poisson's ratio measurement method is currently in preparation. The study on parallel flexible fiber is an on going work and we would like to fully understand the origin of the instability before considering publication.

In the future, we would like to study the lubricated friction between the hydrogel and the PDMS walls. Indeed all movement of a compressed hydrogel particle in a microchannel implies friction between the particle and the PDMS surrounding walls. In our models presented in chapter III we neglected friction arguing that the latter depends on the hydrogel velocity and is zero when the hydrogel does not move. In order to verify this statement, with the help of Vincent d'Herbement, intern in the group, we performed some preliminary experiments to investigate friction between a moving hydrogel disk and two lateral PDMS walls. The hydrogel disk of initial diameter D and height h was transported by an external flow in a rectangular cross section channel of width $W < D$ and height $H > h$. The experiment was very similar to the one used for the measurement of Poisson's ratio of hydrogels presented in chapter III, the only differences were the geometry of the particle (disks instead of rectangular slabs) and the fact that after passing through the constriction the compressed hydrogel was forced to travel along the channel by applying a pressure difference. Measuring the velocity of the disk V for different pressure differences applied across the particle ΔP we obtained the results shown in Figure VII.1. We observe that even for low pressure differences the particle moves. The absence of a pressure threshold above which the hydrogel starts to move implies the absence of solid

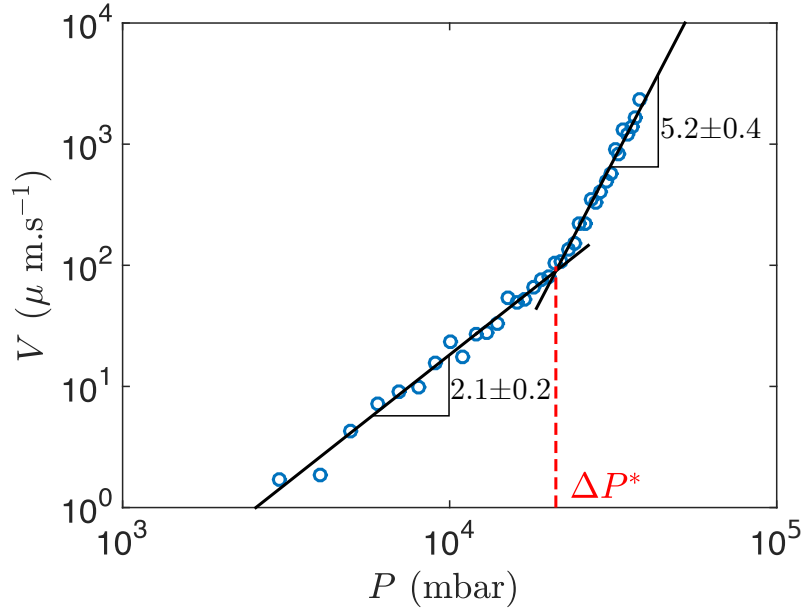


Figure VII.1: Velocity of a compressed hydrogel disk in a narrow channel as a function of the imposed pressure difference in log-log scale. One can observe two regimes: for $\Delta P < \Delta P^*$, $V \propto \Delta P^2$ and for $\Delta P > \Delta P^*$, $V \propto \Delta P^5$.

friction between the particle and the side walls. Two regimes are visible in Figure VII.1: for low pressure differences the particle velocity is proportional to ΔP^2 and for large pressure differences $V \propto \Delta P^5$. The first regime could be seen as a signature of elasto-hydrodynamic friction where the friction force is proportional to the velocity at a power $1/2$ [100, 101]. In our case friction is balanced by the pressure force applied on the disk leading to $\Delta P h W \propto V^{1/2}$ and thus $V \propto \Delta P^2$. The cross-over between these two regimes is obtained for a pressure difference $\Delta P^* \sim E = 27 \pm 7$ kPa, with E the Young's modulus of the hydrogels. Note that according to Li *et al.* [58], for pressure differences comparable to the Young's modulus of an hydrogel flow starts to occur through the pores of the hydrogels.

The origin of the power coefficient 5 remains unclear. It could be due to poroelastic effects or to the complex deformation of the hydrogel due to the applied pressure difference and the compression by the channel lateral walls.

These are promising results yet we realized that the geometry used for the particle was not ideal. Indeed uniaxial compression of a disk, known as Brazilian test [37, 102], leads to complex strain and stress distributions inside the material and thus the role of elasticity is difficult to quantify. An option could be to carry out similar experiments, with rectangular particles and vary the width and thus the compression of these particles.

In this PhD, we limited ourselves to the study of the transport dynamics of isolated fibers but the study of fibers suspensions will also be of great interest. Such complex fluids are expected to have non-Newtonian properties reflecting the interactions at a microscopic scale between the suspending fluid and the suspended objects. They will

depend on the geometry and the elastic properties of the suspended objects. Indeed, under flow the fibers may reorient, deform and even create topological entanglements, leading to a macroscopic response of the material [50]. In particular, the theoretical study of Becker *et al.* [48] predicts that the buckling of individual fibers under shear leads to the macroscopic appearance of normal stresses. Moreover, it has been shown theoretically by Banaei *et al.* that at finite inertia the first normal stress increases with the Reynolds number [103]. They also evidence that the relative viscosity of the complex suspension depends on both the fiber flexibility and the Reynolds number [103].

In this manuscript, we presented several techniques to control and characterize the fibers properties (geometry and flexibility) that are of paramount importance in order to establish a link between the macroscopic properties of suspension made of these objects and their microscopic properties. Moreover, increasing the characteristic size of our experiment, we could extend the range of possibilities and explore the rheology of complex suspensions at finite inertia.

In summary, we believe that our model investigation of flexible and complex-shaped individual particles in confined flows, paves the way not only for promising applications but also opens numerous novel fundamental questions.

Appendix A

Microfluidic channel fabrication

A.1 Fabrication of the channel mold

We use standard soft lithography methods to fabricate the negative mold of the microfluidic channel. The main steps of the fabrication process are sketched in Figure [A.1](#).

We design the mask using the softwares Clewin or Adobe Illustrator and we print these masks using the maximal resolution available (2400 dpi) at Institut Pierre Gille de Gennes (IPGG) or in the FGN company. Once the masks are printed we fabricate the molds of the microfluidic channels in the clean room of IPGG. Two options are available to fabricate the molds. The first one consists of spin-coating a negative photoresist (SU8 20XX series, MICROMECH) onto a silicon wafer previously cleaned using isopropanol and ethanol and baked at 200°C for 10 minutes. The second option uses the dry film lamination technique: we deposit a dry film of well defined thickness directly onto the wafer instead of spin-coating the resin. After the spin-coating step or the film lamination, the wafer is soft baked at 65°C and 95°C. The wafer is then placed in a mask aligner where it will be exposed to UV-light (365nm) through the lithography mask. Only the region corresponding to the transparent areas of the mask will be exposed. The exposing step is followed by the curing of the resin - named post bake - which consists of placing the wafer on the hot plates at 65°C and 95°C once again. After the post bake step the wafer is placed in a bath containing a developer (PGMEA, Propylene Glycol Monomethyl Ether Acetate), which dissolves the resin that has not been exposed to UV-light. As a result, we obtain a channel mold presenting positive relief. The two dimensional geometry corresponds to the mask shape and the height is defined by the choice of the photoresist, the rotation speed of the spin-coating and the duration of soft and hard bake for the first technique and by the choice of the film height in the second. A last bake of the wafer at 200°C during 15 minutes is needed in order to remove any solvent which can be still present in the cured resist.

After fabrication, the height of the molds are measured using either a mechanical profilometer (Veeco Dektak 6M) or an optical profilometer (Veeco Wyko NT9100). The accuracy of the measurement is in the order of 1µm.

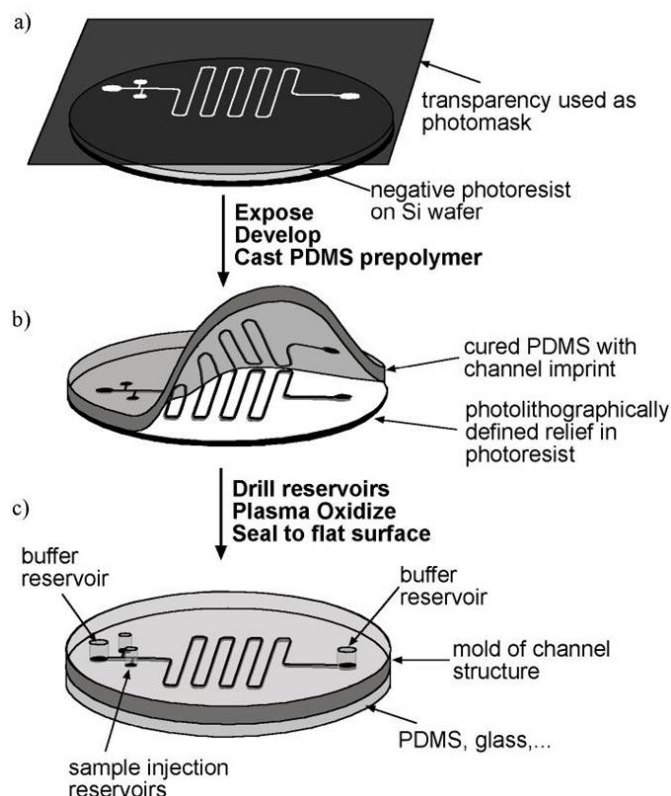


Figure A.1: Sketch of the main steps of the microfluidic channel fabrication. (a) Fabrication of the mold by illuminating a photoresist through a mask on which the desired channels are drawn in transparency. (b) Fabrication of the top part of the channel using PDMS. (c) Assembly of the two parts of the channel by sealing the PDMS channel onto a flat surface. Source: Bdmsl.stanford.edu.

A.2 Fabrication of the all-PDMS microfluidic channels

As seen in the chapter II, the lithography technique used for the fabrication of the hydrogel particles requires the microchannel to have all PDMS walls. It ensures the presence of an inhibition layer close to the walls due to the permeability of PDMS to oxygen which prevents the particle to stick on the walls and allows the fiber to flow in the channel. The channel is composed of two parts: the top of the channel and the bottom. The top part is obtained by pouring PDMS with 20 wt% of crosslinkers and is then half cured for 40 minutes in an oven at 70°C. The bottom part of the channel is fabricated by spin-coating PMDS with 5 wt% of crosslinkers on a glass slide (10 s at 500 rpm followed by 40 s at 1000 rpm). The glass slide is, as well, cured for 40 minutes at 70°C. The top part of the channel is then peeled off the wafer, the inlet and outlet holes are drilled and it is placed on the top of the PDMS-coated glass slide. The full channel is then left in the oven at 70°C for one day to fully cure.

Appendix B

Cantilever experiment

In the chapter II, we introduced the cantilever measurement technique of Young's modulus. This technique is based on the measure of the deformed shape of a beam bent by its own weight. In this appendix, we derive the mathematical formula which relates the shape of the beam and its Young's modulus.

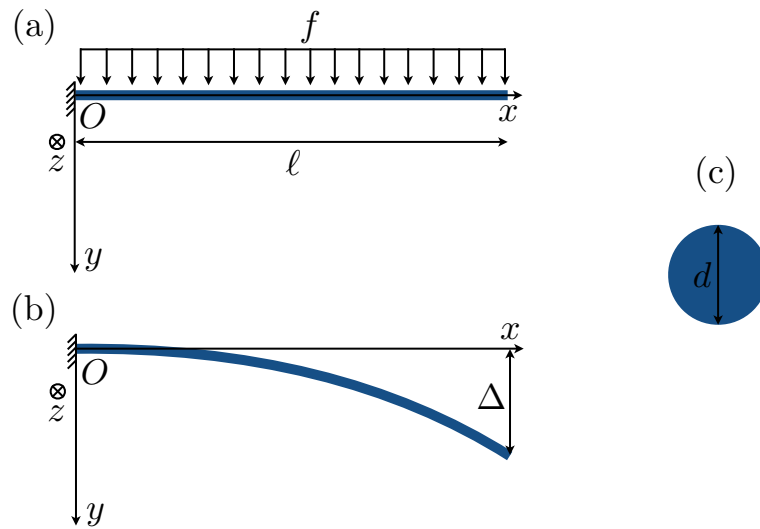


Figure B.1: Bending of a beam subjected to its own weight. (a) The beam of length ℓ is subjected to a constant force per unit length f . (b) Sketch of the deformed beam under its own weight. Δ corresponds to the deflection of the beam. (c) Sketch of the circular cross section of the beam. The diameter of the cross section is d .

We consider the general case, illustrated in Figure B.1, of a beam of length ℓ , of circular cross section (diameter d), clamped at $x = 0$. The other edge of the beam is free and the beam bends under its own weight.

The force per unit length applied on the beam of constant section is $f(x) = \rho g \pi d^2 / 4$,

with ρ the beam density and g the gravitational acceleration. One can derive the deformation of the beam $\delta(x)$ from the Euler-Bernoulli equation (equation I.15):

$$\frac{\partial^2}{\partial x^2} \left(EI_z \frac{\partial^2 \delta}{\partial x^2} \right) = \rho g \pi d^2 / 4, \quad (\text{B.1})$$

with I_z the moment of inertia relative to the z -axis and E the Young's modulus.

If the section of the beam is constant, I_z is also constant and equation B.1 becomes:

$$EI_z \frac{\partial^4 \delta}{\partial x^4} = \rho g \pi d^2 / 4, \quad (\text{B.2})$$

with $I_z = \pi d^4 / 64$ for a beam of circular cross section of diameter d . Equation B.2 simplifies further as:

$$\frac{\partial^4 \delta}{\partial x^4} = 16 \frac{\rho g}{E d^2}. \quad (\text{B.3})$$

Integrating four times equation B.4 one obtains:

$$\delta(x) = \frac{2\rho g}{3Ed^2} x^4 + Ax^3 + Bx^2 + Cx + D, \quad (\text{B.4})$$

with A, B, C and D constants that need to be derived from the boundary conditions.

The beam being clamped at $x = 0$, $\delta(x) = \delta'(x) = 0$. At $x = \ell$ the beam is free - no point force and no point torque are applied on the beam edge - and we have $\delta'''(\ell) = \delta''(\ell) = 0$. The Boundary conditions give:

$$A = -\frac{8\rho g}{3Ed^2} \ell, \quad B = -\frac{4\rho g}{3Ed^2} \ell^2, \quad C = 0 \quad \text{and} \quad D = 0. \quad (\text{B.5})$$

The shape of the deformed beam is thus given by the following equation:

$$\delta(x) = \frac{2\rho g}{3Ed^2} (x^4 - 4\ell x^3 + 6\ell^2 x^2). \quad (\text{B.6})$$

One can also derive the deflexion of the cantilever:

$$\Delta = \delta(\ell) = \frac{2\rho g}{Ed^2}. \quad (\text{B.7})$$

Using the equations B.6 and B.7 one can derive the Young's modulus of the beam by a fit of its deformed shape.

Appendix C

Convergence of numerical simulations

In order to ensure convergence of the numerical implementations presented in chapter IV, the influence of the mesh parameter m_h on the fiber velocity and the normalized maximum deflection is analyzed for $\beta = 0.8$ for the 2D and the 3D models and is depicted by Figure C.1. A convergent behavior can be observed for both models with respect to the observed quantities. Especially in the case of the 3D model, the necessary computational power increases strongly with increasing number of mesh elements. Consequently, a compromise between efficiency and accuracy leads to $m_h = 50$ ($\sim 7 \times 10^5$ mesh elements) for the 3D model and $m_h = 60$ ($\sim 3 \times 10^4$ mesh elements) for the 2D model. Note that the mesh is independent of the confinement for the 2D model.

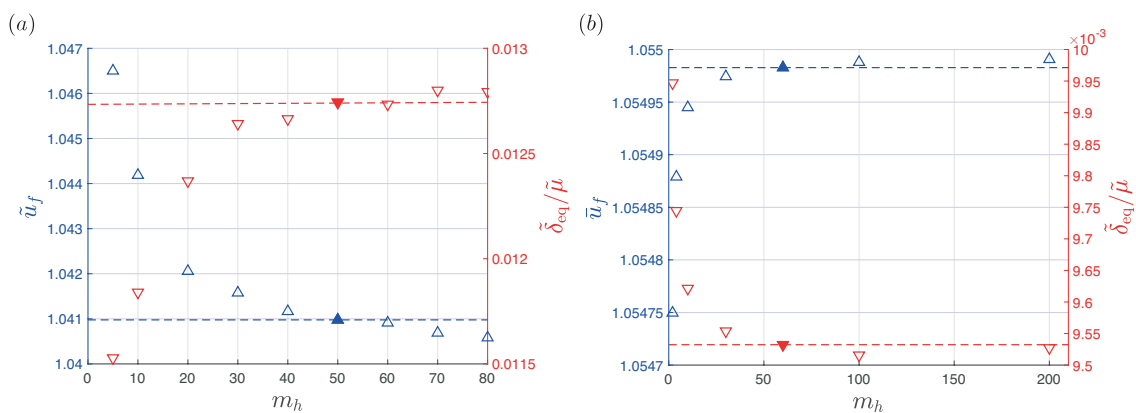


Figure C.1: Dependencies of fiber velocity \tilde{u}_f or, respectively, \bar{u}_f , and normalized maximum deflection $\tilde{\delta}_{\text{eq}}/\tilde{\mu}$ on the mesh parameter m_h for (a) the 3D model and (b) the 2D model, with $\beta = 0.8$ in both cases. The highlighted configuration is chosen for all calculations in this work and the dashed lines indicate the corresponding value for the sake of readability.

Appendix D

Velocity of a freely transported parallel fiber

D.1 Presentation of the system

As in chapter V, we consider a free fiber with a square cross section of height h , width $w = h$ and length $\ell \gg h$ transported at a velocity u_f by an external flow of mean velocity u_0 and viscosity μ . The channel has a length L , height H and width W , with $H \ll L$ et $h \ll L$. The gap in between the fiber and the top or bottom wall has an height $b = (H - h)/2$ and we define the confinement as $\beta = h/H$.

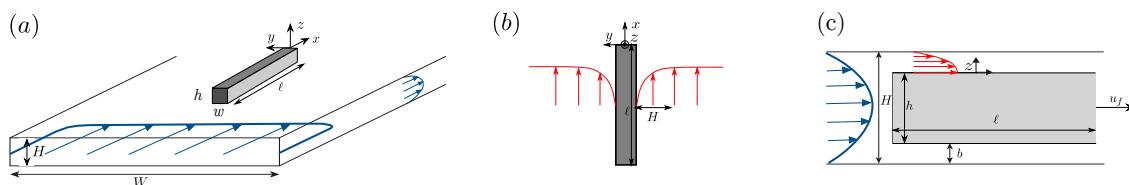


Figure D.1: (a) Geometry of the fiber and the channel. (b) Top view of the freely transported fiber. The flow on the two sides of the fiber is represented in red. (c) Side view of the system. The flow in the gap between the fiber and the top wall is assumed to be Couette-Poiseuille-like.

When the fiber is parallel to the flow direction, three different forces are acting on the fiber (see chapter V): the pressure force acting on the front and the back of the fiber F_p , the viscous forces per unit length acting on the top and bottom sides of the fiber f_t^x and the viscous forces per unit length acting on the lateral sides of the fiber f_{lat} . We will lead the calculation of these forces in the referential of the fiber.

D.2 Pressure force acting on the fiber

We consider that the presence of the fiber does not modify the pressure gradient ($w \ll W$). Thus this pressure gradient is given by $\partial p / \partial x = -\Delta p / \ell = -\frac{12\mu}{H^2} u_0$. The pressure force acting on the fiber is $F_p = \Delta p h w = \frac{12\mu}{H^2} u_0 h w \ell$.

D.3 Force on the top and bottom of the fiber

To derive the viscous force acting on the top and bottom sides of the fiber, we first describe the flow in the (x, z) plane. We assume that there is a Couette-Poiseuille flow in the gaps, and the flow in a gap is given by:

$$v_{xt}(z) = \frac{1}{2\mu} \frac{\partial p}{\partial x} z(z-b) - v_f \frac{z}{b}. \quad (\text{D.1})$$

The stress is then given by

$$\tau_t = \mu \left. \frac{\partial v_x}{\partial z} \right|_{z=0} = -\frac{b}{2} \frac{\partial p}{\partial x} - \mu \frac{v_f}{b}, \quad (\text{D.2})$$

And then the viscous force per unit length is

$$f_t^x = 2\tau_t w = -2w\ell \left(\frac{b}{2} \frac{\partial p}{\partial x} + \mu \frac{v_f}{b} \right). \quad (\text{D.3})$$

Here the factor 2 takes into account the viscous forces acting on the top and bottom sides.

From the expression of the pressure gradient we obtain:

$$f_t^x = -2w \left(-\frac{b}{2} \frac{12\mu}{H^2} u_0 + \mu \frac{v_f}{b} \right). \quad (\text{D.4})$$

D.4 Force on the lateral sides of the fiber

To determine the viscous force acting on the lateral sides of the fiber, we assume that the flow in the (x, y) plan is Poiseuille-like in a region of length H close to the fiber side (see Figure D.1).

Thus the stress acting on one lateral side of the fiber is

$$\tau_{lat} = \frac{2(u_{max} - v_f)\mu}{H} = \frac{(3u_0 - 2v_f)\mu}{H}. \quad (\text{D.5})$$

Consequently the lateral force is

$$f_{lat} = 2\tau_{lat}h = 2h \frac{2(u_{max} - v_f)\mu}{H} = 2 \frac{(3u_0 - 2v_f)\mu}{H} h. \quad (\text{D.6})$$

D.5 Determination of the fiber velocity

Assuming that f_{lat} and f_t^x do not vary along the fiber length, we determine the fiber velocity from the zero force condition:

$$f_{lat}\ell + f_t^x\ell + F_p = 0 \Leftrightarrow 2 \frac{(3u_0 - 2v_f)\mu}{H} h\ell - 2w\ell \left(-\frac{b}{2} \frac{12\mu}{H^2} u_0 + \mu \frac{v_f}{b} \right) + \frac{12\mu}{H^2} u_0 h w \ell = 0, \quad (\text{D.7})$$

with $h = w = \beta H$ and $b = \frac{1-\beta}{2} H$.

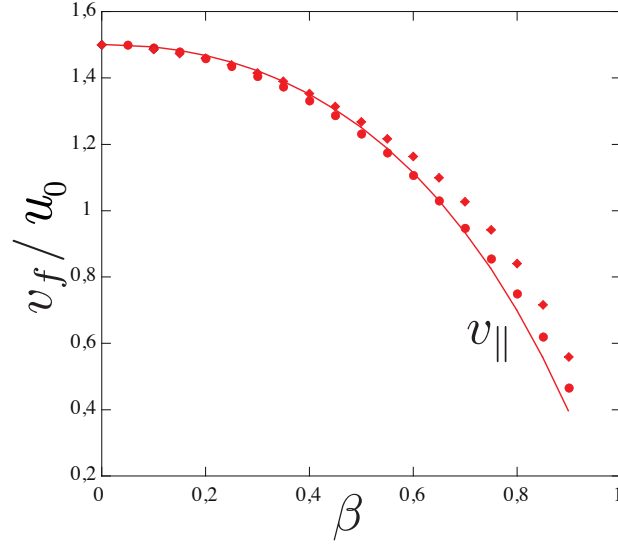


Figure D.2: Evolution of the fiber velocity as a function of the confinement. The curve corresponds to the equation D.11, the bullet (●) to a 2D simulation and the diamond (◆) to a 3D simulation. Both simulations have been done by Berthet *et al.* [13].

Equation D.7 is equal to:

$$2\beta \frac{(3u_0 - 2v_f)}{H} - 2\beta \left(-3(1 - \beta)u_0 + \frac{2}{1 - \beta}v_f \right) + 12\beta^2 u_0 = 0 \quad (\text{D.8})$$

$$(3u_0 - 2v_f) - \left(-3(1 - \beta)u_0 + \frac{2}{1 - \beta}v_f \right) + 6\beta u_0 = 0 \quad (\text{D.9})$$

$$3(2 + \beta)u_0 - 2\frac{2 - \beta}{1 - \beta}v_f = 0. \quad (\text{D.10})$$

Thus,

$$\frac{v_f}{u_0} = \frac{3(1 - \beta)(2 + \beta)}{2(2 - \beta)}. \quad (\text{D.11})$$

The evolution of the velocity as a function of the confinement is given in Figure D.2. The bullet (●) are obtained using a 2D simulation and the diamond (◆) using a 3D simulation. Both simulations have been done by Berthet *et al.* [13]. The red curve corresponds to the above calculation of the parallel fiber velocity. An excellent agreement between the simulations and the analytical expression of the fiber velocity is obtained. Thus, our simple model correctly describes the fiber velocity.

Bibliography

- [1] F. LUNDELL, L. D. SÖDERBERG & P. H. ALFREDSSON; «Fluid Mechanics of Paper-making»; *Annual Review of Fluid Mechanics* **43**, p. 195–217 (2011). ISSN 0066-4189. xi
- [2] M. V. D'ANGELO, B. SEMIN, G. PICARD, M. E. POITZSCH, J. P. HULIN & H. AURADOU; «Single Fiber Transport in a Fracture Slit: Influence of the Wall Roughness and of the Fiber Flexibility»; *Trans. Porous Med.* **84**, p. 389–408 (2009). ISSN 0169-3913. <http://link.springer.com/10.1007/s11242-009-9507-x>. xi
- [3] E. LAUGA & T. R. POWERS; «The hydrodynamics of swimming microorganisms»; *Reports on Progress in Physics* **72**, p. 096601 (2009). ISSN 0034-4885. <http://stacks.iop.org/0034-4885/72/i=9/a=096601?key=crossref.736a5c13368e75b7395f94099aead8e4>. xi
- [4] L. J. HALL, V. R. COLUCI, D. S. GALVÃO, M. E. KOZLOV, M. ZHANG, S. O. DANTAS & R. H. BAUGHMAN; «Sign change of Poisson's ratio for carbon nanotube sheets»; *Science* **320**, p. 504–507 (2008). xi
- [5] D. R. GOSSETT, W. M. WEAVER, A. J. MACH, S. C. HUR, H. T. K. TSE, W. LEE, H. AMINI & D. DI CARLO; «Label-free cell separation and sorting in microfluidic systems»; *Analytical and bioanalytical chemistry* **397**, p. 3249–3267 (2010). xii, 108
- [6] D. DI CARLO; «Inertial microfluidics»; *Lab on a Chip* **9**, p. 3038–3046 (2009). xii, 108
- [7] J. P. BEECH, S. H. HOLM, K. ADOLFSSON & J. O. TEGENFELDT; «Sorting cells by size, shape and deformability»; *Lab on a Chip* **12**, p. 1048–1051 (2012). xii, 108
- [8] G. JEFFERY; «The Motion of Ellipsoidal Particles Immersed in a Viscous Fluid»; *Proceedings of the Royal Society of London . Series A* **102**, p. 161–179 (1922)<http://www.jstor.org/stable>. xii, 22
- [9] G. K. BATCHELOR; «Slender-body theory for particles of arbitrary cross-section in Stokes flow»; *Journal of Fluid Mechanics* **44**, p. 419 (1970). ISSN 0022-1120. http://www.journals.cambridge.org/abstract/_S002211207000191X. xii, 5
- [10] R. COX; «The motion of long slender bodies in a viscous fluid part 1. general theory»; *Journal of Fluid mechanics* **44**, p. 791–810 (1970). xii, 5, 108

- [11] B. SEMIN, J.-P. HULIN & H. AURADOU; «Influence of flow confinement on the drag force on a static cylinder»; *Physics of Fluids* **21**, p. 103 604 (2009). [xii](#), [10](#), [11](#), [12](#)
- [12] SEMIN; «Interaction d ' une fibre et d ' un écoulement en géométrie confinée To cite this version : Discipline : MÉCANIQUE Présentée par Benoît Semin Interaction d ' une fibre et d ' un écoulement en géométrie confinée»; (2010). [xii](#), [10](#), [11](#)
- [13] H. BERTHET, M. FERMIGIER & A. LINDNER; «Single fiber transport in a confined channel: Microfluidic experiments and numerical study»; *Physics of Fluids* **25** (2013). ISSN 10706631. [xii](#), [11](#), [12](#), [13](#), [23](#), [25](#), [63](#), [64](#), [67](#), [72](#), [75](#), [76](#), [81](#), [137](#)
- [14] H. BERTHET; *Single and collective fiber dynamics in confined microflows*; Thèse de doctorat; Université Pierre et Marie Curie-Paris VI (2012). [xii](#), [11](#), [23](#)
- [15] D. DENDUKURI, S. S. GU, D. C. PREGIBON, T. A. HATTON & P. S. DOYLE; «Stop-flow lithography in a microfluidic device»; *Lab on a Chip* **7**, p. 818 (2007). ISSN 1473-0197. <http://xlink.rsc.org/?DOI=b703457a>. [xii](#), [25](#), [26](#)
- [16] D. DENDUKURI, P. PANDA, R. HAGHGOOIE, J. M. KIM, T. A. HATTON & P. S. DOYLE; «Modeling of oxygen-inhibited free radical photopolymerization in a PDMS microfluidic device»; *Macromolecules* **41**, p. 8547–8556 (2008). ISSN 00249297. [xii](#), [25](#), [26](#), [27](#), [29](#), [31](#), [89](#)
- [17] W. E. USPAL, H. BURAK ERAL & P. S. DOYLE; «Engineering particle trajectories in microfluidic flows using particle shape»; *Nature Communications* **4**, p. 1–9 (2013). ISSN 2041-1723. <http://www.nature.com/doifinder/10.1038/ncomms3666>. [xii](#), [14](#), [15](#), [108](#), [121](#)
- [18] J. CAPPELLO, M. BECHERT, C. DUPRAT, O. DU ROURE, F. GALLAIRE & A. LINDNER; «Transport of flexible fibers in confined microchannels»; *Physical Review Fluids* **4**, p. 034 202 (2019). [xv](#), [63](#), [125](#)
- [19] M. BECHERT, J. CAPPELLO, M. DAÏEFF, F. GALLAIRE, A. LINDNER & C. DUPRAT; «Controlling transport dynamics of confined asymmetric fibers»; *EPL (Europhysics Letters)* **126**, p. 44 001 (2019). [xv](#), [14](#), [107](#), [125](#)
- [20] H. A. STONE & C. DUPRAT; «CHAPTER 2. Low-Reynolds-Number Flows»; dans «RSC Soft Matter Series», p. 25–77 (Royal Society of Chemistry (RSC)) (2016). [2](#), [3](#), [5](#), [22](#)
- [21] E. GUYON, J.-P. HULIN & L. PETIT; *Hydrodynamique physique*; BOOK (interéditions) (1994). [2](#), [46](#)
- [22] O. S. PAK, E. LAUGA, C. DUPRAT & H. STONE; «Theoretical models of low-Reynolds-number locomotion»; *Fluid-Structure Interactions in Low-Reynolds-Number Flows* p. 100 (2015). [3](#)
- [23] E. GUAZZELLI & J. F. MORRIS; *A physical introduction to suspension dynamics*; tome 45 (Cambridge University Press) (2011). [4](#), [5](#)

- [24] W. B. RUSSEL, E. J. HINCH, L. G. LEAL & G. TIEFFENBRUCK; «Rods falling near a vertical wall»; *Journal of Fluid Mechanics* **83**, p. 273–287 (1977). ISSN 1469-7645, 0022-1120. 7
- [25] B. TEN HAGEN, F. KÜMMEL, R. WITTKOWSKI, D. TAKAGI, H. LÖWEN & C. BECHINGER; «Gravitaxis of asymmetric self-propelled colloidal particles»; *Nature Communications* **5**, p. 4829 EP – (2014)<http://dx.doi.org/10.1038/ncomms5829>. 8, 15, 108, 111
- [26] E. J. TOZZI, C. T. SCOTT, D. VAHEY & D. J. KLINGENBERG; «Settling dynamics of asymmetric rigid fibers»; *Physics of Fluids* **23**, p. 1–10 (2011). 8, 9, 108
- [27] M. PALUSA, J. DE GRAAF, A. BROWN & A. MOROZOV; «Sedimentation of a rigid helix in viscous media»; *Physical Review Fluids* **3**, p. 124 301 (2018). 9, 108
- [28] B. SEMIN, A. DECOENE, J.-P. HULIN, M. FRANÇOIS & H. AURADOU; «New oscillatory instability of a confined cylinder in a flow below the vortex shedding threshold»; *Journal of Fluid Mechanics* **690**, p. 345–365 (2012). 10
- [29] M. V. D’ANGELO, J. P. HULIN & H. AURADOU; «Oscillations and translation of a free cylinder in a viscous confined flow»; *Physics of Fluids* **25**, p. 1–18 (2013). ISSN 10706631; [arXiv:1202.5293v1](https://arxiv.org/abs/1202.5293v1). 11, 67
- [30] M. NAGEL, P.-T. BRUN, H. BERTHET, A. LINDNER, F. GALLAIRE & C. DUPRAT; «Oscillations of confined fibres transported in microchannels»; *Journal of Fluid Mechanics* **835**, p. 444–470 (2018). 13, 14, 23, 63, 64, 67, 70, 71, 72, 73, 75, 76, 78, 81, 83, 109
- [31] B. SHEN, M. LEMAN, M. REYSSAT & P. TABELING; «Dynamics of a small number of droplets in microfluidic Hele-Shaw cells»; *Experiments in Fluids* **55** (2014). ISSN 07234864. 15, 108
- [32] W. E. USPAL & P. S. DOYLE; «Scattering and nonlinear bound states of hydrodynamically coupled particles in a narrow channel»; *Physical Review E - Statistical, Nonlinear, and Soft Matter Physics* **85**, p. 1–5 (2012). ISSN 15393755. 15
- [33] W. E. USPAL & P. S. DOYLE; «Collective dynamics of small clusters of particles flowing in a quasi-two-dimensional microchannel»; *Soft Matter* **8**, p. 10676 (2012). ISSN 1744-683X. <http://xlink.rsc.org/?DOI=c2sm25931a>. 15
- [34] B. BET, S. SAMIN, R. GEORGIEV, H. B. ERAL & R. v. ROIJ; «Steering particles by breaking symmetries»; *Journal of Physics: Condensed Matter* **30**, p. 224 002 (2018). 15, 16, 108, 121
- [35] M. P. PAIDOUSSIS; *Fluid-structure interactions: slender structures and axial flow*; tome 1 (Academic press) (1998). 16, 17
- [36] O. BAUCHAU & J. CRAIG; *Structural Analysis. Solid Mechanics and Its Applications, Vol. 163 (pp. 173–221)* (Springer, Dordrecht) (2009). 16

- [37] L. LI, H. MANIKANTAN, D. SAINTILLAN & S. E. SPAGNOLIE; «The sedimentation of flexible filaments»; *Journal of Fluid Mechanics* **735**, p. 705–736 (2013). ISSN 0022-1120. http://www.journals.cambridge.org/abstract/_S0022112013005120;1306.4692. 19, 20, 102, 126
- [38] B. MARCHETTI, V. RASPA, A. LINDNER, O. DU ROURE, L. BERGOUGNOUX, É. GUAZZELLI & C. DUPRAT; «The deformation of a flexible fiber settling in a quiescent viscous fluid»; to be submitted p. 1–23 (2018). 19
- [39] X. XU & A. NADIM; «Deformation and orientation of an elastic slender body sedimenting in a viscous liquid»; *Physics of Fluids* **6**, p. 2889–2893 (1994). ISSN 1070-6631. <http://scitation.aip.org/content/aip/journal/pof2/6/9/10.1063/1.868116>. 19
- [40] J. S. WEXLER, P. H. TRINH, H. BERTHET, N. QUENNOUZ, O. DU ROURE, H. E. HUPPERT, A. LINDER & H. A. STONE; «Bending of elastic fibres in viscous flows: the influence of confinement»; *Journal of Fluid Mechanics* **720**, p. 517–544 (2013). ISSN 0022-1120. http://www.journals.cambridge.org/abstract/_S0022112013000499. 21, 23, 68
- [41] C. DUPRAT, H. BERTHET, J. S. WEXLER, O. DU ROURE & A. LINDNER; «Microfluidic in situ mechanical testing of photopolymerized gels.»; *Lab on a chip* **15**, p. 244–52 (2014). ISSN 1473-0189. <http://www.ncbi.nlm.nih.gov/pubmed/25360871>. 21, 23, 36, 37, 39, 68, 69, 111
- [42] K. B. MOSES, S. G. ADVANI & A. REINHARDT; «Investigation of fiber motion near solid boundaries in simple shear flow»; *Rheologica acta* **40**, p. 296–306 (2001). 23
- [43] C. A. STOVER & C. COHEN; «The motion of rodlike particles in the pressure-driven flow between two flat plates»; *Rheologica Acta* **29**, p. 192–203 (1990). 23
- [44] Y. LIU, B. CHAKRABARTI, D. SAINTILLAN, A. LINDNER, & O. DU ROURE; «Tumbling, buckling, snaking: morphological transitions of semiflexible filaments in shear flow»; arXiv:1803.10979 (2018). 23
- [45] O. FORGACS & S. MASON; «Particle motions in sheared suspensions: X. Orbits of flexible threadlike particles»; *Journal of Colloid Science* **14**, p. 473–491 (1959). 23
- [46] M. HARASIM, B. WUNDERLICH, O. PELEG, M. KRÖGER & A. R. BAUSCH; «Direct observation of the dynamics of semiflexible polymers in shear flow»; *Physical review letters* **110**, p. 108 302 (2013). 23
- [47] H. NGUYEN & L. FAUCI; «Hydrodynamics of diatom chains and semiflexible fibres»; *Journal of The Royal Society Interface* **11**, p. 20140 314 (2014). 23
- [48] L. E. BECKER & M. J. SHELLEY; «Instability of Elastic Filaments in Shear Flow Yields First-Normal-Stress Differences»; *Physical Review Letters* **87**, p. 198 301 (2001). 23, 127

- [49] J. K. NUNES, H. CONSTANTIN & H. A. STONE; «Microfluidic tailoring of the two-dimensional morphology of crimped microfibers»; *Soft Matter* **9**, p. 4227–4235 (2013). 27
- [50] A. PERAZZO, J. K. NUNES, S. GUIDO & H. A. STONE; «Flow-induced gelation of microfiber suspensions»; *Proceedings of the National Academy of Sciences* **114**, p. E8557–E8564 (2017). 27, 127
- [51] M. SLUTZKY, H. A. STONE & J. K. NUNES; «A quantitative study of the effect of flow on the photopolymerization of fibers»; *Soft matter* (2019). 27
- [52] C. A. SCHNEIDER, W. S. RASBAND & K. W. ELICEIRI; «HISTORICAL commentary NIH Image to ImageJ : 25 years of image analysis»; *Nature Methods* **9**, p. 671–675 (2012). ISSN 1548-7091. <http://dx.doi.org/10.1038/nmeth.2089>. 34, 55
- [53] N. QUENNOUZ; Thèse de doctorat; UPMC, Paris, France (2013). 40
- [54] B. AUDOLY & Y. POMEAU; *Elasticity and Geometry*; p. 1–35 (World Scientific Publishing Co) (2000). 40
- [55] F. GIORGIUTTI-DAUPHINÉ & L. PAUCHARD; «Painting cracks: A way to investigate the pictorial matter»; *Journal of Applied Physics* **120**, p. 065 107 (2016). 41
- [56] H. M. WYSS, T. FRANKE, E. MELE & D. A. WEITZ; «Capillary micromechanics: Measuring the elasticity of microscopic soft objects»; *Soft Matter* **6**, p. 4550–4555 (2010). 43, 53
- [57] Y. LI, E. KUMACHEVA & A. RAMACHANDRAN; «The motion of a microgel in an axisymmetric constriction with a tapered entrance»; *Soft Matter* **9**, p. 10 391–10 403 (2013). 43
- [58] Y. LI, O. S. SARIYER, A. RAMACHANDRAN, S. PANYUKOV, M. RUBINSTEIN & E. KUMACHEVA; «Universal behavior of hydrogels confined to narrow capillaries»; *Scientific reports* **5**, p. 17 017 (2015). 43, 126
- [59] J. P. GONG; «Friction and lubrication of hydrogels its richness and complexity»; *Soft matter* **2**, p. 544–552 (2006). 45, 60
- [60] T. SHOAI, J. HEINTZ, J. A. LOPEZ-BERGANZA, R. MURO-BARRIOS, S. A. EGNER & R. M. ESPINOSA-MARZAL; «Stick–slip friction reveals hydrogel lubrication mechanisms»; *Langmuir* **34**, p. 756–765 (2017). 45
- [61] J. DELAVOPIÈRE, Y. TRAN, E. VERNEUIL, B. HEURTEFEU, C. Y. HUI & A. CHATEAUMINOIS; «Friction of poroelastic contacts with thin hydrogel films»; *Langmuir* **34**, p. 9617–9626 (2018). 45
- [62] M. FILONENKO-BORODICH; *Theory of Elasticity*; Dover books on physics and mathematical physics (Dover Publications) (1965). <https://books.google.fr/books?id=2akQnwEACAAJ>. 47

- [63] X. REN, R. DAS, P. TRAN, T. D. NGO & Y. M. XIE; «Auxetic metamaterials and structures: A review»; *Smart materials and structures* **27**, p. 023 001 (2018). 53, 61
- [64] Y. LI, Z. HU & C. LI; «New method for measuring Poisson's ratio in polymer gels»; *Journal of applied polymer science* **50**, p. 1107–1111 (1993). 53
- [65] J. LI; *Advances in Chemical Engineering: Characterization of Flow, Particles and Interfaces*; tome 37 (Academic Press) (2009). 53
- [66] T. BOUDOU, J. OHAYON, C. PICART & P. TRACQUI; «An extended relationship for the characterization of Young's modulus and Poisson's ratio of tunable polyacrylamide gels»; *Biorheology* **43**, p. 721–728 (2006). 53
- [67] D. C. HURLEY & J. A. TURNER; «Measurement of Poisson's ratio with contact-resonance atomic force microscopy»; *Journal of Applied Physics* **102**, p. 033 509 (2007). 53
- [68] K. EVANS; *Measurement of Poisson's Ratio* (Springer) (1999). 53
- [69] M. MORAM, Z. BARBER & C. HUMPHREYS; «Accurate experimental determination of the Poisson's ratio of GaN using high-resolution x-ray diffraction»; *Journal of applied physics* **102**, p. 023 505 (2007). 53
- [70] T. GERVAIS, J. EL-ALI, A. GÜNTHER & K. F. JENSEN; «Flow-induced deformation of shallow microfluidic channels»; *Lab on a Chip* **6**, p. 500–507 (2006). 56
- [71] R. M. JONES; *Buckling of bars, plates, and shells* (Bull Ridge Corporation) (2006). 57
- [72] M. E. ONYIA & E. O. ROWLAND-LATO; «Determination of the Critical Buckling Load of Shear Deformable Unified Beam»; *International Journal of Engineering and Technology* **10**, p. 647–657 (2018). <http://www.enggjournals.com/ijet/docs/IJET18-10-03-026.pdf>. 57
- [73] S. CAI, Y. HU, X. ZHAO & Z. SUO; «Poroelasticity of a covalently crosslinked alginate hydrogel under compression»; *Journal of Applied Physics* **108**, p. 113 514 (2010). 60
- [74] Y. HU, X. ZHAO, J. J. VLASSAK & Z. SUO; «Using indentation to characterize the poroelasticity of gels»; *Applied Physics Letters* **96**, p. 121 904 (2010). 60
- [75] S. GABLER, J. STAMPFL, T. KOCH, S. SEIDLER, G. SCHULLER, H. REDL, V. JURAS, S. TRATTNIG & R. WEIDISCH; «Determination of the viscoelastic properties of hydrogels based on polyethylene glycol diacrylate (PEG-DA) and human articular cartilage»; *International Journal of Materials Engineering Innovation* **1**, p. 3–20 (2009). 60
- [76] A. G. LEE, C. P. ARENA, D. J. BEEBE & S. P. PALECEK; «Development of macroporous poly (ethylene glycol) hydrogel arrays within microfluidic channels»; *Biomacromolecules* **11**, p. 3316–3324 (2010). 60

- [77] R. SKALAK & P. BRANEMARK; «Deformation of red blood cells in capillaries»; *Science* **164**, p. 717–719 (1969). 63
- [78] C. POZRIKIDIS; «Numerical simulation of the flow-induced deformation of red blood cells»; *Annals of biomedical engineering* **31**, p. 1194–1205 (2003). 63
- [79] D. VESPERINI, O. CHAPUT, N. MUNIER, P. MAIRE, F. EDWARDS-LEVY, A.-V. SALSAC & A. LE GOFF; «Deformability-and size-based microcapsule sorting»; *Medical engineering & physics* **48**, p. 68–74 (2017). 63
- [80] O. DU ROURE, A. LINDNER, E. NAZOCKDAST & M. SHELLEY; «Dynamics of flexible fibers in viscous flows and fluids»; *Annual Review of Fluid Mechanics* (2019). 66, 67, 108
- [81] A. A. S. CHAMPMARTIN & B. ABDERRAHIM; «Kinematics of a free particle moving between two parallel walls»; *Proceedings of the ASME 2010 3rd Joint US-European Fluids Engineering Summer Meeting* p. 1–9 (2010). 67
- [82] E. WANDERSMAN, N. QUENNOUZ, M. FERMIGIER, A. LINDNER & O. DU ROURE; «Buckled in translation»; *Soft Matter* **6**, p. 5715 (2010). ISSN 1744-683X. <http://xlink.rsc.org/?DOI=c0sm00132e>; 1003.5832. 67
- [83] N. QUENNOUZ, M. J. SHELLEY, O. DU ROURE & A. LINDNER; «Transport and buckling dynamics of an elastic fiber in a viscous cellular flow»; *Journal of Fluid Mechanics* p. 387–402 (2014). ISSN 0022-1120. 67
- [84] H. BERTHET, O. DU ROURE & A. LINDNER; «Microfluidic Fabrication Solutions for Tailor-Designed Fiber Suspensions»; *Applied Sciences* **6**, p. 385 (2016). ISSN 2076-3417. <http://www.mdpi.com/2076-3417/6/12/385>. 68
- [85] L. CHEN, K. X. WANG & P. S. DOYLE; «Effect of internal architecture on microgel deformation in microfluidic constrictions»; *Soft Matter* **13**, p. 1920–1928 (2017). ISSN 1744-683X. <http://xlink.rsc.org/?DOI=C6SM02674E>. 69
- [86] G. XU, K. S. WILSON, R. J. OKAMOTO, J.-y. SHAO, S. K. DUTCHER & P. V. BAYLY; «Flexural Rigidity and Shear Stiffness of Flagella Estimated from Induced Bends and Counterbends»; *Biophysj* **110**, p. 2759–2768 (2016). ISSN 0006-3495. <http://dx.doi.org/10.1016/j.bpj.2016.05.017>. 70
- [87] D. COOMBS, G. HUBER, J. O. KESSLER & R. E. GOLDSTEIN; «Periodic Chirality Transformations Propagating On Bacterial Flagella»; *Phys. Rev. Lett.* **89**, p. 118102 (2002). <https://link.aps.org/doi/10.1103/PhysRevLett.89.118102>. 70
- [88] J. GITTES, F; MICKEY, B; NETTLETON, J; HOWARD; «Flexural Rigidity of Microtubules and Actin Filaments Measured from Thermal Fluctuations in Shape»; *The Journal of Cell Biology* **120**, p. 923–934 (1993). 70
- [89] B. N. PERSSON, C. GANSER, F. SCHMIED, C. TEICHERT, R. SCHENNACH, E. GILLI & U. HIRN; «Adhesion of cellulose fibers in paper»; *Journal of Physics: Condensed Matter* **25**, p. 045002 (2012). 70

- [90] B. BET, R. GEORGIEV, W. USPAL, H. B. ERAL, R. VAN ROIJ & S. SAMIN; «Calculating the motion of highly confined, arbitrary-shaped particles in Hele-Shaw channels»; (2017)<http://arxiv.org/abs/1710.04561>; [1710.04561](https://doi.org/10.1016/j.cmpfluid.2014.10.016). 74
- [91] M. NAGEL & F. GALLAIRE; «Boundary elements method for microfluidic two-phase flows in shallow channels»; *Computers and Fluids* **107**, p. 272–284 (2015). ISSN 00457930. <http://dx.doi.org/10.1016/j.cmpfluid.2014.10.016>; [arXiv:1411.2728v1](https://arxiv.org/abs/1411.2728v1). 75
- [92] F. GOSSELIN, P. NEETZOW & M. PAAK; «Buckling of a beam extruded into highly viscous fluid»; *Physical Review E* **90**, p. 052718 (2014). 92
- [93] M. PAIDOUSSIS; «Dynamics of cylindrical structures subjected to axial flow»; *Journal of sound and vibration* **29**, p. 365–385 (1973). 98
- [94] M. MASAELI, E. SOLLIER, H. AMINI, W. MAO, K. CAMACHO, N. DOSHI, S. MITRAGOTRI, A. ALEXEEV & D. DI CARLO; «Continuous inertial focusing and separation of particles by shape»; *Physical Review X* **2**, p. 031017 (2012). 108
- [95] G. D’AVINO, F. GRECO & P. L. MAFFETTONE; «Particle migration due to viscoelasticity of the suspending liquid and its relevance in microfluidic devices»; *Annual Review of Fluid Mechanics* **49**, p. 341–360 (2017). 108
- [96] T. W. SECOMB; «Blood flow in the microcirculation»; *Annual Review of Fluid Mechanics* **49**, p. 443–461 (2017). 108
- [97] B. LIEBCHEN, P. MONDERKAMP, B. TEN HAGEN & H. LÖWEN; «Viscotaxis: microswimmer navigation in viscosity gradients»; *Physical review letters* **120**, p. 208002 (2018). 108
- [98] H. C. FU, T. R. POWERS, R. STOCKER *et al.*; «Separation of microscale chiral objects by shear flow»; *Physical review letters* **102**, p. 158103 (2009). 108
- [99] F. CANDELIER & B. MEHLIG; «Settling of an asymmetric dumbbell in a quiescent fluid»; *Journal of Fluid Mechanics* **802**, p. 174–185 (2016). 108
- [100] T. KUROKAWA, T. TOMINAGA, Y. KATSUYAMA, R. KUWABARA, H. FURUKAWA, Y. OSADA & J. P. GONG; «Elastic- Hydrodynamic Transition of Gel Friction»; *Langmuir* **21**, p. 8643–8648 (2005). 126
- [101] P. M. LUGT & G. E. MORALES-ESPEJEL; «A review of elasto-hydrodynamic lubrication theory»; *Tribology Transactions* **54**, p. 470–496 (2011). 126
- [102] C. LIU; «Elastic constants determination and deformation observation using Brazilian disk geometry»; *Experimental mechanics* **50**, p. 1025–1039 (2010). 126
- [103] A. A. BANAIEI, M. E. ROSTI & L. BRANDT; «Numerical study of filament suspensions at finite inertia»; *arXiv preprint arXiv:1903.12007* (2019). 127

